Finite Element Models of Volcano Deformational Systems Having Structural Complexity

Erika Ronchin

FINITE ELEMENT MODELS OF VOLCANO DEFORMATIONAL SYSTEMS HAVING STRUCTURAL COMPLEXITY

Erika Ronchin

PhD Thesis

Universitat de Barcelona
Department of Geodynamics and Geophysics

Barcelona 2015

Universitat de Barcelona
Faculty of Geology
Department of Geodynamics and Geophysics
Doctorat en Ciències de la Terra

FINITE ELEMENT MODELS OF VOLCANO DEFORMATIONAL SYSTEMS HAVING STRUCTURAL COMPLEXITY

Erika Ronchin
PhD Thesis

Thesis Directors

Prof. Joan Martí Molist

Prof. Timothy Masterlark

Institute of Earth Sciences Jaume Almera - CSIC
Department of Geophysics and Geohazards

Thesis Tutor
Prof. Joan Manuel Vilaplana Fernández

Barcelona 2015

Acknowledgements

First of all, I want to thank the great person and scientist without whom this dissertation would never have come to an end, my co-director Dr. Tim Masterlark. Tim, I do not have enough words to express my gratitude for all the help you gave me in these years, and particularly in the last months. Thank you for listening to me, for understanding, and for discussing my ideas with enthusiasm. All this greatly improved my work. Thank you for inspiring me and encouraging me through the long work of this dissertation and for the long conversations on the phone. Thank you for having reformulated the "it's easy" into "it's straightforward" through the years: it was nice and it worked, making me think that maybe it's not easy but it's reachable, and making me look ahead to where I could find the answers. And, of course, thank you for hosting me at the University of Alabama.

I also want to thank my director Dr. Joan Martì for teaching me so much about calderas in the field, for wisely encouraging me to pursue field work, but also for supporting me when I decided to continue the research in the FEM direction. Also, I want to thank my friend Dr. Gerardo Aguirre for having greatly improved my understanding of how calderas work. Whenever I build a new model, I always keep in mind the geology and structures I saw in the field with you.

Thank you to Dr. James Quick, who had the great intuition of introducing me to Tim Masterlark and the University of Alabama. A thank you goes to the friends and colleagues that I met at UA: Drs. Wei Tao, Sarah Needey, Christodoulos Kyriakopoulos, Kristin Hellem Hughes, Jonathan Stone, Theodor Donovan, and Jay Sui Tung M.Sc., for their discussion, inputs, good questions, and help. And I want to thank the friends and colleagues of the Institute Jaume Almera: Drs. Joan Andujar, Fidel Costa, Stefania Bartolini, Rosa Sobradelo, Lavinia Tunini, Dario Pedrazzi, Stepanie Barde-Cabusson, Xavier de Bolòs, and Eva Cabrera for their support, guidance though the difficult choice of the topic and their help in many burocratic steps. A thank you goes also to Dr. Ilazkiñe Iribarren Rodríguez for the last-minute suggestions.

Special thanks go to Dr. Adelina Geyer, who put me back on the right track when I got lost, and pushed me by showing me how to look at the work in a constructive way.

I must not forget to thank all those who gave me technical help with the analyses and models, making this study possible: Dr. Maria Charco for her advice about the inversion, Dr. Chiara Montagna for her model advise (in the end the chamber is not cubic as expected! ;)), Dr. Stephan Arndt for his support with ABAQUS topography, and Dr. John Dawson, who so generously provided the InSAR data. I would like to thank also those who provided information that greatly helped me to understand the dynamics of Rabaul caldera: Drs. Wally Johnson and Caroline Bouvet De La Maisonneuve. In this sense, a special thank you goes to Dr. Steve Saunders for sharing his ideas and giving advice for the understanding of Rabaul system.

A warm thank goes to the friends who hosted me during the months I was back in Trieste, giving me a nice office and, most importantly, fun, lovely, and enjoyable days. In particular, I want to thank the Prof. Princivalle for always welcoming me, Prof. DeMin for the interesting discussions

about the Rabaul structures and petrography, Davide (Prof. Lenaz) for always being my reference point there, and Dr. Filippo Parisi for being the best officemate ever.

Thank you to the CSIC for founding my research and allowing me to pursue it and thank you to the friends who first helped me, addressing me to the Group of Volcanology of Barcelona, and making the beginning possible: Drs. Joachim Gottsmann and Roberto Carniel.

I want also to thank the friends who in these years listened to me, supported me, and greatly encouraged me: Drs. Silvina Guzmann, Olaya Garcia, and Roberto Sulpizio for the extra self-confidence trainings. I'm also very grateful for the discussions with Dr. Adriano Nobile and Benedetta Antonielli that pushed me back with new enthusiasm on the difficult task of the Quadtree reduction algorithm for the InSAR data. Thank you to Julie Herrick for making the impossible possible and find impossible papers.

A great thank you goes to Tobi Meinel, the man who in the last three years was always there for me, comforting me, helping me to reorganize the thousands of ideas, making me think that it was possible, always supporting me, giving me the time, the space, and the state of mind to find new strategies and finally finishing the work.

Last, I want to thank my family that saw me struggling during the sinuous path of this work and that was always there for support and love. Thank you so much to Viviana, Tino, Savi, Fabia, Enzo e Nonno Nino.

Contents

List of Figures

List of Tables

List of abbreviations

1-D	one-dimensional
2-D	two-dimensional
3-D	three-dimensional
a.s.l.	Above sea level
ALOS	Advanced Land Observing Satellite
b.s.l.	Below sea level
BB	Blanche Bay
BBCC	Balche Bay Caldera Complex
BBCC	Blanche Bay Caldera Complex
BMHGZ	Baining Mountain Horst and Graben Zone
Bmt	Baining Mountain block
BP	Before present
C	Compressibility
CAE	Computer-Aided Engineering
cm	centimeter
DEM	digital elevation model
E	Young's modulus or Modulus of Elasticity
EDM	Electronic Distance Meters
E_{dy}, ν_{dy}	dynamic Young's modulus and Poisson's ratio
E_{st}, ν_{st}	static Young's modulus and Poisson's ratio
FE	Finite Element
FEM	Finite Element Model
G	shear modulus or modulus of rigidity
GFs	Green's functions
GIS	Geographic Information System
GPS	global position system
h	Fraction of gas exsolved
HEHS	Homogeneous, elastic, half-space
HIPHS	Homogeneous, isotropic, Poisson, half-space
IRF	Input Response Function
InSAR	Interferometric Synthetic Aperture Radar
ISS	Index of strength of stability
J	Joule
k	Bulk modulus
K	Kelvin
ka	Thousand years

Kb	Kabiu
Kbv	Karavia Bay Volcanics
kg	Kilograms
km	kilometer
LOS	Line-of-sight
LVA	Low velocity anomaly
m	meter
Ma	Million years (myr)
MAPD	Mean absolute percent difference
MI	Matupit Island
Ms	surface wave magnitude
Mw	moment magnitude
PALSAR	Phased Array type L-band Synthetic Aperture Radar
PDE	partial differential equation
PNG	Papua New Guinea
PMP	Pinned Mesh Perturbation method
PS	Persistent Scatterer
q	Mass flux
R	Universe gas constant
RMS	root mean square
RMSE	Root mean square error
RVO	Rabaul Volcanological Observatory
s1	Principal stress
SAR	synthetic aperture radar
SNR	signal-to-noise ratio
SNR	Signal to noise ratio
SRTM	shuttle radar topography mission
StaMPS	Stanford Method for Persistent Scatterers
T	temperature
Tav	Tavurvur
Tur	Turanguna
Ulos	Displacement in the line-of-sight (LOS)
Ur	Horizontal displacement
UTM	Universal Transverse Mercator
Ux	Displacement in the x direction
Uy	Displacement in the y direction
Uz	Displacement in the z direction
VARLIM	Variance Limit
VEI	Volcanic Explosivity Index
VI	Vulcan Island
VNS	Vulcan North Shore
VQT	Variance Quadtree Algorithm
VUL	Vulcan
WBF	Wide Bay Fault
WLS	Weighted least square
WLSD	Weighted and dumped least square

WTZ	Watom-Turanguna zone
WTZ	Watom-Turangunan Zone
yrs	years
β	Bulk modulus. In the inverse analysis: dumping parameter
ε	strain
λ	Lamé constant
ρ	Material density
ρ_c	Crystal density
ρ_g	Gas density
ρ_m	Magma density
υ	Poisson's ratio

Abstract and Resumen

Abstract

The main focus of this work is to build 3-D FEM models with structural complexities in order to simulate the volcanic systems in a more realistic way. We use Rabaul as an example to show the application of the methods and strategies proposed to an active volcano.

Rabaul caldera is an active, monitored, and dangerous volcanic system whose dynamics still need to be understood to effectively predict the behavior of future eruptions. Many simplified analytical models have been proposed to explain data collected during the seismo-deformational crisis of 1983-85 and the period leading to the 1994 plinian and vulcanian twin eruption. However, more realistic models, such as Finite Elements Models (FEMs), are needed to more accurately explain recent deformation and understand the actual shallow magmatic system. After the eruption of 1994 extensively destroyed the monitoring system, a new frontier in monitoring the volcano was opened when the ALOS-PALSAR sensor started to record geodetic images of the area. By inverting the InSAR data collected between February 2007 and December 2010, using linear inversions based on FEMs, we investigate the sources of surface displacement and provide insights about the actual shallow magmatic system.

FEMs are numerical models that allow for the inclusion of realistic features such as topography and mechanical heterogeneities. We provide strategies to use geophysical and geological information to build complex 3-D parts and assemble them into 3-D models having domains characterized by a heterogeneous material property distribution that resembles the geology of the area, as well as the geometric complexity of topographic relief. We propose a study of the effects of different material properties configurations on the deformation signal and on the deformation source estimates at Rabaul caldera. In this study, we compare the effects on the deformational signal and on the pressure source estimates of pressurized cavities with regular shapes or with a blob-shape cavity, inferred from the tomography and seismic data. Due to unsatisfactory results of these models in terms of new insights provided for the understanding of the shallow magmatic system at Rabaul caldera, our study extends to the generation of FEMs with an array of sources. For the purposes of this work, the deformation sources in the final model proposed take the form of an array of potential expanding/contracting fluid-filled cavities that simulate magma migration and storage at depth.

We ultimately provide a strategy to perform a linear inversion based on an array of FEM sources that allows us to identify, from a least-squares standpoint, a distribution of flux of fluid (or change in pressure) over a volume, without imposing an a-priori source shape and depth. We use Rabaul caldera deformation data and the 3-D model as an example to show the model's validity and applicability to active volcanic areas. The methodology is based on generating a library of forward numerical displacement solutions, where each entry of the library is the displacement generated by injecting a mass of fluid of known density and bulk modulus into a source of the array. The

sources are simulated as fluid-filled cavities that can accept a specified flux of magma. As the array of sources is an intrinsic geometric aspect of all forward models and the sources are activated one at a time by removing the corresponding elements, the domain only needs to be discretized once. This strategy precludes the need for remeshing for each activated source and greatly reduces computational requirements. By using an array of sources, we are not investigating the geometric and pressure parameters of a simplified, unique source with a regular shape. Instead, we are investigating a distribution of flux of fluids over a volume of potential sources responsible for the pressure changes in the medium as dictated by the data. The results allow us to image in space and time the complex shape of the source that generates the deformation without having to use any a-priori sources or a source with an over-simplified shape. This takes source modeling a step towards more realistic source models.

The application of the methodology discussed above to the Rabaul case shows a shallow magmatic system under the caldera made of two interconnected lobes located at the two opposite sides of the caldera. These lobes are suggested to be the feeding reservoirs of the ongoing Tavuvur volcano eruption of andesitic products, on the eastern side, and of the past Vulcan volcano eruptions of more evolved materials, on the western side. The interconnection and spatial distribution of sources find correspondence in the petrography of the products described in literature and in the dynamics of the single and twin eruptions that characterize the caldera.

The good results obtained from the application of the method to the real case of Rabaul caldera show that the proposed linear inversion based on the FEM array of sources can be considered suitable to generate models of the magmatic system. It can be easily applied to any volcano, because it accounts for volcano deformation without having to specify the shape of the deformation source prior to inversion.

Resumen

El objetivo principal de este trabajo es la construcción de modelos FEM 3-D que incluyen complejidades estructurales con el fin de simular los sistemas volcánicos de una forma más realista. Utilizamos la caldera de Rabaul como ejemplo para enseñar las aplicaciones de los métodos propuestos en este trabajo en el caso de sistemas volcánicos activos.

La caldera de Rabaul es un sistema volcánico activo, bajo vigilancia, y peligroso. Una completa comprensión de su dinámica es todavía hoy en día un tema pendiente y necesario para poder predecir con eficacia su comportamiento de futuras erupciones. En los últimos años se han propuesto muchos modelos analíticos simplificados enfocados a explicar los datos recogidos durante la crisis sismo-deformacional de 1983 a 1985 y el período previo a las erupciones pliniana y vulcaniana acontecidas en 1994. Sin embargo, se necesitan modelos más realistas, tales como modelos de Elementos Finitos (FEM), para explicar con mayor precisión la deformación reciente y comprender el sistema magmático superficial actual. La erupción de 1994 destruyó extensivamente la red de vigilancia de la época, pero una nueva puerta se abrió cuando el sensor ALOS-PALSAR comenzó a grabar imágenes geodésicas de la zona. Invirtiendo los datos de InSAR recolectados entre febrero de 2007 y diciembre de 2010, y mediante inversiones lineales basadas en FEMs, en este trabajo investigamos las fuentes causantes de la deformación en superficie y proporcionamos todo un conjunto de información detallada sobre el sistema magmático superficial real.

Los FEMs son modelos numéricos que permiten la inclusión de características realistas, como la topografía y las heterogeneidades mecánicas de las rocas. En este trabajo proporcionamos estrategias para utilizar la información geofísica y geológica para construir piezas complejas en 3D y para

montarlas en modelos 3-D. Los modelos construidos tienen dominios caracterizados por distribución heterogénea de materiales que respeta la geología de la zona, así como la complejidad geométrica del relieve topográfico. Proponemos el estudio de los efectos de las diferentes configuraciones de materiales en la señal de deformación y en las estimaciones de los parámetros de las fuentes de deformación de Rabaul. Por esto, comparamos los efectos sobre la señal de deformación y sobre las estimaciones de los parámetros de fuentes, las cuales están simuladas por una descompresión de cavidades de formas regulares o con forma de burbuja, inferidas a partir de la tomografía y datos sísmicos. Debido a los resultados insatisfactorios que los modelos con fuentes predeterminadas proporcionan en términos de nuevos conocimientos del sistema magmático superficial de la caldera de Rabaul, nuestro estudio se extiende a la generación de FEMs con una matriz de posibles fuentes. A los efectos de este trabajo, las fuentes de deformación del modelo final propuesto toman la forma de una serie de posibles cavidades llenas de líquido en expansión/contracción que simulan la migración y el almacenamiento de magma en profundidad.

Finalmente, proporcionamos una estrategia para llevar a cabo una inversión lineal basada en una matriz de fuentes de FE que permite investigar la distribución de flujo de líquido (o cambio de presión) sobre un volumen, sin imponer a priori una forma de fuente específica y su profundidad. Aplicamos los datos de deformación de la caldera de Rabaul y su modelo 3-D como un ejemplo para demostrar la validez de la estrategia y su aplicabilidad en otras áreas volcánicas activas. La metodología se basa en la generación de una biblioteca de soluciones numéricas de desplazamiento, en la cual cada entrada de la biblioteca corresponde al desplazamiento generado por la inyección de una masa de fluido, con densidad y compresibilidad conocida, en una fuente de la matriz. Las fuentes están construidas como cavidades en las que se aplica un flujo de magma. Como la matriz de las fuentes es un aspecto geométrico intrínseco de todos los modelos directos y las fuentes se activan una a la vez mediante la eliminación de los elementos correspondientes, el dominio necesita ser discretizado una sola vez. Esta estrategia excluye la necesidad de remallar el dominio para cada fuente activada y reduce en gran medida los requisitos computacionales. Mediante el uso de una matriz de fuentes no se investigan los parámetros geométricos y la presión de una única fuente simplificada con una forma regular. En su lugar, se investiga una distribución de flujo de fluidos a través de un volumen de posibles fuentes responsables de los cambios de presión en el medio según lo dictado por los datos. Los resultados permiten generar imágenes de la forma compleja de la fuente que genera la deformación, en el espacio y en el tiempo, sin tener que utilizar ninguna fuente con una forma a priori excesivamente simplificada. Esto lleva el modelado de fuentes un paso adelante hacia modelos más realistas.

En el caso de Rabaul, la aplicación de la metodología discutida anteriormente, muestra un sistema magmático superficial bajo la caldera hecho de dos lóbulos interconectados situados en los dos lados opuestos de la caldera. Estos lóbulos se interpretan como los depósitos magmáticos que alimentan la erupción continua de productos andesíticos del volcán Tavuvur, en el lado oriental, y de las últimas erupciones de materiales más evolucionados del volcán Vulcan, en el lado occidental. La interconexión y la distribución espacial de las fuentes encuentran correspondencia en la petrologia de los productos descritos en literatura y en la dinámica de las erupciones, de Tavurvur solo o conjuntas con Vulcan, que caracterizan a la caldera.

Los resultados satisfactorios obtenidos mediante la aplicación del método en el caso real de la caldera de Rabaul demuestran que la inversión lineal basada en la matriz de fuentes de FE propuesta puede ser considerada adecuada para generar modelos de sistemas magmáticos. Se puede aplicar fácilmente a cualquier volcán, ya que tiene en cuenta la deformación del edificio sin tener que especificar la forma de la fuente de deformación antes de la inversión.

Chapter 1

Introduction

This dissertation is about linear inversions of geodetic data based on finite elements models (FEM). The main attention of this work is focused on modeling the natural system with 3-D FEMs and on integrating them in the linear inversion. In particular, we propose strategies to build 3-D complex parts and a method to image the sub-surface changes of fluid mass (or change of pressure) over an array of finite element sources by using the same array to build the Green's function for the inversion. We use Rabaul as an example to show the application of the methods and strategies proposed to a real active volcano.

In the following section, we introduce some information about Rabaul caldera in order to outline the motivation for choosing it as case study and we provide an overview of volcano modeling to put the proposed strategies and methods in context.

1.1 Motivation and objectives

1.1.1 Rabaul caldera

Rabaul caldera is a dangerous, documented, well monitored, but still not well understood volcanic system. The Rabaul volcanic complex is located on the northeastern tip of Gazelle Peninsula, on New Britain Island, Papua New Guinea (PNG). It lies on a very active tectonic area characterized by the subduction on the New Britain Trench occurring at a very fast rate of about 10 to 13 cm/yr (*Tregoning et al.*, 1998) and the volcanic activity ongoing along the arc.

Within the New Britain arc, eight young caldera systems have been identified (*McKee et al.*, 2011), suggesting a high regional potential for eruptions. Over the last 20 kyrs, McKee et al. (2011) calculated a major (VEI 5) eruption return period of 1 kyrs, which could be even shorter due to the additional major eruptions still not defined. The intense space-time concentration of large scale volcanism on the New Britain Island, together with the presence of settlements in proximity of volcanoes capable of large-scale eruptions, points out the importance and the urgency of surveying and understanding the magmatic systems in order to cope with the inevitable outbreak of major eruptive activity (*McKee et al.*, 2011) and minimize the effects on the people.

Rabaul caldera is an active volcano complex of the New Britain arc whose recent activity culminated in 1994 with the twin eruptions of two cones at opposite sides of the submerged caldera: Tavurvur (Fig. 1.1.1, b) and Vulcan. The start of the 1994 eruptive activity, which is still ongoing at Tavurvur with sporadic eruptions, seemed already to be eminent during the seismo-deformational crises of 1983-85, but did not occur until approximately nine years later. Again, although being

closely monitored, on October 7, 2006, Tavurvur volcano unexpectedly went sub-plinian, erupting >0.2 km^3 of material in less than 6 hours, with non-unambiguous medium to short-term precursors. At that time, the only indicator that there was a build-up to major eruption was an uplift of about 14 cm in the center of the caldera that started in January 2005 (*Saunders et al.*, 2007).

Information obtained over the last 20 years include heat-flow surveys in 1989-1992 (*Graham et al.*, 1993), a seismic-refraction and tomography survey in 1997-98 (*Gudmundsson et al.*, 1999; *Finlayson et al.*, 2003; *Gudmundsson et al.*, 2004; *Bai and Greenhalgh*, 2005), a reflection survey of Blanche Bay (*Pono*, 1990), Ar-Ar dating of rock samples, as well as geothermal-geochemistry surveys (*Johnson et al.*, 2010). More recently, a petrographic study about the 2006 eruptive products provided some insights about magma chamber dynamics (*Bouvet de Maisonneuve et al.*, 2014 in press).

The 1994 eruptions produced a plume whose height was estimated to be about 18 km (Fig. 1.1.1, c) and led to the evacuation of Rabaul City. Eruptions at Rabaul caldera do not only affect the local community, infrastructures (Fig. 1.1.1, a) and the domestic aviation industry, but also international flights when ash-rich plumes enter the flight paths, as the disruption of air traffic from and to Australia during the most recent eruption of August 29, 2014, showed. Rabaul thus represents an hazard for a wide area.

Although very active, potentially very dangerous, and well monitored, the Rabaul volcanic system is not yet well understood and much work is still do be done. The Geoscience Australia is studying the feasibility of a broad-scale volcano monitoring in Papua New Guinea using InSAR images (*Romeyn and Garthwaite*, 2012) to collaborate with the Rabaul Volcano Observatory in monitoring the PNG volcanic activity, as well as Rabaul caldera.

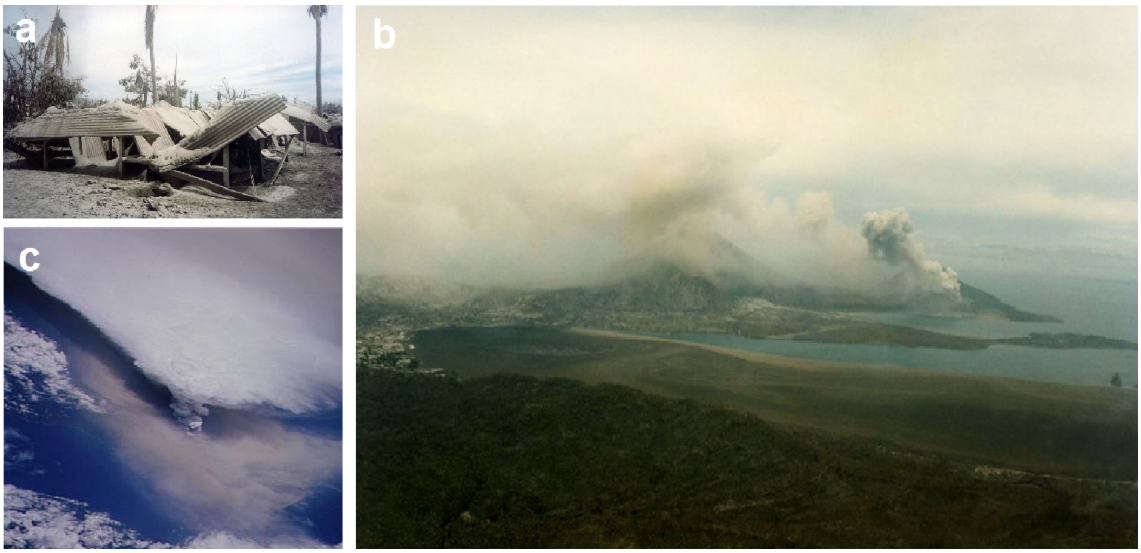

Figure 1.1.1. Effects of the 1994 eruption at Rabaul caldera.
(a) Collapse of structures. Carport, Turanguna Street, 5 October 1994 (http://www.pngaa.net/). (b) The aftermath of the eruption: pumice floating on Simpson Harbor. In the background: plume from Tavurvur (http://www.pngaa.net/). (c) Plume from Vulcan photographed from Space Shuttle; its height was estimated to be at least 18 km (http://www.geo.mtu.edu).

The 1994-95 eruption considerably disrupted the monitoring network at Rabaul, so InSAR images can greatly improve the monitoring and understanding of caldera dynamics. Rabaul caldera now is monitored by continuous GPS, leveling, tiltmeters, and a seismic network of 11 stations (www.wovo.org). From 2007, ALOS PALSAR satellite acquired SAR images of Rabaul caldera

(*Hutchinson and Dawson*, 2009), extending the ability of monitoring the Rabaul system as well as other volcanoes spread all over New Britain Island. The aim of geodetic imaging is to monitor known sources of deformation, to discover new crustal deformation processes, and to estimate the values and uncertainties of parameters that control these processes (*Hetland et al.*, 2012). In May 2011, the satellite was declared dead in orbit. Since May 24, 2014, the new ALOS-2 PALSAR is acquiring images generating great expectations for the future improvement of monitoring Rabaul and the other PGN volcanoes.

As the InSAR method is limited by the orbital passages of the satellite over the same area, it cannot be implemented into a real-time method. Furthermore, unlike the GPS technique that allows the registration of the displacements in 3-D, the InSAR method only describes the deformation in 1-D (displacements in the Line of Sight direction) and has lower accuracy (about 1 cm, improvable with time-series/stack, versus about 1 mm/yr of continuous GPS) (https://c3.nasa.gov/nex/projects/26/). Nevertheless, its strength is its ability to provide more spatially continuous information over a good spatial coverage and it has the great advantage of being cheap, free of field requirements, and able to reach inaccessible or remote areas.

Since interferograms require good coherence between the images, high latitude regions are more suitable for InSAR studies. Low latitude areas, where the land cover changes rapidly due to the tropical climate and where microwave propagation is disturbed by high water content in the atmosphere, make the application of InSAR not so easy for images acquired at C-band wavelengths (λ=5.6 cm). InSAR studies in these areas are therefore limited. As ALOS operates at L-band wavelengths (λ=23 cm), penetrating the vegetation, it allowed the first InSAR measurements at many volcanoes in the northern Andes, Indonesia, Caribbean, and Central America (Ebmeier et al., 2013 and references therein). Despite its potential as a hazard monitoring tool for numerous volcanoes in the region, this technique has yet to be applied widely in Papua New Guinea, for example to Rabaul caldera monitoring and understanding in primis. In fact, to our knowledge, a single conference abstract has been presented about deformation registered at Rabaul with InSAR (Ampana and Kimata, 2011) and no further works have been published about the topic.

1.1.2 Volcano models: state of the art

Active volcanoes provide an opportunity to observe and study natural impulse-response of dynamic systems. By simulating the magma intrusion -the impulse- with models (forward models), and comparing the obtained results (i.e. predicted deformations) to the observed data (i.e. InSAR, leveling, GPS) -the response- we can quantify parameters that describe the magma intrusion (*Masterlark et al.*, 2012). Numerical models are therefore used because they are a key to linking surface observations to inaccessible interior processes and to advancing our knowledge of volcanic area processes. In an active volcano deformational system, the interaction between the complex internal structure and the magma migration controls the deformation patterns that can be observed at the surface and can be mapped through geodetic data. Numerical models simulate the kinematic response due to magma migration and storage within the surrounding internal structure and provide a linkage between surface deformation and the movements of magma at depth.

The ability of a model to represent a natural system directly impacts the accuracy of model results. Relatively simple analytical solutions (*Mogi*, 1958; *Yang et al.*, 1988; *Okada*, 1992) and superposition of multiple deformation sources (e.g., *Lundgren and Rosen*, 2003b; *Sturkell et al.*, 2008; *Wright et al.*, 2003) are commonly used to model volcanic deformation because they provide fast, precise, and computationally inexpensive solutions. However, they are ultimately inaccurate

because their assumptions oversimplify the models. Simulating the deformation of active volcanoes is challenging due to inherent mechanical complexities associated with heterogeneous distributions of rheologic properties and irregular geometries associated with the topographic earth surface, as well as complexities of the sources. Homogenous half-space models, by definition, assume that the rocks that comprise the volcano have identical physical properties. However, volcanoes are the result of successive eruptive episodes and thus the physical properties of the rock that compose the edifice are likely to be included in wide range. For this reason, conventional homogenous half-space volcano models have recently been considered an oversimplification that could lead to misinterpretation of the derived source parameters (*Manconi et al.*, 2010; *Heap et al.*, 2014).

In order to obtain more accurate results, FE models can be used to implement the inversion of geodetic data. FEMs are known to be mathematical models capable of simulating elastic equations in arbitrary domain, partitioned to account for the 3-D distributions of elastic properties and having the irregular relief of a volcano (e.g. *Trasatti et al.*, 2003; *Meo et al.*, 2008; *Charco et al.*, 2007; *Currenti et al.*, 2008; *Hautmann et al.*, 2010; *Lyons et al.*, 2012; *Masterlark et al.*, 2012; *Ronchin et al.*, 2013). The use of finite element models (FEMs) to study volcano deformation is not new and has been used for more than four decades. Since the beginning of the application of FEMs to volcanic studies, axisymmetric and two-dimensional models were extensively used. Owing to computational limitations, the early FE studies predominantly used two-dimensional or axisymmetric modeling to optimize the limited computational resources, forcing to model the magma chamber as a regular shape cavity. As a consequence, the geometric fidelity had a large margin of improvement. Dieterich and Deker (1975) investigated prediction sensitivities to various source geometries in a homogeneous, isotropic, Poisson-solid half-space domain and concluded that horizontal components of deformation are much more sensitive to the source geometry than vertical components. Sensitivities to the geometry of the expansion source were also investigated by Yang et al. (1988). FEMs were also used to account for heterogeneous caldera configurations and structural discontinuities (*De Natale and Pingue*, 1993; *Troise et al.*, 2003; *Folch and Gottsmann*, 2006) and deformation predictions (*Bonaccorso et al.*, 2005; *De Natale and Pingue*, 1993; *De Natale et al.*, 1997; *Orsi et al.*, 1999; *Poland et al.*, 2006; *Trasatti et al.*, 2003, 2005; *Geyer and Gottsmann*, 2010). Still, many approaches for 2-D and 3-D modeling volcano crustal deformation and stress distribution are based on applying forces to homogeneous elastic or heterogeneous layered half-space, assuming horizontal layers of constant thickness and rheology. Considerable improvement of these models may be attained by taking into account 3-D variations in the rheological characteristics of the lithospheric and astenospheric layers (*Cattin et al.*, 2005; *Masterlark*, 2007; *Pedersen et al.*, 2009).

The main goal of modeling is to understand the fundamental controls that drive the dynamics of volcanic eruptions and surface deformations detected by monitoring tools (ultimately these models may provide a forecasting tool). By modeling ground-deformation data, authors provided important information on the subsurface configuration of the volcanoes' magma reservoirs and their associated hydrothermal system described through parameters that define their size, pressure, shape, and depth (*Van der Laat*, 1996). All these parameters are inverted from the deformation data using analytical (e.g. *Mogi*, 1958; *Okada*, 1992) or numerical (e.g. FEM) models. Most of the time the main goal of FEM-based or the analytical-based inversions is to find the parameters that describe the geometric parameters of a simplified cavity, its depth and its strength (change in pressure or change in volume). Some of these parameters are linearly related to the deformation (e.g. the change of pressure), so that they can be estimated with linear inversion strategies; some others are not linearly correlated to the deformation and need nonlinear estimations. This way, if we want to solve the problem in a quantitative way for all parameters, the inverse problem results in a nonlinear optimization

problem (*Charco and Galán del Sastre*, 2014). To solve this problem, Camacho et al. (2007) and Masterlark et al. (2012) proposed explorative strategies. Masterlark et al. (2012) randomly sample the 3-D parameter space for the source parameters and compile the Green's matrix with the surface displacements generated by each random source. The fact that this method requires the generation of many sources to investigate the parameter space means a high computational cost in the case the problem is approached with more realistic models like the FEMs. In a recent study, Carco and Sastre (2014) overcame this limitation by introducing a deformation source independent of the simulation mesh through three orthogonal dipoles. The algorithm that they proposed has the advantage of minimizing the computational time in fully automated schemes by preventing remeshing and the assembly the linear system of algebric equations that defines the numerical approximation (*Charco and Galán del Sastre*, 2014).

The problem of understanding the source can be addressed by imaging an amorphous distribution of point-sources over a grid of investigation. This way, the source is not defined by an a-priori geometry and there is no need to define the geometric parameters of an arbitrary, but still regular source (e.g. ellipsoid, sphere,...), leading to a more realistic interpretation of the complex deformational source. This approach is mainly suitable for analytical models, for which the solutions are quickly and easily computed and used to assemble the linear system of equations that defines the response of the model, used in the inverse scheme. Masterlark and Lu (2004a) used this strategy in a linear dumped least squares inversion scheme to retrieve amorphous clusters of deformation point-sources whose strength is magma injection, poroelastic contraction, or thermoelastic contraction. A similar approach was also successfully applied to define a distribution of point-source volume changes or mass changes by other authors (*Mossop and Segall*, 1999; *Vasco et al.*, 2002; *Camacho et al.*, 2011). The strategy is more challenging if applied to an inverse scheme based on FEMs, due to the problem of remeshing the domain for each source. Trasatti et al. (2008) overcame this problem by building a FEM of Mount Etna with cubic elements, some of which were considered potential sources. In their work, the source is generated by choosing a cubic element of the ready-mesh and loading its faces with three dipoles and three double couple forces, assembled in a stress tensor that mimic the behavior of a point source. By estimating the values of the six stress tensor parameters for each source through the inversion of geodetic data, this method allows the investigation of both changes of volume and shear displacements with no volume changes as source of deformation. However, from a computational point of view, estimating six parameters in order to define each source during the inverse analysis becomes a very expensive problem that also needs to be justified by the quantity and the quality of available data sets (*Trasatti et al.* 2008). In fact, Trasatti et al. (2008) restricted their investigation to a single point-source and, to our knowledge, they did not extend the study towards a more realistic source in further papers.

FEMs allow describing in a more realistic way the domain that hosts the sources of deformation. An efficient method for using them in an FEM-based inversion scheme still needs to be find in order to image a more realistic source through an arbitrary distribution of sources, taking advantage of the FEMs capabilities.

1.1.3 Rabaul models: state of the art

In light of the volcano models presented in the previous section, an area of study that is underrepresented for Rabaul caldera, in addition to InSAR studies, is the use of advanced models.

Most of the published models of Rabaul caldera aim to explain the magmatic system behavior during the deformation crisis of 1983-85 through analytical-based inversion of geodetic data (*McKee*

et al., 1984; *Archbold et al.*, 1988; *McKee et al.*, 1989). McKee et al. (1984) analyzed tilt and leveling data identifying two spherical sources, one under Greet Harbor with an estimated depth between 1.5 and 2 km and the second one near Vulcan at 3 km depth. McKee et al. (1989) later confirmed an estimate of 1.8 km for the source under Greet Harbor from leveling and gravity data.*Archbold et al.* (1988), identified a point-source at 1.2 km depth southeast of Matupit Is. based on EDM and leveling data. DeNatale and Pingue (1993) explained the deformation with the response of caldera structures (central elliptical faults) to the stresses generated by a magma source at 4 to 5 km depth. DeNatale et al. (1997) confirmed the validity of the interaction between annular faults and a source at 4 km depth with a FEM. Saunders (2001) related the leveling data registered between 1990 and 1994, prior to the 1994 twin eruption, to the ascent of magma through the fractures system using a FEM and suggesting the annular seismicity as evidence of the migration of fluids into the elliptical faults. Ronchin et al. (2013) investigated the uplift that occurred between 1992 and 1993 on a leveling line across Matupit Is. They used an linear inversion scheme that combined the estimation of pressure change in a complex FE cavity at 2 km depth and slip along a fault simulated with Okada analytical model (*Okada*, 1992). They concluded that the registered uplift could have been the result of the overpressure in the cavity and slip along the fault patch (*Ronchin et al.* 2013). Ampana and Kimata (2011) defined the more recent activity of Rabaul system, using a Mogi model and InSAR data of the post-eruptive deformation of 2006 eruption, as a deflation source at 2 km depth under Greet Harbor.

Although FEMs are widely used to model deformation at volcanoes to help the understanding of the dynamics of magmatic systems, only three works have been published about Rabaul caldera using FEMs (*Saunders*, 2001, 2005; *Ronchin et al.*, 2013). Furthermore, to our knowledge, no studies have been recently published about the continuous recent deformation registered at Rabaul caldera.

Despite Rabaul's almost constant activity since the 1994 eruption, models of Rabaul caldera, mostly analytical, are mainly focused on explaining the deformation registered during the deformational crisis of 1983-85 and the period just before the 1994 eruption. In light of the recent Tavuvur eruption of August 29, 2014, which led to the evacuation of the communities near the volcano (Smithsonian Institute), new models are needed in order to model the recent deformation registered and give some insights about the actual activity of the shallow magmatic system. The fact that Rabaul volcanic system is dangerous but well monitored, as well as poorly understood but sufficiently documented, makes of Rabaul caldera a very interesting subject for the application of finite elements models and ultimately for PhD research.

1.1.4 Goals

Choosing an a priori model is a prerequisite for both forward and inverse modeling and the choice of model configuration strongly influences results and their interpretations. For this reason, in designing a FEM, special attention has to be paid in defining the configuration of boundary conditions, loads, and material properties. Internal structures, loading processes, end effective boundary conditions of a volcano control the deformation that we observe on the Earth's surface. Considerable improvement of these models may be attained by taking into account 3-D variations in the rheological characteristics of the lithospheric and asthenospheric layers (*Cattin et al.*, 2005; *Masterlark*, 2007; *Pedersen et al.*, 2009). Understanding how the heterogeneous distribution of material properties could affect the displacement signal at Rabaul caldera is the first step to understand the observed deformation. The first aim of this study is thus to provide a complex 3-D model of Rabaul caldera that integrates all studies available for the area: geological, structural, petrological, tomographic, seismic, and

previous interpretation of the observed deformations. The goal is to capture the full complexity of the material properties distribution in a FEM capable of reproducing the observed displacements and image the structure of the interior magma chamber. The methods presented here allow us to construct deformation models that integrate seismic models with geologic observations, in an effort to achieve a deeper understanding of active volcanoes.

As the best information about the position, size, and shape of the magma chamber can be inferred from the tomography and the distribution of shallow earthquake in the caldera, we use them to build a magma cavity with an irregular blob-like shape. The goal is to understand if very the complex magma chamber inferred from geophysical data could better simulate displacements at Rabaul with respect to simpler shapes commonly used to describe magma chambers (e.g. sphere, prolate ellipsoid, oblate tri-axial ellipsoid) and if there are any limitations to the information that they can provide about the shallow magmatic system.

A higher goal is to complement the approach proposed by Masterlark and Lu (2004a) with a FEM geometry similar to that proposed by Trasatti et al. (2008) in order to be able to perform a linear dumped least square inversion with a FEM-generated Green function. The aim is to calibrate the flux of magma (or change in pressure) through an array of sources and thus image the magma chamber as a distribution of flux of mass (or pressure changes). This would give a more realistic model of the magma chamber allowing a better understanding of the shallow magmatic system, at the same time avoiding the ad hoc trial and error approach using magmatic pressure sources with a-priori definition of shape, volume, and position. This model can be used to understand the stress distribution and the rupture mechanisms in Rabaul volcanic system. This is needed because, although well monitored, Rabaul until now erupted unexpectedly after short premonitory signals. Thus, a better understanding of the magmatic system is needed in order to forecast future eruptions.

The FEM-based inverse analysis proposed in this work is a straightforward and inexpensive strategy applicable to any volcanic system. In addition, nowadays most of the commercial softwares can deal with the same splines and lofting operations used for the construction of the Rabaul model parts are made in Abaqus/CAE. This way, the same strategies proposed in this dissertation may be easily used with other FE model softwares.

1.2 Approach to the problem

In this work, we study the Rabaul shallow magmatic system by combining linear elastic 3-D FEMs and InSAR data into a linear inverse scheme. Complications on forward models are due to: non-uniform elastic structure effects, topography, complex geometry, viscoelasticity, poroelasticity, and thermoelasticity. We are going to consider the first three of them.

A model is always a simplified way to describe the world around us in order to understand it better. In describing the geological process by a simple model, the first decision to make is the number of dimensions (spatial or temporal) (*Stüwe*, 2007). The choice of using 3-D models is driven by the complexity of the topography and of the structures of the Rabaul caldera system imaged by geophysical investigations, geological surveys, and petrographic studies. By wanting to take into account all previous studies, such a complex problem cannot be simplified, and thus has to be solved using a spatial 3-D model. Three-dimensional models are difficult to design, as well as hard to understand, to explain, and to show graphically. This is why 3-D analyses involve integration of many software packages and scripts (*Stüwe*, 2007). Therefore, beside Abaqus, we use Python and IDL to write procedures and illustrate the results.

The construction of parts having complex geometries is performed in Abaqus CAE by inte-

grating the lofting and Boolean operations with a Python script that automates the construction of the splines using discrete geo-referenced control points obtained from geologic maps, earthquakes location, and tomographic images as described in Ronchin et al. (2013). The capability of Abaqus CAE is thus implemented with a Python script that allows for automated execution of hundreds of commands necessary for importing the control points and generating the splines of parts having substantial geometric complexities.

As the InSAR image available for this study consists of more than 55,000 data, a number too big to perform an inversion analysis, we need to reduce it to a more manageable number. The data reduction is here performed using an algorithm based on a Quad-tree reduction, written in IDL specifically for this work. In order to preserve the information of the signal west of the caldera after the reduction, the algorithm rewards the scatterers that have higher stability of movements in the time investigated.

Finally, the FEM-based inversion is both applied to the investigation of a single source parameter (change of pressure or change of mass), assuming an a-priori well-defined source in shape and depth, and to the investigation of a 3-D distribution of multiple sources over a grid of sources, using a procedure based on damped least squares.

1.3 Structure of the dissertation

This work is structured in seven different parts, each of them representing a fundamental aspect of the scientific investigation:

1. **Introduction**: this chapter introduces the general topic of this study, the motivations, the goals, and the approaches use to solve the problem and reach the goals. Rabaul caldera and its impact on the society are also explained, as well as the importance of studying the area and the need of a method that integrates complex 3-D FEMs and geodetic data into an inverse procedure in order to image a more realistic magma chamber.

2. **Rabaul geology, volcanic activity, and data**: this part is dedicated to the collection of information to describe the study area and build the 3-D models. It includes a regional tectonic setting in which Rabaul caldera is located; it describes the geological setting of the caldera, the magmatic system and its historic volcanic activity past and recent. It also includes a brief description of the InSAR method and the description and a study of the deformational data used in this work.

3. **Methods**: describes all the methods used and implemented to study and interpret the data deformation of volcanic areas (e.g. construction of geometric bodies, InSAR reduction, inversion methods, and FE array of sources at the base of the FEM-based inversion).

4. **Results for the Rabaul caldera**: collects all the results obtained by applying the methods and strategies described in chapter 3 to the study of Rabaul deformation data. Results of the effects of elastic heterogeneities distribution on the inversion of InSAR data for Rabaul caldera during the period 2007-2010 are presented, as well as the results of the application of a FEM model with an array of sources to the linear inverse scheme.

5. **Discussion**: in this section all results are summarized and discussed. The main goal of this section is to find and understand where and why some models fail to predict the observed deformation. Comparison with data and observations from other disciplines (i.e. petrology, dynamics of the eruptions) are integrated into the discussion helping us to identify the best models and better understand the Rabaul shallow magmatic system.

6. **Conclusions, recommendations, and future works**: this section is a collection of main conclusions. Recommendations for results interpretations are also provided, as well as topics

for future works.

7. **References**: list of references cited in the text.

Chapter 2

Rabaul geology, volcanic activity, and data

2.1 Tectonic setting of New Britain and Gazelle Peninsula

Rabaul caldera is a volcanic complex located at the northeastern tip of Gazelle peninsula, at the northeastern end of New Britain Island, Papua New Guinea (Fig. 2.1.1). New Britain Island is a sector of the oceanic island arch generated along the active convergent plate boundary that extends from the north coast of New Guinea to Gazelle Peninsula in the north east of New Britain Island (*Denham*, 1969; *Emeleus*, 1977). New Britain volcanic island, with the typical elongated arcuate shape, is considered to be the volcanic arc generated by the subduction of Solomon plate under South Bismark plate to the NNW along the presently active convergent plate (Fig. 2.1.1). Besides the shape, other features of a typical island arc are present: an oceanic trench (New Britain Trench), an incline zone of earthquake foci dipping beneath the island (*Curtis*, 1973a; *Denham*, 1969; *Patia*, 2004; *Johnson and Molnar*, 1972), and a belt of volcanism along the north coast (*Johnson*, 1979; *Wiebenga*, 1973). The curved axis of New Britain Island, concave to the north, appears to stop in the northeast of the island, where a narrow low-lying isthmus between Open Bay and Wide Bay connects the arc to the eastern part of the island: the Gazelle peninsula, which is considered to be a dislocated block (*Johnson et al.*, 2010).

The Solomon plate subduction, northward under a pronounced bend in the New Britain Trench (*Frohlich*, 2006), is the main tectonic feature that dominates the region. *Cooper and Taylor* (1989) presented cross sections of the bend that occurs near New Ireland and New Britain. Using focal mechanism and the distribution of earthquakes, they showed a coherent and continuous subduction on both sides of the bend to about 100 km depth. A v-shaped notch in the seismicity extending from 150 km downward may indicate a tear in the lithosphere along the fold hinge, which accommodates northeast subduction beneath Bouganville and northwest subduction beneath New Britain (*Cooper and Taylor*, 1989). The tear is also clearly defined by *O'Kane* (2008), although the gap he defines using more recent seismological data seems narrower than the one described by *Cooper and Taylor* (1989). The distance between the south coast of central New Britain and the trench axis is fairly constant at about 50 km, but increases abruptly at Wide Bay to about 100 km, corresponding to the north-westward strike-slip displacements of the Gazelle Peninsula and to the beginning of the trench bending southward. Thus, Blanche Bay is about 200 km away from the closest point of New Britain Trench axis, where it changes its trend bending through about 75°

south of New Ireland and running down the southwestern side of Bouganville Island (*Johnson et al.*, 2010).

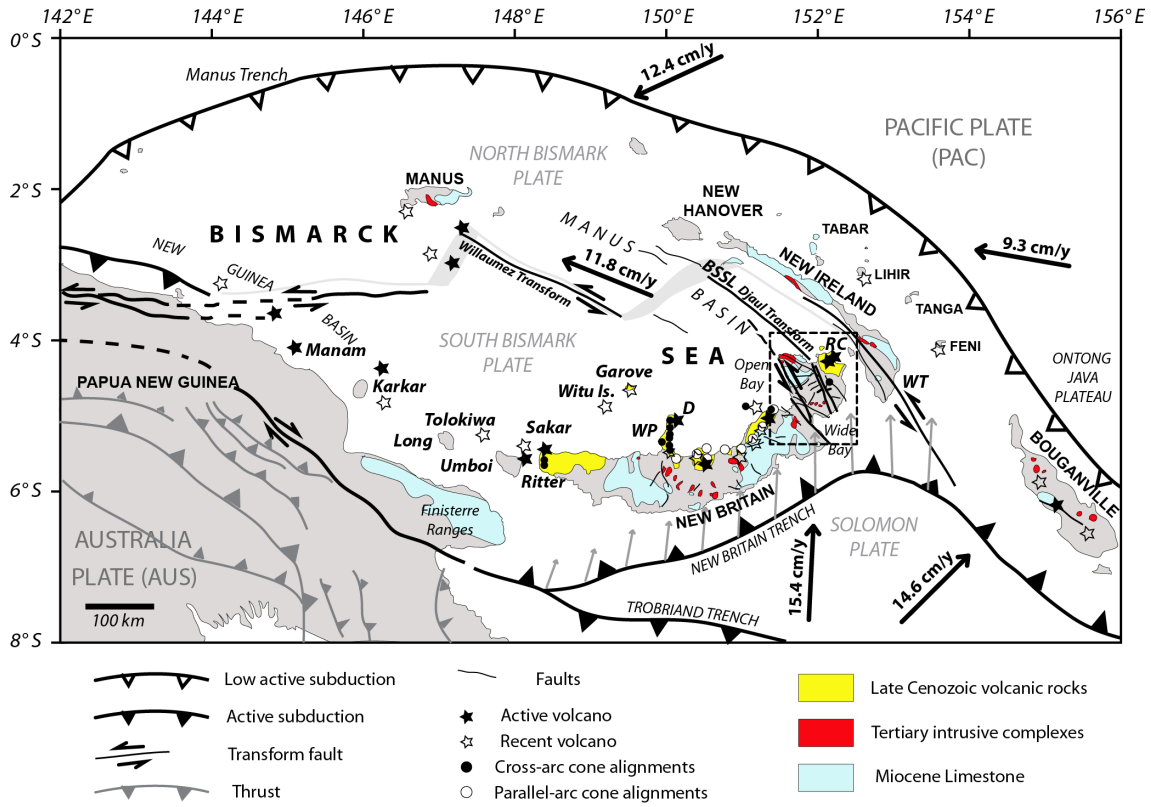

Figure 2.1.1. Location map showing the regional tectonic setting of the Bismask Volcanic Arc in the New Britain region modified from Lee and Ruellan (2006) and Park et al.(2010). *Location map showing the regional tectonic setting of the Bismask Volcanic Arc in the New Britain region modified from Lee and Ruellan (2006) and Park et al. (2010). From west to east, some of the modern and recent volcanoes are indicated with filled or hollow stars, respectively. Volcanic centers of the New Britain volcanic arc are subdivided into cross-arc cone alignments and parallel-arc cone alignment, black filled and hollow dots, respectively. They include among, others: Willaumez Peninsula (WP) composed of north-south cross-arc alignment of volcanoes, Dakatawa (D), Rabaul Caldera (RC). Gazelle peninsula in squared dashed box. The Late Cenozoic volcanic rocks (yellow), the volcanic centers of New Britain, and fault patterns are modified from Macnab (1970), D'Addario et al. (1976), and Lindley (1988). Miocene limestone (sky-blue) and Tertiary intrusive complexes (red) modified from Griffin (1983), Kroenke (1984) and Lindley (2006). Predicted motion of the Solomon Sea Plate at the New Britain Trench (gray arrows) relative to the South Bismarck Plate, modified from Tregoning et al. (1998), show the transition of the direction of the subduction along the New Britain Trench. Motion of plates (solid black arrows) relative to the South Bismarck Plate modified from Park et al. (2010). WBF: Wide Bay Fault system; WT: Weitin Transform system; BSSL: Bismark Sea Seismic Lineation.*

The tectonic plate velocities in the New Britain region are exceptionally high: Solomon Sea (140 mm/yr northeast), Pacific (110 mm/yr northeast), Australian (110 mm/yr northeast), South Bismark (80 mm/yr northeast), (*Bird*, 2003; *McKee et al.*, 2011; *Tregoning et al.*, 1998). In this context, Solomon Sea slab under New Britain takes place with a dip that is slightly steeper towards the southwestern part of the slab, as shown by maps of slab-top contours which widen towards the northeastern part (*Cooper and Taylor*, 1989; *Johnson et al.*, 2010; *Syracuse and Abers*, 2006). *Krause* (1973) calculated a doubling of convergence rate along the New Britain Trench from 6.2 cm/yr in the southwestern area to 12.4 cm/yr in the northeast consistent with a relative pole of rotation (*Johnson et al.*, 2010). *Tregoning and McQueen* (2001) and *Wallace et al.* (2004) confirmed

this trend. Later, *Tregoning et al.* (1998) calculated a variation of convergence rates from 8 cm/yr to 15 cm/yr. Different models of the Solomon subduction disagree about the trend of variation of subduction rate and direction along the New Britain Trench. The subduction was found to vary along the trench either with discontinuous changes (*Abers and McCaffrey*, 1994) or smoothly from 20º oblique in the west to normal eastward along the trench, and becomes very oblique when the trench turns sharply southward (*Tregoning et al.*, 1998), thus producing the bending of the trench. As answer to the oblique subduction of Solomon plate, strike-slip movements were recorded by *Denham* (1969) and *Curtis* (1973a) from shallow earthquakes (58-65 km) along the New Britain Trench . Sinistral strike-slip motion and arc-normal tensional stresses associated with the Ms 7.1 central New Britain earthquake in 1985 (*Mori and McKee*, 1987a) were also recorded as answer to the oblique subduction.

2.1.1 Regional tectonic evolution

Papua New Guinea (PNG) is a complex tectonic region at the convergence of the Australian and Pacific Plates. Up to four minor plates may be trapped in this collision in response to the convergence of the two major plates generating a wide region of active and dormant volcanoes and intense, frequent earthquake activity at all depths (*Tregoning et al.*, 1998).

The complexity of the area, its high tectonic activity, the lack of detailed publications of geological and structural studies, and the limitation of geophysical data in defining only the very recent plate movements led to different -sometimes contrasting- interpretations of the tectonic evolution of the area. At least eight plate tectonic models based on geology and seismicity have been proposed for the region (*Curtis*, 1973b; *Davies et al.*, 1984; *Hamilton*, 1979a; *Johnson and Molnar*, 1972; *Krause*, 1973; *Tregoning et al.*, 1998). As pointed out by *Lindley* (2006), plate boundaries in the New Guinea region are mainly defined by the distribution of earthquakes recorded since 1964 (*Curtis*, 1973a; *Denham*, 1969; *Johnson and Molnar*, 1972) and only more recently (since 1990), GPS observations have been used to constrain movements across these plate boundaries (*Tregoning*, 2002; *Tregoning et al.*, 1999, 1998, 2000). As *Lindley* (2006) points out, earthquake records restricted to such a limited period cannot possibly define all structures related to the Tertiary tectonic evolution of the New Guinea islands region, thus making the tectonic reconstruction difficult.

According to the recent tectonic reconstruction of Bismark Sea, the northern New Guinea region is thought to have developed from two lines of arc (*Lee and Ruellan*, 2006) with opposite polarity. The geology of New Britain has been interpreted in terms of reversal arc polarity during the Miocene (*Johnson et al.*, 2010) based on paleomagnetic results (*Falvey and Pritchart*, 1982) and plate-tectonic reconstructions (e.g *Kroenke*, 1984). The origin of proto-New Britain starts in late Eocene/early Oligocene and is related to the formation of the Melanesian arc (Fig. 2.1.2). The proto-New Britain arc is thought to have initially formed as a result of southward subduction of the Pacific Plate (PAC) under the Australian Plate (AUS), with the Solomon Sea in the back arc (*Hall*, 2002; *Tregoning et al.*, 1998; *Yan and Kroenke*, 1993). Proto-New Britain and proto-New Ireland were considered to be side-by-side in the Outer Melanesian Arc at this time (*Lee and Ruellan*, 2006). The original alignment of the New Britain fragments together with that of New Ireland Island defined the volcanic axis of the West Melanesian Island Arc that appears to have been active throughout most of the Oligocene, perhaps into the earliest Miocene (*Kroenke*, 1984). Due to the absence of recognizable volcanoes, the volcanic axis of the arc is thought to be best determined by the Miocene intrusions representing the plutonic phase of the arc volcanism (*Kroenke*, 1984; *Page*, 1976). Kroenke (1984, page 37) suggested that the cessation of arc volcanism in early Miocene (about

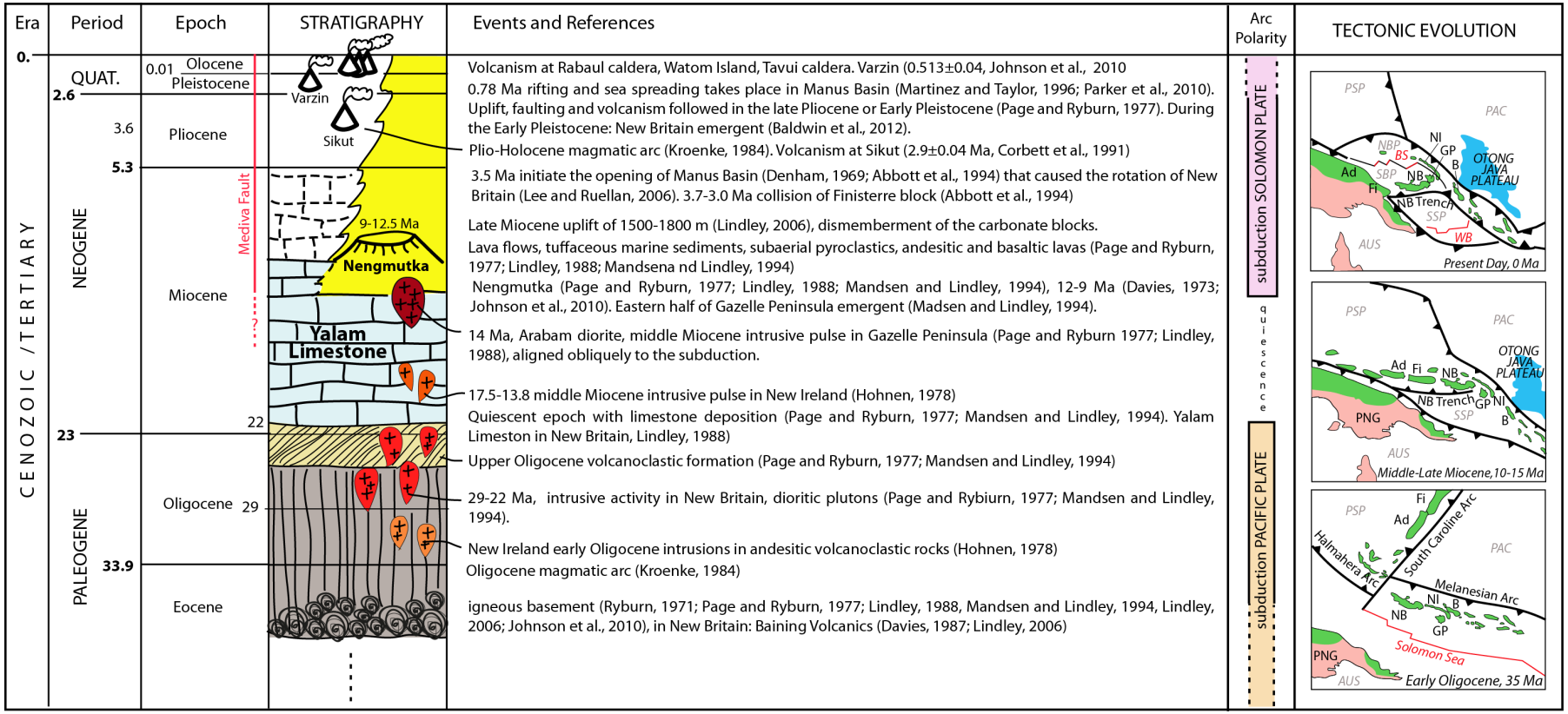

Figure 2.1.2. Stratigraphy and regional tectonic evolution

In the stratigraphic column: the brown-gray layer (intermediate and basic pillow lavas, breccias) and pale yellow layer (volcanoclastic products) represent the igneous basement intruded mainly by dioritic plutons. Red and orange simplified plutons represent the intrusions in New Britain Island and New Ireland Island, respectively. Sky-blue bricks represent the limestone formed during the period of quiescence. Lindley (1988, 1989) suggests that the limestone and the Miocene volcanic products (yellow) are partially coeval, but horizons of volcanic products have not yet been recognized within the limestone, so the lateral boundary is marked with a dashed line. In the right column three insets show three stages of the tectonic evolution: Early Oligocene, 35 Ma (Hall, 2002; Hill and Hall, 2003); Middle-Late Miocene, 15-10 Ma (Francis and Deibert, 1988; Abbott, 1995; Hall, 2002); and the Present Day, 0 Ma, modified from Hall (2002). Green areas are mainly arc, ophiolitic, and blocks formed at plate margins during the Cenozoic; the Otong Pacific Plateau is represented by a sky-blue area, and pink areas are parts of the Australian continental margins (Hall, 2002). Adelbert block (Ad), Finisterre block (Fi), New Britain Island (NB), New Ireland Island (NI), Gazelle Peninsula (GP), Bouganville Island(B), Pacific Plate (PAC), Philippine Sea Plate (PSP), Solomon Sea Plate (SSP), Australian Plate (AUS), South Bismarck Plate (SBP), North Bismarck Plate (NBP), Woodlark Basin (WB), Bismarck Sea(BS). The end of the Pacific Plate subduction is based on the fact that the West Melanesian Island Arc is thought to be active throughout most of the Oligocene, perhaps into the earliest Miocene (Kroenke, 1984). After a period of quiescence, the Solomon Plate subduction started in the Middle Miocene.

22 Ma) could have been related to the entry in the subduction zone of large oceanic plateaus, like the Otong Java Plateau, that, due to their great thickness of the lithosphere, where unable to bend, terminating the subduction and ceasing the arc volcanism. In fact, the Ontong Java Plateau, the world's largest volcanic oceanic plateau, comprises a thick sequence of basaltic lava flows overlain by 1 km of pelagic sediments (*Davies*, 2012). After the cessation of both subduction and volcanism, the Miocene was, for the most part, a relatively quiescent epoch characterized by limestone deposition in the New Britain and New Ireland areas (*Page and Ryburn*, 1977). A short lived rifting event that caused the translation of Manus Island to its present position could have been the input of intrusive pulse registered in New Ireland and New Britain in the middle Miocene (*Johnson et al.*, 2010). The new northward subduction, still active, started in the middle Miocene (*Francis and Deibert*, 1988; *Abbott*, 1995; *Johnson et al.*, 2010) and led to the formation of the New Britain trench and the New Britain volcanic arc. While for *Hill and Hall* (2003) the counterclockwise rotation of New Britain and New Ireland was induced by the spreading of the Salomon Plate during the Pliocene only, for *Lee and Ruellan* (2006) the counterclockwise rotation of proto-New Britain that moved it to its west-east oriented actual position south of New Ireland, appeared to be a consequence of the opening of Bismarck Sea initiated around 3.0-3.7 Ma (*Lee and Ruellan*, 2006). The Bismark Sea (BS) opening began with the formation of the New Guinea Basin in the west due to the collision of the Finisterre Range with northern New Guinea (*Abbott et al.*, 1994a; *Lee and Ruellan*, 2006). Only in the last 0.78 Ma or so (*Martinez and Taylor*, 1996; *Park et al.*, 2010) the rifting and the seafloor spreading took place in the Manus Basin generating the plate boundary north and east of the Gazelle Peninsula between the North Bismark and South Bismark Plates, initially called Bismark Sea Seismic Lineation-BSSL (*Denham*, 1969). This boundary is understood in terms of left-lateral, strike-slip motion and related extensional movements (*Johnson et al.*, 2010). At about the same time, southeast from the New Britain Trench across the Solomon Sea, the Woodlark Basin (WB) had also been opening since at least 3.5 Ma (*Weissel et al.*, 1982). Since 3.5 Ma, northward subduction of the Solomon Sea has resulted in arc magmatism in the New Britain and some authors related the formation of the Manus Basin within the Bismark Sea to a back-arc basin formation (*Closs*, 2005; *Hill and Hall*, 2003; *Taylor*, 1979) that started to displace the South Bismark plate (which contains the presently active New Britain arc) to the southwest relative to the Pacific Plate.

2.1.2 Stratigraphy and main structures of New Britain Island and Gazelle peninsula

The New Britain arc is a relatively long-lived feature with volcanism active during the late Eocene, late Oligocene, and Mio-Pliocene (*Lindley*, 1988) related to arc subduction with opposite polarity. Thus, New Britain as a whole is an oceanic island arc whose lower crust age and composition are in fact unknown. It also remains unclear how much of New Britain is the result of volcanic construction during the Melanesian Arc formation, prior to the opening of the Bismarck Sea, and how much of the construction is the result of volcanism related to Solomon plate subduction (*Park et al.*, 2010). The actual volcanism is related to the subduction of the Solomon Sea Plate and occurs behind the remnant Paleogene arc, which also includes the island of New Britain (*Hoffmann et al.*, 2008). The first, and only, systematic nation-wide regional geological mapping was conducted between 1956 and 1973 by the Australia's Bureau of Mineral Resources, Geology and Geophysics (BMR) and, in the latter years, the Geological Survey of Papua New Guinea, and coincided with the emergence and general acceptance of plate tectonics (*Lindley*, 2006). The early geological maps of the area completed by *Macnab* (1970), *Davies* (1973) and *Lindley* (1988) were followed by more detailed maps

compiled during some mineral exploration by *Corbett et al.* (1991), and *Madsen and Lindley* (1994). In summary, the stratigraphic column relative to New Britain island shows an igneous basement consisting mainly of upper Eocene to upper Oligocene volcanic rocks and associated sediments (intermediate and basic pillows lava, breccias and volcanoclastics with numerous lenses of coralline limestones) intruded mainly by dioritic plutons and partly mantled by extensive Miocene limestones, upper Tertiary (Pliocene) volcanic and sedimentary deposits, and quaternary (Pliocene-Holocene) volcanoes (*Ryburn*, 1971; *Page and Ryburn*, 1977; *Griffin*, 1983; *Lindley*, 2006; *Johnson et al.*, 2010).

The Basement outcrops extensively throughout New Britain (Baining volcanics) (*Lindley*, 2006). *Madsen and Lindley* (1994) regarded the rocks of the basement as typical of embryonic island arc, overlain by upper Oligocene volcanoclastic formations and intruded by upper Oligocene-lower Miocene dioritic plutons. This intrusive igneous activity occurred between 22 and 29 Myrs (*Page and Ryburn*, 1977) in New Britain, while in New Ireland a thick pile of adesitic volcanoclastic rocks was laid down and later intruded in the early Oligocene (*Hohnen*, 1978). During the low to mid Miocene, the cessation of both the subduction and volcanic activity allowed the accumulation of thick carbonate sequences on a platform extended across much of the region (*Madsen and Lindley*, 1994) including the Gazelle Peninsula. Exception is the Arabam diorite intrusive pulse that occurred at 14 Ma in the Gazelle peninsula of New Britain (*Page and Ryburn*, 1977) and between 13.8 and 17.5 Ma in the Lemau district of New Ireland (*Hohnen*, 1978). These Tertiary intrusive complexes in the New Ireland and New Britain islands, mainly having taken place during the Miocene, are oriented obliquely to the New Britain Trench and show a general decrease in age in a northwest direction along the trend (*Lindley*, 2006) . Another exception to the deposition of the platform is that at this time the eastern half of Gazelle Peninsula was emergent and shoshonitic andesitic to rhyolitic ashflow sheet covering a 600 km^2 area erupted from a caldera complex (Nengmutka volcanics) (*Madsen and Lindley*, 1994). In fact, volcanism resumed along the length of New Britain in the late Miocene or early Pliocene; during this period, tuffaceous marine sediments were intercalated with subaerial pyroclastics and andesitic-basaltic lavas (*Page and Ryburn*, 1977) and marine and terrestrial sediments (*Griffin*, 1983). *Macnab* (1970) also described volcanic eruptions in the central part of Gazelle peninsula in late Miocene-Pliocene lava flows and ash flow tuff semi-welded tuff of dacitic-andesitic composition. Lindley (1988; 1989) reported that the 14 Ma Arabam diorite (*Page and Ryburn*, 1977), the youngest intrusive event in New Britain, is partly coeval with Nengmutka volcanics. This would mean that Nengmutka volcanics are also contemporaneous with the middle Miocene Yalam limestone in the Gazelle peninsula. As horizons of Nengmutka volcanics have not yet been recognized within the limestone, some authors suggested that the beginning of the volcanism is more probable in the late Miocene (*Davies*, 1973; 9-12.5 Ma as suggested by *Johnson et al.*, 2010).

In the late Miocene, the regional uplift resulting from the tectonic activity along the edge of the Pacific Plate and the influx of volcaniclastic sediments due to the presence of a discontinuous volcanic arc may have caused the death of the reef complex (*Lindley*, 2006). The following quaternary volcanism in New Britain, that define the eastern part of the Bismarck volcanic arc, produced rocks of typical island-arc affinities (*Baldwin et al.*, 2012). The arc volcanis in the central part of New Britain Island has taken place above an exceptionally wide range of depths of the Wadati-Benioff zone: from about 100 km deep at the southern volcanic front, closer to the submarine trench don to about 600 km in the northwest beneath the Witu Islands (*Woodhead et al.*, 1998). The quaternary volcanic rocks from the island arc show a wide range in chemical compositions found to be the result of complex inter-play between a slab-derived flux and the melting process (*Woodhead et al.*, 1998). New Britain magmas contain a slab-derived component which, in contrast to many other arcs, is dominated by altered oceanic crust rather than by sediment (*Woodhead and Johnson*, 1993). Another

peculiar aspect of the arc and back-arc volcanic rocks of this area is that the lavas erupted from Rabaul and from the easternmost rift segments of Manus Basin are more radiogenic in terms of Sr and Pb (Woodhead et al., 1998). These geochemical signatures are thought to be a paleo-enrichment inherited from a prior episode of subduction and related volcanism. The enrichment related to this early subduction even that took place along the now-inactive Melanesian trench (*Woodhead et al.*, 1998) and that abruptly terminated in the lower Miocene (*Coleman and Kroenke*, 1981) is now mostly affecting the volcanism closer to the old inactive trench (*Woodhead et al.*, 1998).

Although the interpretation of structures through New Britain Island, and in particular in the Gazelle Peninsula, led at first to accept that compressional tectonic prevailed throughout the Cainozoic (*Macnab*, 1970; *Davies*, 1973; *D'Addario et al.*, 1976; *Dow*, 1977; *Johnson*, 1979; *Davies et al.*, 1984), *Wiebenga* (1973) suggested, through seismic and gravity survey in the New Britain-New Ireland area, that the New Britain trench and the associated structures observed in the Gazelle peninsula are generated under extensional tectonism. This was later confirmed by Lindley (1988, 1989) in his review of early Cainozoic geology of the Gazelle peninsula and by *Madsen and Lindley* (1994) in their geological mapping of Gazelle peninsula fault systems. Recently, *Lindley* (2006) suggested a left transcurrent tectonic regime to explain the existence of New Britain Trench and the extensional tectonic features of Gazelle peninsula. As the regional tectonic studies were mainly designed to understand the tectonic evolution at plates-scale of the region, subjected to large movements of tectonic plates and to dynamic evolution of tectonic borders, the explanation of peculiar local structural complexities mapped in the north eastern Gazelle Peninsula of New Britain Island was of second order of importance. So, even among the authors who suggested large movements of tectonic plates during the Pliocene-Pleistocene and an actual compressional boundary along the New Britain Trench, there is no agreement about the tectonic movements involved. Some suggested a solid motion of New Britain and Gazelle peninsula (*Curtis*, 1973b; *Taylor*, 1979) identifying the Weitin Fault system (WT, New Ireland) as plate border between North Bismark and South Bismark plate, while others proposed the Wide Bay Fault system (WBF, New Britain) as plate border, suggesting a relative movement between the Gazelle peninsula and the southern part of New Britain Island (*Tregoning et al.*, 1998). *Lindley* (2006) didn't agree with the theory of large plates movements; he observed that the present-day disposition of Miocene carbonate slabs does not support the significant movements between New Britain and New Ireland proposed by *Taylor* (1979),*Curtis* (1973b), and *Struckmeyer et al.* (1993). In fact, despite their location in a tectonically dynamic area, the large slabs of formerly extensive Miocene platform have been preserved intact and appear to have undergone a gentle tilting and a regionally uniform uplift in the order of 1500-1800 m a.s.l. since the upper Miocene (*Lindley*, 2006). This suggests that New Ireland and New Britain have undergone gentle tilting and uniform uplift.

As Rabaul caldera is located in the Gazelle Peninsula, the next paragraphs will summarize the main structures of this area. The first maps of Gazelle Peninsula compiled in the early 1970s proposed the existence of two main fault structures: the Baining fault segments and the northwest-trending graben (*Davies*, 1973; *Johnson et al.*, 2010; *Macnab*, 1970) and a major north-west trending fault system, which was supposed to constitute a graben in the 'neck' area (Fig. 2.1.3) of Open Bay and Wide bay that connects Gazelle Peninsula to the rest of New Britain island (*Macnab*, 1970). A transcurrent motion along these faults was suspected, but could not be proven by *Macnab* (1970) (in *Johnson et al.* (2010) and *Ryburn* (1974)). Later studies proposed different major fault structures: the northwest-trending faults in the Wide Bay and Open Bay area that define the main part of a largely strike-slip Wide Bay fault system rather that a graben, and a 10-15 km wide

Baining Mountain Horst and Graben zone (BMHGZ) characterized from west to east by the west-dipping Vudal Fault and, 5 km to the east, by the east-dipping active Mediva Fault (*Lindley*, 1988; *Madsen and Lindley*, 1994) (Fig. 2.1.3). The Mediva Fault, active since the Miocene, controlled the emplacement of middle Miocene Arabam diorite (*Lindley*, 1988; *Madsen and Lindley*, 1994) and movements continued along the Mediva fault during the late Pleistocene and recently with the displacements of the Rabaul ignibrites erupted 1400 bp (*Madsen and Lindley*, 1994). The north-south Baining Mountain Horst and Graben zone (BMHGZ) dissects the Gazelle Peninsula from coast to coast with a wide zone of north-northwesterly trending horst and graben structures, indicative of extensional tectonic regime since the lower Miocene (*Lindley*, 1988, 1989; *Madsen and Lindley*, 1994) which is also defined by well-developed north-easterly extensional joints of upper Oligocene-lower Miocene age in the central Gazelle Peninsula (*Lindley*, 2006).

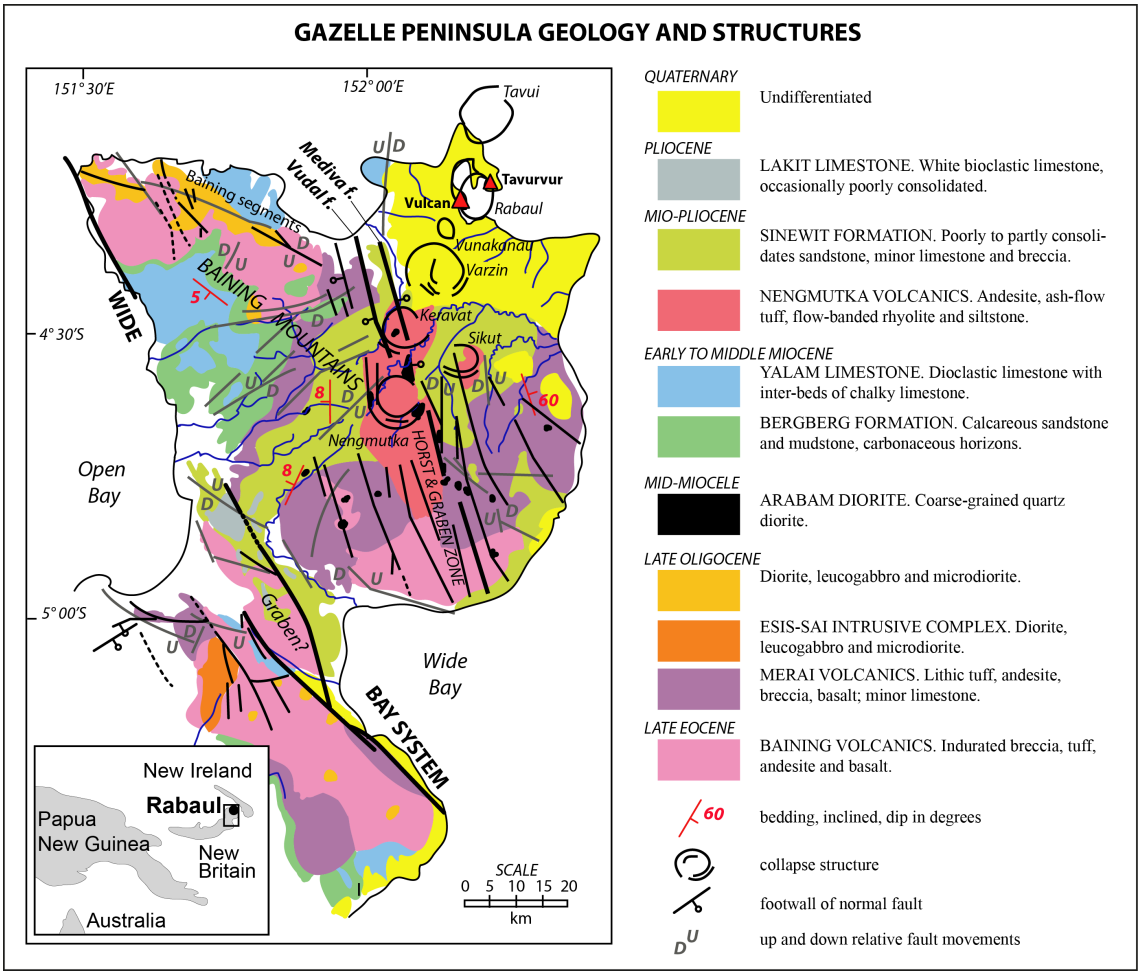

Figure 2.1.3. Simplified geological map of Gazelle Peninsula area, east New Britain. *Geological map from Lindley (1988). Collapse structures of the volcanic centers in the Gazelle volcanic zone modified fromJohnson et al. (2010): Nengmutka,Keravat and Sikut (from Lindley, 1988, 1989); Varzin and Vunakanau (fromNairn et al., 1995). Dip and azimuth of geologic unit from Lindley (1988). Gray faults are adapted from Johnson et al., 2010 (from Davies, 1973; after Macnab, 1970).*

Between WBF and BMHGZ, to the west of the Horst and Graben zone, lies a crustal block with an average thickness of 18 km. To the eastern part of the Gazelle Peninsula the average depth to mantle is greater than 30 km. The Baining Horst and Graben zone coincides with a west-to-east abrupt crustal thickening and divides the Gazelle peninsula into two distinct geological provinces: the high relief of undisturbed flat-lying limestone to the west, between WBF and BMHGZ, under

which the average crustal thickness is 18 km, and the Rabaul volcanic sequences, in the eastern part of the Gazelle Peninsula, under which the average crustal thickness is 30 km (*Wiebenga*, 1973; *Finlayson and Cull*, 1973a; *Patia*, 2004; *Johnson et al.*, 2010). The west-to-east thickening of the crust beneath Gazelle Peninsula is thought to be defined by the Mediva fault (*Finlayson and Cull*, 1973a; *Wiebenga*, 1973). The presence of such a deep vertical fault suggests the deep extension of WBF and Mediva fault continuing through the crust and great vertical and lateral movements of crustal blocks (*Lindley*, 2006).

Other extensional features express local tensional stresses along the New Britain Island: the St. George's Channel, a graben that separates New Ireland from New Britain (*Brooks et al.*, 1971; *Lindley*, 2006) and the arc-normal alignment of active and extinct quaternary volcanoes along the Willademez Peninsula (*Johnson*, 1979; *Ryburn*, 1975). This volcanic alignment, together with the northerly trending extensional faults, could be the expression of an east-west crustal tension that induced the peninsula to develop in a north-trending rift zone (*Ryburn*, 1975). *Lindley* (2006) suggested that the clockwise rotation of the South Bismark plate, accommodated by the thrust and strike-slip movement along New Britain trench, can account for the documented alternating regimes of compression and extension, which are characteristic of major strike-slip systems (*Reading*, 1980).

More recent studies (*Lindley*, 2006 and references therein) pointed out that, although high angle structures predominate throughout the region and indicate major vertical movements of crustal blocks driven by extensional regimes along the arc, transcurrent movements also play an important role, especially in the Gazelle Peninsula. A left lateral motion that displaces the Gazelle Peninsula toward NW occurs along the Wide Bay Fault (WBF), which is a transcurrent fault with a documented long history of strike and dip-slip movement: sinistral strike-slip movement of 100 km was recorded since the late middle Miocene (*Madsen and Lindley*, 1994). The Weitin Fault in southern New Ireland and the transform faults in the eastern Manus Basin were thought to drive the active transcurrent motion of Gazelle Peninsula and the intraplate deformation of the South Bismark Plate (*Johnson et al.*, 2010).

The Weitin Fault is commonly considered the current active boundary between the South Bismark and North Bismark (or Pacific) plates (*Johnson et al.*, 2010) and, even if well to the east of the Gazelle Peninsula, the stresses accumulation covers a wide area. This area includes the volcanic centers, as showed by the northwestward movement of the Gazelle Peninsula with vector length decreasing toward the south-west (*Tregoning*, 2002; see also *Tregoning et al.*, 1998, 1999). Thus, magma reservoir in the Blanche Bay area may be subject to stress build-up and strain release determined by the dynamics at the strike-slip Weitin Fault to the east (*Johnson et al.*, 2010).

To include the volcanic northeastern tip of Gazelle Peninsula and the structural features oblique to the New Britain Trench (NW-SE trending), a trend of the active southeast-trending Djaul Transform Fault (DTF) in the Manus Basin was first extrapolated by *Taylor* (1979) and *Hamilton* (1979b). Later, *Taylor et al.* (1994) observed that the fracture zones curves more to the south and lines up with the Mediva fault. More recently, *Lindley* (2006), based on field geological observations, stated that onshore extensional and strike-slip vertical structures in East New Britain show no spatial or genetic relationship to the Bismark Sea Seismic Lineation (BSSL) of the Manus Basin and related transforms (e.g. Djaul Transform Fault). The still active Mediva fault, in fact, already controlled the emplacement of the middle Miocene intrusive, and the probable Nengmutka and Keravat caldera systems were localized within the BMHGZ (*Lindley*, 1988). This means that the long-lived currently active structure pre-dates the middle Pliocene commencement of the opening of Bismark Sea and it is not related to any structures of the Bismark Sea Seismic Zone.

Volcanic deposits and rocks of the Gazelle Peninsula, mapped together as the Rabaul Volca-

nis, are the main sequences forming the north-eastern lowland of the mainly mountainous Gazelle peninsula. Although ignimbrites are found in the area (*Lindley*, 1988, 1989), *Davies* (1973); *Davies et al.* (1984) and *Macnab* (1970) didn't recognize clear caldera structures in the area during their studies. The circular structural patterns found in the area are mapped in different ways in Lindley's works (*Lindley*, 1988, 1989), who defined them as Nengmutka and Keravat caldera sytems localized within the BMHGZ (Baining Mountain Horst and Graben Zone). Due to the difficulties in defining the caldera structures, the numbers and nature of eruptive sources that produced the ash-flow tuff and rhyolite lavas of Nengmutka-Keravat area remain uncertain. There are some uncertainties whether the identified arcuate structures represent complete ring faults or 'sag' structures, so *Johnson et al.* (2010), in a more conservative definition, defined these calderas as depressions. On a regional scale, since the Mio-Pliocene, volcanism in the Gazelle Peninsula seems to have gradually shifted northeastward from the central Baining Mountains to the northeastern tip of New Britain at Tavui (Fig. 2.1.3) and in particular at Rabaul caldera complex, the site of current volcanic activity (*Patia*, 2004). After Nengmutka and Keravat, the Sikut eroded stratovolcano, consisting in basaltic and andesitic lava flows (*Johnson et al.*, 2010), was active in the Pliocene (2.9±0.04 Myrs; *Corbett et al.*, 1991) and is thought to have extended into the Pleistocene (*Lindley*, 1988, 1989). Due to the poor exposure and the mantling effects of younger pyroclastic deposits, little is known about the geology of the Varzin depression and Vunakanau Basin: two eroded conical stratovolcanos are located at the south margin of the arcuate structures that are assumed to define large-scale volcanic collapses that generated the Varzin depression. The northward trending valleys that are identified as Vunkanau Basin are either interpreted to be a possible volcanic center (*Nairn et al.*, 1995) or eroded arcuate faults circumferential to the rim of the Blanche Bay Complex (*Heming*, 1974).

2.2 Rabaul caldera geological setting

Rabaul caldera is a historically active caldera system, partially occupied by a harbor, with an elliptical shape, having major and minor axes of 14 and 9 km, respectively. The maximum height of the emerged caldera scarp is approximately 450 m a.s.l. height in the south-west, whilst in the north it reaches heights between 100 m and 180 m a.s.l. in the north. The caldera floor is 295 m b.s.l. at its deepest part in Karavia Bay (Fig. 2.2.1). At least two caldera events are evident from the morphology of the elliptical scarps that host Simpson Harbour in the north-western part of Blanche bay (Fig. 2.2.1, a). The entire area is referred to as Rabaul Volcanic Complex; it includes the Watom-Turagunan Zone (WTZ) and the Blanche Bay Caldera Complex (BBCC). The BBCC is made of the complex multiple 'nested' Rabaul calderas and the hosted intra-caldera volcanoes. The BBCC dated eruptions post-date many of the volcanism of the Watom-Turagunan cones (*Johnson et al.*, 2010). Moreover, the Tavui Caldera located in St. Georges channel at the northeast of the Gazelle Peninsula, together with the volcanic centers of WTZ and BBCC forms part of the Gazelle Volcanic Zone. The main volcanic eruption types that characterize the volcanic activity at Rabaul caldera are:

- basaltic to andesitic volcanism, with local fall deposits and lava flows associated with composite cone building eruptions;
- dacitic and (rarely) rhyolitic explosive eruptions producing plinian fall deposits with proximal pyroclastic surges and widespread ignimbrite (*Nairn et al.*, 1995; *Wood et al.*, 1995;*Nairn et al.*, 1995; *Wood et al.*, 1995).

In compiling the geological maps and the effective stratigraphy of the Rabaul area, authors report serious problems due to many reasons, among those: poor exposure, unconformities, erosion, and an intense volcanic activity with simultaneous active vents. These aspects leave a number of large explosive eruptions and collapses, that led to the present shape, still unsolved (*Johnson et al.*, 2010). Despite the difficulties of mapping such an active area, authors studied the volcanic sequences and tried to reconstruct the volcanic history of the area since the early 1970s (*Heming*, 1974; *Walker et al.*, 1981). However, the first systematic geologic mapping studying the eruption history of Rabaul caldera and surrounding areas was done by *Nairn et al.* (1995).

Geologic relations document successive overlapping caldera forming events during the past few hundred thousand years accompanied by the eruption of dacitic ignimbrites, which largely filled the collapse depression (*Heming and Carmichael*, 1973; *Heming*, 1974, 1977; *Nairn et al.*, 1995). Although previous researchers (*Fisher*, 1939; *Heming*, 1974) thought that large basaltic ancestral volcanoes had grown at Rabaul prior to the caldera collapses, they found little evidence to support this concept. The events resulted in a complex caldera shape and topography, and in mechanical properties of caldera-fill succession conspicuously different from the surrounding rocks. Heming (1974; 1977) inferred that Rabaul caldera had been formed by two collapse episodes from an older basaltic volcano, the latest of which breached the caldera on its southeastern side allowing the sea to enter in the caldera and to form the harbor. Radiocarbon dating of the ignimbrites emplaced during the collapse events assigned ages of 3500 and 1400 yr BP to the collapse episodes. *Nairn et al.* (1995) confirmed the 1400 yr BP age of the youngest ignimbrite, but suggested that the 3500 age of the penultimate major eruption was not correct. Instead, they proposed an age of 7000 yr BP for the second last caldera forming eruption. Authors do not agree on the number and the age of possible collapses before the last 1.4 km collapse, but agree on the fact the last caldera event occurred 1.4 ka ago, resulting in an elliptical plan-view shape collapse structure of 9.8x7.2 km that

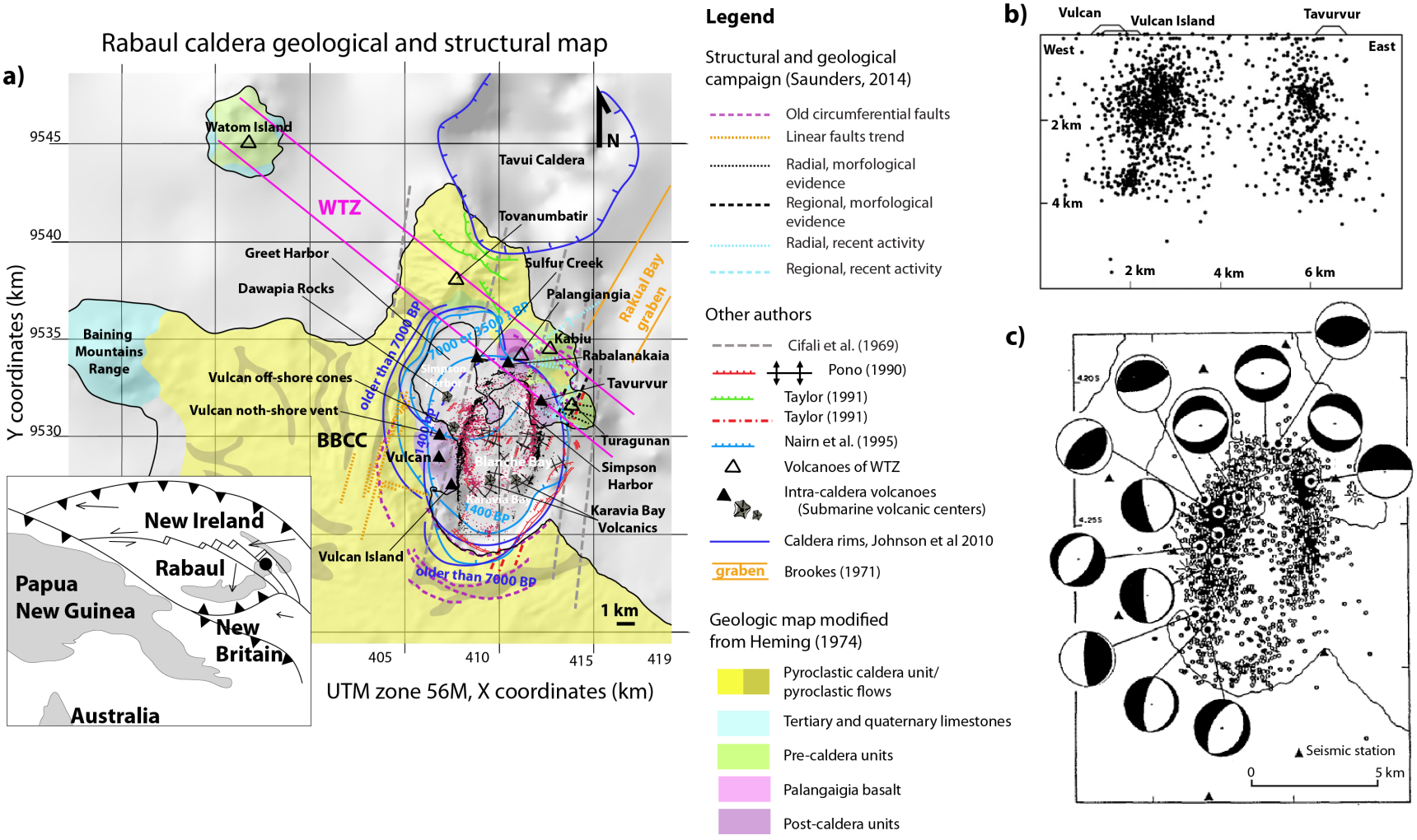

Figure 2.2.1. Gazelle volcanic zone: Rabaul caldera geology and structures.

(a) Location of Rabaul caldera (inset). Geology of the Rabaul Caldera (adapted from Heming, 1974). Active regional and local faults from different authors are also shown. The caldera borders following Taylor (1991), Nairn et al. (1995) and Johnson et al. (2010) are marked, as well as the seismicity recorded between 1971 and 1992 (with pink and black dots for epicenters shallower and deeper than 2 km, respectively). (b) W-E section showing the outward-dipping seismicity inside the caldera (Modified from Mori and McKee, 1987a). (c) fault plane solutions and locations of some of the larger caldera earthquakes (after Mori et al., 1989)

nowadays hosts most of Blanche Bay. The only well preserved scarp of the last 1.4 ka ago collapse is located 2 km to the east and north-east of the active annular seismicity (Fig. 2.2.1, a). *Walker et al.* (1981) described the products of the last collapse episode as a plinian fall deposit (Rabaul Plinian Fall) and a low aspect ratio ignimbrite (Rabaul Ignimbrite) deposited by a high-velocity pyroclastic flow to distances greater than 50 km from a source located in the center of the actual caldera, now under water. A total of 11 km^3 of pyroclastic materials were erupted during the last caldera-forming event. Later, *McKee et al.* (1985) estimated that the eruption of 1400 yr BP, which formed the caldera's present dimension and produced approximately 3 km^3 of air fall tephra and more that 8 km^3 of ignimbrite, probably enlarged a former caldera which formed approximately 6000 yr BP. The penultimate major eruption generated less voluminous deposits of airfall basaltic scoria covered by a rhyolitic ignimbrite, named Raluan Pyroclastics by *Nairn et al.* (1995). The source of the penultimate major eruption is consistent with the actual Simpson Habour (*Walker et al.*, 1981; *Nairn et al.*, 1995) although *Johnson et al.* (2010) did not exclude the possibility of the Tavui caldera as source of the Raluan Ignibrite, based on the composition evidences, on the finding of the biggest pumice (60 cm) at Cape Tavui, and on the fact that the presence of coral fragments and accretionary lapilli in the Raluan Ignimbrite is consistent with a submarine source. The Tavui caldera, roughly rectangular and north-west oriented, is about 10 km wide and 1 km deep and appears to be generated by a single caldera collapse event. The Raluan Ignimbrite and the Raluan scoria, erupted just before the ignimbrite, have no mixing evidence (*Wood et al.*, 1995) and it is likely that they were erupted from different sources. Thus, *Johnson et al.* (2010) proposed that the eruption of voluminous basal material came from Palangiagia/Kabiu area, whereas the ignimbrite came from either Tavui or Blanche Bay.

On the basis that any eruption of a particular large volume plinian deposit must have been followed by caldera formation, *Nairn et al.* (1995) proposed between five and nine possible periods of caldera formation in the last 0.1 Ma (Tab. 2.2.1), although only few topographic escarpments are visible around Blanche Bay (*Johnson et al.*, 2010). Among these escarpments, only the Karavia escarpment, thought to have formed in 1400 BP, is referred to as a caldera. It has an elliptical plan-view shape collapse structure of 9.8x7.2 km, and is thought to have taken place in the caldera center of the actual bay, breaching the eastern caldera wall and allowing the sea to flood most of the caldera area that is actual Blanche Bay. The escarpment is exposed clearly north and east of the Greet Harbour area and along the southern margin of Karavia Bay Caldera, while it is poorly defined in the northwest and the north of the sea floor between Vulcan and Rabalanakia due to the deposition of intracaldera eruptive and sedimentary material, sea floor erosion and slumping, and anticlinales formation due to the uplift of the seafloor related to the volcanic activity. The next oldest collapse feature -either a caldera or a major slump- is thought to be represented by the escarpment forming the northern and eastern side of Simpson Harbor. An older caldera escarpment of unknown age on the western side of Blanche Bay runs close, northwest of the Simpson Harbor Escarpment. Finally, a small escarpment immediately south of Karavia Bay may be either part of a caldera or a slump feature (*Johnson et al.*, 2010).

Age Years BP (^{14}C)	Event	Magma Type	Volume (km^3)
~1400	"Rabaul Pyroclastics" eruptions and **caldera collapse**	D	>10 Fall: ~3 Ign: >8
1400-4400	"Talili Subgroup", multiple (>7) pyroclastic eruptions of fine vitric ashes and pumice deposits. Roughly coeval with:	D	1?
? ? ?	Late cone-building Palangiangia lavas and scorias, and Youngest Kabiu scorias, and Turanguna scorias	B B B	0.3? 0.2? 0.1?
7000?* (3500?)**	"Raluan Pyroclastycs" eruptions and **caldera collapse**	B R	5?
?-?	"Talwat Subgroup" multiple (>4?) pyroclastic eruptions of fine ashes, roughly coeval with:	D?	0.5?
? ? ?	Older cone building Turanguna scorias, and Kabiu cone-building scorias/lavas, and Palangiangia scorias/lavas, early cone-building	B B B	0.5? 2? 1?
~15 ka	"Vunabugbug Pyroclastics" eruptions and caldera collapse?	D	5?
?	"Tatoko Subgroup" multiple (>4?) pyroclastic eruptions	D	1?
~16 ka	"Namale Pyroclastics" eruption and caldera collapse?	D	5?
<~17 ka	Four unnamed and uncorrelated pyroclastic eruptions (Kerevat)	D	?
<? 20 ka	"Kulau Ignimbrite" major ignimbrite eruptions and caldera collapse?	D	>10?
>? 20 ka	"Kabakada Subgroup" multiple (>6) pyroclastic eruptions with at least 3 (small?) ignimbrites	B? R? D	1?
?	"Vunairoto Lapilli" pyroclastic fall deposit	A/D	0.1?
37 ka	"Latlat Pyroclastics" **caldera collapse**	D	5
?-?	"Talakua Subgroup", multiple (> 7?) pyroclastic eruptions	D	0.5?
40? ka	"Barge Tunnel Ignimbrite", caldera collapse?	D	5?
?	Karavia Welded Scorias	D	1?
?-?	"Tavui Subgroup" multiple (> 5) pyroclastic eruptions with at least one ignimbrite	D/B	0.5?
0.1 Ma	"Malaguna Pyroclastics" eruption and caldera collapse'?	D/A	10?
0.1 Ma	"Boroi Ignimbntes", **caldera collapse**	D	10?
?	East Wall Lavas	D	?
0.19 Ma	"Rabaul Quarry" lavas	D	?
?	"Seismograph" lavas	B	?
0.5 Ma	"Tovanumbatir Lavas" and scoria	B	2?

B= basalt, A= andesite, D= dacite, R= rhyolite; Ign= ignimbrite

* Nairn et al., 1995

** Heming, 1974

Table 2.2.1. Early eruptive activity.
Modified from Nairn et al. (1995) and McKee and de Sain-Ours (2000).

2.2.1 Volcanoes pre- and post- caldera formation

Watom-Turangunan Zone (WTZ): volcanoes pre-caldera formation

Watom-Turagunan (WTO) Zone is a line of volcanoes that mainly predate the eruptions at BBCC. The W-T lineation is made of the Watom Island northwest offshore of the Blanche Bay and the Tovanumbatir, Palangiangia, Kabiu, and Turagunan volcanoes aligned along the north-eastern side of Blanche Bay (Fig. 2.2.1, a). The general age of these volcanic centers decreases from northwest to southeast along the WTO.

Watom is the summit of a large conical stratovolcano growing from the seafloor and building a 5-km island about 15 km from the northern rim of Blanche Bay (*Heming*, 1974). A mean Ar-Ar age of 1281±40 ka has been obtained for the late stage lava of the Watom summit (*Johnson et al.*, 2010 and reference therein). Tuvanumbatir is an old pre-caldera conical stratovolcano whose southern flank has been cut by the Simpson Harbour collapse. Its lavas were dated to be 0.5 Ma old using K-Ar radiometric dating (*Nairn et al.*, 1995). Like Watom, the subaerial part of Tuvanumbatir is late

Pleistocene, but the volcanoes must have begun their activity significantly earlier (*Johnson et al.*, 2010). Kabiu is the highest of all stratovolcanoes of the Rabaul area. It seems to be so strongly coalescent with Palangiangia that some authors regarded it as an overgrow satellite volcano on the flanks of its parent cone, Palangiangia (*Johnson et al.*, 2010). It is mantled by the deposits of 1400 BP eruption, but weakly dissected by the caldera border in comparison to Palangiangia. This has led researchers to consider Kabiu younger than Palangiangia, although Kabiu has not been historically active, while Palangiangia crater now hosts the young Rabalanakaia crater whose early eruptive activity is dated about 250-230 BP (*Johnson et al.*, 2010 and reference therein) and that still retains a quasi-permanent thermal activity (*Perry and Crick*, 1974). All three volcanoes can possibly be part of the same volcanic system whose conduits have changed over the time as a response of the caldera forming events (*Fisher*, 1939; *Johnson et al.*, 2010). Turagunan is the smallest of the large stratovolcanoes of the Rabaul area at the southeastern end of the Watom-Turagunan line. As one of its andesitic lava flows has flowed down its western flank covering the 1400 BP escarpment of Karavia Bay caldera, it is probably the most recently active of the volcanic line (*Johnson et al.*, 2010).

Almond (1981) mapped large magnetic anomalies coinciding with Tovanumbatir, Kabiu, and Turagunan. The anomaly at Tuvanumbatir was used to model the existence of a conduit dipping 60° to the south. *Almond* (1981) concluded that the distribution of anomalies was consistent with a model of three conduits radiating outwards from a source located about 10 km beneath the actual caldera. *Harrison* (1971) reported higher gravity values over Watom, Tuvanumbatir, and Palangiangia than elsewhere in the Blanche Bay area, this way explaining a distribution of rocks with greater densities, presumably corresponding to solidified conduits and dikes of mafic materials.

In the past, geologists interpreted the basaltic volcanoes of WTZ as peripheral and parasitic, thus implying that their nature and their position are somehow controlled by the caldera circumpherential faults (*Nairn et al.*, 1995; *Saunders*, 2005). Now the stratovolcanoes of the WTZ -especially Watom and Tuvanumbatir- are considered long-lived independent volcanoes producing not only basalt, but also differentiate products up to dacite as well (*Johnson et al.*, 2010). *Davies et al.* (1984) concluded that the WTZ lineation of volcanoes and the northwest- trending 'graben' that *Heming* (1974) speculated might exist immediately south-west were the result of transpressional warping. The N040°-045°W trend of the volcano alignment in the WTZ is similar to those of many geotectonic features in the region, among others: the nearly Wetin and Sapom Faults (N040°W) in New Ireland (Fig. 2.1.1), the New Britain Trench axis southwest of Bouganville, the absolute motion of the Pacific Plate, linear faults running through the Kabiu-Palangiagia area (*Davies et al.*, 1984) and parts of the Wide Bay Fault (WBF) System and Baining Fault (*Johnson et al.*, 2010). The WTZ volcanism has been interpreted by *Johnson et al.* (2010) as a cross-arc chain representing a mantle-wedge magmatism that exploits a deep, steep fracture zone of a transform fault related to the back-arc rifting of the Manus Basin that began in the Pliocene.

Volcanoes post-caldera formation: modern eruptions and intracaldera cones

Several small intracaldera volcanic cones form an irregular ring (Fig. 2.2.1, a). Some of them are submarine centers like the two submarine Karavia Bay cones east of Vulcan Island (*Taylor*, 1991), Dawapia Rocks that are considered to be the remains of the northwestern flank of a pyroclastic cone of uncertain age that possibly generated the Matupit Beds, the Vulcan off-shore cones immediately to the north east of the onshore lineation of Vulcan Island, the Vulcan Cone, and Vulcan north-shore vent. Vulcan Island was generated during the eruption of 1878 and later joined to mainland as a

result of the eruption at Vulcan Cone in 1937. The main cone and crater of Vulcan were produced largely by the eruptions of 1937 and 1994, the last one of which started at the Vulcan north-shore vent. The volcanic centers that close the irregular ring of cones on the north and east sides of the caldera are Sulfur Creek, Rabalanakaia, and Tavurvur, which is the most active center of the caldera and whose eruptions in 1878, 1937, and 1994-present were all in part synchronous with those from Vulcan (*Johnson et al.*, 2010).

2.2.2 Evolution of the magmatic system and actual magma chamber

The composition of volcanic rocks in the Rabaul area ranges from basalt to rhyolite, with presence of andesitic products. The chemical composition spread may be the result of combined fractional crystallization and crystal contamination due to mafic magma inputs in the shallow magma chamber (*Walker et al.*, 1981; *Johnson et al.*, 1995). Lavas and tephras record changes in composition from basalt to andesite, with a minimum silica content of 48.4% (*Wood et al.*, 1995). The basalts are usually porphyritic with Ca plagioclase phenocrysts. The abundance of basalts, absent in the BBCC products, is a distinctive aspect of the WTZ rock suites (*Johnson et al.*, 2010). The WTZ volcanism appears to be longer lived that that of BBCC; their high-allumina basalts suggest that they are the products of melting in the mantle wedge above the subducting lithosphere (*Wood et al.*, 1995). The rocks of older WTZ volcanoes in the northwes are slightly richer in K_2O and light rare-earth elements, this is consistent with the fact that the products of volcanoes overlying the deeper part of the Wadati-Benioff zone are more potassic than those erupted by volcanoes over the shallower part (*Johnson et al.*, 2010). Felsic compositions range from dacite (silica 69.3%) to a rare sodic rhyolite (silica 73% - 75%) that contains quartz and hornblende and is thought to be a product of co-genetic magma mixing (*Wood et al.*, 1995).

The $^{86}Sr/^{87}Sr$ values of Rabaul rocks are low, so partial melting of crustal rocks appears not to have influenced the evolution of Rabaul magmas (*Cunningham et al.*, 2009a) and fractional crystallization is considered to be the primary process that generates the andesite and dacites of the Rabaul series (*Heming*, 1974; *Wood et al.*, 1995). Heming (1974; 1977) also demonstrates that the bulk compositional variations in historic and prehistoric Rabaul volcanic products are consistent with magma evolution by fractional crystallization. In addition, *Patia* (2004) suggested the evolution of dacitic magma by fractional crystallization from parental high-allumina basaltic magma to explain the derivation of dacitic Vulcan products from a common primitive basalt that was first erupted from the older neighboring Rabaul stratovolcanoes. Exception to the fractional crystallization origin hypothesis seems to be the formation of the rhyolitic Raluan ignimbrite. *Smith and Johnson* (1981) and *Wood et al.* (1995) proposed partial melting of crustal rocks as process for the low-K_2O, sodium rich rhyolite of Raluan Ignimbrite whose similar magmas, recorded in other arc-trench systems (*Johnson et al.*, 2010), are attributed to melting of newly formed young basaltic crust (*Atherton and Petford*, 1993; *Wood et al.*, 1995). Although *Johnson et al.* (2010) did not ignore the likelihood that the closed-system crystal fractionation has at time been the dominant process at Rabaul, they pointed out that other petrogenic processes are perfectly acceptable in a young active volcanic system and should be considered, among others: melting of the crust, AFC (combined assimilation and crystal fractionation) and mixing or mingling of different magmas. Since the last caldera forming eruption about 1.4 ka ago, the shallow magma system at Rabaul Caldera has been subjected to repeated mafic magma injections that maintain a near steady-state volcanic system characterized by the presence of a large volume of dacitic magma at shallow level (*Finlayson et al.*, 2003; *Mori et al.*, 1989) and by the eruption of similar crystal-poor magma of dacitic composition. *Patia* (2004)

suggested that the repeated injection of mafic magma on a decadal time-scale would periodically heat the otherwise cooling dacite magma body and would explain the relative crystal-poor nature of the Rabaul dacites. In addition to crystal fractionation, magma mixing is therefore an important process during the compositional evolution of Rabaul magmas.

Processes occurred in the actual volcanic system have been hypothesized studying the volcanic products of the recent eruptions. *Patia* (2004) observed that the dacitic magmas erupted from both Vulcan and Tavurvur during the 1994 eruption have similar whole-rock geochemical composition and phenocryst mineral chemistry. This suggests the provenience of the magma of both vents from the same magma reservoir. Hybridized andesitic magmas have been erupted only from Tavuvur (*Patia*, 2004), so injection of a new basaltic magma is thought to be confined in the eastern/northeastern sector of a shallow dacite-filled caldera reservoir. This theory was previously proposed by *Roggensack et al.* (1996) whose study showed a moderately large volume of SO_2 flux observed in the 1994 Tavurvur plume, in contrast to low sulfure dioxide emission of Vulcan. In fact, the SO_2 was thought to be supplied to the system from the eastern side of the magma chamber by a mafic melt that may also have been the source of the mafic crystal assemblage found in Tavurvur products (*Johnson et al.*, 1995). Hybridized basaltic and dacitic magmas are prominent among the 1994 eruption volcanic products (*Johnson et al.*, 1995; *Roggensack et al.*, 1996). They are reported in older volcanic products of Latlat Pyroclastics (36 to >39 ka) and Malaguna Pyroclastics (110±20 ka) (*Nairn et al.*, 1995; *Wood et al.*, 1995). *Patia* (2004) suggested that the presence of anorthite plagioclase phenocrysts overgrown with thick andesine rims in the dacite magma composition of sample erupted during the recent prehistoric era and during the twin eruption of 1878 and 1937-1943, confirm the evidence of old basalt-dacite magma interaction events. Patia's study (2004) of dacite products erupted from Vulcan during the last historic eruptions of 1878, 1937 and 1994 showed that the 1937 dacite composition would require derivation from the 1878 dacite by a small amount of fractional crystallization (about 4.5%), whilst the more mafic composition of 1994 dacite would reflect an input of more mafic magma component. In addition, to confirm the mixing processes, *Patia* (2004) also confirmed the existence of a single dacitic magma reservoir. In fact, he showed that during the 1994 eruption, the eruption of the same dacitic magma occurred at both Vulcan and Tavuvur on the opposite side of the caldera suggesting a common magma reservoir for the volcanoes, whilst mafic magma component has been erupted only from Tavurvur. He reported that evidence supporting magma mixing/mingling are also observed in products erupted at Vulcan during 1878 and 1937-1943 twin eruptions, during which Vulcan and Tavurvur erupted dacite of similar composition points to the persistence of the same dacitic magma body for at least 15 years.

Finlayson et al. (2003) published the first tomographic images based on the RELACS (Rabaul Earthquake Location and Caldera Structure) tomograhic survery (*Gudmundsson et al.*, 2004) and identified a low velocity anomaly (<5 km/s) about 7 km wide and 3 to 5 km deep under the central part of the BBCC that was related to a magma system of 30-35 km^3 (Fig. 2.2.2). *Gudmundsson et al.* (2004) suggested caution in interpreting the anomaly as a large molten body, pointing out the anomalous attenuation registered on seismic waves coming from the center of the caldera was caused by fracturing of rocks and by the presence of geothermal fluids (*Johnson et al.*, 2010). *Bai and Greenhalgh* (2005), including additional results from the RELACS survey to the data used by *Finlayson et al.* (2003), produced new tomographic images of the Rabaul Caldera subsurface. Their results show a shallow anomaly of dimensions of 6x8x2 km at a depth between 2 and 4 km, that somewhat correspond to the deeper velocity anomaly identified by *Finlayson et al.* (2003). A second LVA is identified at depths 12-18 km, much deeper in the crust than the one identified by *Finlayson et al.* (2003) and consistent with the proposal of *Almond* (1981) that a central source at 15 km

depth could have radiated upwards and outwards the cylindrical conduits that fed Tovanumbatir, Kabiu, and Turagunan. These anomalies were identified by *Bai and Greenhalgh* (2005) as magma chambers; however they did not discuss the geological meaning of the high velocity feature that divides these chambers. Due to no direct tomographic or seismic evidence of conduits or dikes, the nature, origin, and role of the Mid-crustal LVA is still not clear. It could be an intrusive complex underplating the crust beneath the northeastern Gazelle Peninsula, could alternatively be a zone of melting, assimilation, solidification, and homogenization, or could be a remnant of an igneous system (*Johnson et al.*, 2010). A third LVA at a depth of 2-4 km with a volume of 32 km^2 north of the BBCC was interpreted as the magma chamber at Tavui Caldera. This anomaly is totally absent in the tomography of *Finlayson et al.* (2003) who concluded that Tavui Caldera is an inactive volcanic system.

Before the 1994 eruption, magma chamber models of Rabaul, based on the changes in tilt, elevation, gravity, and caldera seismicity had inferred the presence of magma bodies between Tavurvur and Vulcan at about 2 km and 4 km depth (*Patia*, 2004). The RELACS seismic tomography project essentially confirmed the presence of an anomalous low velocity region between 3-6 km depth, with lateral dimensions of 7 km, and centered between Vulcan and Tavurvur. *Patia* (2004) suggested that the geometry of this low velocity region is consistent with the presence of a magma sheet of similar extent, but thickness of the order of $\leq$1-2 km. Considering that this thickness could be interpreted as an upper bound due to smearing effects, Patia (2004) suggested that the true thickness may be possibly of order of 0.5 km or less. The relatively low water content (2.0-2.3 wt%) of dacite melt inclusions in plagioclases from the first phase of 1994 eruptions is also compatible with the shallow depth of magma sheet inferred from the tomography. In fact, it corresponds to about 50 MPa solubility limit of H_2O in silicious melts and to an estimated lithostatic load at about 3 km depth (*Roggensack et al.*, 1996; *Patia*, 2004). This depth is interpreted to be the depth at which the dacitic magma was stored and crystallized (*Patia*, 2004). From the analysis of H_2O and CO_2 contents of basaltic melt inclusions hosted in olivines derived from the first phase of 1994 Tavurvur andesite eruption, *Roggensack et al.* (1996) stated that olivine crystallization occurred at a depth greater than 5-9 km, significantly deeper than crystallization of dacitic magma. This led to the hypothesis of the presence of a deeper reservoir from which the new mafic inputs enter into the shallow (about 3 km depth) dacitic reservoir.

The estimate of the current magma reservoir volume are: 30 km^3 based on RELACS experiment results (*Finlayson et al.*, 2003), a more conservative value of 10 km^3 based on the boundaries of the seismically active caldera structure (30 km^2 ellipse) between Vulcan and Tavurvur (*Jones and Stewart*, 1997), and a magma sheet thickness of about 0.3 km (*Patia*, 2004).

2.2.3 Inside the caldera: bulge, circular seismicity, and caldera structures

In the Blanche Bay area, the earthquake activity is mainly focused along a ring-shaped zone located in the interior of the last Rabaul caldera collapse structure (Fig. 2.2.1 a, c, and Fig. 2.2.2,b). This happens also in Campi Flegrei, where the inner depression, even not apparent on the surface, has much stronger geophysical signature than the outer depression (*Acocella*, 2008 and references therein). A concentric annular shape of the seismicity, registered between 1971 and 1994, showed epicenters located around an earthquake-free area extending between Greet Harbor and Karavia Bay and defining an outward-dipping trend of nodal planes with dips range from ~45° to ~85° (*Mori and McKee*, 1987a). *Almond and McKee* (1982) first described two facing arcuate zones of hypocenters based on the locations of the 1977-1982 events. The annular shape of the hypocenters

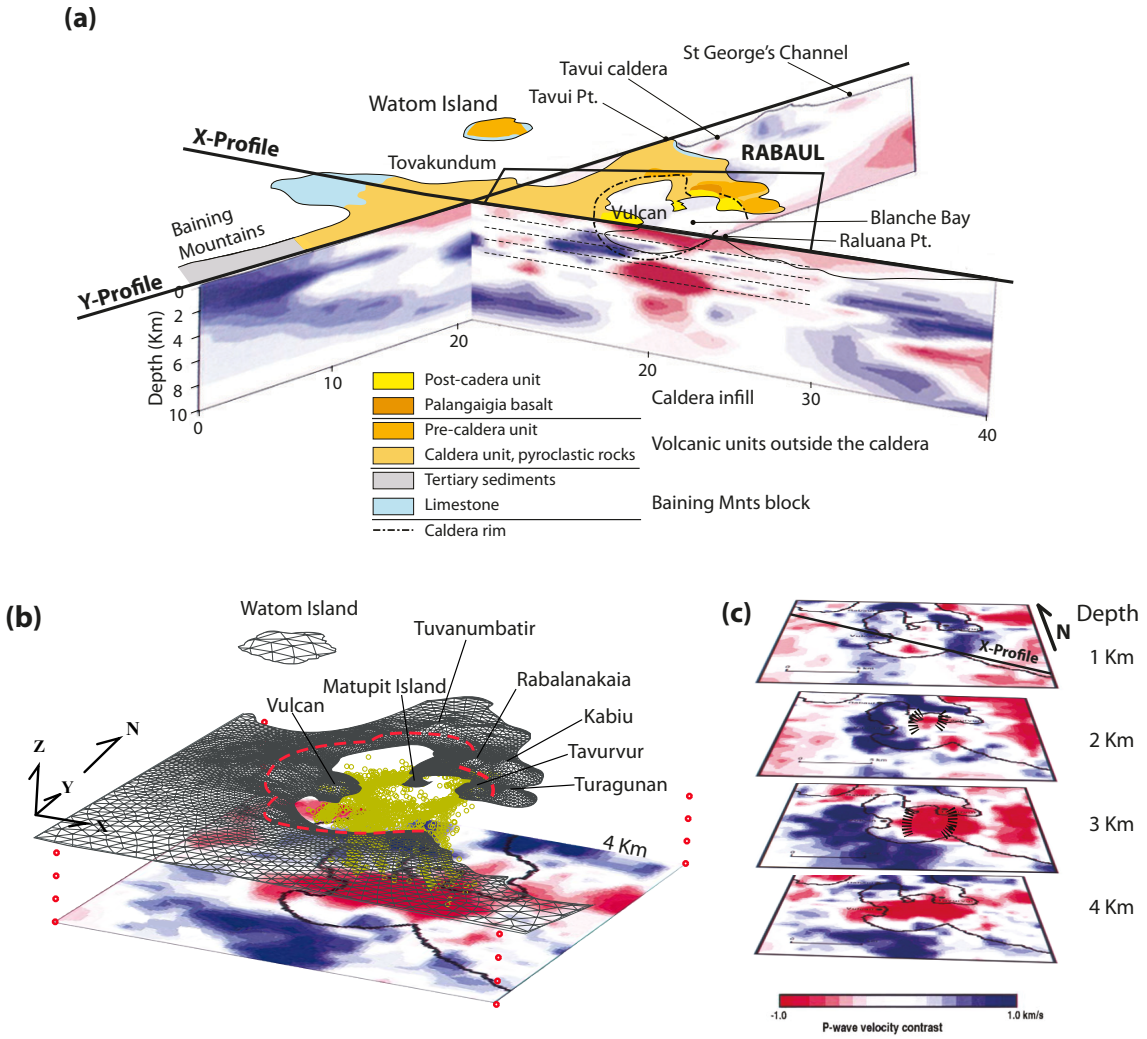

Figure 2.2.2. Tomography and elliptical seismicity at Rabaul caldera. *(a) 3-D view of tomographic profiles intersection adapted from Ronchin et al. (2013): geology of the Rabaul caldera (adapted from Heming, 1974) on top of two tomographic profiles (adapted from Finlayson et al., 2003), the footprint of the tomographic slices is shown (boxed area centered on Rabaul harbor), dashed lines on X-Profile show the position of the slices at different depths; (b) 3-D view of annular seismicity and tomographic slice at 4 km depth (adapted from Finlayson et al., 2003) as reference for the low Vp contrast area; (c) Slices at 1, 2, 3, and 4 km depths under the central Rabaul caldera adapted from Finlayson et al. (2003), dashed lines on the slices at 2 km and 3 km represent the seismically active portions of the ring fault above 2 km and below 3 km, respectively.*

became clearer when earthquakes positions were added during the seismo-deformational period of 1983-1985 (*Mori and McKee*, 1987a; *Mori et al.*, 1989). Evidence of intrusion into the ring fault of the seismic annulus was not found by *Mori et al.* (1989), so they concluded that the seismic annulus represents a zone of weakness caused by the increased magma pressure in the reservoir (*Johnson et al.*, 2010). The earthquake hypocenters of the seismic annulus were shown to be very shallow up to depths of about 4 km (*Mori et al.*, 1989; *Jones and Stewart*, 1997), whereas at the surface, the seismic annulus has no topographic expression. Later, *Itikarai* (2008) in an unpublished work relocated the earthquakes using a new 3-D velocity model. He showed that the earthquakes extend to depths of about 5 km, rather than 4 km, increasing in depths to the south, and he reported that during the seismo-deformational crisis were in fact recorded hybrid earthquakes of both high and low

frequency, suggesting that there was intrusion into the faults of the annulus (*Johnson et al.*, 2010). The main aspect of the studies of the annulus is that most of the proposed annulus follows the trace of the Karavia Bay Caldera escarpment, but not along the eastern side where it is at least 1 km from the escarpment northeast of Greet Harbor, so the seismic zone appears to be narrower that the caldera escarpment. *Jones and Stewart* (1997) recognized two elliptical distributions of earthquakes at different depths that were interpreted as two sectors of a ring fault: an outer ring shape (black dots in Fig. 2.2.1, a) which embraces a smaller inner one in its northern end (pink dots in Fig. 2.2.1, a). The intracaldera volcanic cones are all outside but within 1 km of the elliptical annulus, except the two Karavia Bay submarine cones, which appear to be located on the seismically poorly defined southern side of the smaller and northern ellipse identified by *Jones and Stewart* (1997). The role of the elliptical outward-dipping active faults, both during the last caldera forming event and during the 1994 eruption, is not clear. *Mori and McKee* (1987a), for example, claimed that it was the expression of a system of faults along which cauldron subsidence occurred at the time of the 1.4 ka ago caldera event. For other authors, however, it is a more recently formed or still-forming unfounded structural border of a caldera block (*Saunders*, 2001).

Besides the elliptical concentric structures related to the caldera collapses, other structures and fault systems related to both regional structures and volcanic activity were identified from seismic reflection profiling (*Cifali et al.*, 1969; *Greene et al.*, 1986; *Pono*, 1990) and from a more recent structural field campaign (*Saunders*, 2014 report in prep. Fig. 2.2.1, a). Except for a bulge at the sea floor near the center of the caldera and the caldera margins, no faulting has occurred in the caldera floor (*Greene et al.*, 1986). Through seismic reflection profiles, *Greene et al.* (1986) showed that the bulge consists of two domal uplifts bounded and separated by two main north-south trending fault zones. They did not find any evidence of expression of the annular faults at the caldera floor, this means that the annular faults terminate under the actual surface and are covered by post-caldera products. Angular unconformities separate the acoustic basement made of crystalline volcanic rocks, breccias, thick scorias and well solidified agglomerate from the overlying tephra sedimentary sequences (*Greene et al.*, 1986). With later survey, *Pono* (1990) was able to define more anticlinal folded strata with a trend parallel to that of the domes found by *Greene et al.* (1986), a well-defined NNE-SSW faults trend in the northern part of Blanche Bay, and a local subsidence in the southern and western parts of Blanche Bay. In general, the *Pono* (1990) seismic data show some small areas of minor uplift and subsidence with only minor deformation of young sediments.

From the collection of all structures and lineation reported in the bibliography and compiled in Fig. 2.2.1 is shown that the Rabaul caldera area is interested by a complex structure of both tectonic and local caldera-related fractures still to be solved by structural studies.

2.2.4 A wide picture of the study area through tomography and material velocities inferred from the tomography

Finlayson et al. (2003) tomographic study provided a wide picture of the subsurface material velocities distribution, thus allowing, together with the geological map (*Heming*, 1974), an interpretation about the presence and distribution of geologic blocks in the area (Fig. 2.2.3).

Finlayson et al. (2003) identified a slab of high velocities features (Baining Mountain Block, Bmt) that finds at the surface the correspondence of the Tertiary/Quaternary limestone mapped by *Heming* (1974). The same authors interpreted the prominent high-velocity features, visible from the topographic Vp-contrast slices and localized under the rim of the caldera, as mafic rock material

intrusion (Dikes) to shallow depth. Another very characteristic signal of *Finlayson et al. (2003)* tomography is the low-velocity areas at the surface, in correspondence of the caldera depression, and at about 4 km below the caldera. The first is interpreted to be the signal of the soft and loose material filling the caldera depression (Infill) and the second, the deeper one, is interpreted to be the signal of shallow region of hot magma accumulation. At the surface, the materials out of the caldera (Extra-caldera) show smaller velocity deviation from the regional model indicating the presence of extra-caldera deposits characterized by higher Vp velocities.

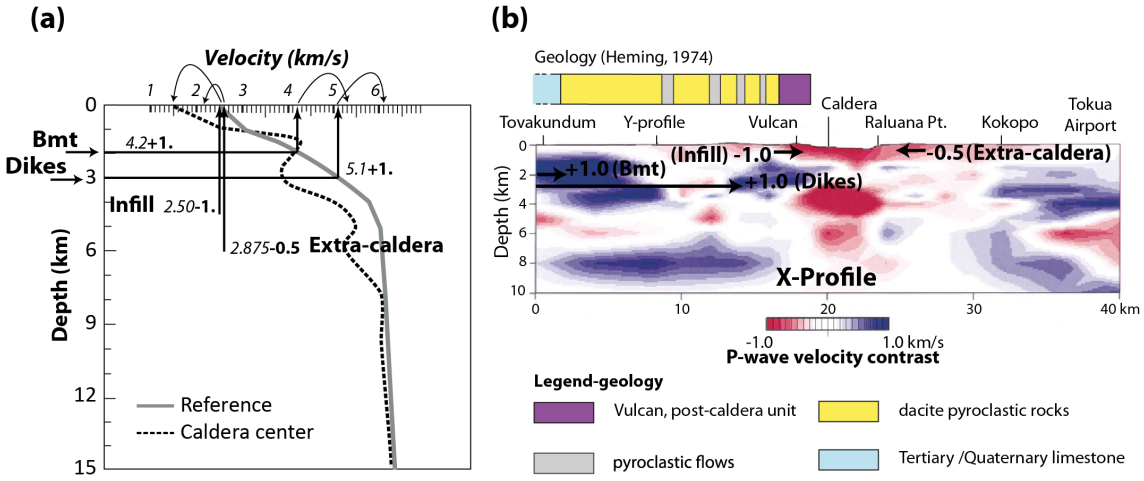

(c)

Geologic unit	P-velocities and contrasts (km/s)		
	Regional, Vp*	Vp contrast, Vpc**	Local Vp, Vpl=Vp+Vpc
Infill (0 m)	2500.	-1000.	1500.
Extra-caldera (-1000 m)	2875.	-500.	2375.
Baining Mountains (-2000 m)	4200.	+1000.	5200.
Dikes (-3000 m)	5100.	+1000.	6100.

*derived from panel (b)
**derived from panel (a)

Figure 2.2.3. One dimensional P-wave velocities, tomographic contrast and derived Vp for the main geologic domains.
(a) 1-D regional velocity and caldera center velocity models (modified from Finlayson et al., 2003). The process to derive the Vp for the main geologic domains is also illustrated: italic characters show the regional Vp velocities of the representative depths chosen for each main Vp anomalies recognized from the profile of the velocity contrast (panel b), bolt characters show the corresponding velocity contrast (panel b). (b) Residual velocity difference after subtracting the regional 1-D velocity (modified from Finlayson et al., 2003. (c) tables of the derived Vp for the main geologic domains recognized in the profile of the residual velocities.

2.3 Rabaul caldera eruptive activity

2.3.1 Historical eruptions up to the 1980s' crisis and 1994 twin eruption

The recent eruptive history at Rabaul caldera is defined as the part of the eruptive history since the last caldera forming at about 1400 yrs BP (*Patia*, 2004). It consists of recent historical eruptions, recorded by observers in about the last 235 years, and prehistoric eruptions occurred between the 1400 yrs BP caldera collapse and the historical period (Tab. 2.3.1). The recent eruptive history involved activity from intra-caldera cones Tavurvur and Vulcan, vents at Rabalanakaia, Sulphur Creek, and Dawapia Rocks, as well as submarine cones in Karavia Bay and Simpson Harbor (*Greene et al.*, 1986; *Patia*, 2004).

The peculiar volcanic activity at Rabaul caldera is represented by the twin eruptions of Tavurvur and Vulcan cones recorded three times in recent history. In fact, Tavurvur and Vulcan erupted simultaneously during the eruptions of 1878, 1937, and 1994. The 1878 eruptions, preceded by local changes of ground level and strong local earthquakes, started with the formation of Vulcan Island; Tavurvur became active few hours later with the development of a new crater. Vulcan and Tavurvur erupted again simultaneously in 1937, killing 507 people. The eruption was preceded by an intense seismo-deformational crisis initiated by a strong earthquake about a day before the beginning of the eruptive activity and by ten hours of uplift that culminated with more than 2 m uplift in the Vulcan area. The eruption started with violent activity that built a cone connecting Vulcan Island to the mainland. Tavurvur followed the Vulcan eruption and, with the intermission of a short period of repose, lasted until late 1943 (*Fisher*, 1976). After 1943, the caldera was quiescent until November 1973, when the unrest started with a progressive change in uplift and tilt, possibly due to the change in stress regime of Rabaul area induced by two strong tectonic earthquakes (Mw=8.0) below Solomon sea in July 1971.

The most recent and better documented twin eruption occurred in 1994. During this eruption the Rabaul Airport was completely destroyed by falling ash from the nearby vents. The airport was rebuilt outside the caldera at Tukua, but despite its location further to the southeast, it has been closed by ash fall produced by the volcanic activity of the Rabaul caldera (January 21st, 2013). The long eruptive activity that started on September 19, 1994, and lasted until 2011 was preceded by a long unrest period. Seismic activity and the ground deformation (*McKee et al.*, 1984, 1989; *Mori et al.*, 1989), together with an increasing of sub-surface mass, presumably due to magma intrusions (*McKee et al.*, 1987), marked the build-up to the 1994 eruption. The seismic activity started in 1971 and defined an elliptical annulus in the center of the caldera (*McKee et al.*, 1984, 1985; *Mori and McKee*, 1987a; *McKee et al.*, 1989; *Mori et al.*, 1989; *Saunders*, 2001, 2005) with seismic swarms of generally increasing intensity with time until mid-1984. Since 1973, the seismicity was associated with a significant deformation of the Sulphur Creek-Matupit Island area. Over 35% of the about 1.8 m uplift that occurred in the south end of Matupit Island between 1973 and 1984 occurred during the seismo-deformational crisis between September 1983 and October 1984. Domal uplift of the caldera floor was also revealed by a marine geophysical survey by *Greene et al.* (1986). The origin of this uplift is still under debate. Whereas some authors suggest that the deformation was due to the pressurization of shallow magmatic or hydrothermal sources in the caldera block (*McKee et al.*, 1984; *Mori et al.*, 1987b; *Geyer and Gottsmann*, 2010), others suggested overpressure of a deep magma reservoir (*De Natale and Pingue*, 1993), or the partial intrusion of a dike along the ring-fault structure(*Saunders*, 2001, 2005). After May 1985, seismicity significantly decreased and the uplift continued at variable rates. In general, the activity returned to pre-crisis levels without

an eruption until the outbreak and the eruption of 1994. On September 19, 1994, Rabaul began an explosive phase with the simultaneous vulcanian and vulcanian-plinian eruptions of two volcanic cones, located at opposite sides of the caldera: Tavurvur and Vulcan. The activity at Vulcan ceased by October 2, 1994, whilst,, intermittent vulcanian and strombolian eruptions restricted to Tavurvur continue to occur intermittently since November 1994.

On both 1937 and 1994 eruptions, the drainage of 0.3 to 0.4 km^3 of magma from the central caldera reservoir resulted in a rapid subsidence of the caldera floor from about 20 cm at its perimeter to about 1 m near its center (*McKee and de Sain-Ours*, 2000). In the period after the 1994 eruption, both seismicity and deformation occurring at the caldera confirmed the restless status of the caldera.

Date	Source	Event	Magma Type	Volume (km^3)
1994-98	Tavurvur	Pyroclastic and lava eruptions		0.1 Lava:0.04-0.05
1994	Vulcan	Pyroclastic, cone-building eruption		0.3
1937-43	Tavurvur	Pyroclastic eruption	A/D	0.01*
1937 29/05-02/06	Vulcan	Pyroclastic, cone-building eruption	D/A	0.3
1878 (31/01-26/02)	Tavurvur Vulcan	Pyroclastic eruption Submarine, pyroclastic cone-building eruption	 D/A	0.05 0.3?
1850	Sulfur Creek	Pyroclastic/phreato-magmatic, crater-forming eruption	A	0.01?
1791	Tavurvur	Pyroclastic (and lava?) cone building eruptions	A/D	0.1?
1767	Rabalanakaia?	Pyroclastic (and lava?) eruptions		
	Tavurvur?	Pyroclastic and lava eruptions, cone-building	A/D	0.1?
Approximate date (^{14}C)				
1775±30	Rabalanakaia	Pyroclastic eruptions, (pyroclastic flows)		
1750±50	Tavurvur	Prolonged pyroclastic (and lava?) eruptions		0.1?
?	Vulcan	Submarine pyroclastic eruption		
1715±20	Rabalanakaia	Lava and pyroclastic eruptions, (pyroclastic flows)	A	0.2?
1700±50	Tavurvur	Pyroclastic (and lava?) eruptions		
?	Sulfur Creek	Lava and pyroclastic, cone-building eruptions, (pyroclastic flows)	A	0.1?
1200±50	Dawapia?	Submarine, pyroclastic, cone-building eruption	D	0.3?
	Karavia Bay?	Pumice rafts led to formation of "Matupit Pumice Sediments"		

B= basalt, A= andesite, D= dacite

*0.005 estimated by Patia (2004)

Table 2.3.1. Recent historic eruptions.
Modified from Nairn et al. (1995) and McKee and de Sain-Ours (2000).

2.3.2 Recent volcanic activity: period from February 27, 2007 to December 8, 2010

The unrest at the caldera has continued to the present with intermittent eruptions in 1995, 2002, 2005, 2006, 2010, 2011, and most recently in January 2013, still continuing at Tavurvur (RVO report in Smithsonian Global Volcanism Program Archives, 2013). The period spanned by the InSAR data used in this work was preceded by a vulcanian to sub-plinian eruption occurred on October 7, 2006.

According to the RVO (Smithsonian institute report) the eruption at Tavuvur began at 8:45 on October 7 with sub-plinian activity that continued into the afternoon and ejected an ash plume rising to a height of about 18 km. The eruption changed to strombolian at 14:15, with frequent explosions accompanied by shockwaves and rhythmic air blasts, and subsided by 17:30. By the end October the eruption had died down with occasional ash emissions that generated ash plumes up to

2.5 km and rare explosions. The approximately estimated volume of dacitic magma erupted is 0.1 km^3 (DRE=0.04 km^3) (*VOGRIPA*, 2013 website). Recently it was reported to be 0.2 km^3(*Bouvet de Maisonneuve et al.*, 2014).

From December 13, 2006, to the end of March 2007, generally low level seismicity and mild eruptive activity continued with occasional ash plumes rising 1.5-3.7 km above the Tavurvur summit. Ground deformation measurements showed no significant movement apart from a slight subsidence of about 1 cm in the last few days of January. During April and May 2007, the eruptive activity continued at Tavurvur with ash plumes rising up to 1.5 km. Seismicity continued to remain at low levels with the exception of a peak of low-frequency events during the third week of May. No apparent changes of ground deformation were recorded during the month. The volcanic activity continued at Tavuvur at low-level through mid-June 2007. During June-July 2007, several explosions at Tavuvur raised vapor clouds and ash plumes up to about 2.7 km; occasional weak to moderate red glow was visible at night. Deformation registered by the GPS and water-tube tiltmeter show insignificant to slight uplift and subsidence alternating during the entire period; GPS at the caldera's center showed that centimeter-scale movements often occurred every few hours. Similar volcanic activity was recorded during August 2007, with almost continuous emission of ash and vapor plumes and moderate seismicity that increased in the last week of the month. During September-October 2007, seismicity stayed at moderate to moderately-high levels and the eruptive activity was characterized by the ejection of incandescent fragments accompanied by ash plumes emissions from Tavurvur summit. After five weeks of low level activity, a new vent opened on the NE Tavurvur crater rim as consequence of the lava dome blocking the vent on the caldera floor. Eruptive activity was characterized by vapor and ash emissions from November 2007 through January 2008, while no deformation notes were reported in the RVO report (Smithsonian Global Volcanism Program Archives, 2013).

An uplift starting January 23 and peaking to 2 cm during January 25-26 was recorded as superimposed on the gradual 6 months long subsidence. In February and March 2007 the volcanic activity slightly changed: explosions with projection of lava fragments were also recorded accompanying incandescence at the summit. Activity during March 27 into July 2008 continued the activity of the previous moths. Displacements continued with stable small and continuing rapid fluctuations (about 1 cm); the overall deformation of 5 cm of subsidence recorded at Matupit suggested a deflation of the deeper source. The eruptive activity consistent of intermittent emissions of ash plumes and less frequent explosions sometimes ejecting incandescent lava fragments continued until the end of September 2009. During this period, the ground deformation measured from the water-tube tiltmeter continued to show a modest down-tilt toward the caldera, confirming the long-term deflationary trend at the central part of the caldera since July 2007. Ground deformation measured by tide gauge and GPS continued to show deflation during mid-December 2008 through mid-March 2009.

In mid-March 2009 deflation slowed down and then ceased. The non-deformational period lasted until September 2009, when deflation slightly increased.

Eruptive activity at Tavuvur cone continued during September-December 2009 with ash plumes reaching altitude up to 2.7-3 km and occasional ejection of incandescent lava fragments. GPS and tide gauge stations generally recorded deflation during the first three weeks of September while in October the data showed a slow deflationary trend.

At the end of December 2009, the sub-continuous activity at Tavurvur ceased and the cone was quiet during the first quarter of 2010 with few emissions or earthquakes. On April 9 the RVO reported that deformation measurements at Rabaul caldera during the previous 3-4 months showed

an inflationary trend with a total of 4 cm of uplift (RVO report in Smithsonian Global Volcanism Program Archives, 2013). During April 2-8 seismicity was low and variable amounts of white vapor rose from Tavurvur cone.

Eruption at Tavurvur cone resumed on 23th July 2010, after nearly seven months without ash emissions. Increased seismicity, which began with a few small hybrid earthquakes and was followed by small low-frequency earthquakes, was recorded the days before the eruption. The eruption began with discharge of diffuse white plumes followed by pink-gray fumes with low ash content. Ash emissions and ashfall continued in areas to the NW. GPS data showed slight deflation after the eruption of July 23-25, 2010. During the period from July 26 to August 12, 2010, only very small volumes of vapor were released, no ash emission occurred from Tavurvur cone, and in addition, seismicity was very low. GPS measurements on Matupit Island continued to show inflation that slowly increased in rate from mid-February 2011 (Bulletin of Volcanism Network, 2011).

2.4 Rabaul caldera data

The available data for this study are separated into two categories, based on the usage from a modeling perspective: the *constraining data* and the *calibration data*.

The constraining data are treated as a priori information and are built into the models. For this study, topography and bathymetry constrain the geometry of the free surface, whereas geology, tomography, and seismicity constrain the distribution of material properties within the problem domain.

Calibration targets (data) are used to estimate the calibration (or adjustable) parameters. InSAR data serve as calibration targets, which are used in inverse methods to calibrate parameters describing the strength of a deformation source .

2.4.1 Relief data (topography and bathymetry)

The terrain relief describing the geometry of the Earth's surface for both onshore and offshore regions of the model domain was compiled from three types of data having different resolution: the 90 m resolution SRTM data obtained from the EROS-USGS website acessed December, 2011 (data were downloaded in DTED format: .dtl), the relatively coarse resolution (1-minute) gridded bathymetry data available from the GEBCO project website accessed December, 2011 (data available in NetCDF format: .nc), and bathymetric data of Blanche Bay (RVO data from HMAS 'Flinders' survey, 1995) provided by the Rabaul Volcano Observatory (xyz.txt file).

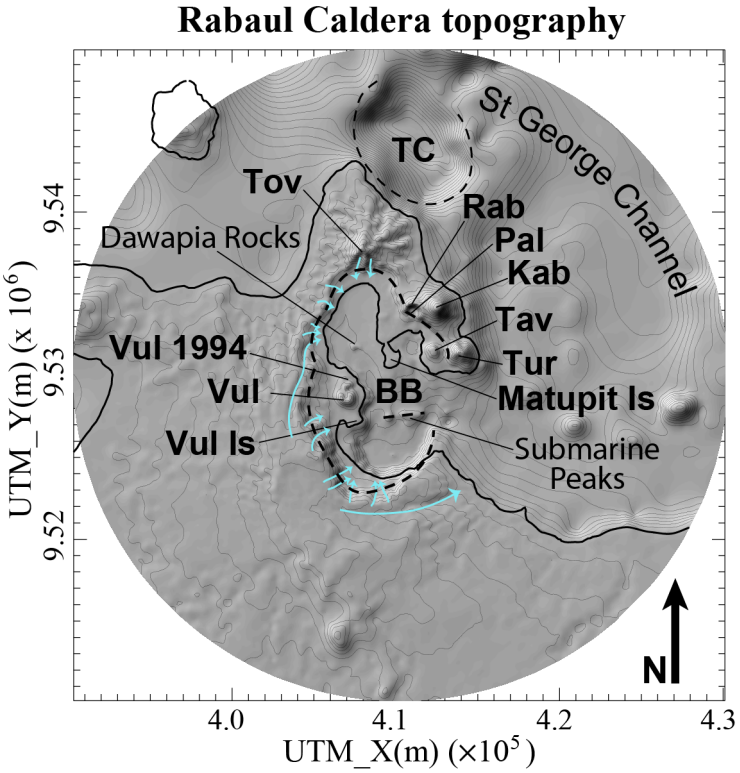

Figure 2.4.1. Topography of Rabaul caldera area.
Volcanic edifices: Tovanumbatir (Tov), Rabalanakaia (Rab), Palangiagia (Pal), Kabiu (Kab), Tavurvur (Tav), Turanguna (Tur), Vulcan (Vul), Vulcan Island (Vul Is), Vulcan 1994 vent (Vul 1994), Dawapia Rocks, and Submarine Peaks. Matupit Island (Matupit Is), Tavui Caldera (TC), Blanche Bay (BB) and part of the main drainage network are also indicated.

Due to the different resolution of the three data sets, the shaded relief map produced by these data shows different degrees of surface smoothness (Fig. 2.4.1). Smoothed surfaces of the submerged areas outside of the caldera are characterized by lower resolution, whereas the land surface and the bathymetric surface of the Blanche Bay, inside the caldera, are represented by more details (Fig. 2.4.1).

The area is characterized by the presence of a sea-filled caldera which measure about 14x9 km and hosts Blanche Bay, by Tavui depression that supposedly hosts another caldera to the north-east and by the volcanic cones aligned along a NW-SE line on the north-east side of Blanche Bay. The land west and south of the caldera is characterized by a gentle, low-lying topography that is interrupted by the caldera walls and intracaldera cones and the satellite cones to the northeast. In the north east and east the topographic walls of the caldera is a single, nearly vertical, scarp while in the west two scarps are present. In the south-east the caldera wall is breached letting the sea filling the caldera depression.

The land relief surface reaches its maximum elevation at Kabiu 688 m a.s.l., while the bathymetry of the Blanche Bay reaches it maximum depth of 295 m b.s.l. in Karavia Bay. Other topographic features are the cones Tovanumbatir (532 m a.s.l.), Turanguna (482 m a.s.l.), the nested crates Palangiagia and Rabalanakaia, the intracaldera centers Tavurvur (232 m a.s.l.) and Vulcan (225 m a.s.l.), and Matupit Island, a peninsula extending from the north-eastern part of the caldera southward near to its center. A west-east line of submarine peaks east of Vulcan is evident from the bathymetry. Other small vents to the north and south of Vulcan include the 1994 vent and Dawapia Rocks (or Beehive).

Although generally low-lying and gentle, the areas north and west of the caldera are dissected by deep v-shape valleys that extend towards the coast radially to the caldera walls. On the western and southern flanks of the Rabaul complex the drainage patterns are tangential to the caldera.

2.4.2 ALOS PALSAR and PS-InSAR basic concepts

In the last two decades the use of Interferometric Synthetic Aperture Radar (InSAR) and Global Positioning System (GPS) measurement of Earth surface deformations has seen rapid growth. These improvements have been driven by the proliferation of high precision space geodetic instrumentation and by the wide range of application to study the different earth processes that cause the surface deformations (e.g. distributed interseismic, postseismic, magmatic, landslides).

Unlike the GPS that provides measurements of three-dimensional surface position with high temporal resolution but limited spatial resolution, InSAR provides high spatial resolution at low temporal resolution dependent on the times the satellite passes over the area. Despite its low temporal resolution, it is an indispensable tool to define the spatial dimensions of the volcanic system and to study magmatic processes that can last months or years (charging/discharging the system).

By bouncing signals from radar satellite off the ground in successive orbits and looking at the differences between the images, InSAR can detect small differences in the distance between its position and the ground as land surface moves (*Helz*, 2005).

To detect the changes in the position of the surface, at least two radar images of the study area are acquired from approximately the same position in the space but at two different times. In fact, an interferogram is calculated from two SAR images (called master and slave) acquired at two distinct times and provides a measure of the distance change in the look direction of the satellite, which is inclined to the vertical. There are ascending and descending satellite paths, each

with a look direction defined by a unit vector (i, j, k) LOS (line-of-sight). The steps to calculate the interferograms are described in detail by *Dzurisin* (2007). Here we provide a summary of the general processing steps that have to be performed to generate interferograms: 1) co-registration of overlapping radar images, 2) creation of the interferogram by simply differencing the phase values of corresponding pixels, 3) removal of the effects of different viewing geometry at the two times (orbital corrections by removal of linear or quadratic trend and curvature correction due to small additional effects of earth curvature), 4) removal of topographic components, 5) filtering and phase interpolation (to reduce the effects of the short-wave length and facilitate visual correlation), and finally 6) phase unwrapping. After this processing the interferogram shows the component of ground deformation that occurred along the line-of-sight (LOS), between the ground and the satellite, during the period between the two observations.

InSAR can detect only movement toward or away from the satellite. For this reason, there is an ambiguity in entirely defining the movement with its horizontal and vertical components. In fact, the inclined look direction of the satellite captures at the same time the components of the vertical and horizontal displacement, resulting in a skewed and offset pattern of range change (*Dzurisin*, 2007).

Great advantages of InSAR are 1) it gives a wide areal image of the deformation field showing spatial patterns at centimeter-scale accuracy and not just deformation at specific points on the surface as the GPS, 2) it can be applied to remote volcanoes that otherwise could not be monitored, 3) can be applied in dangerous areas without subjecting field crews to hazardous conditions on the ground. Present weaknesses of InSAR are 1) susceptibility to contamination by atmospheric signals, 2) ambiguity in horizontal vs. vertical motion, 3) low temporal resolution limited by orbit repeat time, 4) difficulty to see through vegetation to the ground beneath.

The ability to measure volcanic deformations using SAR interferometry depends on the stability of phase coherence over the time and over surveyed surfaces (*Sedze et al.*, 2012). One of the largest limitations of conventional InSAR is signal decorrelation caused by diffusive scattering from vegetation. The decorrelation is particularly significant for short wavelength sensors, such as X- and C-band (*Samsonov*, 2010). In regions with dense vegetation, time series techniques using C-band (5.63-5.8 cm wavelength) have been unsuccessfully applied due to the loss of coherence in time between subsequent images (*Hole et al.*, 2007; *Samsonov et al.*, 2011). By contrast, radar images from the L-band PALSAR sensor show a much higher coherence in densely vegetated areas (*Samsonov*, 2010).

ALOS PALSAR basic concepts

InSAR concepts, procedures, and issues related to volcaninc areas are extensively treated in the recent book by *Lu and Dzurisin* (2014). In the following we summarize some general concepts oriented to understand the utility of L-band ALOS PALSAR images for Rabaul caldera area.

The Advanced Land Observing Satellite (ALOS) was launched in 2006 by the Japan Aerospace Exploration Agency (JAXA) and worked until 2011. ALOS was equipped with Phased Array L-band Synthetic Aperture Radar (PALSAR) with a sensor with 23.6 cm wavelength and with accuracy and duration suitable to monitor slow crustal deformation (*Rosenqvist et al.*, 2007; *Sandwell et al.*, 2008). The recurrence cycle was of 46 days, which was the time it took to the satellite to revisit the same site. This was therefore the minimum time interval between deformation events.

A major limitation of InSAR for geophysical applications is that the technique is only sensitive to one dimensional motion along the satellite's line-of-sight, the LOS (Fig. 2.4.2, a), which is the

ALOS	
Space Agency	JAXA
Period of operation	01/2006-04/2011
Lifetime	~5 yrs
Recurrence cycle	46 days
Altitude	697 km
SAR wavelength	L-band (23.6 cm)
Incidence angle at swath center	7.9 - 60°
Look direction	right
Resolution	10 -100 m

Table 2.4.1. ALOS information modified from Romeyn and Garthwaite (2012).

projection of the full 3-D displacement vector onto the LOS. Thus, the InSAR technique can detect only the component of displacement in the LOS direction (*Grandin et al.*, 2010), although most deformation is better characterized using three dimensional geodetic data (*Bechor and Zebker*, 2006). Ideally, it is possible to reconstruct the 3-D displacement vector measuring more than one projection of the full displacement vector (*Bonforte et al.*, 2011). This is possible imaging the area of interest with more than one satellite track (ascending and descending passes, with variable incidence angles). So, in order to better constrain models representing geophysical processes, it is desirable to have more images with ascending and descending passes (*González et al.*, 2013). Unfortunately, the limitation of ALOS is that mostly ascending acquisitions are available due to the JAXA's acquisition strategy; thus the vertical and horizontal components cannot be derived.

Observations are made obliquely below the satellite (Fig. 2.4.2, b) following ascending orbits, where the observations are made from the west towards east, and descending orbits, where observations are made from east towards west. Due to the fact that only the component of displacement in the LOS of the satellite can be detected, depending on the nominal incidence angle of the SAR the measurements are more sensitive to vertical motion (i.e. ERS satellites with incidence angle of 23°) or to horizontal motion (i.e. ALOS and Radarsat with incidence angle of 7.9-60° and up to 59°, respectively) (*Williams and Wadge*, 2000; *Grandin et al.*, 2010; *González et al.*, 2013).

The difference in viewing geometry between two images (Fig. 2.4.2, c), caused by any shift in orbital trajectory between the two image acquisitions, produces a regular pattern of phase differences between the images (*Massonnet and Feigl*, 1998; *Dzurisin*, 2007), which needs to be removed through the orbital correction. In the case of a perfectly flat area (without earth curvature), these differences would manifest themselves in the interferograms as a series of nearly parallel bands called orbital fringes that, removed from the initial interferogram, produce a flattened interferogram (*Dzurisin*, 2007).

In hilly terrain, it sometimes occurs that the slope angle is more than the satellite look angle and the projection of slopes onto the LOS is reversed due to the fact that returns from the top of the slope (closer to the radar) will arrive before those from the bottom (in Fig. 2.4.2, d objects B, C, and D are masked by E, F, and G). This phenomenon is referred to as layover and generates noise. As the radar progresses, it finds the slope greater than that of the incidence angle of the LOS and facing the other direction. The area cannot be imaged by the sensor generating a shadow area (Fig. 2.4.2, d). In the case of slopes that do not exceed the satellite look angle (Fig. 2.4.2, d objects H and I), the volcano slope facing the satellite becomes foreshortened. This means that they are mapped as having a compressed ground-range scale relative to flat-lying areas (*Lu and Dzurisin*, 2014).

InSAR technique has limitations in temporal resolution, coherence, and noise related to decorrelation. Accuracy of SAR interferograms is mainly affected by decorrelation that is the term used to describe the situation in which two radar images of the same area cannot be registerd pixel by pixel (*Dzurisin*, 2007) and therefore cannot perform an accurate measurement of the displacement.

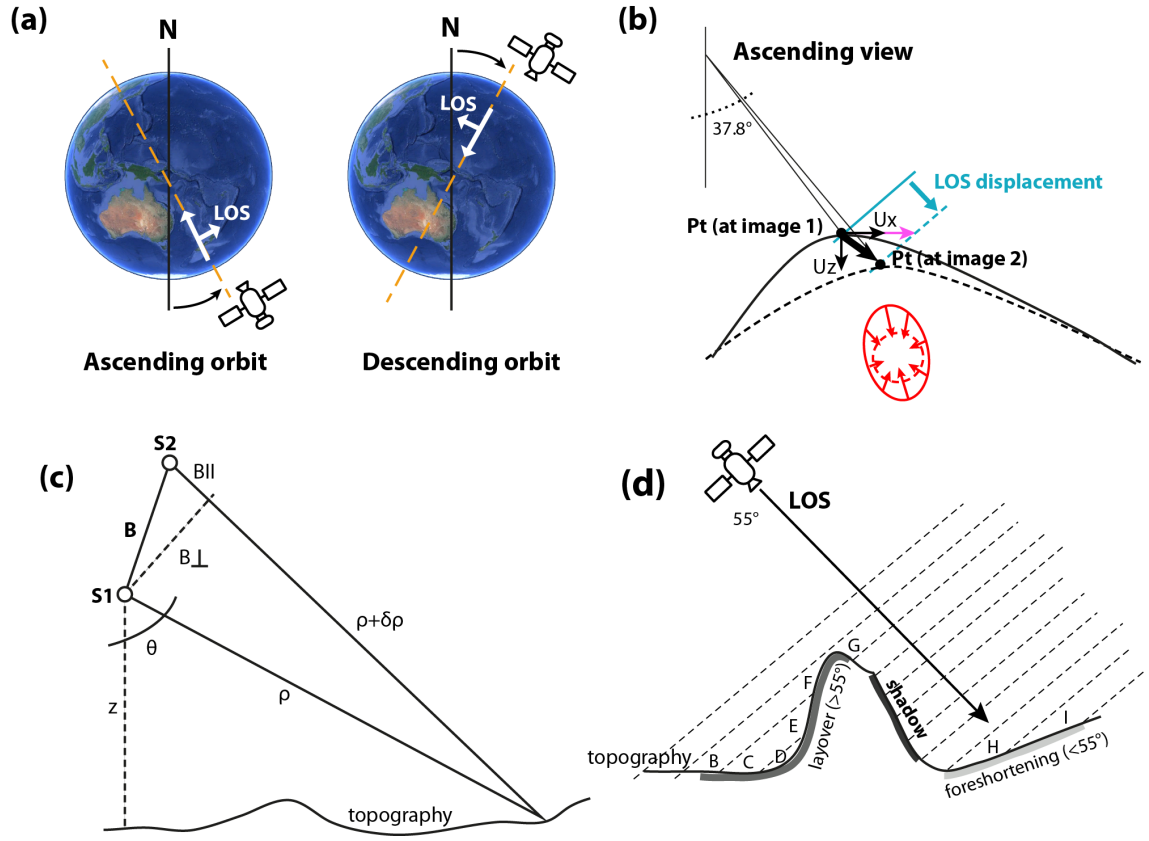

Figure 2.4.2. Orbit and look geometry.
(a) Ascending and descending orbit of the satellite (dashed orange line) with respect to the true North-South (solid black line) and line-of-sight (LOS) (image of earth is from Google Earth). (b) Simplified image that shows the real deformation (black thick arrow) of two displacement components (Ux and Uz) and the corresponding measured LOS displacements (blue arrow) for the ascending geometry (geometry of all Rabaul images), modified from Bonforte et al. (2011). Note the ambiguity of the LOS measurement: the same LOS displacements can be measured for a different deformation due to only horizontal displacement of the point, Ux (pink horizonal arrow). Note also that, depending on the incidence angle, LOS measurements could be more sensitive to one component of the displacement (e.g. with high incidence angles it is more sensitive to the horizontal component). (c) Schematic diagram of the geometry of InSAR (modified from Zebker et al., 1997), where S1 and S2 represent the satellite positions, ϑ is the "look" angle, ρ and $\rho+\delta\rho$ the distances of the satellite from the images point. B, baseline, is the separation between two satellite positions, and B⊥, is the perpendicular baseline, the satellite separation in the direction perpendicular to the look vector. (d) Cartoon showing foreshortening, layover, and shadow.

Usually, longer time differences between observations decrease the coherence of the interferogram images which is the cross-correlation between two co-registered images that ranges from 0 (no correlation, the interferometric phase is just noise) to 1 (perfect correlation, complete absence of noise). The coherence is estimated, after the removal of the topography signal and the orbital ramp (due to imaging geometry changes), by cross-correlation of the SAR image pair over a small window of pixels (*Sedze et al.*, 2012):

$$\gamma = \frac{|\sum_{i=1}^{L} z_{1i} z_{2i}^{*}|}{\sqrt{\sum_{i=1}^{L} |z_{1i}|^2 \sum_{i=1}^{L} |z_{2i}|^2}} \tag{2.4.1}$$

where Z1 and Z2 are the complex signals, * stands for the complex conjugate, and L is the total number of pixels. Thermal decorrelation is due to system noise and can be related to the signal-

to-noise ratio (SNR) of the radar system (*Zebker and Villasenor*, 1992). Due to very high SNR in ALOS data, the thermal noise can be ignored (*Sedze et al.*, 2012), so the remaining significant factors that cause decorrelation in the interferograms are spatial decorrelation and temporal decorrelation (*Zebker and Villasenor*, 1992; *Sedze et al.*, 2012):

$$\gamma = \gamma_{spatial} \cdot \gamma_{temporal} \tag{2.4.2}$$

The spatial baseline decorrelation is related to the different look angles of the two SAR acquisitions and occurs when the interferometric baseline is not exactly zero. The radar receives the contribution of all scatterers in the resolution cell in slightly different ways due to different look geometry. This leads to the concept of critical baseline, above which the coherence is totally lost and the interferometric phase is pure noise. The long wavelength of the L-band increases the critical baseline threshold. Interferograms with spatial baselines less than the 1-1.5 km threshold tend to be useful (*Romeyn and Garthwaite*, 2012). This results in more usable interferometric pairs (*Sandwell et al.*, 2008).

In terms of temporal decorrelation, coherence depends on surface scattering and temporal stability of the surface scattering properties. *Lu et al.* (2005) comparing C- and L-band radar images noticed that besides the vegetation, the nature of the surface material (e.g. unconsolidated volcanic deposits) can also affect the definition of the deformation field by reducing the coherence due to the fact the material could be unstable on the scale of a few centimeters on the time between two acquired SAR images. Temporal decorrelation is due to changes of the surface mainly at the scale of the radar wavelength (*Zebker and Villasenor*, 1992). InSAR data acquired with longer wavelength, such as L-band, are affected by lower temporal decorrelation (Strozzi et al., 2003). The long wavelength of the L-band has lower sensitivity for vegetation(*Sandwell et al.*, 2008; *Ernst et al.*, 2008), which allows a deeper penetration of vegetated areas, resulting in less temporal decorrelation and enabling longer time separation between images used to form the interferograms (*Rosen et al.*, 1996).

Accuracy indicates proximity of measurement results to the true value. In the case of LOS measurements, the accuracy can be estimated from comparison with independent geodetic measurements such as GPS displacements (*Massonnet et al.*, 1993; *Zebker et al.*, 1994; *Fialko et al.*, 2001; *Pritchard and Simons*, 2004; *Vilardo et al.*, 2010). Accuracy is strictly related to the ability of the sensor to resolve the displacements, which is dependent on the wavelength of the instrument. Due to the 24 cm wavelength of ALOS PALSAR, the measurement accuracy is generally about 1-2 cm yr^{-1} (*Samsonov et al.*, 2011). Similar values were also found in a previous study by *Sandwell et al.* (2008). Surface deformation velocity accuracy depends also on the coherence of InSAR, which is usually better in arid climates (*Grandin et al.*, 2010).

All in all, due to its long wavelength, the L-band has some advantages. The main advantages are: lower sensitivity for vegetation (*Ernst et al.*, 2008; *Sandwell et al.*, 2008) allows a deeper penetration of vegetated areas, resulting in less temporal decorrelation, enabling longer time separation between images used to form the interferograms (*Rosen et al.*, 1996), and making it suitable for monitoring ground deformation in tropical regions; the longer wavelength increases the critical baseline threshold, resulting in more usable interferometric pairs (*Sandwell et al.*, 2008). On the other hand, the disadvantage due to the long wavelength is that a lower fringe rate may result in less precise crustal-motion measurement (*Sandwell et al.*, 2008).

PS-InSAR technique basic theoretical concepts

The InSAR data used in this work are processed and kindly provided by John Dawson of the Geoscience Australia Institute. The data were processed with the Stanford method for Persistent Scatterers (StaMPS) developed by Hooper et al. (2004; 2007). The persistent scatterer InSAR (PSInSAR) is a multi-temporal InSAR (MTInSAR) advanced processing technique that uses a series of InSAR observations with the purpose of characterizing the deformation signal, artifacts, and noise sources (e.g. orbit errors, atmospheric delay) by fusing information from several interferograms of the same area (*Lu and Dzurisin*, 2014).

The simplest approach to utilizing multiple interferograms is to average them (*Hetland et al.*, 2012), both in case the target is a single event that occurred quickly or is a gradual process occurring at constant rate.

The main driver for the development of the first PSInSAR strategy was the need to remove the atmospheric errors in the signal phase values. The multiple images are examined by selecting one of the scene as master to which all the others become slaves. The master is ultimately the level of decorrelation noise that defines whether pixels are PS pixels or not, although an initial pre-selection of candidate PS pixels is done by using various proxies (*Hooper et al.*, 2012). The selection of the PS pixels requires the search in each pixel (resolution cell) for radar targets that display a stable amplitude and a coherent phase throughout all registered images (data stack). Information of both amplitude dispersion and phase stability with time are used to determine which pixel can be considered as a PS. The found targets are the Permanent, or Persistent, Scatterers (PS). This way, a sparse grid of point-like targets with high SNR is identified across the area of interest (www.treeuropa.com). This process permits the reduction of the decorrelation phase differing from InSAR images for which the value of each pixel remains the coherent sum of all returns from many scatters in the pixel. In InSAR images decorrelation happens more easily due to the fact that all scatters, moving or changing scattering properties with respect to each other in the time between satellite passes, return a phase that varies in a random manner in time.

Non-dominant scatterers are considered as noise sources for the PS pixels. Increasing their number can lead to an increase in decorrelation noise (*Hooper et al.*, 2012). This is why no filtering or multilooking, which degrade resolution thereby adding more scatterers to each resolution element, are applied in PS processes (*Hooper et al.*, 2012).

In the StaMPS, the approach for estimating decorrelation noise relies on the spatial correlation of most of the phase term (*Hooper et al.*, 2004, 2012). For each PS candidate the spatial filter is applied to estimate the spatially-correlated phase terms (i.e. orbit error phase, atmospheric, deformation). The spatially-correlated phase is then subtracted and the residual contribution of DEM errors is modeled for the whole time series, the residuals between the model and remaining phase provides an estimate of the noise of the pixel (*Hooper et al.*, 2012). Compared to the first PS approach proposed by *Ferretti et al.* (2001), the StaMPS approach has the advantage that the phase unwrapping algorithm is applied to the chosen PS pixels without assuming a particular model for the temporal evolution. All unwrapped displacement measurements in the LOS direction are relative to a stable and non-moving pre-selected point (out of the area of deformation to be measured). Thus the resulting deformation is relative in time (referring to a master image) and space (referring to a stable point). The deformation phase is then separated from the other phase contribution, atmospheric and noise, by filtering in time and space with the assumption that the deformation is correlated in time, the atmosphere is correlated in space but not in time, and the noise is uncorrelated both in space and time (*Hooper et al.*, 2012).

At the end of the StaMPS processing procedure, we obtain PS time series of the LOS displacements at each acquisition date and a map of the mean PS velocities along the LOS of the satellite over the entire period, reffered to a stable area chosen (where no movements are observed). A map of the mean velocities standard deviations is also provided, which gives an idea about the variability of the velocities of the area in time.

The advantage of PSInSAR technique is that we can use all the images without limitation due to the baseline, the resulting deformation is associated to a specific scatterer, typically on the order of several meters, instead of being associated to a resolution cell whose dimension depends on the radar system. This level of detail could be useful to separate local deformation of specific structures from crustal deformation (*Hooper et al.*, 2012).

Besides the factors already discussed in the previous chapter, the accuracy of the deformation resulting from the application of the PSInSAR methods depends on the number of processed images, the distance from the reference stable point, and the coherence of the PS.

2.4.3 Rabaul ALOS-PALSAR data: PS images, mean velocity, and velocity standard deviation

The data set used in this work is composed of 20 PALSAR scenes acquired by ALOS satellite in ascending orbit (i.e. ascending track 352, frame: 7090, heading -12.06°, incidence 37.8° at the center of the swath). The mean LOS unit vector computed at the center of the caldera, $\hat{n} = [East, North, Up]$, is $\hat{n} = [-0.617, -0.131, 0.775]$. The scenes cover the period spanning February 27, 2007, to December 8, 2010, for a total of 1380 days. ALOS-PALSAR data information is summarized in Table 2.4.2.

Aspect	Specifications
Images	ALOS-PALSAR from February 2007 to December 2010
Total days	1,380
Wavelength	L-band/0.236 m
Pass	Ascending
Track	352
Frame	7090
Heading (center of the swath)	-12.06°
Incidence (center of the swath)	37.8°
L (line-of-sight), [East, North, Up]	[−0.617, −0.131, 0.775]
Pixel dimensions	nominal pixel size is 4.7 x 3.5 m (range x azimuth)
N (coherent pixels)	55,148
Area covered	70x70 km
N (coherent pixels) of Rabaul area	22,123
Rabaul area covered	23x23 km

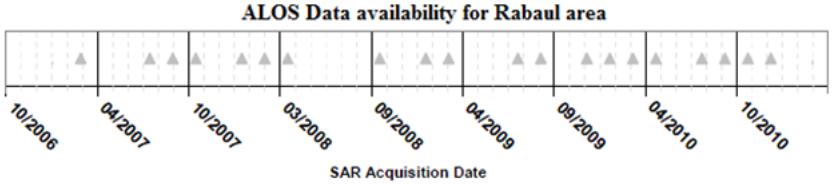

Table 2.4.2. Rabaul ALOS PALSAR data summary.
Data summary of the available ALOS-PALSAR scenes revelant for Rabaul caldera (modified from Romeyn and Garthwaite, 2012). Gray triangles indicate the available images covering Rabaul area.

The Stanford Method for Persistent Scatterers (StaMPS) (*Hooper et al.*, 2007) has been used by the Geoscience Australia Institute to generate the interferogram time-series from 2007 to the end of 2010 for the ALOS-PALSAR tracks through STAMPS (*Hooper et al.*, 2004). The time-series analysis was used to isolate the best target pixels (those that show more coherence in time) and to estimate the spatially correlated look angle errors and the master/orbit errors due to the master image (*Hooper et al.*, 2007).

More than 55,000 persistent scatterers (PS) in ascending geometry have been identified within an aerial extent of about 70 km^2 (Fig. 2.4.3). Each "slave" image shows the deformation with respect to the image of March 4, 2009, that is called "master" image. Thus, red positive values in the images preceding the "master" correspond to positions of the scatterers closer to the satellite in the LOS direction with respect to the position they have at the master image. In other words, they show that the scatterers moved away from the satellite along the LOS direction during the time between the images' acquisition. For the images collected after the "master," the reverse is valid. Blue negative values correspond to position of the scatterer further away from the satellite with respect to the position they have at the master image. That means that in these images the green-blue colors represent scatterers that moved far from the satellite in the LOS direction.

The signal observed in the March 2008 image has been interpreted to be an atmospheric signal because it is not correlated in time with signals observed in the images before and after this image. For this reason this image was not taken into account. For the same reason, the image of April 2010 was also discharged from further analysis and considerations.

Insights from the temporal series

As the largest deformation effects are mainly centered at the Rabaul caldera, with the exception of a weaker but wide-length deformation spreading toward Keravat (i.e. west), it was decided to use only the portion of SAR images that shows these deformations. Interested by deformations that could be related to the volcanic activity of the caldera, we thus reduced the study area to the area around Rabaul caldera (Fig. 2.4.4). The number of PS is reduced to 22,123 over an area of 23x23 km. Working with a smaller area simplifies the inversion process by reducing the computational effort.

From Fig. 2.4.4(b), we can observe that some areas are not covered by PS. The lack of persistent scatterers at the Rabaul caldera could be associated with the decorrelation of the signal due to the loss of coherence in some part of the caldera. In the Eastern part of the Rabaul caldera, three areas of lack of persistent scatterers are evident. At Tavurvur (Fig. 2.4.4,b (1)), the lack of persistent scatterers is due to the incoherence associated with the significant ash fall, ground cracks, debris, and lava block, which alter the surface significantly in this area. In fact, pyroclastic deposits are typically characterized by low coherence (*Sedze et al.*, 2012). The old airport (Fig. 2.4.4,b (2)) and Sulfur Creek area (Fig. 2.4.4,b (3)), are also characterized by incoherence of the signal and lack of persistent scatterers due to the fact that the whole area is a drainage area characterized by high soil mobility. Due to the combination of the looking angle of the satellite and the high terrain gradients, the western steep slopes experience a general loss of correlation. This is particularly evident over the wide uncovered area corresponding to the east-facing slopes in the western side of the caldera (Fig. 2.4.4,b (4)).

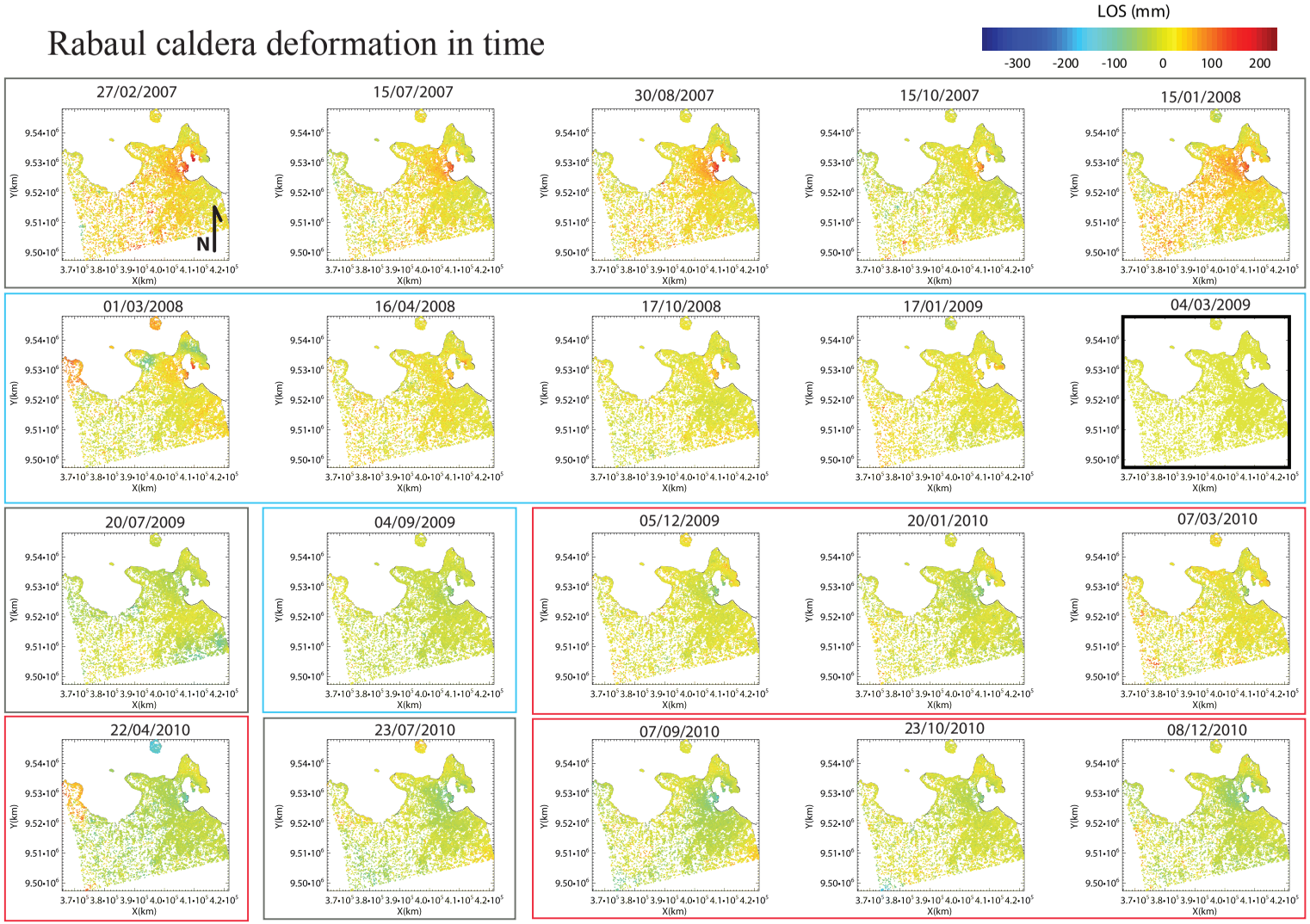

Figure 2.4.3. Unwrapped InSAR interferograms.
Each interferogram is calculated with respect to the master image (thick black frame). The LOS displacements during the time interval given on each interferogram are shown by color, where blue indicates an increase in the LOS (i.e. the PS moves away from the satellite) with respect to the position it has in the master image, and red represents a LOS decrease (i.e. the PS is closer to the satellite) with respect to the position it has in the master image.

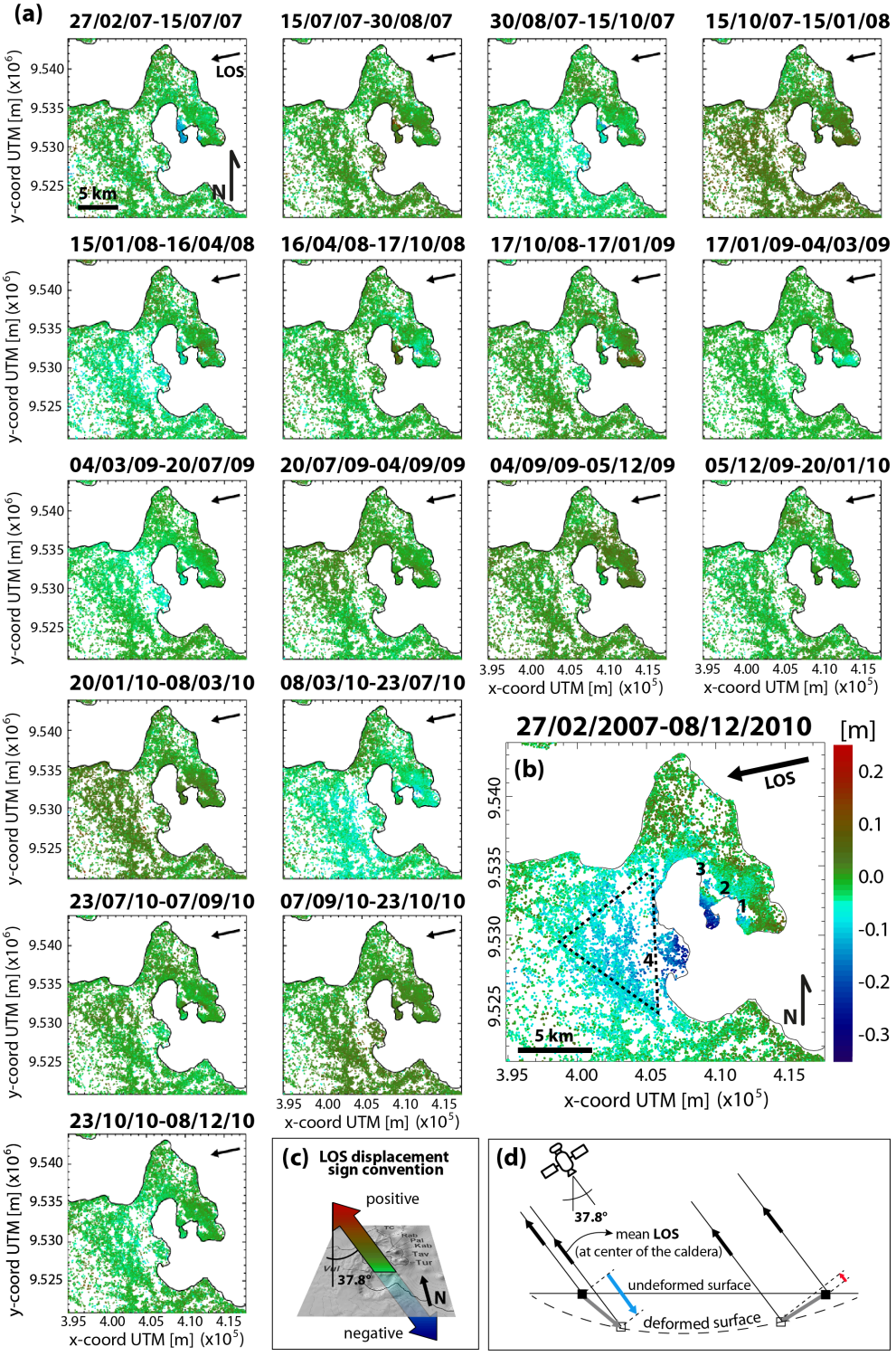

Figure 2.4.4. LOS displacements of selected dates at Rabaul area.
A black arrow on each image in top-right corner represents the LOS vector projection. The south-west corner of each image has UTM coordinates: x= 394,860 m; y= 9,520,893 m. The LOS displacements are shown by colors as color-bar in panel b and LOS sign convention illustrated in panel c. (a) Temporal sequence of images. Each image shows change since the previous image. (b) Total displacement over the entire period. The area delimited by the dashed lines is the Delta-shaped area referred in the text. The numbers indicate the areas of lack of persistent scatterers described in the text. (c) LOS displacement sign convention. (d) Interpretation of LOS displacements in the Rabaul area due to subsidence. Filled and empty pixels show the position of the terrain points over the undeformed and deformed surface, respectively. Gray arrows show the movement of the pixels, the blue and the red arrows represent the negative and positive movements along the LOS of the satellite, respectively.

Using the chosen images of the area of interest, we generated a temporal sequence of LOS displacements to observe the variable deformation in space and time (Fig. 2.4.4, a) and an interferogram of LOS displacements between the first and the last images to observe the total deformation over the entire period (Fig. 2.4.4, b).

Over the entire period, a wide area including the caldera and an area west of the caldera appear to experience a subsidence (Fig. 2.4.4, b). Negative LOS displacements (i.e. PS move far away from the satellite) are recorded inside the caldera and west of the caldera, while positive LOS displacements (i.e. PS move towards the satellite) are recorded in the eastern areas out of the caldera border (Turanguna, Kabiu, Tuvanumbatir slopes). The most negative LOS displacements are recorded between the south-western tip of Matupit Island and Vulcan north-eastern side. The LOS negative displacements spread west of the caldera, across the western caldera border, and over a Delta-shaped area centered at about the latitude of Vulcan edifice.

From the temporal series (Fig. 2.4.4, a), we can observe that some areas, especially at the eastern side of the caldera (Matupit Island, Tavurvur and Turanguna), experience a highly non-linear deformation, with variable positive and negative LOS displacements over the entire period. These movements are likely to be related to shallow volcanic processes. Displacements registered at Matupit Island and Tavurvur could be related to the shallow magma movements, cracks opening and the eruptive events periodically occurring during the entire period. The high non linear deformation on time recorded in the Turanguna area could be driven by the presence of a dilating fracture or of movements along the Talwat fault (*Saunders*, 2001; *Ronchin et al.*, 2013).

Insights from cumulative displacements

In order to look for a significant signal related to the volcanic system activity, once we have observed the spatial variations of LOS displacements over the area of interest, it is important to study the variation of LOS displacements in time. This helps to choose the most appropriate time lapse for further investigations. An easy and straightforward way to investigate the displacements in time is to plot the cumulative LOS displacements of specific areas of interest (Fig. 2.4.5).

We decided to plot the average cumulative LOS displacements for the areas inside the caldera that experience higher displacements (Vulcan and Matupit Island), for a point located at the SDA GPS station from where the RVO registered the observations about uplift and subsidence in their reports, as well as for the Delta-shaped area outside the caldera.

From the profiles (Fig. 2.4.5, a), we can observe that all areas experience a general subsidence that is more pronounced in the inner part of the caldera (on Matupit Island and Vulcan edifice). Short time variations of LOS displacements make the trends non-linear, especially for the Matupit Island area. They are probably related to some volcanic activity of the shallow volcanic or hydrothermal system. Interestingly, also the more linear average displacements trend of the broad distal Delta-shaped area seems to smoothly follow these variations, suggesting a common deeper source responsible to be a component of the registered deformation.

Taking into consideration the observations reported by the RVO, we notice that the first images do not agree with the period of rest observed, but considering a longer period, between February 27, 2007, and December 5, 2009, we find a good agreement with the RVO observations (i.e. a long term deflation). The same good agreement is valid for the positive LOS displacements values between December 5, 2009, and March 7, 2010, where RVO observed an uplift of about 4 cm in the first 4 months of 2010. Instead of recording a general rest during the next period, the InSAR show a deflation on July 23, 2010. This is possibly due to the fact that the SAR image has been

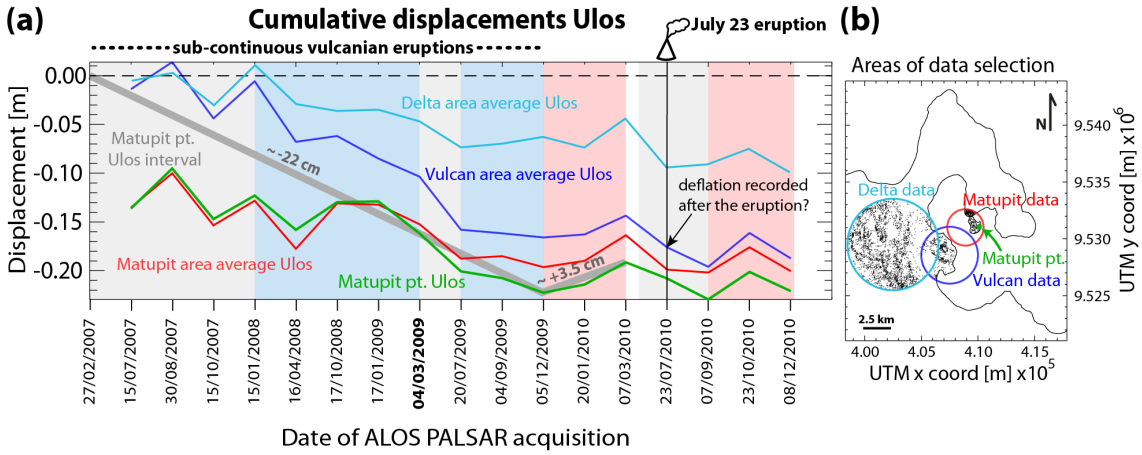

Figure 2.4.5. Cumulative line-of-sight deformation time series.
(a) Average cumulative LOS displacements from February 27, 2007, for the Delta-shaped area (light blue), Vulcan area (dark blue), Matupit Island area (red line), and SDA GPS station on the eastern tip of Matupit Island (green). Gray solid lines show the InSAR intervals whose displacements are concordant with RVO observations. The blue and red backgrounds mark the periods during which the RVO observed at Matupit Pt. subsidence or uplift, respectively (from the Smithsonian Institute reports, (Smithsonian Institution-National Museum of Natural History, 2013)). Gray background represents periods of no movements located at the same point. On top is indicated the main volcanic activity during the period: a long period of sub-continuous vulcanian eruptions at Tavurvur cone and the Tavurvur eruption of July 23, 2010. On the bottom are shown the days of the ALOS PALSAR acquisition. The bold date refers to the master image's day of acquisition. (b) Location of the PS used for the calculation of the average displacements.

acquired on the exact day of the eruption, recording the very short-term deflation associated with it and observed by the RVO.

Comparisons between the InSAR deformations and RVO observations are possible only for Matupit Island area. For this area, the short term disagreement between the InSAR and the observations could be due to the intrinsic accuracy of the ALOS probe, not suitable for monitoring little displacements due to its long wavelength, and to the fact that Matupit is not an ideal location for interferogram processing since it is a small area of land surrounded by water and therefore prone to unwrapping errors (John Dawson personal communication).

Insights from mean velocity and its STD

The temporal variations of LOS displacements affect the velocity deformation field and are represented in its related standard deviation. The PS product of the velocity deformation field (in m/yr) and its standard deviation, covering the period from February 2007 to December 2010, result from the analysis of 20 ascending radar images shown in Fig. 2.4.6. The standard deviation of the velocity field is mainly affected by the deviation of the PS motion from the linear model in time. Since the standard deviation is associated with the average rate of deformation in the time lapse studied, a strong non-linear motion of PS point during the time lapse would result in large residuals in respect to the linear model, and thus in a high standard deviation value. High standard deviation values allow identifying areas affected by motion-dynamics that are more complex than the linear model, showing the deviation form a linear velocity pattern of ground deformation (*Lagios et al.*, 2012).

Velocity results (Fig. 2.4.6, a) indicate a LOS displacement rate of about -60 mm/yr centered between Matupit Island and Vulcan and extending for a distance of about 7-8 km west of the caldera border. Very low positive values are observed on the edifices east of the caldera (Tovanumbatir,

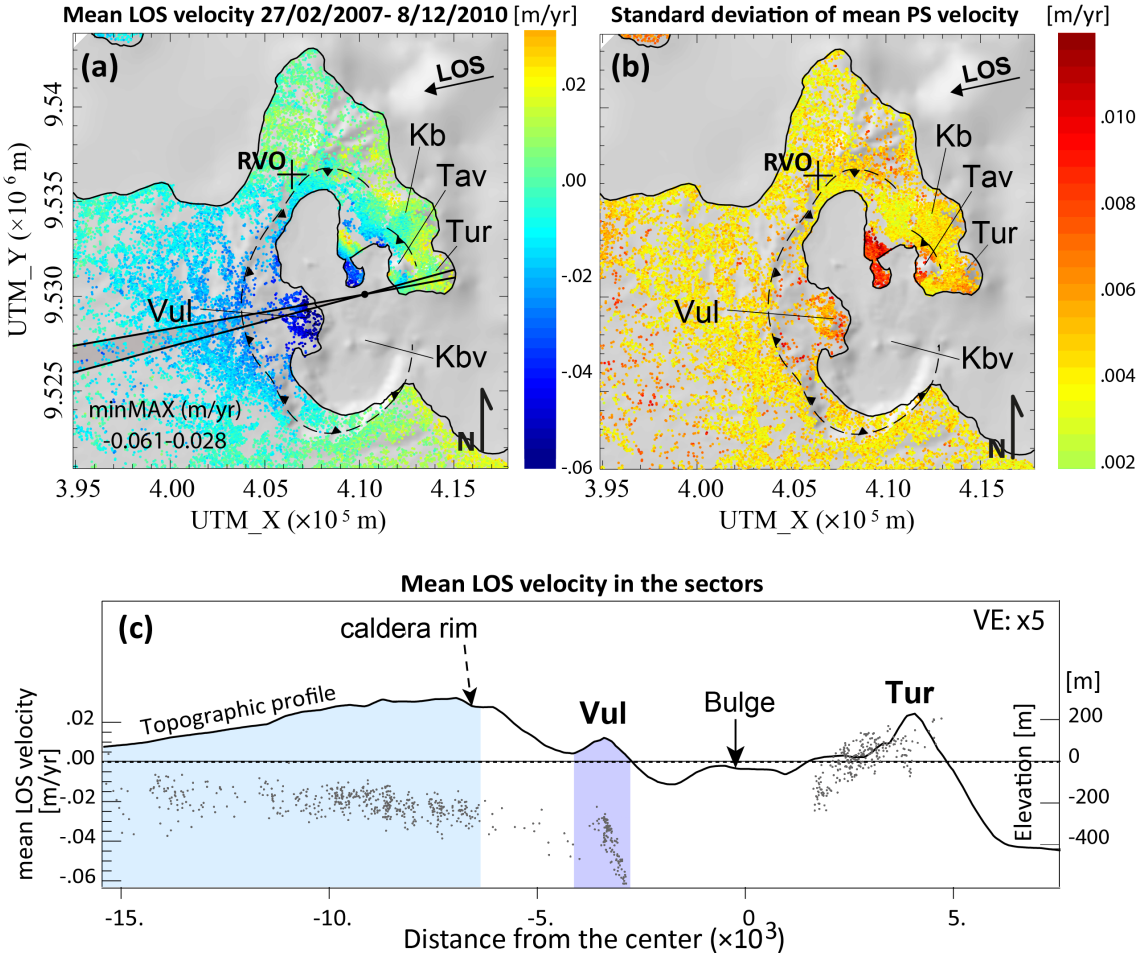

Figure 2.4.6. Mean LOS velocities and correspondent STD spanning the period of time 27 February 2007-8 December 2010.

(a) Mean velocities. The sectors include the PS plotted in the profile underneath. A minus sign on the scale bar represents lengthening of LOS range. The black arrow in the upper-right corner of the panels shows the surface projection of the mean LOS unit vectors (direction towards the satellite). (b) Standard deviation of the correspondent mean velocities. c) LOS deformation vs radial distance from the possible source (represented by a black dot at the south -east of Matupit Island in panel a). The LOS displacements are superimposed on the topographic profile (5x vertical exaggeration). The caldera rim, Turanguna, and Vulcan edifices are also indicated. The bulge is inferred from the bathymetric and reflection campaign (Greene et al., 1986). The sky-blue area indicates the long wave-length surface deformation of the area west of the caldera, the dark-blue area indicates the short wave-length, but with higher amplitude, surface deformation characteristic of the inner areas of the caldera (i.e. Vulcan and Matupit Is.).

Kabiu, and Turanguna) and on the south-eastern area outside the caldera. A little area of anomalous positive LOS displacements rate is observed along the south-western side of the old airport strip. Because this is a drainage area characterized by high soil mobility facilitated by the topography and the lack of vegetation on the airport strip, we can suspect that this anomaly corresponds to areas where soil is periodically removed and deposited. The drainage system of the area is clearly visible in a Google Earth picture of September 18, 2006 (GoogleEarth, 2014). The distribution of the correspondent standard deviation values (Fig. 2.4.6, b), low for constant removals from the slopes and high for complex alternate deposition and removal from lower areas, is also consistent with the previous considerations.

Standard deviation high values are clustered on Matupit Island and on the slopes of Tavuvur

(Fig. 2.4.6, b). The maximum values are located along the south-western side of the old airport strip. Somewhat high values are also observed on Vulcan slopes, while low values are observed in correspondence with the Delta-shaped area.

A profile path was chosen in a way that conveniently represents the signal over the entire area of interest (Fig. 2.4.6, c). Although missing to represent the high deformation area above Matupit Island, the profile shows the most important features of the signal: the long wave deformation of the Delta-shape area, a maximum of the deformation above Vulcan, and a portion of the signal on the eastern side of the caldera (over Turanguna). Along the profile, we can recognize the long-wave of low negative LOS displacements outside the caldera (light blue background in Fig. 2.4.6, c), a high velocity gradient above Vulcan edifice (dark blue background, 2.4.6, c), loss of data in the area occupied by water, and positive LOS displacements above Turanguna and the southern part of Tavurvur.

Chapter 3

Methods and procedures

3.1 Analytical models and finite element models (FEMs)

Relatively simple analytical solutions are commonly used to model volcanic deformation because they provide fast, precise, and computationally inexpensive solutions. This solutions, however, are ultimately inaccurate because the models are oversimplified by their assumtions. In order to obtain more accurate results, analytical solutions can be complemented with FEM analysis. FEMs are mathematical models capable of simulating elastic equations in arbitrary domain, partitioned to account for the 3-D distributions of elastic properties, and having the irregular relief of a volcano.

In this chapter, we provide an overview of models used to simulate volcano deformation, with particular attention to the FEM.

3.1.1 Analytical models for volcanoes: point source, finite spherical pressure source, and others

Relatively simple analytical solutions for deformation sources embedded in homogeneous, elastic half-space (HEHS) are commonly used to simulate observed volcano deformation because of their computational simplicity. The analytical solutions of *Mogi* (1958) produce readily predictable deformation patterns due to a spherical expansion source (or hydrostatic pressure change within a spherical source) embedded in a homogeneous, isotropic, Poisson-solid half-space problem domain (HIPSHS). The solutions of the Mogi's equations (recast for 3-D Cartesian coordinates and expressed in index notation) are given here to illustrate their simplicity:

$$\begin{pmatrix} u_i \\ v_i \\ w_i \end{pmatrix} = \alpha^3 \triangle P \frac{(1-\nu)}{G} \begin{pmatrix} \frac{x_i}{R_i^3} \\ \frac{y_i}{R_i^3} \\ \frac{d}{R_i^3} \end{pmatrix} \tag{3.1.1}$$

where d is the depth of the cavity center; u_i, v_i, w_i are displacement components at the i-esim point on the flat free surface whose position vector (x_i, y_i, 0) is defined with respect to the center of the cavity, the center of the cavity; is at (0, 0, -d); ΔP is the change in pressure within the magma chamber (which can be related to the flux injected of ejected from the magma chamber); α is the radius of the magma chamber; G is the shear modulus of the rock; and R_i is the Euclidean distance

separating the center of the cavity and point i-esim on the free surface, $R = \left(x_i^2 + y_i^2 + z_i^2\right)^{1/2}$. To fulfill the requirements of a point-source, the radius of the cavity has to be much smaller than the depth of the cavity center ($\alpha << d$). Fig. 3.1.1 displays the configuration of these components.

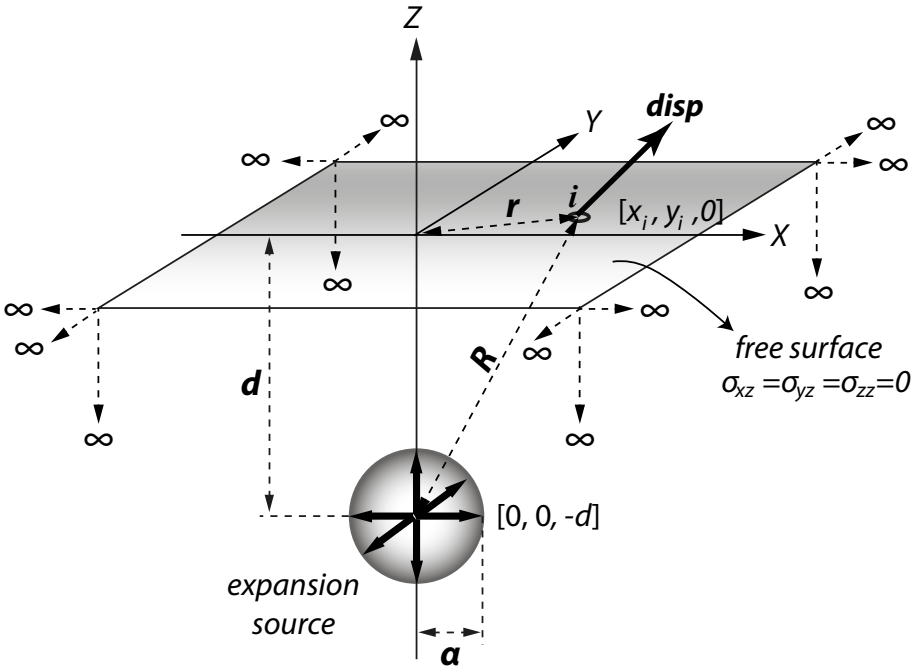

Figure 3.1.1. Mogi source geometry.
3-D Cartesian coordinate system and geometric relationships for a spherical expansion source embedded in a homogeneous, isotropic, Poisson-solid half-space (modified from Masterlark, 2007). The displacements (disp) components are inversely proportional to the cube of the Euclidean distance (R) between the center of the spherical expansion source and a generic point on the free surface (i). This model is subjected to the following assumptions: (1) lateral and depth boundaries extending to infinity, (2) no topography, (3) no layering or spatial variation in the crust, (4) isotropic material with no preferred orientations or fabrics, and (5) Poisson's ratio=0.25.

The Mogi point source is computationally simple and precisely predicts radial symmetric deformation caused by magmatic intrusion events (*Masterlark*, 2007), where the surface displacement vector radial to source is:

$$U_{Ri} = \sqrt{u_i^2 + v_i^2 + w_i^2} = \alpha^3 \triangle P \frac{(1-\nu)}{G} \frac{1}{R_i^2} \tag{3.1.2}$$

The scaling coefficient, representing the strength of the source, lumps together the radius of the cavity, α, the pressure change ΔP in the cavity, the material properties shear modulus G, and Poisson's ratio υ (*Lisowski*, 2006). As their contribution cannot be separated, a small pressure change in a big cavity will produce the same deformation of a big pressure change in a small cavity. The strength of the source, s, can be expressed as a change in pressure, ΔP, along the sphere's surface and as a volumetric change, ΔV, of the sphere as well:

$$s = \triangle V \frac{(1-\upsilon)(1+\upsilon)}{2\pi(1-2\nu)} = \triangle P(1-\nu)\frac{\alpha^3}{G} \tag{3.1.3}$$

We can use ΔP to estimate the equivalent cavity volume change, ΔV. In the case of a Poisson's medium, the relation between the two quantities is (*Lisowski*, 2006):

$$\triangle V_{cavity} \simeq \frac{\triangle P}{G}\pi\alpha^3 \tag{3.1.4}$$

Thus equation 3.1.1 can be rewritten as a function of ΔV:

$$\begin{pmatrix} u_i \\ v_i \\ w_i \end{pmatrix} = \triangle V \frac{(1-\nu)}{\pi} \begin{pmatrix} \frac{x_i}{R_i^3} \\ \frac{y_i}{R_i^3} \\ \frac{d}{R_i^3} \end{pmatrix} \tag{3.1.5}$$

It is important to note that this change of volume, ΔV_{cavity}, is not equivalent to the compressible volume of fluid injected, ΔV_{magma}, as it only considers the mechanical properties of the surrounding half-space. In fact, the volume of magma, ΔV_{magma} , intruded into a magma chamber accommodated by a combination of expansion of the chamber and compression of the stored magma, $\Delta V_{magma} = \Delta V_{cavity} + \Delta V_{compression}$ (Johnson et al., 2000). It is also important to note that the volume of the surface deformation, ΔV_{surf}, is not the same as the change in volume in the spherical magma chamber unless the surrounding crust is incompressible (υ=0.5). Integrating the vertical displacement over the free surface, the volume of the uplift generated by $\Delta V_{cavity}$of a spherical cavity is *Segall* (2010):

$$\triangle V_{surf} = 2(1-\nu)\triangle V_{cavity} \tag{3.1.6}$$

In order to relax the limitation of the point source assumption for which the dimension of the source are very small compared to its depth (point condition), *McTigue* (1987) provides an analytical solution that includes higher-order terms taking into account the finite shape of a spherical body:

$$\begin{pmatrix} u_i \\ v_i \\ w_i \end{pmatrix} = \left(\alpha^3 \triangle P \frac{(1-\nu)}{G} \left(\left(1 + \left(\frac{\alpha}{d}\right)^3 \times \left(\frac{(1+\nu)}{2\left(-7+5\nu\right)} + \frac{15d^2\left(-2+\nu\right)}{4R^2\left(-7+5\nu\right)}\right)\right)\right)\right) \begin{pmatrix} \frac{x_i}{R_i^3} \\ \frac{y_i}{R_i^3} \\ \frac{d}{R_i^3} \end{pmatrix} \tag{3.1.7}$$

Another method to generate the Mogi solution is to make use of Green's elastic tensor to generate an isotropically expanding point source (*Segall*, 2010), known as center of dilation. This considers three pairs of double forces acting in the three mutually orthogonal directions.

Others developed analytical solutions to simulate non-spherical expansion source geometries (e.g. ellipsoids *Yang et al.*, 1988; and faults, dikes, and sills *Okada*, 1992). Complicated deformation patterns can be simulated by superposition of multiple deformation sources (e.g., *Lundgren and Rosen*, 2003a; *Sturkell et al.*, 2006; *Wright et al.*, 2006).

Formulation for nonhomogeneous problem domains includes spherical expansion sources either embedded in horizontally layered elastic half-space (e.g. *Fernández et al.*, 1997; *Rundle*, 1980) or surrounded by thin viscoelastic shells that are embedded in an elastic full-space (*Dragoni and Magnanensi*, 1989).

Fundamental assumptions of these analytical solutions are that (1) the material properties of the volcano are elastic and do not vary in space and (2) the free surface -the land surface- is flat (e.g. the model does not consider topographic or bathymetric relief). These assumptions oversimplify the models which represent the volcanic systems. In fact, contrary to these assumptions, the presence of a volcano implies a localized weakness in the crust, and thus a heterogeneous distribution of properties. Furthermore, a volcano edifice often has a substantial topographic relief that cannot be accounted for by a homogeneous elastic half-space model. This limitation can be overcome by using corrections for the topography (*Williams and Wadge*, 2000). Finally, the HEHS assumptions can severely bias both source parameter estimations and forward model predictions for deformation and stresses in volcano deformational systems (*Behn et al.*, 2006; *Bianchi et al.*, 1987; *Bonaccorso et al.*, 2005; *De Natale and Pingue*, 1996; *Gudmundsson*, 2002; *Gudmundsson and Brenner*, 2004; *Gudmundsson and Loetveit*, 2005; *Gudmundsson and Philipp*, 2006; *Masterlark*, 2007; *Masterlark et al.*, 2010; *Newman et al.*, 2001; *Newman et al.*, 2006; *Trasatti et al.*, 2003, 2005).

Despite their limitations, all the above deformation models, particularly that of *Mogi* (1958), are computationally inexpensive, and thus easily integrated into linear inverse analysis seeking to characterize the source strength of the magma chamber and non-linear inverse analysis that seek to quantitatively define geometric parameters of the magma source. For example, Mogi solution is still widely used and successfully applied to a number of volcano deformation studies including Taal Volcano, Philippines (*Bartel et al.*, 2003), Unzen volcano, Japan (*Kohno et al.*, 2008), Soufrière Hills Volcano, Montserrat(*Mattioli et al.*, 2010).

Thus, they are still fundamental for the understanding of volcano deformation. In addition, they have a fundamental role to control the construction of a good FE model during the mesh refinement and validation of the model (see subchapter 3.5).

3.1.2 Finite element models (FEMs)

FEMs are mathematical models capable of simulating heterogeneous elastic properties, arbitrary shapes and the irregular topographic relief of a volcano. FEM methods divide a problem domain into small finite elements. The mechanical behavior is defined piecewise over each element in a way that integrates to satisfy constitutive mechanical relationship. This capability allows creation of more complex problem domains than those simulated by analytical methods. FEM domains complexities can closely resemble real conditions, producing more accurate results for analysis of geodetic data (InSAR, GPS, and leveling).

The use of finite element models (FEMs) to study volcano deformation is not new and has been used for more than four decades. *Dieterich and Decker* (1975) investigated prediction sensitivities to various source geometries in a HIPSHS domain and concluded that horizontal components of deformation are much more sensitive to the source geometry than vertical components. Sensitivities to the geometry of the expansion source were also investigated by *Yang et al.* (1988) through FEMs, while Newman et al. (2001; 2006) used FEMs to investigate deformations due to spherical and prolate spheroid expansion sources, having viscoelastic shells. FEMs were also used to account for heterogeneous caldera configurations and structural discontinuities in stress (e.g. *Troise et al.*, 2003) and deformation predictions (*Bonaccorso et al.*, 2005; *De Natale and Pingue*, 1996; *De Natale et al.*, 1997; *Orsi et al.*, 1999; *Poland et al.*, 2006; *Trasatti et al.*, 2003, 2005; *Geyer and Gottsmann*, 2010).

The greatest advantage of FEM is its ability to handle truly arbitrary geometry. Probably its next most important features are the ability to deal with general boundary conditions and to include non-homogeneous and anisotropic materials. This means that they can treat systems of arbitrary

shape that are made up of numerous different material regions. To these features we can add a large amount of freedom in prescribing the loading conditions.

In this method of analysis, a complex region defining a continuum is discretized into simple geometric shapes called finite elements. The material properties and the governing relationships are considered over these elements and expressed in terms of unknown values at element corners. An assembly process, together with prescribed loads and constraints, reduces the model to a form which is solvable by a finite number of equations. This means that the approximate solution has to be characterized by a finite number of parameters, called degrees of freedom. Solution of the equations gives us the approximate behavior of the continuum.

Here we use the commercial finite element software Abaqus (http://www.simulia.com). In addition, Abaqus models are modified manipulating the Abaqus .inp file and implemented with Python codes.

The finite element method solves partial different equations. Here it is used to predict the deformation field within solid bodies subjected to external forces in which relationships between the forces applied and the displacements produced are linear, materials are history independent (we don't use plastic or viscoelastic materials), and the load is applied instantaneously (no load history). Here we are also interested in determining the behavior of a solid body that is in static equilibrium. That means that the sum of all forces (external and internal) is zero and the finite element method solves the equilibrium equations:

$$\sum \mathbf{F} = \mathbf{0} \tag{3.1.8}$$

To set up any finite element calculation of a linear static problem, we need to specify (*Bower*, 2009):

1. the geometry of the solid. This is done by generating the finite element mesh for the solid. Usually generated from a CAD representation of the solid

2. the properties of the materials. This is done by specifying a constitutive law for the solid

3. the load applied to the solid, done by specifying the boundary conditions for the problem

4. if the analysis involves contact between solids, we need to specify the surfaces in contact and the properties of the contact

In general, in order to generate a model, run an analysis, and interpret the results, commercial software like Abaqus is comprised of three main steps: pre-processing, analysis, and post-processing. The goals of pre-processing are to generate the model geometry, develop an appropriate finite element mesh, assign material properties, and apply boundary conditions and loads. In many cases the commercial softwares provide CAE interfaces to allow interactions with the program and facilitate the pre-processing procedures. The post-processing phase is dedicated to the check of problems that could have occurred during the solution through the interpretation of warning or errors provided by the software, and to the study of the results. While these two phases are interactive and time-consuming for the analyst, the analysis (solution) is often a batch process and requires computer time and resources that need to be planned based on the available computer resources. In the analysis step, the governing equations are assembled into matrix form and are numerically solved. The Abaqus work-flow and output files are illustrated in Fig. 3.1.2. In this figure, the levels at which Python and IDL procedures operate are illustrated. These procedures are generated in this

work to implement the complex geometries generation and automate the analysis run during the pre-processing phase.

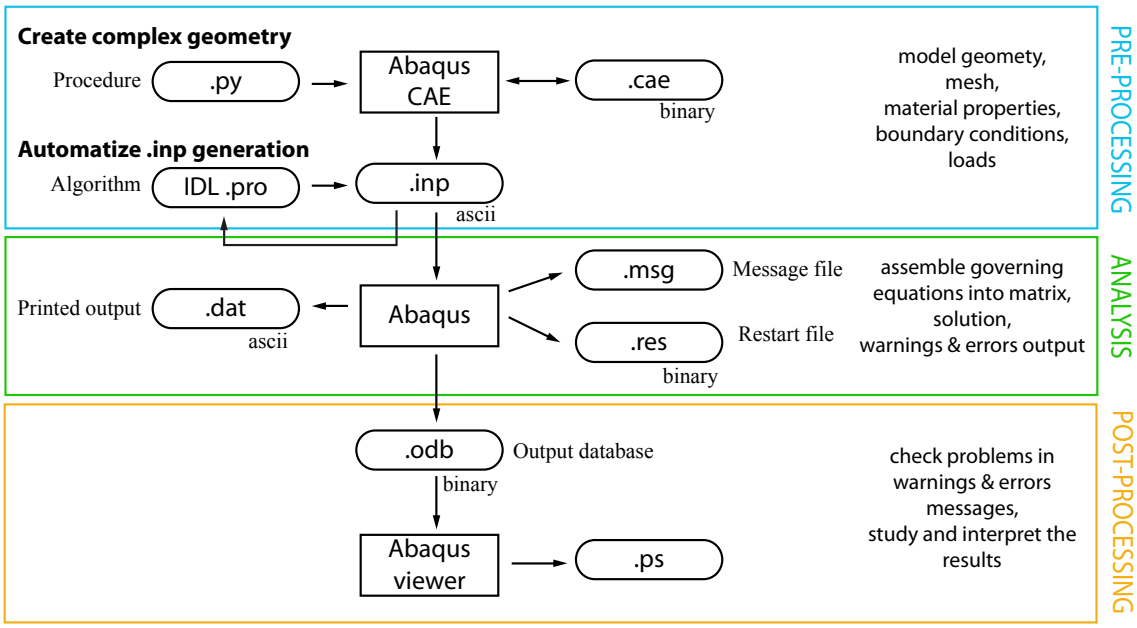

Figure 3.1.2. Abaqus workflow.
Pre-processing, analysis, and post-processing steps with their related input and output files. Input and output files are represented by boxes with rounded corners and are identified by their extension.

In defining the geometry of the model, the first concern is about the dimentions and the size of the domain. The dimensions and symmetry of the model are related to the complexities and symmetry of the system to be modeled. Instead, the size of the domain is regulated by the source depth, shape, and size as they also control the shape and the extent of the deformation field. In order to obtain an accurate numerical solution, as a rule of thumb, the domain size must be at least twice the deformation field extent (*Currenti et al.*, 2008).

The elements in which the domain is parceled are organized in a finite element mesh. This mesh is defined by a set of nodes together with a set of finite elements. The nodes are discrete points within the solid identified by an integer number, having spatial coordinates. At each node boundary conditions can be applied and the nodal displacements are calculated. Other unknown quantities can be calculaed at each node (i.e. temperature), the collection of all unknown quantities at each node are known as degrees of freedom. The nodes are connected to form the elements that are used to partition the solid into discrete regions. Each element is identified by a integer number, a geometry (in this work we use 4 noded tetrahedron and 8 noded brick for 3-D domains, see Fig. 3.1.3), a set of faces which are the sides of the elements, a set of nodes attached to the element, and an interpolation sheme.

The purpose of a finite element is to interpolate the displacement field u between the values defined at the nodes. Different interpolation schemes exist for different elements. The elements used in this work are linear elements and use a linear scheme of interpolation to provide displacement values of location between nodes.

Meshing the domain is not a trivial process. It requires refinements of the mesh and the validation of the metric. Due to the importance of working with a good mesh, and the complexity of steps required to achieve a good mesh, the subchapter 3.5 is dedicated to the mesh construction.

The three governing equations that define elasto-static displacement (u) at nodes in a 3-D

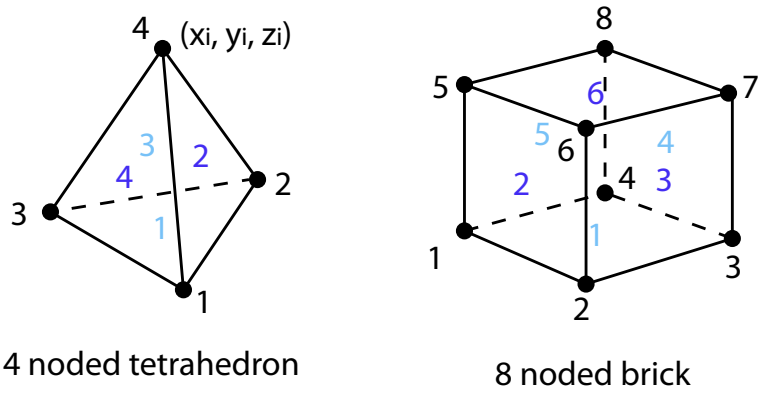

Figure 3.1.3. Geometry of the elements used in this work.
Black integer numbers identify the nodes in the element. Each node have also spatial coordinates (x_i, y_i, z_i). Blue and sky-blue numbers positioned in the middle of the faces identify the number of front faces and back faces, respectively.

domain are:

$$G\nabla^2 u_1 + \frac{G}{1-2\upsilon}\left[\frac{\partial^2 u_1}{\partial x^2} + \frac{\partial^2 u_2}{\partial x \partial y} + \frac{\partial^2 u_3}{\partial x \partial z}\right] = -F_x \tag{3.1.9}$$

$$G\nabla^2 u_2 + \frac{G}{1-2\upsilon}\left[\frac{\partial^2 u_1}{\partial y \partial x} + \frac{\partial^2 u_2}{\partial y^2} + \frac{\partial^2 u_3}{\partial x \partial z}\right] = -F_y \tag{3.1.10}$$

$$G\nabla^2 u_3 + \frac{G}{1-2\upsilon}\left[\frac{\partial^2 u_1}{\partial_z \partial x} + \frac{\partial^2 u_2}{\partial z \partial y} + \frac{\partial^2 u_3}{\partial z^2}\right] = -F_z \tag{3.1.11}$$

where G is the shear modulus, υ is Poisson's ratio, and F is a body force per unit volume (*Wang*, 2000). The subscript i spans orthogonal direction components, so displacements in the x, y, and z direction (east, north, and vertical) are designated by u_1, u_2, and u_3.

Elastic strain (ε) is a function of the change in displacement and stress (σ) as follows:

$$\varepsilon_{xx} = \frac{\partial u_1}{\partial x} = c_1\sigma_{xx} + c_2\sigma_{yy} + c_3\sigma_{zz} \tag{3.1.12}$$

$$\varepsilon_{yy} = \frac{\partial u_2}{\partial y} = c_4\sigma_{xx} + c_5\sigma_{yy} + c_6\sigma_{zz} \tag{3.1.13}$$

$$\varepsilon_{zz} = \frac{\partial u_3}{\partial z} = c_7\sigma_{xx} + c_8\sigma_{yy} + c_9\sigma_{zz} \tag{3.1.14}$$

$$\varepsilon_{xy} = \frac{1}{2}\left(\frac{\partial u_1}{\partial y} + \frac{\partial u_2}{\partial x}\right) = c_{10}\sigma_{xy} \tag{3.1.15}$$

$$\varepsilon_{xz} = \frac{1}{2}\left(\frac{\partial u_1}{\partial z} + \frac{\partial u_3}{\partial x}\right) = c_{11}\sigma_{xz} \tag{3.1.16}$$

$$\varepsilon_{yz} = \frac{1}{2}\left(\frac{\partial u_2}{\partial z} + \frac{\partial u_3}{\partial y}\right) = c_{12}\sigma_{yz} \tag{3.1.17}$$

where c_1-c_{12} are constants (*Wang*, 2000).

3.2 Modeling protocol

The ability of a model to efficiently and accurately represent a natural system directly impacts the results and the usefulness of the model (*Compton*, 2013). Thus, the validation of the model mesh and the integration of geology and geophysical data into deformational modeling is a critical and necessary advancement toward more reliable and accurate predictions (*Masterlark*, 2003). In this study we followed a formal modeling protocol (*Masterlark and Hughes*, 2008) to ensure the models of Rabaul caldera simulate the natural system in the most efficient, accurate, and reproducible way possible. The protocol goals are: to guide and test the model design, to ensure that the modeling progression honors the available information, and to provide the mechanism for iterative reassessment (*Masterlark and Hughes*, 2008). In fact, the protocol is iterative. This means that each step leads to the next step or to the modification and re-evaluation of the step itself.

Here follows a short description of each step of the modeling protocol. Specific topics that require extended explanations, such as the lofting strategy to build 3-D bodies in Abaqus (subchapter 3.3) and the validation of the model (subchapter 3.3), are described in subsequent subchapters.

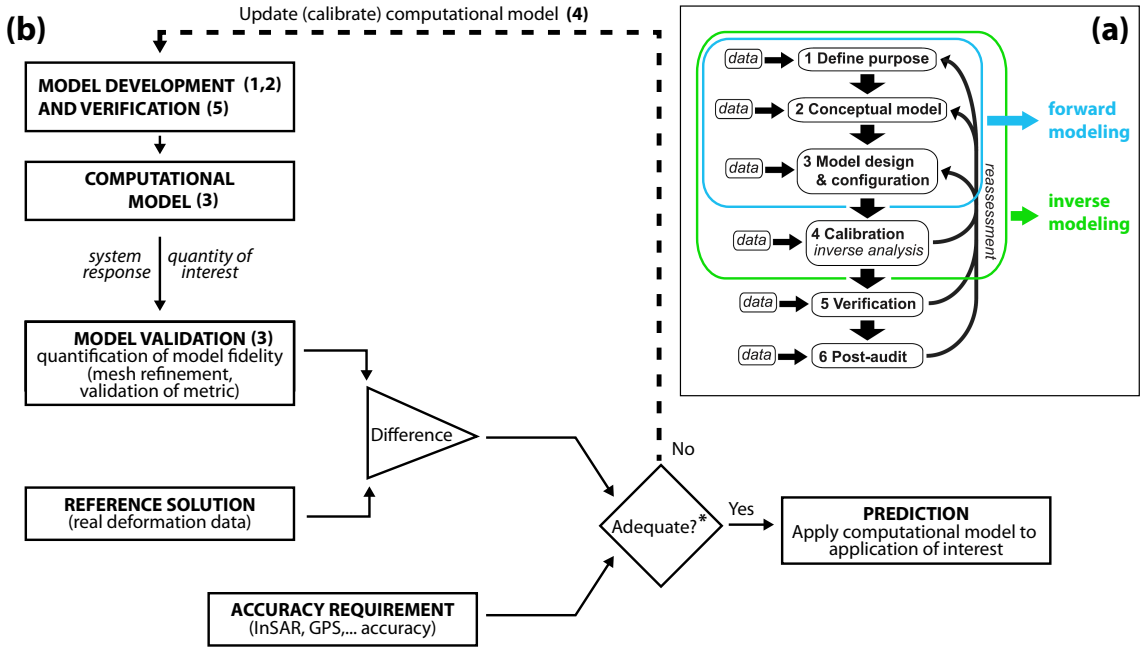

Figure 3.2.1. Iterative modeling protocol and workflow.
(a) Iterative modeling protocol utilized in this study, modified from Masterlark and Hughes (2008). The protocol ensures the modeling progression honors the available information and provides the mechanism for iterative reassessment (Masterlark and Hughes, 2008). (b) The steps of the protocol (same numbers of panel b) used for the fem-forward modeling and fem-integrated inverse modeling are shown in the validation, calibration, and prediction workflow. (*) Adequate in terms of 1) accuracy requirement and 2) meaningfulness of solution.

3.2.1 Define purpose

Defining the purpose of the analysis is the first step of the modeling protocol. Because the purpose of the model drives the entire modeling process, it must be explicitly defined at the beginning of the analysis process.

The purpose of our model depends on what system and which data we want to simulate.

3.2.2 Conceptual model

The conceptual model is the general design of the model; it is the foundation of the deformation modeling protocol and therefore a fundamental consideration for predicting volcano deformation. Implications of the conceptual model propagate throughout the modeling analysis (*Masterlark and Hughes*, 2008): inaccurate input to the model creates unreliable predictions, which can have dangerous implications regarding analysis of stress regimes, subsequent deformations (*Hughes*, 2011), and the interpretation of subsurface magmatic processes, which can bias eruptions forecasts.

In addition to the choice of the dimension of the problem (i.e. 1-D, 2-D, 3-D, axis-symmetrical), the geologic constraints and general geometry, the decision of physical processes to simulate is part of the conceptual model definition. The physical processes that bring to magma storage and magma migration are many, different in nature, and very complex. Any computer model simulating volcanic systems has to ignore or simplify some of the processes by imposing limitations to the model configuration that needs to be explained in the conceptual model step in order to be taken into account when it comes to interpreting the surface deformations.

The reassessment of the conceptual model design is an avenue toward future improvements of any model configuration (*Masterlark and Hughes*, 2008).

3.2.3 FEM model design and configuration

The model is configured to simulate and quantify the processes and relationship of the conceptual model (*Hughes*, 2011).

In this step, the geometry of the problem and the material properties are defined in the FEM model. The geological, topographic, and geophysical data are combined to guide the design and configuration of the finite elements model geometry and its material property distribution. In the subsequent subchapter 3.3, we extensively describe the strategy used to build the 3-D bodies in Abaqus. In addition, the general governing equations, satisfied by the model, are described, as well as boundary conditions, loading specifications, and initial conditions.

Because the validity of a given deformation model configuration will influence the associated interpretations of forward model predictions (*Masterlark and Hughes*, 2008), model validation is a necessary and critical step in the modeling process (*Anderson and Woessner*, 1992). Validation ensures that a numerical model is working properly (*Wang and Anderson*, 1982), that it accurately represents the conceptual description of the model, and that it is solved correctly and accurately. In the validation process, it is important to estimate the discretization errors that are the errors in the solution attributable to meshing. Model validation is extensively explained and discussed in subchapter 3.5.

3.2.4 Calibration (inverse analysis)

The source strength is calculated and calibrated to the data (InSAR in this study) by computing an inversion of the data for a model that honors the geological information (the known structure of the magmatic system). As defined by the *ASME* (2006), calibration is the process of adjusting physical modeling parameters in the computational model to improve agreement with experimental or, in our case, with observed data.

This step includes the data preparation (QUADtree reduction discussed in subchapter 3.6), the data inversion (Linear inversion method discussed in subchapter 3.7), and statistical tests (like the f-test) to test the significance of the results.

3.2.5 Verification and Post-audit

The verification and post-audit are two steps that are often done to discern best-fit parameters and require data that are independent from the data already used from the previous steps.

The verification step is an assessment of the model predictive reliability, in which we test if the model successfully predicts data that are independent of the calibration process (*Masterlark and Hughes*, 2008). This step is done once the calibrated model predicts deformations statistically similar to the observed deformations. In the case of Rabaul, GPS, leveling and tilt data could provide useful datasets for this purpose.

The final step is to post-audit the model using future surface deformation. Post-audits are usually tenuous because the system often changes from the time the data used for calibration is collected, requiring a new model design or new inputs (*Compton*, 2013).

3.3 Building strategy for 3-D parts in Abaqus

This subchapter is an extract of the paper "Solid modeling techniques to build 3D finite element models of volcanic systems: An example from the Rabaul Caldera system, Papua New Guinea", (*Ronchin et al.*, 2013). Some parts are extended with new images for a better explanation of the treated concept. The Python code is provided in Appendix A.

The meshing procedure is preceded by the initial phase of constructing a suitably smooth solid geometric representation of the geologic body volumes deduced from geologic maps, earthquake locations, and tomographic images.

Advancements in computer resources and computational techniques have opened the possibility to apply 3-D solid modeling and simulation to large-scale deformation of geological structures. Since the beginning of the application of finite element models (FEMs) to volcanic studies, axisymmetric and two-dimensional models were extensively used (*Bianchi et al.*, 1984; *Dieterich and Decker*, 1975; *Yang et al.*, 1988). Owing to computational limitations, the early FEM studies predominantly used two-dimensional or axisymmetric modeling, which simulates a magma chamber as a regular shaped fluid-filled cavity. Consequently, these early models lacked geometric fidelity to a natural volcanic system. In fact, model symmetry poorly reflects the highly heterogeneous distribution of properties of volcanic areas, as well as their topography and bathymetry. As increased computational power became more widely available, larger 3-D models became feasible and results from three-dimensional models were increasingly reported in the literature (*Currenti et al.*, 2011a; *Masterlark et al.*, 2012; *Meo et al.*, 2008; *Trasatti et al.*, 2008). Up to now, most approaches for 2-D and 3-D modeling of volcano crustal deformation and stress distributions have been based on applications of pressure loads, embedded in either homogeneous or layered elastic half-spaces (*Dieterich and Decker*, 1975; *Geyer and Gottsmann*, 2010; *Gottsmann et al.*, 2006; *Gudmundsson and Brenner*, 2004; *Pritchard and Simons*, 2004; *Trasatti et al.*, 2003).

Due to the complex history and array of physical and chemical processes occurring in volcanic areas, volcanic systems are characterized by abrupt spatial variations of material properties, both lateral and vertical. Considerable improvement of volcano deformation models thus may be attained by taking into account spatial variations in the rheological properties (*Currenti et al.*, 2011b; *Masterlark et al.*, 2012; *Pedersen et al.*, 2009). Geologic maps, tomographic images, and seismicity data provide information on the distribution of material properties and stress regime, which often reveal a complex picture of the volcanic system.

This part of the dissertation explores the capabilities of Abaqus software (Abaqus, 2009) in modeling and assembling 3-D complex rheologic parts. We provide a strategy to use the spatial information on the distribution of material properties inferred from tomographic studies, among other geophysical and geological information, in order to create 3-D representation of geological bodies and assemble them in a 3-D geologic model using the Abaqus/CAE environment. The bulk of this section is devoted to creating parts using the Abaqus geometry definition functions: splines and solid lofts, implemented with Python scripts to automate execution of Abaqus commands.

3.3.1 3-D modeling strategy using Python script to implement Abaqus CAE

Abaqus is a commercial software that uses Python commands during the model creation. The Python code provides access to Abaqus functions. We take advantage of this versatility developing some Python routines which significantly increases the flexibility of Abaqus functions and allowes

for automated execution of hundreds of commands, as is necessary to produce complex 3D parts. To construct the 3D model, a CAE approach that allows simple creation and alteration of model geometries is used in combination with the Python script, written to control the input points and the creation of splines and lofted volumes (Fig. 3.3.1, a). For each recognized geologic region, an Abaqus part is first built with the help of the Python script and then modified by using boolean operations in the CAE environment during the assemblage of the model. Finally, all parts are assembled and merged into a single entity, preserving the numerically welded boundaries of the individual parts (Fig. 3.3.1, a).

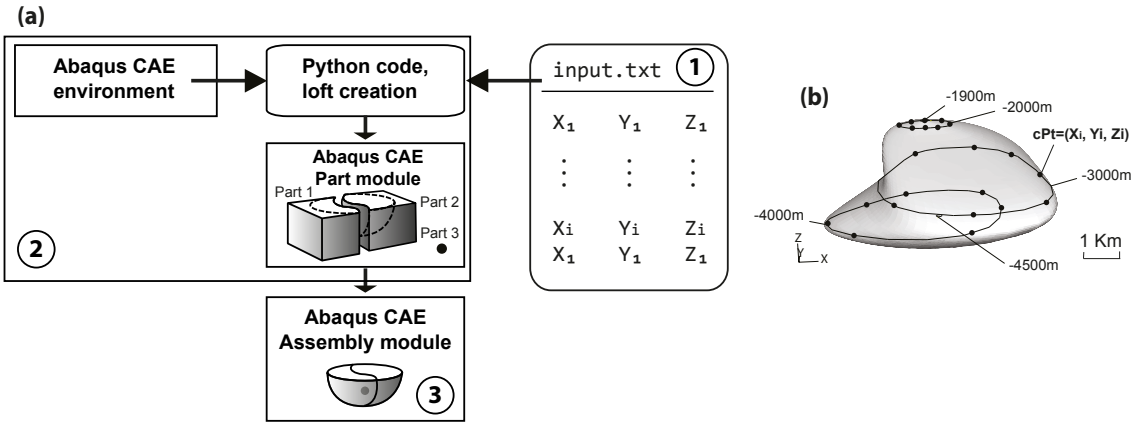

Figure 3.3.1. Conceptual diagram of the steps of the model geometry construction, modified from Ronchin et al. (2013).
(a) 1) Identification of control points coordinates (as in panel b) and input file generation (a1), 2) Importing control points, creating part contours, and generate the lofted solids (a2), 3) assembling the model. (b) Example of magma chamber contour splines.

Geologic bodies such as magma chambers have complex 3-D shapes, so their solid representation assumes complex three-dimensional shapes that can be built by lofting the body through cross-sectional closed splines (Fig. 3.3.1, b). In fact, considering a contour as a continuous curve representing the intersection of a plane and the surface of an object, one technique for creating a solid volume is to imagine contours from different hypothetical slices and to loft a solid through these contours. The same technique can be used to construct a surface through many surface sections (*Fuchs et al.*, 1977; *Meyers et al.*, 1992). Because the Abaqus solid-loft function uses a series of consecutive 2-D cross sections bounded by closed splines to generate a volume, we need to first identify some contours from the geological and geophysical data at different depth (Fig. 3.3.1, b). Two-dimensional contouring involved fitting splines through a number of control points (*Zhang et al.*, 2005), cPT,located along the 2-D cross sections of the body. We first createcontours and then sculpted the solid objects (magma chamber, caldera infill, etc.) by lofting them through their contours (Fig. 3.3.1, a2). The lofted object geometries are later modified and adjusted to the surrounding objects they are in contact with using partitions and boolean operations. The boolean operation makes use of primitive solid objects and utilizes the regularized boolean operators (union, difference, etc.) to combine the primitive objects into new solid objects. Finally, we assembled the entire model combining all the objects into one single part (Fig. 3.3.1, a3).

The process of building a 3-D geometry for an FEM consists of three main steps: (1) Choosing the control points and create the input file, (2) Building the 3-D parts, and (3) Assembling the parts to build the model. Here follows the description of each steps of the procedure:

1-Identify control point coordinates and create an input file

Tomographic and geologic images need to be geo-referenced to the Universal Transverse Mercator (UTM) projection system. This can be done through the open-source GIS software package QGIS (Quantum GIS Project Team, 2011). The UTM system has some advantages for Abaqus users. In this global coordinate system, a grid constructed on the Transverse Mercator projection of each longitude zone is used to locate points. The grid system is rectangular, decimal based, and has uniform units of measure that are amenable to Cartesian coordinate mathematics and suitable for the large scale domain of volcano deformation problems. This procedure enabled us to choose and obtain the spatial coordinates of strategic points which are later imported in Abaqus CAE and used as control points for the object spline contours (Fig. 3.3.1, b). Points with UTM coordinates (X_i, Y_i, Z_i for East, North, and up) are easily imported in the Abaqus cartesian space and ready to be used to build more evolved objects. In the UTM system, coordinate precision is readily understood; for our purposes, coordinates are measured in meters and they translate directly to distances on the ground, allowing the user a rough preliminary control of the geometric model.

A good approach for the selection of spline control points is to choose strategic points along the contour we want to be represented by a spline in Abaqus. Thus, the control point coordinates cPt_i=X_i, Y_i, Z_i) can be obtained by manual selection of points along the chosen body contours on a geo-referenced horizontal tomographic slice. For very precise 3-D representation, this could be a drawback as it can lead to pronounced geometric discrepancies between the spline and the parent cross section perimeter (*Young et al.*, 2008). However, this technique is suitable for geological purposes where the sections along which we select the control points are tomographic images characterized by resolution of kilometers (*Finlayson et al.*, 2003) and smooth changes of Vp, which cannot resolve sharp boundaries between velocity anomalies. For a reference guide about the format requirements of the .txt file containing the cPt coordinates, see Appendix A.

2-Importing control points, creating part contours, and generating the lofted solids.

All processes of importing points and generating closed splines were automated in the CAE-SPLINE.py Python script that can be called and executed in Abaqus CAE (see Appendix A). The script reads the input .txt file, imports the control point coordinates, recognizes the different depth values (Z_i), and calls the Abaqus function WireSpline, which generates a series of planar closed loops (one spline contour for each depth value encountered).

The construction of the 3-D volumes is finalized by lofting the body thought the splines.

3-Assembling the model

Once we had all the parts needed (one for each geologic region), the model was assembled in the CAE Assembly module. With the use of boolean operations, two or more solids can be combined. Solid combination by boolean operators provides great flexibility to create a variety of shapes. First, all parts were reshaped using boolean operations in order to fit the neighbor part surfaces. The advantage of using boolean operations is that they allow us to obtain new objects whose surfaces are precisely coincident with the adjoining parts, avoiding the formation of unwanted gaps in the model. The resulting parts were then stacked together from the upper crust parts to the mantle part forming a pile. The cavity for the magma chamber was created by subtracting the magma

chamber solid from the pile, while the far field was shaped as a hemisphere by building a mold as a separate object and using it, through boolean operation cutting tools, to remove any exceeding volumes (outside of the wanted far field boundaries) of the piled layers.

3.4 Effective material properties

The physical and mechanical properties of the volcano edifices have been discussed and modeled in several ways by other authors. Apuani et al. (2005) defined lithotechnical units based on the relative percentage of breccia versus lava fraction in rock masses; some authors modeled the volcano using homogeneous and isotropic blocks (e.g. *Poland et al.*, 2006; *Masterlark et al.*, 2012); others (e.g. *Trasatti et al.*, 2003; *Gudmundsson*, 2008; *Geyer and Gottsmann*, 2010) modeled layered volcanoes regarding each individual layer as homogeneous and isotropic; other authors use the 1-D or 3-D tomography to introduce a smooth variation of mechanical properties over the domain (e.g. *Currenti et al.*, 2008; *Manconi et al.*, 2010). The most common approach to include the heterogeneities in the models is to regard each "block", or geologic region, as homogeneous and isotropic. The anisotropy in the model is thus introduced through contacts and discontinuities with different mechanical properties (*Gudmundsson*, 2008). To fully describe the elastic behavior of a homogeneous and isotropic region, two independent constants are needed: e.g. the Young's modulus (E) and the Poisson's ratio (υ), or the shear modulus and the bulk modulus. Note that there are five used elastic constants G (shear modulus), λ (Lamé constant), K (bulk modulus), E (Young's modulus), υ (Poisson's ratio). Any two of these properties are sufficient to define the elastic behavior, since from their definitions they are not independent. They are linked by relationships (*Graham and Houlsby*, 1983) such as the following:

$$G = E/2(1+\nu) \tag{3.4.1}$$

$$K = E/3(1-2\nu) \tag{3.4.2}$$

where G is the shear modulus and K is the bulk modulus. Tab. 3.4.1 resumes the relationships between the elastic constants. As reported by Gudmundsson (2008), the two elastic constants most commonly used in rock physics are Young's modulus and Poisson's ratio.

In-situ values of the elastic constants are preferable for large-scale tectonic and volcanic models. As these models are built to represent wide areas and high depths, the variety of rocks to be included in the model is huge. *In-situ* analysis for the characterization of materials could be very expensive and sometimes impossible to perform (in the case of materials at high depths or in areas of difficult access); this is why *in-situ* and laboratory-derived static values on representative rocks of the volcano to be modeled are usually rare. To overcome this problem, the researchers use the tomographic velocities to derive the dynamic elastic properties. Thus, when an *in-situ* field test for static elastic properties cannot be performed, a way to determine field strength is using the correlation between the dynamic rock strength and its seismic wave velocity, and the relationship between dynamic and static moduli.

3.4.1 Poisson's ratio

Poisson's ratio (υ) is the measure of the tendency of a sample of material compressed in one direction to get thicker in the other directions. It is defined by the ratio of the lateral unit strain to the longitudinal unit strain (ϵ_r/ϵ_z) in a body that has been stressed longitudinally within its elastic limit (*Dzurisin*, 2007).The Poisson's ratio is influenced by two independent factors: the solid rock and dry or wet cracks. Pores and cracks -the latter defined as flat cavities of low aspect ratios- lower (in case they are dry) or heighten (in case they are wet) the Poisson's ratio of the rock.

	E	ν	G	K	λ
λ, G	$\frac{G(3\lambda+2G)}{\lambda+G}$	$\frac{\lambda}{2(\lambda+G)}$	G	$\lambda+\frac{2}{3}G$	λ
λ, E	E				λ
λ, ν	$\frac{\lambda(1+\nu)(1-2\nu)}{\nu}$	ν	$\frac{\lambda(1-2\nu)}{2\nu}$	$\frac{\lambda(1+\nu)}{3\nu}$	λ
λ, K	$\frac{9K(K-\lambda)}{3K-\lambda}$	$\frac{\lambda}{2(\lambda+G)}$	$\frac{3(K-\lambda)}{2}$	K	λ
G, E	E	$\frac{E-2G}{2G}$	G	$\frac{GE}{3(3G-E)}$	$\frac{G(E-2G)}{3G-E}$
G, ν	$2G(1+\nu)$	ν	G	$\frac{2G(1+\nu)}{3(1-2\nu)}$	$\frac{2G\nu}{1-2\nu}$
G, K	$\frac{9KG}{3K+G}$	$\frac{3K-2G}{6K+2G}$	G	K	$K-\frac{2}{3}G$
E, ν	E	ν	$\frac{E}{2(1+\nu)}$	$\frac{E}{3(1-2\nu)}$	$\frac{E\nu}{(1+\nu)(1-2\nu)}$
E, K	E	$\frac{3K-E}{6K}$	$\frac{3KE}{9K-E}$	K	$\frac{3K(3K-E)}{9K-E}$
K, ν	$3K(1-2\nu)$	ν	$\frac{3K(1-2\nu)}{2(1+\nu)}$	K	$\frac{3K\nu}{1+\nu}$

Table 3.4.1. Summary of the elastic constant relationships (from Gudmundsson, 2011). *The elastic constants are represented in terms of two other constants.*

There are two methods to determine the Poisson's ratio of a rock. The first is a uniaxial loading test to compute the ration of radial strain and axial strain (ϵ_r/ϵ_z). This test leads to the determination of the static Poisson's ratio of the rock (υ_{st}). The second is to measure compressional and shear velocities (Vp and Vs) from the seismic data, tomography, or sonic well logs, and to define the dynamic Poisson's ratio (υ_{dy}) through the formula:

$$\nu_{dy} = \frac{0.5\,(Vp/Vs)^2 - 2}{(Vp/Vs)^2 - 1} \tag{3.4.3}$$

As the Poisson's ratio increases, the body will tend to respond to the loading with a change of shape rather than a change of volume. A perfectly incompressible material, like a fluid at rest, does not change its volume in response to any loading. The Poisson's ratio of such a material would be exactly 0.5 and its bulk modulus, K, would be very high. Fluids such as water have a Poisson's ratio of 0.5 and are assumed as incompressible. However, there are no materials purely incompressible. Thus, in modelling the dynamics of fluid-filled reservoir such as magma chambers and ground-water reservoirs, we have to take into account the compressibility of the fluids involved. The Poisson's ratios for typical crustal rocks are $0.1<\upsilon<0.4$ (*Turcotte and Schubert*, 2002). Bulk crustal representations are $0.25<\upsilon<0.32$ (*Christensen*, 1996) and may be appropriate for volcano-wide deformation assessments, which have spatial extension of a few tens of kilometers (*Masterlark*, 2007). Therefore, the Poisson's-solid assumption (υ=0.25), widely used for analytical and numerical models, represents a lower bound of this range rather than the bulk average. Thus, the 0.25 is a fairly approximate value of a realistic Poisson's ratio. In addition, even if Poisson's ratios of the rocks that commonly constitute composite volcanoes, have a narrow range (Poisson's ratio of many basaltic lava flows is, for instance about 0.25, which is the same as that of many volcanic tuffs (*Bell*, 2000), the local presence of saturated materials and pores of fractured rocks can greatly affect the Poisson's ratio. Even in this case, the value of 0.25 is only an approximate estimate. The presence

of pore fluids, which exist in the crust to a depth of several kilometers (*Nur and Walder*, 1992), exacerbates the sensitivity to the Poisson-solid assumption (*Masterlark*, 2007).

3.4.2 Young's modulus

Young's modulus is a measure of rock stiffness (*Gudmundsson*, 2008), and is often referred to as stiffness. It is defined as the ratio of the stress applied along an axis over the strain along the same axis ($\sigma_{ii}/\epsilon_{ii}$, where i=x, y or z) within the elastic limit. In other words, it relates stress and strain for the special case of uniaxial stress (*Segall*, 2010). The dynamic Young's modulus can be calculated from the elastic formulas:

$$E_{dy} = 2G \cdot (1 + \nu_{dy}) \tag{3.4.4}$$

knowing Lame's second constant, G, from G=$Vs^2\rho$ (*Telford et al.*, 1976), where G is the shear modulus and Vs the velocity of s-waves often inferred from the tomography. Being the shear modulus (G) of fluid zero, the Young's modulus for fluid is also zero. This makes it possible to model a fluid-filled cavity (i.e. cavity totally filled with molten magma) as an empty cavity.

In choosing the Young's moduli to represent rocks in numerical models, there are several aspects to take into account: first, for a given rock body, particularly at shallow depths, the dynamic modulus (calculated from Vp and Vs) is normally much higher than the static modulus (*Goodman*, 1989; *Schön*, 2004; *Gudmundsson*, 2008); second, dynamic and static small sample laboratory measurements are normally 1.5-5 times greater that *in-situ* field modulus derived from quasi-static experiments (*Heuze*, 1980); third, with increase of depth the mean Young's modulus generally increases (*Heuze*, 1980; *Gudmundsson*, 2008); fourth, with the increase of temperature, porosity, or water content, the Young's modulus decreases (*Gudmundsson*, 2008), so for example, hydrothermal systems may alter the values of mechanical strength of the rocks, causing local stiffness variations as large as two orders of magnitude (*Watters et al.*, 2000; *Manconi et al.*, 2007).

Laboratory measurements show that basaltic materials have values of the Young's modulus (E) between 10 and 100 GPa and that pyroclastic and sedimentary rocks commonly have values of 1–10 GPa or even less (*Goodman*, 1989; *Bell*, 2000; *Manconi et al.*, 2007). Some volcanic tuff stiffness, for example, have values as low as 0.05-0.1 GPa (*Afrouz*, 1992; *Bell*, 2000; *Gudmundsson*, 2008).

All rocks contain cavities, elastic inclusions, flaws, and solid interfaces that affect the elastic constants so that the *in-situ* values are different from those obtained from the theoretical formulas discussed above or from small-sample laboratory specimens. A big limitation to more realistic heterogeneous models is that in situ measurements of mechanical properties at active volcanoes are hardly available (*Manconi et al.*, 2010). Field or *in-situ* values of these strengths are normally much lower than the laboratory values (*Gudmundsson*, 2008) and are dominated by the presence of joints and fractures (*Rice and Rudnicki*, 1979). Thus, the laboratory measurements result from using small-scale samples that are not representative for kilometer-scale natural mechanisms (*Manconi et al.*, 2010) and rock mass discontinuities. Thus, both static and dynamic laboratory measurements need to be upscaled in order to be used for a large scale quasi-static 3-D model. For example, normally a fracture system perpendicular to the direction of the applied load tends to decrease the Young's modulus. The simplest model to upscale the Young's modulus for a cube of side length x dissected by a system of discontinuities (fractures or contacts) with $\bar{s}$ average space between discontinuities is proposed by some authors (*Priest*, 1993; *Gudmundsson*, 2011):

$$E_c = \sigma_x \frac{x}{\triangle x} = \left(\frac{1}{E}\right) \tag{3.4.5}$$

where Δx is the contraction in the direction of the applied stress σ_x, E is the Young's modulus of the isotropic, homogeneous body, and k is the stiffness of the discontinuities. This formula allows us to see how the fracture frequency of a single system of fractures affects the Young's modulus. Thus, in absence of *in-situ* analysis, an *in-situ* rock mass classification can help to adjust the elastic properties to more appropriate values.

3.4.3 Dynamic elastic moduli ν_{dy} and E_{dy}, and density

As mentioned in the previous sections, Vp and Vs are needed to determine the dynamic moduli using the elastic formulas: $E_{dy}=2G(1+\nu_{dy})$ and $G=Vs^2\rho$. Empirical relationships can be used to derive the Vs and density (ρ) from the Vp velocities provided by the tomographic studies. The Nafe-Drake curve (*Brocher*, 2005) describes the density as function of Vp between 1500 m/sec and 8500 m/sec:

$$\rho(g/cm^3) = 1.6612\,Vp - 0.4721\,Vp^2 + 0.0671\,Vp^3 + 0.0043\,Vp^4 + 0.000106\,Vp^5 \tag{3.4.6}$$

For sedimentary rocks and Vp between 1500 m/sec and 6100 m/sec, the Gardner's rule for the density is (*Gardner et al.*, 1974):

$$\rho(g/cm^3) = 1.74\,Vp^{0.25} \tag{3.4.7}$$

Brocher (2005) provided different formulas to derive the Vs for different kind of lithologies and different ranges of Vp velocities. The regression fit to calculate Vs using Vp between 1500 m/sec and 7500 m/sec for all lithologies except calcium-rich and mafic rocks (e.g. the sediments and tuff filling the caldera depression and those deposited in the areas surrounding the caldera) is:

$$Vs\,(gkm/sec) = 0.7858 - 1.2344\,Vp - 0.7949\,Vp^2 + 0.1238\,Vp^3 + 0.0064\,Vp^4 \tag{3.4.8}$$

The linear relation for calcium-rich rocks, mafic rocks, and gabbros having Vp between 5250 m/sec and 7250 m/sec covers the remaining lithologies that could be present in volcanic areas and is defined by Brocher (2005) as follows:

$$Vs\,(gkm/sec) = 2.88 - 0.52\,(Vp - 5.25) \tag{3.4.9}$$

defined for $5.25 < Vp < 7.25$ km/sec.

3.4.4 Upscaling of dynamic moduli to more appropriate properties

The elastic properties derived from the elastic wave velocities and density are, by definition, dynamic moduli of rocks. Opposed to these are the static moduli, directly measured in a deformational experiment of undrained compression and shear tests. Therefore, depending on the frequency of the deforming forces applied to calculate the moduli, the parameters can be classified into 'dynamic' or 'static' parameters (*Kümpel*, 1991). Comparison of values obtained from the two different techniques show that static and dynamic modulus may differ significantly (*Tutuncu et al.*, 1998; Wang and Nur, 2000), in particular for unconsolidated sediments (*Kümpel*, 1991).

In undrained conditions (Tab. 3.4.2), no water movement takes place and, therefore, an excess of pore pressure builds up, while applying the deforming force. Whereas, in drained conditions (Tab. 3.4.2), no excess of pore pressure builds up as water tends to flow out of the pores . In the case of impulse load or seismic wave (e.g. earthquake shaking or dynamic tests), the granular soil is permeable, but the duration of loading is short enough to prevent dissipation of excess pore-pressure. Thus, drained conditions do not prevail during the passage of seismic waves (*Kümpel*, 1991). This is why highly porous saturated sediments appear quasi-incompressible (high dynamic Poisson's ratio) when investigated with seismic waves and the behavior can be approximated assuming the undrained conditions (*Sawicki and Świdziński*, 2007). The assumption of undrained behavior means that the volumetric deformation of saturated soil is zero as the pore water is incompressible (assuming that water does not contain gas).

	Conditions	Type of analysis
Undrained	Water is unable to drain out, no water movement, most of the external loading is taken by the water and pore water pressure increases	-low permeability and high loading (e.g. impulse load -short term behavior investigation
Drained	Water flows out and no excess of pore pressure is built up	-high permeability -low rate of loading -long term behavior investigation

Table 3.4.2. Drained and undrained loading conditions and type of analysis application.

When in presence of porous media, the most appropriate way to simulate its behavior is to treat it as a poroelastic medium and distinguish between drained and undrained loading. Nevertheless, resistance to the pore fluid flow during the slow loading (quasi-static) of saturated rock is slight under drained conditions (*Kümpel*, 1991). Deformation in a poroelastic medium can be described, both in the short-term (undrained conditions) and in the long-term (drained conditions), by equivalent elastic media characterized by the appropriate elastic constants (*Segall*, 2010); Rice and Cleary (1976) suggested that the media during the two conditions can be characterized by the same rigidity and different Poisson's ratios (*Kümpel*, 1991; *Trasatti et al.*, 2005).

The reliability of the models relies on the accuracy of the rock physical property used as input parameters (*Heap et al.*, 2014). In design of structures in rocks (rock characterization for quasi-static models), the statically determined parameters are preferred over those obtained by dynamic methods (*Eissa and Kazi*, 1989) since the former are more representative of the magmatic system loading conditions. The dynamically-determined elastic moduli (i.e. those from ultrasonic wave velocities) may not represent the most appropriate values to use in volcano ground deformation modeling (*Heap et al.*, 2014). In fact, the deformation caused by a volcanic source is a quasi-static process rather than a dynamic process and therefore static elastic moduli are likely to be the most appropriate input parameters (*Heap et al.*, 2009; *Manconi et al.*, 2010; *Heap et al.*, 2014).

The static and dynamic moduli of the same rock may significantly differ from each other. The dynamic Young's modulus is generally higher than the static one (*Simmons and Brace*, 1965; *Cheng and Johnston*, 1981; King, 1979). This discrepancy is higher for small Young modulus values and for rocks with higher porosity. Jizba (1991) also found the difference more pronounced at lower pressures (i.e. closer to the surface). In other words, the difference between the moduli decreases at higher pressures and is smaller in rocks with larger moduli. The discrepancy between static and dynamic Poisson's ratio results from strain amplitude and frequency between the dynamic and static tests (*Simmons and Brace*, 1965; *Cheng and Johnston*, 1981; *Eissa and Kazi*, 1989; *Tutuncu*

et al., 1998; *Ciccotti et al.*, 2004; *Ciccotti and Mulargia*, 2004). A comparison of the laboratory measured quantities indicates that $E_{ultrasonic} > E_{log} > E_{lowfreq} > E_{static}$ (*Tutuncu et al.*, 1998). While sonic logs and wave laboratory tests send signals through the sample at small stress and strain. Static tests apply large stress, which generates large strain. The former is elastic while the latter has a considerable portion of irrecoverable deformation (*Tutuncu et al.*, 1998), which derives from the existence of cracks; when strain amplitude is large enough, it collapses cracks and the strain is not recoverable. This leads to ratios of static values versus dynamic values of moduli (e.g. Young's, bulk and shear moduli) of less than one. In additions, in presence of pores saturated by fluids, at high frequencies as in dynamic tests, pore fluids do not have enough time to equilibrate the pressure distribution, and the rock appears to be stiffer. At low frequencies as in static tests, pore fluids have enough time to reach pressure equilibrium among pore spaces, and the rock behaves less stiffly. This results in velocity dispersion, another reason why the ratio of static to dynamic moduli is less than one.

Many authors studied the relationship between dynamic and static elastic moduli (*Cheng and Johnson*, 1981; *Eissa and Kazi*, 1989; *Tutuncu et al.*, 1998; *Ciccotti and Mulargia*, 2004; *Tiğrek et al.*, 2005; *Chang et al.*, 2006) and therefore it is possible to derive approximate static elastic values from the dynamic ones from empirical laws. Previous measurements generally indicate that dynamic Young's modulus in dry rocks is similar or higher, up to twice the static modulus (depending on rock types) (*Rzhevsky and Novick*, 1971; *Ramana and Venkatanarayana*, 1973; *Fjaer*, 1999), and it is generally higher up to three time in the case of saturated rocks (*Lama and Vutukuri*, 1978; *Tutuncu et al.*, 1998). Eissa and Kazi (*Eissa and Kazi*, 1989, Eq.7) proposed a relationship that allows predicting the static Young's modulus of elasticity from the dynamic modulus:

$$log_{10}E_{st} = 0.02 + 0.77\, log_{10}(\rho E_{dy}) \tag{3.4.10}$$

where the values of E_{st} and E_{dy} are expressed in GPa while that of density (ρ) in g/cm^3. Later, Morales and Marcinew (1993) recognize this formula to be representative of the relationship for rocks with low porosity and proposed a more general relationship:

$$log_{10}E_{st} = 0.05 + 0.77\, log_{10}(\rho E_{dy}) \tag{3.4.11}$$

Using the results of seismic tomography, such high dynamic Poisson's ratio for saturated sediments is not necessarily the most accurate representation of the long-term elastic behavior under a quasi-static loading, because seismic waves are sensitive to the undrained response of the medium while long-term deformation may reflect drained conditions.

For linear elastic materials νst=νdy. Rocks are not linear in reality and thus $\nu_{st} \neq \nu_{dy}$, although there are no clear relationships in literature that allow us to univocally derive the static values from the dynamic ones. The Poisson's ratio being highly related to the pores in the rock, drained and undrained Poisson's values have the same value for rocks whose crack density is equal to zero (*Rice and Rudnicki*, 1979). For non-porous and crack-free materials such as steel, static versus dynamic Poisson's ratios are close to one (Wang, 2001). Thus, the equality of $\nu_{dy}$and ν_{st} is a reasonable assumption for rocks that have low porosity due to the nature of rock or to a high confining pressure that forces the cracks pores to close. For the same reason, at pressures greater than 2 kb (>5 km depth) the elastic dynamic properties calculated from velocities are in good agreement with static values (*Simmons and Brace*, 1965). For shallower material the undrained Poisson's ration is always higher than the drained Poisson's ratio (*Jaeger et al.*, 2007); for high porosity sedimentary rocks, the undrained, ν', is typically higher than 0.3, while the drained, ν, could be even lower than 0.25

(*Trasatti et al.*, 2005).

Note that from the elastic theory it can be shown that:

$$E' = \frac{2(1+\upsilon')}{3}E \tag{3.4.12}$$

Since υ'<0.5, E' will be less than E; hence, the deformation under drained loading will be larger than under undrained conditions (*Wesley*, 2009) (remember that σ=$E\epsilon$ and the deformation is ϵ=σ/E). The same consideration can be done for static and dynamic moduli.

An approximation of the drained Poisson's ratio for granular soils, independent from the velocities values, is provided by Trautmann and Kulhawy (1987) (*Das*, 2008):

$$\upsilon = 0.1 + 0.3\left(\frac{\phi_d - 25^\circ}{45^\circ\text{-}25^\circ}\right) \tag{3.4.13}$$

where ϕ_d is the drained friction angle in the triaxial compression test.

In the absence of material property data or tomographic data for a particular volcano of interest, reasonable material property specifications can be extracted from the compilations of material properties derived from laboratory experiments (*Masterlark*, 2007). Compilations are readily available for variety of rock types and compositions (e.g. *Price and Jones*, 1982; *Shultz and Li*, 1995; *Christensen*, 1996; *Wang*, 2000; *Rodriguez-Losada et al.*, 2009)

3.4.5 Effective magma bulk modulus, β

The bulk modulus, β, is a material property that characterizes the compressibility of a fluid, C, that is, how easily a pressure applied on a fluid can change its unit of volume. Bulk modulus and compressibility are related by the equation: C=$1/\beta$. The compressibility of saturated magma plus exsolved gas, expressed as the inverse of the bulk modulus, greatly exceeds that of the host rocks.

Volatiles exsolve from the melt to form a bubble phase, so the magma is typically composed of crystals, liquid melt, exsolved volatiles, and dissolved volatiles. All these components contribute to the magma compressibility; compressibility decreases at higher lithostatic pressures (higher depth in the crust). Higher mass fraction of volatiles, especially exsolved volatiles (bubbles), highly increases the compressibility.

We can describe magma density (ρ) with an explicit relationship of ρ in terms of melt density (ρ_m), crystal density (ρ_c), gas density (ρ_g), crystal fraction (x), and fraction of gas exsolved (n):

$$\rho = \left[\frac{n}{\rho_g} + (1-n)\left(\frac{x}{\rho_c} + \frac{1-x}{\rho_m}\right)\right]^{-1} \tag{3.4.14}$$

to a good approximation, the gas density, which we assumed to be mainly composed of water vapor, follows the ideal gas law (*Huppert and Woods*, 2002):

$$\rho_g = p/RT \tag{3.4.15}$$

which is valid for shallow crustal pressures (*Tait et al.*, 1989; *Woods and Huppert*, 2003). R is the universal gas constant, with value 462 J $K^{-1}kg^{-1}$, p is the pressure, and T is the temperature of the magma measured in Kelvins.

The exsolved mass fraction, n, is calculated using the Henry's law (e.g. *Tait et al.*, 1989). For water, which is frequently the dominant species present, it is:

$$n = N - sp^{1/2}(1-x) \tag{3.4.16}$$

on the assumption that the magma is saturated, where N is the mass fraction of water, p is the pressure and s is the saturation constant, which has a representative value of 4x10^{-6} Pa$^{-1/2}$ for silicic magma (*Holloway and Carroll*, 1994; *Woods and Huppert*, 2003). The assumption is that $n \geq 0$ when the magma is saturated, alternatively, if $sp^{1/2}(1-x) \leq 0$, the magma is undersaturated and n$\equiv$0.

With these relations, we can calculate the compressibility of the bulk magma, $\bar{\beta}$, which is typically much bigger than the surrounding rock if gas exsolved is present, with the following formula (*Huppert and Woods*, 2002):

$$\frac{1}{\bar{\beta}} = \frac{1}{\beta_r} + \frac{1}{\rho}\frac{\partial \rho}{\partial p} \tag{3.4.17}$$

where $\beta_r = E_r/3(1-2\upsilon)$ is the effective bulk modulus of the surrounding rocks; E_r being the Young's modulus of the surrounding rocks. For typical volatile-rich magmas, the second term of the right-hand side of the equation is much larger than the first one. The partial derivative of the bulk magma density, ρ, respect to the pressure is:

$$\frac{\partial \rho}{\partial p} = \frac{\partial}{\partial p}\left(\frac{y}{p} + z\right)^{-1} = \frac{y}{(pz+y)^2} \tag{3.4.18}$$

where $y = nRT$ and z is the second term of the first equation.

3.5 Mesh model validation

The basic input and assumptions of a model (i.e. source strength, boundary conditions, equations that are solved, and discretization) affect its ability to mimic a natural system (*Compton*, 2013). Therefore, it is important to test the model through validation and, if necessary, a refinement process. The test is usually done by designing the model that we want to test with the same assumptions as an accepted model that acts as reference model for the test.

Many authors choose analytical models as reference to test FEMs. FEMs whose source is a spherical cavity expanding (or shrinking) under an overpressure (or depressurization) applied to its walls find their reference in the analytical Mogi (*Mogi*, 1958) and McTigue (1987) models. To use these models as reference for the test, the FE model needs to be designed as a homogeneous elastic half-space model (HEHS). Comparing the solutions of the parameters of interest (i.e. Ux, Uy, Uz, Ur, Ulos, etc.) between the FEM and the relative HEHS model during the validation process ensures that the FEM is working properly and that the boundary conditions, the initial conditions, and the mesh are adequate. Once the FEM is validated, reducing the artifact of the FEM configuration to irrelevant quantities, new inputs can be used (e.g. new material properties, new overpressure, etc.) and their effects can be examined.

3.5.1 The importance of mesh validation

The most important, but also least straightforward aspect in the model validation process is the validation of the mesh. Mesh construction requires careful design, testing, and validation to ensure that the mesh configuration leads to an acceptable solution. In particular, FE model mesh validation is the verification that idealization premises and analysis conclusions are valid. Why is it so important to validate the mesh?

The mesh validation needs to be done because the choice of the finite space resolution during the discretization of the domain introduces discretization errors. In fact, during the Finite Element Analysis, the continuum is approximated by the discretization of the physical structure into a mesh of finite elements. Therefore, the discrete FE model contains approximation errors that correspond to the difference between the approximated solution and the exact solution. As the element size decreases towards zero, making the grid resolution approaching to zero and leading to a model of infinite elements, the approximate solution is closer to the solution of the equations that the system is solving. Thus, the discretized equations will approach the solution of the actual equations.

It is important to keep in mind that the increasing number of elements also increases the time and computational resources needed for calculations. Since we are limited in both of these, we have to deal with an approximation of the solution. We have to find a compromise between the costs of computation and accurate enough solutions.

Accurate enough solutions are reached when the approximation errors introduced by the discretization (difference between the approximated FEM and exact analytical solutions) are quantified and minimized in a way that they are below some accepted tolerance level, usually based on the design and the analysis goal, and that they stay below the observed data accuracy (i.e. accuracy of the data to be simulated).

3.5.2 Estimating discrepancies between the FEM and reference model, and considering an appropriate level of mesh resolution errors

The accuracy of the numerical solutions is estimated by calculating the discrepancies between solutions of the numerical (FEM) and the corresponding reference model. The parameter solution chosen to check the convergence of the model needs to be a numerical variable (or a mathematical expression of variable e.g. the tilt expression) measured at a single point of interest or at some nodes of the mesh.

In the case of a numerical variable measured at many nodes of the mesh, the differences between the numerical (FEM) and analytical parameter solutions that solve the same problem can be quantified by the mean surface absolute misfit function (*Williams and Wadge*, 2000), δp, defined as the ratio of mean misfit between the estimated displacements at the nodes of each model to the average magnitude of displacement of the reference model:

$$\delta p = (\Delta(Up)/M(Up)) \tag{3.5.1}$$

where p is the parameter chosen of the deformation (i.e. component of the deformation).

The mean misfit between the finite element and the analytical solutions is:

$$\Delta(Up) = \frac{\sum_{i=1}^{N} \left| Up_i^{FE} - Up_i^{HEHS} \right|}{N} \tag{3.5.2}$$

Where $Up_i^{FE}$is the parameter (i.e. deformation component) computed from the FEM at node i-th having coordinates (x_i, y_i, z_i), Up_i^{HEHS} is the equivalent result generated from the HEHS model, and N is number of control nodes in which the misfit is computed.

To provide a reference for the quality of the fit, the mean misfit is normalized by the average magnitude for that parameter (*Williams and Wadge*, 2000). The average magnitude of the parameter is defined as:

$$\Delta(Mp) = \frac{\sum_{i=1}^{N} \left| Up_i^{HEHS} \right|}{N} \tag{3.5.3}$$

Local discrepancies evaluated at a single node are calculated by the normalized difference at the node as follows:

$$\Delta(Up_i) = \frac{\left| Up_i^{HEHS} - Up_i^{FE} \right|}{\left| Up_i^{HEHS} \right|} \tag{3.5.4}$$

The same strategy of local discrepancies evaluation is used by Pascal et al. (2014) who utilized it to calculate the misfit of the maximum and the minimum of the displacement components.

Appropriate mesh refinements can improve the model, reducing these errors and resulting in a better approximation of the mathematical model. Mesh refinements are tested in a convergence process made up of an iterative sequence in which FEA results are evaluated and compared to analytical solution, the mesh is refined, and the equations are solved.

The minimization of errors and convergence of the errors is usually done with increasing grid refinements and assessing the effects of grid resolution in the process that is called the grid refinement study. An appropriate level of grid resolution of the model is reached when at the same time two conditions are verified: the misfit function, δp, is below a certain tolerance value and the discrepancies are smaller than the accuracy of the observed data to be simulated.

A termination convergence tolerance is usually set to a maximum of 5% error. The problem solution is said to converge and the iterative cycles of remeshing are stopped when this condition is met and when a finer mesh does not sensibly improve the solution

Excellent agreement between the finite element and the analytical solution is given by values of the misfit function $\delta p < 0.05$ (*Williams and Wadge*, 2000). The value of 0.05 indicates that, within the solutions computed at the control nodes, the numerical and analytical solutions are 95% similar (*Compton*, 2013). Using the same misfit function, δp, *Currenti et al.* (2008) considered that the models are in good agreement when the $\delta p < 0.1$ and no significant improvement are obtained when refining the mesh.

3.5.3 About the importance of choosing the appropriate reference model and nodes for mesh testing

We can validate the FEM configuration by comparison of model predictions to known benchmarks, which ideally come from exact analytical solutions. The advantage of using the analytical models as reference is that the reference solutions can easily be computed in the exact location of the mesh nodes at the free surface of the FE model.

Usually the models are centered in the area of interest, usually the area covered by the observed data (e.g. GPS, InSAR, tilt, etc.), and at the source of deformation where the system is perturbed by the greatest displacements to avoid the boundary effects on the solution. So, choosing the node locations to control the accuracy of the numerical solution in the central area of interest ensures that the boundary effects of the FEM at those points are not significant. This way, the calculated misfit can be considered related only to the errors introduced by the discretization of the domain.

In the case of the FE model simulating the shape of pressure source with spherical cavity, the simplest and still largely used equivalent analytical solution to compare FEM and analytical results is provided by the Mogi model (1958). The Mogi model simulates the pressure source as a point source. The conceptualization of the source as punctual source brings the limitation that its size should be "seen" very small if observed from any point at the surface (i.e. point of displacement measurement at the surface). This condition is satisfied when the radius of the source is very small compared to its depth. Due to the fact that in many cases magma bodies are not deep, they cannot be properly represented by a point-source model, and the Mogi model is not an appropriate reference model anymore. Instead, the model proposed by *McTigue* (1987) that simulates a finite spherical cavity is more appropriate. The terms of correction introduced by McTigue to the Mogi displacement function have the ratio of cavity radius to source depth $(a/d)^3$ as common factor. This means that are very small except when the radius of the cavity is similar to its depth ($0.2 \leq (a/d) < 1$) (*Lisowski*, 2006); this is the case with a shallow magma chamber. To a first approximation, the maximum displacements for a finite sphere are about $1+(a/d)^3$ times those for a point source. This means that, for the case of a shallow pressure source, the discrepancies of deformation between the two exact analytical solutions (Mogi and McTigue) could be easily greater than the accuracy of the data to be simulated; a model whose mesh is validated with a Mogi model can therefore mislead to solutions affected by significant errors. Therefore it is important to choose the appropriate analytical model to validate the mesh.

The important steps to follow in order to perform a model validation are:

1) Choosing the right analytical reference model

2) Ensuring that the finite boundary conditions do not affect the solution

3) Choosing the interest benchmark-nodes for validation that are not affected by boundary conditions

Taking as reference the case of Rabaul caldera which represents a magmatic system with a shallow source pressure, we perform the mesh validation of a simplified FE model taking as reference two analytical HEHS models, Mogi and McTigue, in order to investigate the most appropriate one. A preliminary calibration of the FE model using the InSAR data of Rabaul caldera shows that the data at the center of the caldera could be fit by a FE model that predicts about 40 cm of vertical displacements in a 3.7 years time lapse (1380 days). The characteristics of the FE models to validate are resumed in Tab. 3.5.1.

Aspect	Specification
Domain space origin	x=0, y=0, z=0
Center of cavity, $\mathbf{C_0}$	[0, 0, -3300] m
Radius of cavity (r_s)	1300 m
Analysis type	Elastic
Maximum domain depth	60 km
Maximum domain radius	60 km
E (Young's modulus)	50 GPa
υ (Poisson's ratio)	0.25
ΔP	50 MPa
Far-field boundary conditions	Zero displacements, pinned
Top of model domain	Flat free surface (zero traction)
Max Uz displacement (McTigue)	0.397 m
Max Ur displacement (McTigue)	0.151 m
Elements (1st order tetrahedra)	
Mesh_0 elements	52,451
Mesh_1 elements	92,462
Mesh_2 elements	136,140
Mesh_3 elements	263,389

Table 3.5.1. Model and mesh configuration.
Configuration of the model to investigate the mesh validation process using analytical solutions as reference solutions.

The center of the model free-surface is located above the spherical pressurized cavity and the far-field boundaries of the domain are located far away from it (Fig. 3.5.1, a) in a way that the boundary conditions do not affect the solutions around the source of deformation. The general rule is to build the FE model in a way that the boundaries are located at a distance equal to the double of the deformation signal (*Currenti et al.*, 2008). The Uz deformation field decreases to 10% of its maximum value within 10 km from the source and Ur decreases to 10% at about 20 km. The far field boundary of the model is located at a distance equal to 60 km from the center of the free surface; this ensures that the boundary conditions applied to the far field are not affecting the solutions for both Uz and Ur components.

Inspired by the model of *Masterlark et al.* (2012), our model has a source cavity embedded in a cylindrical volume (Fig. 3.5.1, a). This partition of the domain allows us to easily control and refine the mesh around the spherical cavity without loading the model with many unwanted elements in the far field areas.

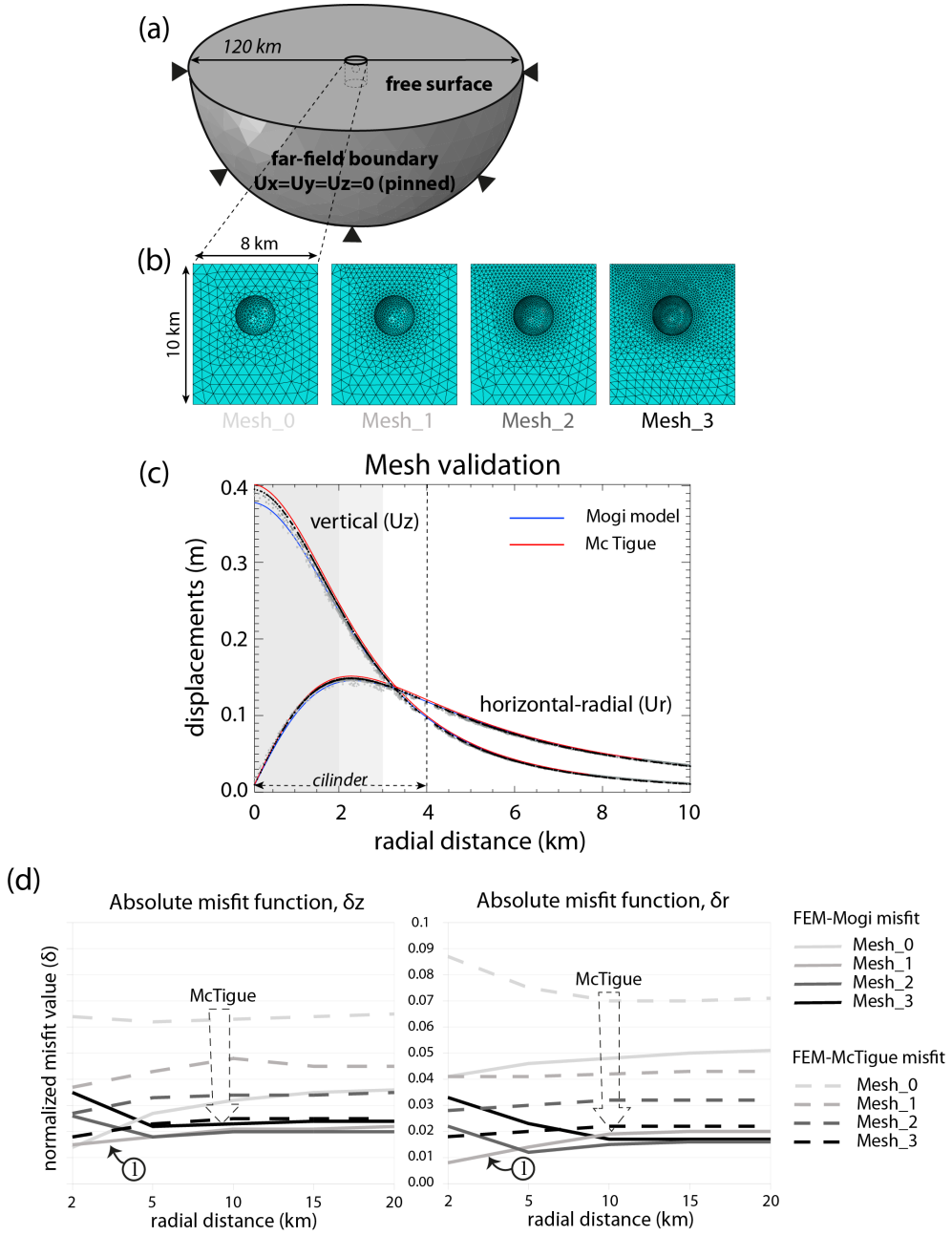

Figure 3.5.1. Domain configuration as summarized in Tab. 3.5.1 and mesh validation. *(a) Model domain: a solid hemisphere with a diameter of 120 km. The flat top of the domain is a free surface (i.e. traction free). The curved lateral far-field boundary conditions are set to zero displacements (pinned). A pressure load is applied to the walls of the internal spherical cavity. (b) Mesh elements of the discretized cylindrical volume that contains the spherical cavity. The four meshes are tested during the mesh validation process and show the mesh refinement of the cylindrical volume. The cylinder was created to guide and help the mesh refinement around the magma chamber. (c) FEM validation. Solid red lines are the radial and vertical components of displacements for a finite source depth of 3300 m and radius of 1300 m (McTigue, 1987). Solid green lines are the radial and vertical components of displacements of a corresponding point-source (Mogi, 1958). The gray to black circles are the corresponding predictions calculated using the FEMs with increasing mesh refinement. The light gray and darker gray areas represent the positions of the nodes (of Mesh_0 and Mesh_1, respectively) where the measured discrepancies with respect to the McTigue (1987) reference model are higher than the InSAR accuracy requirements (1 cm). (d) Uz and Ur absolute misfit values for the four models with increasing mesh refinement. Misfits (δz and δr) of solutions at points of increasing range distance (2, 5, 10, 15, 20 km) from the center of the model are calculated comparing the FEM solution with the analytical solutions of both Mogi model (solid lines) and McTigue model (dashed lines). The dashed arrow shows the consistent decreasing of misfit between the FEM and the McTigue solution for increasing mesh refinement.*

Four meshes with increasing elements number are tested (Fig. 3.5.1, b) by visually comparing the vertical and horizontal components of the displacements with the corresponding Mogi and McTigue analytical solutions (Fig. 3.5.1, c) and by computing the misfits at node position with increasing distance from the source (Fig. 3.5.1, d). The McTigue solution is more peaked over the source with respect to the Mogi one (Fig. 3.1.1, c). The "sensitive area," where the difference between the FEM and McTigue solution is bigger, is on top of the source and is bigger for the Uz component.

The results clearly show that the displacements tend to approach the McTigue solution with increasing the mesh refinement (Fig. 3.1.1, c). Therefore the McTigue solution can be considered more appropriate than the Mogi solution; the misfit with McTigue model persistently decreases with the mesh refinement and tends to increase for the Mogi solution (Fig. 3.5.1, d). The fact that the displacements (especially the vertical component) are lower with a coarse mesh and tend to the exact solution by refining the mesh is due to the fact that, during the discretization of the spherical cavity, the volume of the cavity is reduced and, increasing of the mesh refinement, becomes more similar to the volume simulated by the analytical model (*Masterlark et al.*, 2012).

Although almost all the misfits are low (< 0.05) and would lead us to accept almost all the solutions, not all the models are acceptable.

For example, Mesh_0 has a good acceptable Uz misfit with Mogi model and even if Mesh_1 shows the lower misfits, both models generate unacceptable solutions due to the fact that they have discrepancies bigger than the accuracy of InSAR/GPS data. This is shown in Fig. 3.5.1, c, where gray areas represent the distance of the nodes at which the discrepancies are bigger that 1 cm. Testing the mesh on a Mogi model would thus lead us to accept a model with a mesh refinement that generates solutions that include "unacceptable" errors.

For higher mesh refinements the misfit with the Mogi model is higher for nodes close to the source (Fig. 3.5.1, c1) and decreases if the misfit calculation includes the nodes far away from the source where the deformation is close to zero. On the other hand, the misfit with the McTigue model decreases for nodes close to the source and increases when the nodes close to the far field are included in the calculation. This could be the consequence of the fact that the nodes located close to the far field are affected by the boundary conditions and by the presence of bigger elements (i.e less refined areas). Therefore it is important to confine the area in which to calculate the misfit to the area of interest, in order to get the appropriate misfit for the significant nodes and to avoid, during the misfit calculation, the usage of node solutions that can mislead the choice of an appropriate mesh in favor of non-accurate meshes.

3.6 Weighted Quadtree-based algorithm for data reduction

3.6.1 Introduction to sub-sampling procedures

Usually, InSAR images provide a large amount of data that needs to be filtered and reduced to data sets that are more manageable during the inversion process. In fact, although the InSAR data resolution is about 30 m, we can only use a subset of the entire data due to limited computer capacities. In addition, due to the local sources of decorrelation (i.e. vegetation, slope angle, loose volcanic deposits) the InSAR images contain noise and gaps in spatial coverage that need to be taken into account during the data reduction. The main concern during filtering, reducing, and averaging the data is the loss of part of the signal that, ideally, should not exceed the accuracy of the method used to collect data that are being processed (i.e. 1 cm/yr for the InSAR data). Another concern is the ability of the reduction method to filter and produce reduced data that contain the information of the specific deformation signal of the source that we want to model (e.g. without noises, with a specific wavelength).

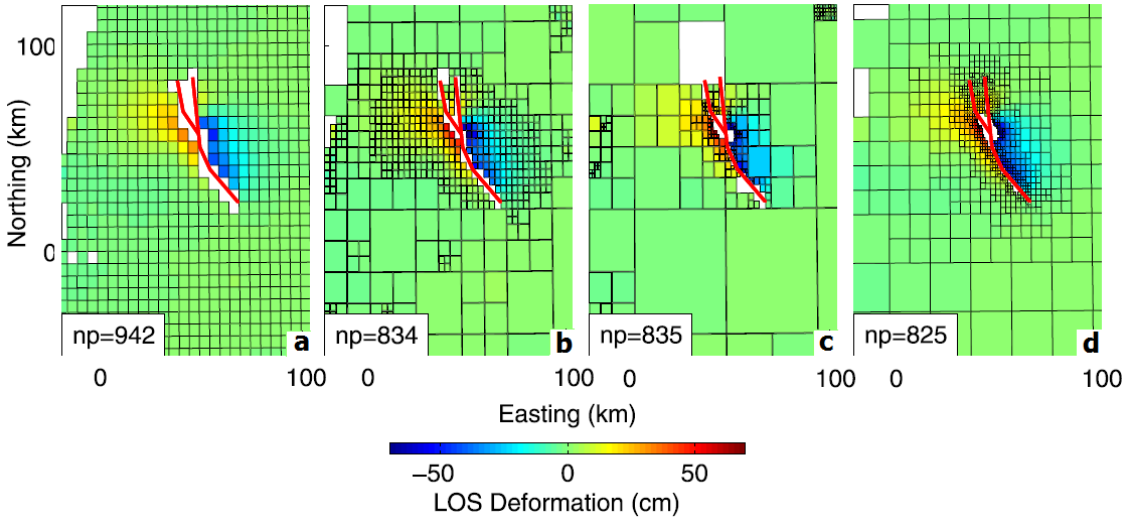

Figure 3.6.1. Methods comparison (modified from Lohman and Simons, 2005). *Resampling results using the algorithms discussed in the text. (a) Uniform sampling. (b) Jónsson et al. (2002) algorithm. (c) Simons et al. (2002) algorithm. (d) R-based algorithm by Lohman and Simons (2005).*

Different strategies have been used to reduce the redundancy of data to a more manageable number of data. The simplest way to reduce InSAR data volume is to sub-sample the data to a coarse grid with regular spacing (Fig. 3.6.1, a) (*Pritchard et al.*, 2002). This can be done by calculating the mean or the median value of the values (pixels or PS) within each box-size area of a previously determined regular grid, and assigning the resulting value to the center of each corresponding area. Although simple to use, this method leads to good data reduction with a remarkable loss of small scale deformation details. In addition, we have to note that using the mean or the median of the values implies some disadvantages that have to be taken into account. The median-filtering is based on the median statistic, which is a robust statistic (i.e. it is not biased by the presence of outliers in the area), but due to the fact that it is a non-linear operator, it is unable to propagate the errors from the original image to the filtered one. The mean-filtering, on the other side, has the disadvantage that the mean value is not a robust statistic and is biased by outliers. *Jónsson et al.* (2002) proposed a spatial variance-based quadtree procedure (Fig. 3.6.1, b) that has been used

and adapted in many works adjusting the algorithm's parameters (*Bathke et al.*, 2013; *Dawson and Tregoning*, 2007; *Decriem et al.*, 2010; *Fukushima et al.*, 2005; *Masterlark and Lu*, 2004a; *Sudhaus and Jónsson*, 2009; *Wicks et al.*, 2013; *Wright et al.*, 2003; *Yun et al.*, 2006). In this method, the areas are divided into four sub-quadrants and the mean of each is calculated. The mean is the function that is removed from the data: if the RMS scatter about the mean (of the residuals about the mean) exceeds a given threshold, the quadrant is divided into four new quadrants and the process continues iteratively until convergence. Another algorithm that samples the data according to the spatial variance is given by *Simons et al.* (2002) (Fig. 3.6.1, c). This differs from the strategy used by*Jónsson et al.* (2002) by the function removed from each sub-quadrant data before estimating the variance; the function used is the best fitting local bilinear ramp (*Lohman and Simons*, 2005). The sampling density is thus proportional to the curvature (second spatial derivate) of the displacement field . Another approach to data subsampling is the resolution-based resampling method proposed by*Lohman and Simons* (2005) (Fig. 3.6.1, d). This is a model-design based method, which means it uses an a-priori model source to estimate where a good coverage of data would be required to resolve the source of displacement. The data are thus down-sampled in a way that the areas close to the source of deformation considered, where the data has the most relevant structure, are more densely sampled. Later, *Funning et al.* (2007) combined the last two strategies into a modified *Simons et al.* (2002) approach driven by the knowledge of the a-priori model.

Each sub-sampling method has downsides. The uniform method needs too many points in order to be able to picture the detail of the deformation near the model source. The variance-based quadtree methods are sensitive to noisy data: *Lohman and Simons* (2005) noted that the sampling density of the *Simons et al.* (2002) algorithm is sensitive to the curvature of the signal, whereas the density of the *Jónsson et al.* (2002) algorithm also depends on the local slope (and the absolute amplitude) of the deformation field. The disadvantages of the *Lohman and Simons* (2005) method is that it needs an a-priori model and that it could down-sample the data in certain areas to a level that it fails to represent sources not considered in the a-priori model. All procedures described above are based on the assumption that one would like to have higher density of data close to the source of deformation where the gradient of displacements is bigger and thus the signal is better resolvable. In the case of optimal data picturing a strong deformation signal due to a single source, ideally known a-priori, the purpose discussed is good. However, the deformation signals of volcanic areas are the result of different superimposed signal components generated by different sources active at different time and frequencies. This makes the study of deep and long-term sources of volcanic systems through the inversion more challenging. In fact, deep sources generate long, steady (constant), broad, and slow deformations that need to be separated from the superimposed stronger, high frequency, and localized signals related to shallower sources (a noise in this case) often localized on top of deeper sources, which mask the stronger part of the deep source signal.

With this in mind, we propose a modified variance quadtree reduction algorithm based on the quadtree reduction structure (*Samet and Webber*, 1988) and driven: 1) by the limitation of the InSAR of resolving spatial variations of the deformation, and 2) by the stability of the signal in time. The algorithm reduces the data taking into account the previous considerations by investigating the data over the area of interest with a quadtree structure in a way that queries are asked for subsequent divided sub-quadrants.

3.6.2 Modified variance-quadtree algorithm (VQT)

The variance quadtree algorithm (VQT) is a spatial sampling algorithm (*Mınasny et al.*, 2007) commonly used to subsample the interferograms in order to prepare the data for the inversion. It is a special space partitioning strategy that resamples and reorganizes the data following a hierarchical data structure based on the principle of recursive decomposition of space. More specifically, it recursively divides the areas in four equal-size subareas, the quadrants, until the content of each quadrant is homogeneous (*Samet*, 1990) in the sense that it does not exceed a variance threshold. By considering the variance as a principle to guide the subdivision, the VQT is considered an object-space hierarchy. This means that it is governed by the characteristics of the inputs, in opposition to image-space hierarchy where the decomposition, called "regular decomposition," is into equal parts at each level. The resolution of the VQT decomposition, defined as the number of times that the decomposition process is applied (*Samet*, 1990), can be fixed beforehand or may be governed by the properties of the input data .

In our case, the VQT is applied to multidimensional data points in order to associate data points with quadrants. In the case of multidimensional point data, the final representation achieved is strongly influenced by the operations to be performed on the data. The VQT is modified in the sense that it is used to make queries on relationships between 2D spatial data based on new specific chosen principles guiding the decomposition process explained in the following paragraphs.

Based on successive subdivision of the area into four equal-size quadrants, the proposed algorithm decomposes the area into increasingly finer patterns in a top-down process represented by a tree of degree four (Fig. 3.6.2, b). Following this scheme, the data of each quadrant are investigated to verify the condition for a further refinement through a query process. The quadrant is divided into sub-quadrants if the data in the quadrant do not satisfy two main criteria: 1) the minimum number of PS (or pixels) must be equal to or greater than a specified number, 2) the variance of the PS (or pixels) values (i.e. mean LOS velocity) must be less or equal to a specify criterion. Once the first criterion is satisfied, in case the second criterion is also satisfied, an additional third criterion needs to be satisfied for further subdivision: 3) the average value of the PS stability indexes (ISS, see explanation below) must be greater than or equal to a specified value.

The criteria used to generate queries and drive the reduction

1) The first criterion sets the minimum number of points accepted to start the following queries. This allows us to reduce the number of big quadrants, especially along the coast line, representing few clustered pixels, but covering big areas where actually no data are recorded.

2) The second criterion represents the maximum variability of PS (or pixel) values within a quadrant. Larger and smaller variance cutoff values yield to fewer quadrants and more quadrants, respectively. The query about the variance has the purpose of taking into account the ability of the InSAR method to resolve spatial variations of deformation. This ability is related to the accuracy of the method. This spatially defines which distribution of PS values needs to be refined. By choosing the accuracy of the method as minimum value of the PS (or pixel) variance, we stop the quadrant subdivision at a level correspondent to the maximum resolvable variance by the InSAR method, unless the third condition is not satisfied.

3) The third and last criterion represents the stability of the signal in time and is investigated with a query about the Index of Strength and Stability of the signal (ISS). This parameter was preferred to the simple variability of the data in time as it also takes into account the magnitude

of the signal, giving more weight to bigger deformation with lower variability in time. In fact, ISS characterizes the signal at i-th PS in terms of its magnitude (value of the mean LOS velocity) and its variability in time (STD of the velocity). It is defined as:

$$ISS_i = (mean\,LOS\,velocity_i)/(STD_i) \tag{3.6.1}$$

ISS is the inverse of the coefficient of variation (*Davis*, 2002) and like the coefficient of variation, Cv, it is a dimensionless measure of variability. ISS provides the characterization of the heterogeneity of the PS values in time. A map of all ISS provides an overview of the consistency of the PS values in time and space. It is common for the variability of the sample to be related to its overall magnitude (*Davis*, 2002). In the case of variability of the sample exclusively related to its magnitude, ISS would be relatively constant over the entire area. Instead, for sample variability of an area depending on different sources we would expect a distribution of different ISS values over the area. By setting a minimum value of ISS tolerance for further subdivision, we can make the program reconsider a further subdivision for those areas that have a more stable displacement in time. This allows those areas where the signal is more stable to be better represented. It is important to note that this further subdivision beyond the accuracy of the InSAR method does not provide any further detail of the spatial variation of the signal. Instead, it has the purpose of better representing the more stable component of the signal during the inversion. Taking into consideration the ISS parameter makes the reduction sensitive to the magnitude of the sample beside its variability.

The algorithm

Before starting the query process, the algorithm calculates the first and the last level of the quadtree structure of the image based on the definition of the maximum and minimum possible size of the quadrants wanted in the data quadtree. By choosing the maximum side length of the quadrant, we force the algorithm to start the data quadtree subdivision from a level p=*rl* (roots level) that contains a regular grid of quadrants (roots) whose side length is equal to or slightly smaller than the chosen maximum length value (Fig. 3.6.2, a), depending on the size required to subdivide the starting area into roots of equal size. This will be the coarser resolution of the quadtree. By choosing the minimum side length of the quadrants, we force the algorithm to stop any further subdivision at a level p=*ll* (last level) whose quadrants have a side length equal to or bigger than the chosen minimum side length (Fig. 3.6.2, a). Thus, by defining the minimum size, we also define the maximum size of the quadtree structure (maximum number of levels of further subdivision= *ll-rl*) and thus its maximum spatial resolution.

The number and the length of quadrants in each level are functions of the level index, p, and are defined as follows:

$$Nquad_p = 4^p \tag{3.6.2}$$

$$Length\_quad_p = side0/(2^p) \tag{3.6.3}$$

where *side0* is the dimension of the area that contains the data to be reduced. In other words, at each level the region quadtree is a partition of the original space into a set of 4^p squares with side that all are a power of two long and corner coordinates that are multiples of the side length. The index of the quadrants are assigned following a z-ordering scheme (Fig. 3.6.2, a).

Starting from the roots level, p=rl, the algorithm generates a storage matrix at each level where it records the information of the 4^p quadrants. For each quadrant, i, the algorithm calculates and stores the following parameters: index of the quadrant in the quadtree structure (id; Fig. 3.6.2, a), the coordinates (x,y) of the bottom left corner, side length, number of InSAR data, values, and statistics of InSAR data (minimum, maximum, average, and variance), average of the ISS values, and a flag index. If FLAG=0, the quadrant does not need further subdivision and thus the information of the correspondent sub-quadrants of the tree-structure are not provided; if FLAG=1, the quadrant needs further subdivision.

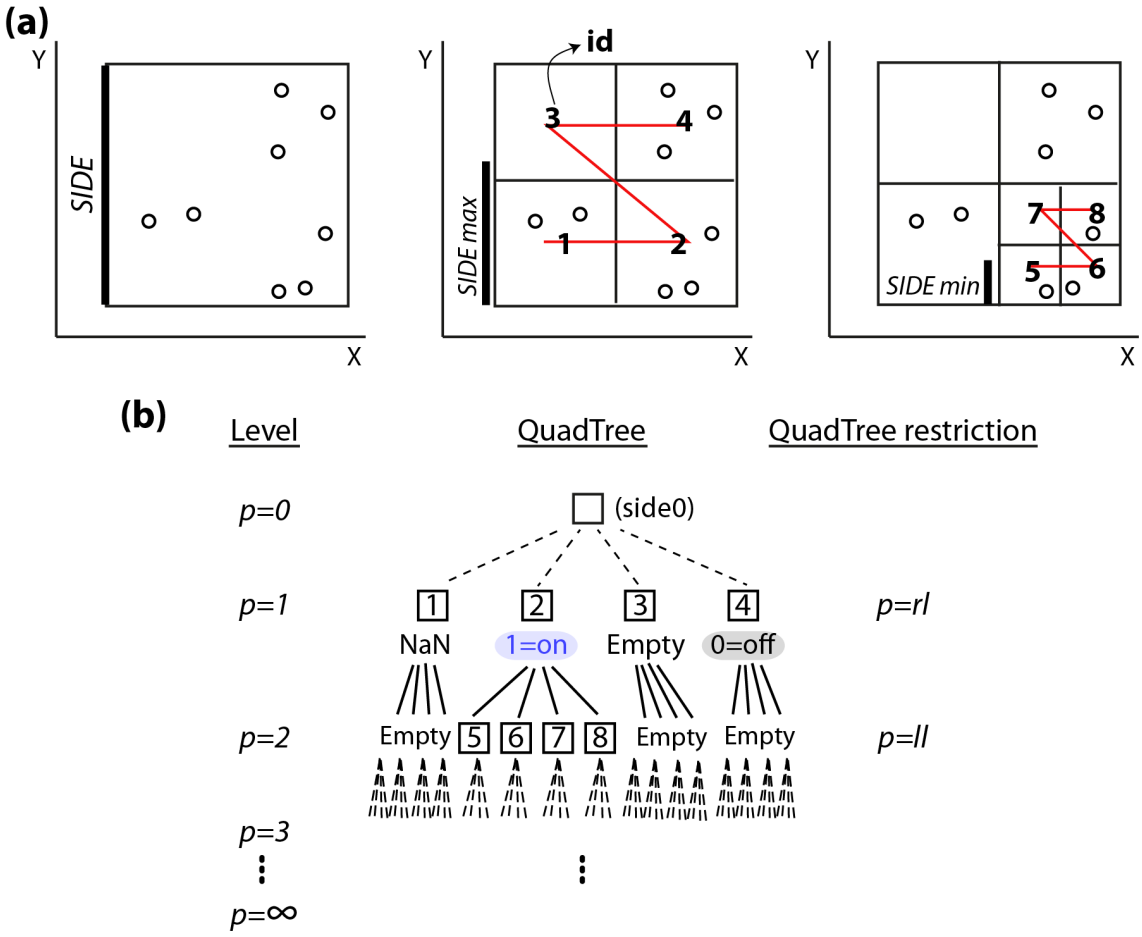

Figure 3.6.2. Quadtree structure and z-ordering.
By defining the maximum and minimum length size of the quadrants, we limit the investigation from quadtree level p=rl (roots level) to level p=ll (last level). (a) Z-ordering and geometric relationships. Hollow dots represent the InSAR data. First criterion (minimum number of data)=3. (b) Possible Quadtree structure relative to geometric subdivision represented in panel (a). The definition of the maximum and minimum side length restricts the quadtree structure between level rl and ll. Levels with hierarchy higher than the rl and lower than ll are not generated (the dashed lines indicate these unnecessary links). FLAG=1 activates the queries of the further sub-quadrants, FLAG=0 and NaN stop the queries at that quadrant and do not record any parameter in the subsequent quadrants (i.e. they are reated as empty).

Starting from the roots-level, p=rl, defined by the chosen maximum dimension of the pixels, the algorithm performs the following actions:

1) Generate the quadrants of the corresponding level *p=rl* (calculate coordinates and size length)

For each quadrant *q*:

2) Count the data for comparison with the first criterion

-If the number of data=0 (e.g. quadrant id3, Fig. 3.6.2, a), the quadrant is empty and data are not recorded

-If the number of data is $<$ the first criterion (e.g. quadrant id1, Fig. 3.6.2, a), then it registers the parameters as NaN and it treats the quadrant as an empty quadrant. In the particular case that the first criterion is equal to zero, thus it assigns NaN to empty quadrants.

-If the number of data is $\geq$ the first criterion (e.g. quadrants id2 and id4, Fig. 3.6.2, a), then it:

3) Calculates minimum, maximum, average, and the variance V_q

-if the $V_q \geq$ the second criterion, then it records FLAG=1 (quadrant needs further subdivision), else follows the next action:

4) Calculates the ISS_q average index for consideration of further subdivision

-if ISS_q average index $<$ the third criterion, then it records FLAG=0
-if ISS_q average index $\geq$ the third criterion, then it records FLAG=1

5) Records the parameters of the quadrants of the level on a .txt file

For the following levels, form *p=rl+1* to *p=ll,* the actions performed on the quadrants, from 2 to 4, are restricted to the quadrants of the previous level, *p-1*, whose flag is equal to 1. The program does this after an evaluation of the flag. If the flag index of the *p-1* quadrants is equal to 0, then the information of the correspondent sub-quadrants in the level *p* of the tree are note filled (Fig. 3.6.2, b).

In the end, the parameters from the different layers are reorganized (empty lines and NaN lines are ignored) in a file that contains the coordinates of the quadrant centers, the correspondent InSAR average values, V_q, the ISS_q average, the lenght of the quadrant side, and the STD average in the quadrant.

3.7 Linear inverse theory and strategies

The least square linear inversion method used in this work is based on the data vector and leads to classic least squares solutions. The assumption of a linear system is valid because the source of deformation used in this work, the flux of magma injected or the change in pressure inside the source, is linearly related to the ground deformation (3.1.1). In the next chapter, we will deal with the overdetermined problem, which represents the case where we can apply the least squares to select a "best" approximate solution (*Menke*, 1989). In the overdetermined problem, there is too much information contained in the equation of the forward problem, $\mathbf{Gm} = \mathbf{d}$, for it to have an exact solution. It means that in the presence of noise in the measurements, which is the case with real measurements, no choice of $\mathbf{m}$ can satisfy the data exactly, therefore we look for the least squares solution. This leads to the advantage of considering the realistic non-exact observations in the inverse problem and relax the estimation of predicted observations, $\mathbf{d}^{pre}$, in favor of predicted parameters, $\mathbf{m}^{pre}$, stability. Improvements over the simple inverse model include the use of a priori information about noise in the data (weight matrix $\mathbf{W}$) and constraints information about the solution (matrix $\beta\mathbf{L}$) that, also more importantly, allow to define the problem as overdetermined by adding information about the system (known characteristics). In the following chapter, bolt lower-case letters symbolize vectors, bold upper-case letters symbolize matrices, italic letters indicate indices, and regular letters indicate parameters. Matrices are written in box brackets and vectors in parentheses.

3.7.1 Linear least squares solution of the inverse problem

The direct (forward) problem is the process of predicting the data based on a (mathematical) model given a set of model parameters. By contrast, the inverse problem is the process of predicting model parameters of an assumed model based on a data set of observations (Fig. 3.7.1).

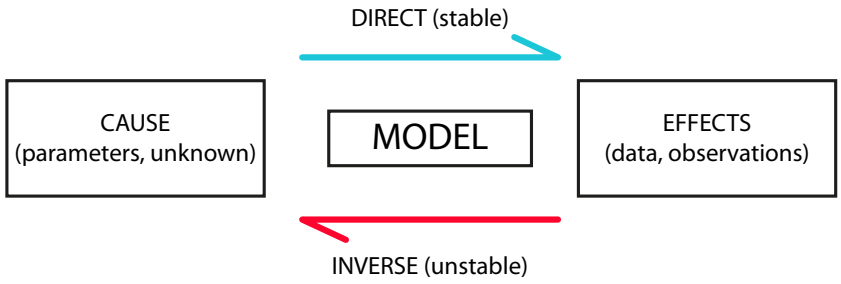

Figure 3.7.1. Direct and inverse problem

In a general mathematical form we conceptualize the forward problem as:

$$\begin{array}{ccccc} \mathbf{d} & = & \mathbf{G} & \mathbf{m} \\ (N \times 1) & = & (N \times M) & (M \times 1) \end{array} \tag{3.7.1}$$

which is the ideal model that mathematically describes how we think nature produces a finite set of data. In the formula, the data is described as a column vector of numbers, $\mathrm{d} = (\mathrm{d}_1, \mathrm{d}_2, \ldots, \mathrm{d}_\mathrm{N})$; $\mathrm{m} = (\mathrm{m}_1, \mathrm{m}_2, \ldots, \mathrm{m}_\mathrm{M})$ is another column vector that describes the parameters of model of interest (e.g., the flux of magma of change in pressure in the magma chamber), and $\mathbf{G}$, the Green's function, is an operator that maps $\mathbf{m}$ to $\mathbf{d}$. As the problems that we are dealing with are linear problems, we have the advantage that they obey the principle of superposition. Thus we

can write each element of $\mathbf{d}$ as a linear combination of the elements of $\mathbf{m}$, e.g.:

$$\begin{array}{ccccccccc} \mathrm{d}_1 & = & \mathrm{G}_{11}\mathrm{m}_1 & + & \mathrm{G}_{12}\mathrm{m}_2 & + & \ldots & + & \mathrm{G}_{1M}\mathrm{m}_M \\ \vdots & & \vdots & & \vdots & & \vdots & & \vdots \\ \mathrm{d}_N & = & \mathrm{G}_{N1}\mathrm{m}_1 & + & \mathrm{G}_{N2}\mathrm{m}_2 & + & \ldots & + & \mathrm{G}_{NM}\mathrm{m}_M \end{array} \tag{3.7.2}$$

where M is the number of columns in $\mathbf{G}$ that corresponds to the number of source parameters (or elements in $\mathbf{m}$), and N is the number of data that corresponds to the number of elements in the data vector $\mathbf{d}$. This means that the operator $\mathbf{G}$ of the forward model is a matrix of numbers (the same number of rows as the length of $\mathbf{d}$ and with same number of columns as the length of $\mathbf{m}$) that operates on an M-dimensional vector $\mathbf{m}$ and returns an N-dimensional vector $\mathbf{d}$.

The problem then becomes inverting the found system of equations to meaningfully estimate the parameters, given $\mathbf{G}$ and $\mathbf{d}$. The least squares (LS) solution to this problem minimizes the total misfit between predicted and observed data in the L_2 norm sense. It takes the following form:

$$\mathbf{m}_{LS} = \left[\mathbf{G}^T\mathbf{G}\right]^{-1}\mathbf{G}^T\mathbf{d} \tag{3.7.3}$$

This solution is based on the length of the data error vector, $\mathbf{e} = \mathbf{d}^{obs} - \mathbf{d}^{pre}$, in the sense that it minimizes the sum of the squared residuals $\mathbf{e}^T\mathbf{e}$, which is the length of the data error (misfit) vector. In fact, among many possible definitions of vector length in the least squares method, we use the Cartesian (L_2) norm:

$$\mathrm{L}_2\text{norm}: \qquad \|\mathbf{e}\|_2 = \left(\sum_{i=1}^{N} |\mathbf{e}_i|^2\right)^{1/2} \tag{3.7.4}$$

Different norms give different weight to the "outliners" in the length calculation. Inverse methods based on the L_2 norm give considerable weight to large errors, which are considered "unlikely" due to the fact that the errors are supposed to have Gaussian distribution. This is why methods based on the L_2 norm are closely tied to the notion that errors in data have Gaussian statistics. The total misfit E between observed and predicted data is defined either as the square of L_2 or as:

$$\mathrm{E} = \|\mathbf{e}\|_2^2 = \mathbf{e}^T\mathbf{e} = \begin{pmatrix} e_1 & e_2 & \cdots & e_N \end{pmatrix} \begin{pmatrix} e_1 \\ e_2 \\ \vdots \\ e_N \end{pmatrix} = \sum_{i=1}^{N} e_i^2 \tag{3.7.5}$$

The least squares method is derived by minimizing a Gaussian likelihood function and is only valid when the law of errors for the data follows a Gaussian curve. Therefore, problems in the application of the least squares methods can be identified by plotting the residuals on a histogram that should have the approximate bell-shape of a Gaussian function (*Gubbins*, 2004). The presence of outliners in the histogram may show that the form of mathematical model that we are trying to fit is incorrect (*Aster et al.*, 2004).

The concept of data error vector, $\mathbf{e}$, and consequently the one of total misfit, $\mathrm{E} = \mathbf{e}^T\mathbf{e}$, is very important because, depending on the observed data error, E value can be relaxed. This is due to the fact that with errors in the data, the goal of having $\mathbf{Gm} - \mathbf{d} = \mathbf{0}$ can be replaced by the more realistic $\mathbf{Gm} - \mathbf{d} \approx \mathbf{0}$. This is the case of inverse problems for which data are contaminated by errors (real case) and for which the goal is fitting the data with a certain degree of tolerance, δ, instead of attempting an exact fit that would mean to also fit the intrinsic error of the data. In fact, if the

data contains noise, there is no point in fitting data and noise exactly. The new formulation of the forward problem is thus:

$$\mathbf{Gm} = \mathbf{d} + \mathbf{e} \tag{3.7.6}$$

where $\mathbf{e}$ is the unknown quantity used to define the error vector. Errors are treated as random variables whose value remain indeterminate and can be described by statistical properties (variance, covariance of pairs of random variables). It is important to note that from this formula, it is reasonable to accept $\mathbf{Gm} - \mathbf{d} \simeq \mathbf{e}^{obs}$, so knowing the errors in the observed data, $\mathbf{e}^{obs}$, we have a tolerance level, $\delta = \mathbf{e}^{obs}$, for the predicted error $\mathbf{e}^{pre}$. In other words, there will be many solutions that adequately fit the data in the sense that E is small enough (within the tolerance level).

Once we have the inverse solution, a sensible question is how well the predicted data and the model parameters are resolved. If the data contain errors, these will cause errors in the estimate of the model parameters. Errors of observed data are mapped into the model parameter errors through any type of inverse. If the data are uncorrelated and all of equal variance σ^2 (simple case), then the formulas for the least squares solution to state how well the estimate data, $\mathbf{d}^{pre}$, match the measured data,$\mathbf{d}^{obs}$, and the uncertainty in the model parameters estimation are, respectively(*Menke*, 1989):

$$[cov\mathbf{d}] = \sigma^2 \boldsymbol{I}_{\mathrm{N}}, \tag{3.7.7}$$

and

$$[cov\mathbf{m}] = \sigma^2 \left[\boldsymbol{G}^{\boldsymbol{T}}\boldsymbol{G}\right]^{-1} \tag{3.7.8}$$

3.7.2 Improvements of model parameters etimation

The relationship in the equation of the forward problem (Eq. 3.7.1) can be appended to a form that includes constraints and a priori information in order to generate an overdetermined problem, stabilize the solution, and to improve the estimates of $\mathbf{m}$ towards meaningful values. A priori information includes the geometry of the problem and the behavior of the system (spatial smoothing). The a priori information are used as parameter constrains to obtain a stable inverse of the geophysical data (*Kim et al.*, 1999).

A way to improve the estimates using the least squares solution is to use weighted measures of the misfit errors $\mathbf{W}$, where $\mathbf{W}$ is a $N \times N$ matrix. We can take any form, but in this work we consider it to be diagonal in form:

$$\mathbf{W} = \begin{bmatrix} \frac{1}{\sqrt{\sigma_1^2}} & & & \\ & \frac{1}{\sqrt{\sigma_2^2}} & & \\ & & \ddots & \\ & & & \frac{1}{\sqrt{\sigma_N^2}} \end{bmatrix} \tag{3.7.9}$$

The diagonal form implies that the errors in the data are uncorrelated. This way, the weighted misfit becomes:

$$\mathrm{E} = \|\mathbf{We}\|_2^2 = \mathbf{e}^T\mathbf{We} = \sum_{i=1}^{N}\left[e_i \sum_{j=1}^{N} \mathrm{W}_{ij} e_j\right], \tag{3.7.10}$$

where

$$\mathrm{W_{ij}} = \delta_{\mathrm{ij}} \frac{1}{\sqrt{\sigma_{\mathrm{i}}}} \tag{3.7.11}$$

with δ_{ij}being a Kronecker delta that is 0 whrn $i \neq j$, and 1 when $i = j$. If the i-th standard deviation, σ_i, is large, then the component of the error vector in the ith direction, $\mathbf{e}_i^2$, has little influence on the size of E. The weighted least squares solution, $\mathbf{m}_{WLS}$, is:

$$\mathbf{m}_{WLS} = \left[\mathbf{G}_w{}^T \mathbf{G}_w\right]^{-1} \mathbf{G}_w{}^T \mathbf{d}_w = \left[\mathbf{G}^T \mathbf{W} \mathbf{G}\right]^{-1} \mathbf{G}^T \mathbf{W} \mathbf{d} \tag{3.7.12}$$

with a weighted least squares operator, $\mathbf{G}_{WLS}^{-1}$, given by

$$\mathbf{G}_{WLS}^{-1} = \left[\mathbf{G}^T \mathbf{W} \mathbf{G}\right]^{-1} \mathbf{G}^T \mathbf{W} \tag{3.7.13}$$

This solution minimizes the sum of the weighted squared residuals, $\mathbf{e}^T \mathbf{W} \mathbf{e}$, where the $\mathbf{W}$ defines the contribution of each individual error to the total prediction error.

A priori information and constraints are used to stabilize the problem and even to make the problem overdetermined, in case not enough data are available to determine the parameters (undetermined problem). In case we are investigating a regular distribution of sources like the one proposed by *Masterlark and Lu* (2004b), we can introduce a Laplacian smoothing (*Freymueller et al.*, 1994) that allows us to control the solution roughness and impose dilatational boundary conditions on the three-dimensional source array. The construction of this operator is described in the following subchapter (Chapter3.7.3).

Considering the a priori weighting matrix, $\mathbf{W}$, and the Laplacian smoothing, $\mathbf{L}$, the forward solution then takes the form:

$$\hat{\mathbf{G}} \hat{\mathbf{m}} = \hat{\mathbf{d}}, \tag{3.7.14}$$

where

$$\hat{\mathbf{G}} = \begin{bmatrix} \mathbf{WG} & \mathbf{xy1} \\ \beta\mathbf{L} & \mathbf{000} \end{bmatrix}; \qquad \hat{\mathbf{m}} = \begin{pmatrix} \mathbf{s} \\ a \\ b \\ c \end{pmatrix}; \qquad \hat{\mathbf{d}} = \begin{pmatrix} \mathbf{Wd} \\ \beta\mathbf{0} \end{pmatrix}, \tag{3.7.15}$$

where $\mathbf{L}$ is the Laplacian operator and β is an adjustable damping parameter that controls the relative importance of fitting the data versus minimizing the roughness of the solution. The zero vectors are used to balance the Laplacian operator, and the parameters a, b, and c are the parameters that define the orbital plane, whose definition is thus integrated in the inversion process.

The damped least squares problem to solve is minimizing both the prediction misfit and the roughness of the solution for a given β:

$$\|\mathbf{We}\|_2^2 + \beta \|\mathbf{Lm}\|_2^2, \tag{3.7.16}$$

where the first term is the norm of the weighted residuals, $\mathbf{e}^T \mathbf{We}$, β is a penalty (damping) factor that weights the a priori information, $\mathbf{Lm}$, and $\mathbf{L}$ is the discrete Laplacian operator. The least squares weighted minimum norm solution to the damped problem (WLSD) is:

$$\mathbf{m}_{WLSD} = \left[\mathbf{G}_w{}^T \mathbf{G}_w + \beta^2 \mathbf{L}^{\mathrm{T}} \mathbf{L}\right]^{-1} \mathbf{G}_w{}^T \mathbf{d}_w \tag{3.7.17}$$

or

$$\mathbf{m}_{est} = \left[\hat{\mathbf{G}}^T\hat{\mathbf{G}}\right]^{-1}\hat{\mathbf{G}}^T\hat{\mathbf{d}} \tag{3.7.18}$$

The equation 3.7.17 is solved by sweeping through the beta parameter space to find the optimal solution form. The penalty factor β plays the role of trade-off parameter between the misfit and roughness of the model. The misfit is defined as the weighted prediction error (misfit norm), $\mathbf{e}^T\mathbf{We}$, while the model roughness is defined by $\|\mathbf{Lm}\|_2^2 = \mathbf{m}^T\mathbf{L}^T\mathbf{Lm}$ (model norm). An L-curve (*Aster et al.*, 2004) can be constructed to find the optimal parameter distribution (Fig. 3.7.2). As β goes to infinity, the misfit becomes extreme, and the roughness decreases generating a smooth distribution of sources. As β goes to zero, the misfit is null but the distribution of sources is rough.

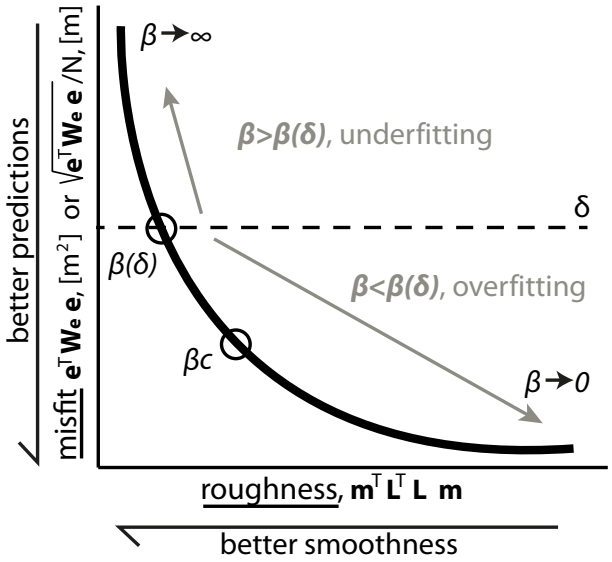

Figure 3.7.2. Calibration with L-curve.
The L-curve (Aster et al., 2004) reveals the trade-off between the misfit and solution roughness. βc is the value of the damping parameter at the bending point. $\beta(\delta)$ is the value of the damping parameter at the reference misfit value (when the misfit axis is represented by the RMSE) of $\delta = \sigma^{obs}$.

The L-curve helps us to find the optimal parameter distribution. A good compromise between misfit and roughness of the solution in case we do not have any information about a possible misfit threshold is the point where the L-curve bends, at βc. When we know the standard deviation of the data that we are inverting, $\delta = \sigma^{obs}$, an L-curve made of root mean square error (RMSE), $e_{RMSE} = \sqrt{\mathbf{e}^T\mathbf{We}}/N$, versus the roughness of the model allows us to idetify the optimal data fitting point on the curve, at $\beta(\delta)$. In this case, $e_{RMSE} > \delta$ would correspond to a data overfitting (when the data noise is also fitted by the solution), while $e_{RMSE} < \delta$ would correspond to a data underfitting (when the solutions do not fit the data well enough).
In the case of generalized inverse, model and data resolution matrix are calculated in a slightly different way with respect to the simple model (Eq. 3.7.7; Eq. 3.7.8). The mode resolution matrix is a function of the data kernel, $\mathbf{G}$, the a-priori information (the weighting matrix, $\mathbf{W}$, and the smoothing matrix, $\mathbf{L}$) and is independent of the data vector. Considering that a true but unknown set of model parameters that solves $\mathbf{Gm}^{true} = \mathbf{d}^{obs}$ exists, we can replace $\mathbf{d}^{obs}$ into the expression of the estimated model $\mathbf{m}^{est} = \mathbf{G}^{-g}\mathbf{d}^{obs}$this way (*Menke*, 1989):

$$\mathbf{m}^{est} = \mathbf{G}^{-g}\mathbf{d}^{obs} = \mathbf{G}^{-g}\left[\mathbf{G}\mathbf{m}^{true}\right] = \left[\mathbf{G}^{-g}\mathbf{G}\right]\mathbf{m}^{true} = \mathbf{R}\mathbf{m}^{true} \tag{3.7.19}$$

$\mathbf{R}$ is the model resolution matrix, with $\mathbf{G}^{-g}= \left[\mathbf{G}^{\mathrm{T}}\mathbf{G}\right]^{-1}\mathbf{G}^{\mathrm{T}}$(generalized inverse). In case the $\mathbf{G}$ matrix is regularized (scalde by a weighting matrix, $\mathbf{W}$, and appended with a smoothing matrix, $\mathbf{L}$) the model resolution matrix is:

$$\mathbf{R} = \hat{\mathbf{G}}^{-g}\hat{\mathbf{G}} \tag{3.7.20}$$

with

$$\hat{\mathbf{G}}^{-g}= \left[\hat{\mathbf{G}}^{\mathrm{T}}\hat{\mathbf{G}}\right]^{-1}\hat{\mathbf{G}}^{\mathrm{T}} \tag{3.7.21}$$

The same way, we can derive the data resolution matrix for the generalized inverse and the specific case, where G is appended with a weighting matrix. Knowing $\mathbf{m}^{est} = \mathbf{G}^{-g}\mathbf{d}^{obs}$from *Menke* (1989):

$$\mathbf{d}^{pre} = \mathbf{G}\mathbf{m}^{est} = \mathbf{G}\left[\mathbf{G}^{-g}\mathbf{d}^{obs}\right] = \left[\mathbf{G}\mathbf{G}^{-g}\right]\mathbf{d}^{obs} = \mathbf{N}\mathbf{d}^{obs} \tag{3.7.22}$$

$\mathbf{N}$ is the data resolution matrix. In the weighted case:

$$\mathbf{N} = \hat{\mathbf{G}}\hat{\mathbf{G}}^{-g}, \tag{3.7.23}$$

where $\hat{\mathbf{G}}$ and$\hat{\mathbf{G}}^{-g}$are the same as specified above.

In order to fully describe the parameter estimates, the uncertainty of the estimates need to be calculated. The root squares of the diagonal elements of the covariance matrix of the model, Cd, provide a measure of the uncertainties of the model parameter estimates. The covariance of the model parameters depends on the covariance of the data and on the way the errors are mapped from the data to the model parameters (*Menke*, 1989).

Assuming that the problem has been scaled and every row has been normalized by the standard error of the associated datum, the covariance matrix of the model parameters is (*Menke*, 1989; *Vasco et al.*, 2002):

$$\mathbf{C_m} = \hat{\mathbf{G}}^{-\mathrm{g}}\hat{\mathbf{G}}^{-\mathrm{gT}} = (\hat{\mathbf{G}}^{\mathrm{T}}\hat{\mathbf{G}})^{-1} \tag{3.7.24}$$

3.7.3 The finite difference laplacian operator, ∇^2 (3D discrete smoothing operator of regular grid sources with zero Dirichlet boundary condition)

Laplace equation is a second order partial differential equation (PDE) which solution requires of certain conditions that need to be satisfied at the boundary of the domain by the unknown function, *f*. In this work we will deal with the Dirichlet boundaries (Fig. 3.7.3) on which the function itself is specified (i.e sources with zero flux, or pressure, at the boundary).

A typical Laplace problem in 3-D, for a field f illustrated in Fig. 3.7.3, is:

$$\nabla^2 f = \frac{\partial^2 f}{\partial x^2} + \frac{\partial^2 f}{\partial y^2} + \frac{\partial^2 f}{\partial z^2} = 0 \tag{3.7.25}$$

The idea behind the application of the finite difference method to generate the Laplacian operator is to discretize the PDE by replacing the partial derivatives with their approximations, the finite differences. We can divide a 3-dimensional region into small regions with increments in the

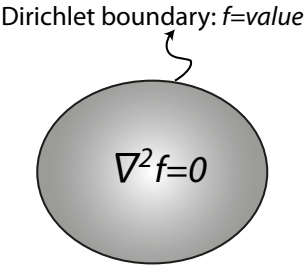

Figure 3.7.3. Laplace's problem with Dirichlet boundary conditions.

x, y, and z directions given as Δx, Δy, and Δz (Fig. 3.7.4). This way f can be represented by a three-dimensional discrete field.

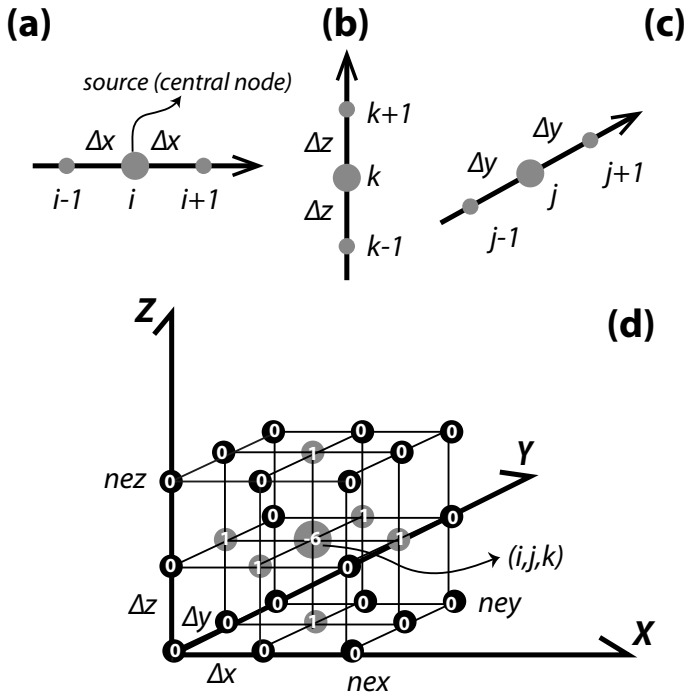

Figure 3.7.4. Finite differencing.
(a) Along x direction, (b) along y direction, and (c) along z direction. (d) 3-D distribution of nodes. The number of nodes in the three directions is: nex, ney, and nez. Gray nodes correspond to the 7-nodes 3-D stencil of the Laplacian operator for the central node. For the stencil considered, in white are the values of all nodes that are used to populate the row of Laplacian operator matrix corresponding to the central node of the stencil (the source).

Each nodal point is thus indexed by a numbering scheme i,j, and k; where i indicates the x increment, j indicates the z increment, and k indicates the y increment (Fig. 3.7.4, a, b and c). The Laplacian equation for the interior nodes of a three-dimensional system can be obtained by considering Laplace's equation at the nodal point (i,j,k):

$$\frac{\partial^2 f_{i,j,k}}{\partial x^2} + \frac{\partial^2 f_{i,j,k}}{\partial y^2} + \frac{\partial^2 f_{i,j,k}}{\partial z^2} = 0 \tag{3.7.26}$$

The finite difference approximation of the second derivatives at the nodal point (i,j,k) along the three spatial directions are computed through Taylor series expansions. The resulting equations are:

$$\frac{\partial^2 f_{i,j,k}}{\partial x^2} \approx \frac{f_{i+1,j,k} - 2f_{i,j,k} + f_{i-1,j,k}}{(\Delta x)^2} \tag{3.7.27}$$

$$\frac{\partial^2 f_{i,j,k}}{\partial y^2} \approx \frac{f_{i,j+1,k} - 2f_{i,j,k} + f_{i,j-1,k}}{(\Delta y)^2} \tag{3.7.28}$$

$$\frac{\partial^2 f_{i,j,k}}{\partial z^2} \approx \frac{f_{i,j,k+1} - 2f_{i,j,k} + f_{i,j,k-1}}{(\Delta z)^2} \tag{3.7.29}$$

Thus, substituting the equations 3.7.27, 3.7.28, and 3.7.29 in the equation 3.7.26, we obtain:

$$\frac{f_{i+1,j,k} - 2f_{i,j,k} + f_{i-1,j,k}}{(\Delta x)^2} + \frac{f_{i,j+1,k} - 2f_{i,j,k} + f_{i,j-1,k}}{(\Delta y)^2} + \frac{f_{i,j,k+1} - 2f_{i,j,k} + f_{i,j,k-1}}{(\Delta z)^2} = 0 \tag{3.7.30}$$

Assuming that $\Delta x{=}\Delta y{=}\Delta z$ (domain partitioned into a regular array of nodes), the finite difference approximation of Laplace's equation for the interior node of a 7-nodes stencil (Fig. 3.7.4, c) can be expressed as:

$$f_{i+1,j,k} + f_{i-1,j,k} + f_{i,j+1,k} + f_{i,j-1,k} + f_{i,j,k+1} + f_{i,j,k-1} - 6f_{i,j,k} = 0 \tag{3.7.31}$$

or

$$f_{i,j,k} = \frac{1}{6}\left(f_{i+1,j,k} + f_{i-1,j,k} + f_{i,j+1,k} + f_{i,j-1,k} + f_{i,j,k+1} + f_{i,j,k-1}\right) \tag{3.7.32}$$

This can be represented by a three-dimensional filter as illustrated in Fig. 3.7.4(c), with the point node (i,j,k) at the center of a 7-nodes stencil. If f satisfies Laplace equation, then at any point of the domain f is the average of the values of f at the six surrounding points in the 7-nodes stencil. In this work we assume no nodes (sources) outside the three-dimensional array of nodes and apply the Dirichlet boundary conditions to the array. This means that the Laplacian matrix is populated with zeros except in the positions where values of stencil nodes are different than zero (the stencil nodes have zero values if they fall out of the array, this happens for example when the central stencil node is located on the border of the array).

The Laplacian operator of sources distributed on a regular grid with Dirichlet boundaries equal to zero is compiled in IDL with the program in Appendix B.

3.8 FE array of sources at the base of the Green's function matrix generation

Inspired by the strategy of domain subdivision of Camacho et al. (2002) and by the work of Masterlark and Lu (2004a), who proposed a three-dimensional regular array of Mogi sources for the inversion, we propose to base the construction of the Green matrix for the inversion on a regular array of hexahedral elements that, once removed, form the cavity for the source (pressure or mass flux source) of deformation. The method is based on sequentially removing one or some elements from the original mesh to generate cubic cavities on whose walls a pressure is applied. This approach is particularly interesting because it allows generating multiple models from the same mesh, avoiding the high computer resource price usually paid to mesh each model. The choice of a regular array allows a systematic selection of the elements to be subtracted and a relatively simple finite difference formulation to achieve the Laplacian smoothing (see sub-chapter 3.7.3) to stabilize the solution. Finally, the solutions at each depth are easily displayed.

The choice of cubic hexahedral elements (C3D8 in Abaqus) is not arbitrary. First, they allow to easily construct a regular array of elements, in a way that the volume is represented by a finite number of non-overlapping, equal-volume cells (sources). Second, it allows simulating a center of expansion. Third, an array of hexahedral elements allows an easy selection of elements to be removed in order to generate the cavity, allowing automatizing the generation of sources without re-meshing the domain. Thus, with this geometric configuration, we are able to minimize time and computer efforts during the meshing stage.

The generation of fluid-filled cavities is automatized by an algorithm that modifies the Abaqus .inp file by removing the structural elements in order to produce the cavity and by using the nodes of these elements in order to generate the hydrostatic fluid elements to fill the cavity with a fluid. The fluid flux is then applied to simulate the expansion source.

3.8.1 Cubic source generation: Fluid elements and aspects of the cavity construction algorithm

Instead of applying isotropic pressures to the faces of the cavity in order to simulate a center of dilatation, Abaqus/Standard offers the possibility of introducing a hydrostatic pressure in the cavity through the use of Abaqus fluid elements (Abaqus code for 3-D, four nodes, fluid elements: F3D4). That is, the pressure is isotropically exerted over the faces of the cavity in response to the injection of new fluid mass (*Abaqus*, 2009). This way, we can introduce a fluid (magma) movement into the analysis, preserving the concept of center of expansion during the simulation. The source of deformation is thus a fluid-filled cavity on which is imposed a mass flux to simulate magma migration. The cavity is assumed to be completely filled with fluid. Changes in pressure within the cavity (ΔP) and volume of fluid-filled cavity (ΔV) are solution variables, with the fluid volume given as a function of the fluid pressure.

The requirements to fully describe a fluid-filled cavity in Abaqus are:

1. standard finite elements to build the walls of the cavity (i.e. Abaqus tetrahedral elements: C3D8, or hexahedral elements: C3D4)
2. hydrostatic fluid elements that cover the inner walls of the cavity. These elements provide coupling between deformation of the fluid-filled structure and the pressure exerted by the fluid on the walls of the cavity (i.e. Abaqus 3-D, four nodes fluid elements: F3D4).

3. a reference node, located inside the cavity, associated with a fluid cavity. This node has a single degree of freedom representing the pressure inside the fluid cavity and is also used in calculating the cavity volume (*Abaqus*, 2009). Thus, it is possible to directly apply hydrostatic pressure to the walls of the cavity by setting the pressure at the reference node as boundary condition (such condition is achieved by setting "Reference node, 8, 8, Pressure" as boundary condition).
4. hydrostatic fluid properties. The requirements to fully describe the fluid for the Abaqus standard flux analysis are: fluid density (ϱ), bulk modulus (k), and mass flux (q).

In an array of cubic hexahedral elements, a cubic cavity can be generated by removing n^3 elements. Multiple cavities can thus be generated sequentially using a systematic selection scheme. No further calculations are performed for the elements being removed, starting from the beginning of the step in which they are removed. By removing the elements from the mesh, the cavity is generated and its structure is made of the faces of the surrounding hexahedral elements.

Before removing the cubic hexahedral elements that will form the cavity, their nodes are used to generate the hydrostatic fluid elements. The chosen way to define hydrostatic fluid elements is to generate node-based elements in a similar way Abaqus defines the faces of the hexahedral (Fig. 3.8.1, a-c). In contrast to the surface-based elements, this allows a more straightforward elements generation as it does not require the search for the surface of the structural elements surrounding the cavity. In fact, in the case of surface-based elements, the search of the surrounding elements is a forced step due to the fact that surface-based elements are only generated by surfaces of existing elements; surface-based elements constructed using the surfaces of the inner elements, which are directly selected and removed for the entire step, would be invalidated during the analysis by the absence of the elements on which they are based. In order to build the fluid cavity, its boundary needs to be defined by hydrostatic fluid elements with normals pointing consistently to the inside of the cavity and hydrostatic fluid elements assembling needs to form a closed volume. The versus of the normal, pointing towards the center of the cavity, is assured by selecting the nodes that constitute the hydrostatic fluid elements in a clockwise manner (Fig. 3.8.1, d). The table in Fig. 3.8.1 (b) provides the position and order of nodes in which Abaqus defines the faces of an hexahedral element (Fig. 3.8.1). The same order can be used to generate six single hydrostatic 4-nodes fluid elements whose normals are pointing inside the element (the cavity, once the element is removed) and that, by definition of element faces, define a closed volume.

In case the cubic cavity is made by removing one single cubic hexahedral element from the cubes array, S [i, j, k] (where i, j, and k are indices for the cube position on the cubes array for the first, second, and the third counting direction of elements in the array, respectively), the nodes of its six faces contribute to the generation of six hydrostatic fluid elements as illustrated in (Fig. 3.8.1, a-d). The fact that these nodes are shared by the hexahedral structural elements that completely surround the cavity ensures the generation of six hydrostatic fluid elements whose assembling forms a closed volume.

In case the cubic cavity is generated by removing a cluster of eight hexahedral elements (Fig. 3.8.2) from the array, each of the eight elements contributes to the boundary of the cluster with three different faces, depending on its position in the cavity. The nodes of the faces are thus used to generate the hydrostatic fluid elements following the scheme of face definition (Fig. 3.8.1). In order to generate non-overlapping cubic cavities of eight elements, a systematic scheme of selection picks one of every two elements of the array. Then, for each picked element [i, j, k], other seven elements with indexes illustrated in Fig. 3.8.2 are identified to form a cluster of eight elements to be removed.

The hydrostatic fluid elements appear as surface elements that cover the cavity boundary,

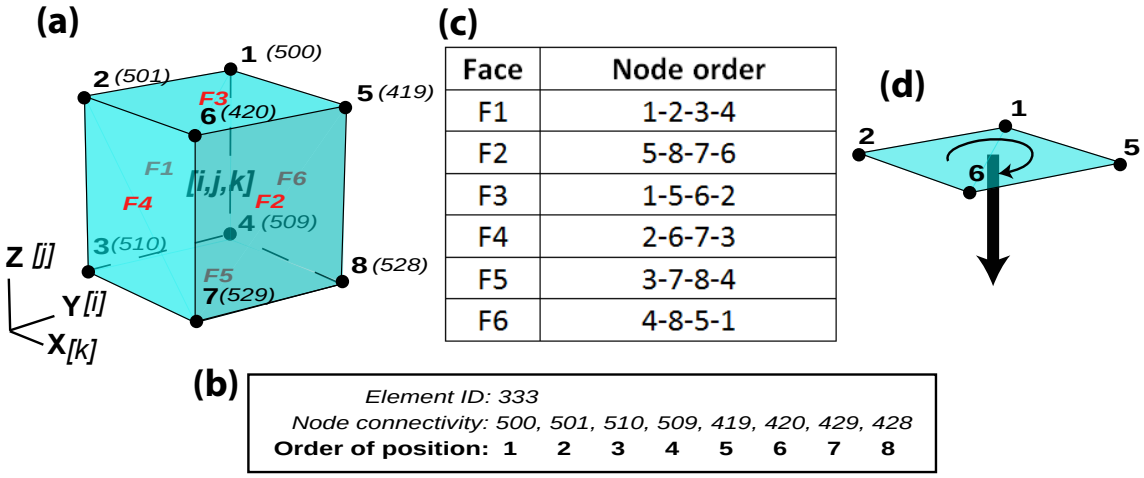

Face	Node order
F1	1-2-3-4
F2	5-8-7-6
F3	1-5-6-2
F4	2-6-7-3
F5	3-7-8-4
F6	4-8-5-1

Figure 3.8.1. Hexahedral element anatomy: node connectivity and faces.
(a) Node ID number (italic number in parenthesis), node connectivity (bold number), and ID number of elements faces (red text). Bold numbers identify the node position in the node connectivity scheme of the element (b). The indices [i, j, k] indicate the position inside the array of the cubic hexahedral element. (c) Order of nodes that define the faces of hexahedral elements. (d) Abaqus uses a clockwise order of nodes to define a face whose normal points inside the element. This can be advantageously used to generate an hydrostatic 4-nodes element.

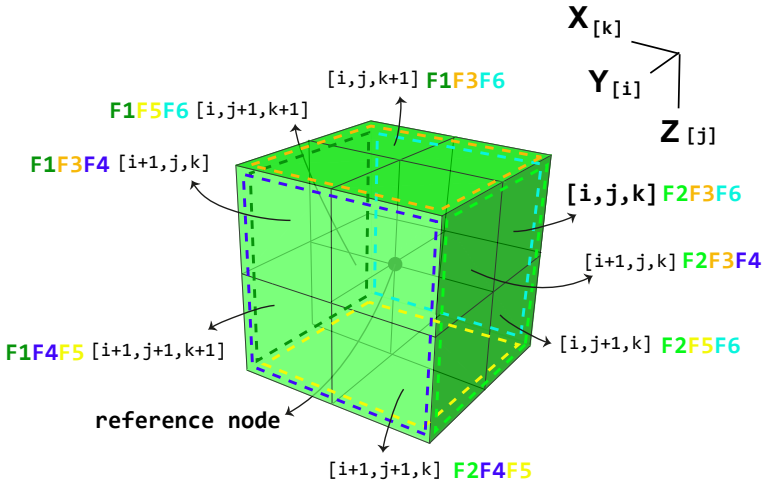

Figure 3.8.2. Cluster of 8 cubic hexahedral elements.
In order to form the cavity, one of every two elements (element [i, j, k],) of the array is picked (reference element), where i, j, and k define the position of the picked element in the array. Once the element [i, j, k] is picked, other seven elements are identified to form a cubic cluster of elements. Each element contributes to the boundary of the cluster with three different faces (F_n marked with different colors), whose node definition is used as guide to generate the hydrostatic fluid elements. The centroid of the cluster is the reference node for the cavity.

but they actually are volume elements when the cavity reference node is accounted for. So, for the case of a cubic cavity with the reference point at its center, the hydrostatic elements are actually squared-base pyramids.

The algorithm written to generate an .inp file with commands for eight elements fluid-filled cavities generation performs the following steps:

1. select the element ID of the cube S [i, j, k]. This allows identifying a cluster of eight elements

whose nodes are at the base of the hydrostatic fluid elements definition. Based on the position (indices) of the elements with respect to the reference element of the cluster, S [i, j, k], nodes ID are selected from their node position in the connectivity scheme of the element.

```
;-------------------------------------------------------------------------------
ENERATE FLUID CAVITY and FLUID PROPERTIES for flux analysis in INP
;-generate the REF NODE inside the cavity (centriod of the solid element chosen as cavity)
    PRINTF,lun,FORMAT="('*************************************************************')"
    PRINTF,lun,FORMAT="('********  FLUID CAVITY: ELSET AND PROPERTIES')"
    PRINTF,lun,FORMAT="('*MODEL CHANGE,TYPE=ELEMENT,REMOVE')"
    PRINTF,lun,var

    PRINTF,lun,FORMAT="('*ELEMENT,TYPE=F3D4')"

    ;-elem S[i+1,j+1,k+1] contributes with faces: F1,F4,F5 ------------------------------
        for n=0, nquadel-1 do begin
            if (S[i+1,j+1,k+1] EQ quadel_structure[0,n]) then begin
                quadel=quadel_structure(*,[n])
                PRINTF,lun,'800001,',quadel[1],",    ",quadel[2],",   ",quadel[3],",   ",quadel[4]
                PRINTF,lun,'800002,',quadel[2],",    ",quadel[6],",   ",quadel[7],",   ",quadel[3]
                PRINTF,lun,'800003,',quadel[3],",    ",quadel[7],",   ",quadel[8],",   ",quadel[4]
            endif
        endfor

    ;-elem S[i+1,j+1,k] contributes with faces: F2,F4,F5 -------------------------------
        for n=0, nquadel-1 do begin
            if (S[i+1,j+1,k] EQ quadel_structure[0,n]) then begin
                quadel=quadel_structure(*,[n])
                PRINTF,lun,'800004,',quadel[5],",    ",quadel[8],",   ",quadel[7],",   ",quadel[6]
                PRINTF,lun,'800005,',quadel[2],",    ",quadel[6],",   ",quadel[7],",   ",quadel[3]
                PRINTF,lun,'800006,',quadel[3],",    ",quadel[7],",   ",quadel[8],",   ",quadel[4]
            endif
        endfor

    ;-elem S[i,j+1,k] contributes with faces: F2,F5,F6 -------------------------------
        for n=0, nquadel-1 do begin
            if (S[i,j+1,k] EQ quadel_structure[0,n]) then begin
                quadel=quadel_structure(*,[n])
                PRINTF,lun,'800007,',quadel[5],",    ",quadel[8],",   ",quadel[7],",   ",quadel[6]
                PRINTF,lun,'800008,',quadel[3],",    ",quadel[7],",   ",quadel[8],",   ",quadel[4]
                PRINTF,lun,'800009,',quadel[4],",    ",quadel[8],",   ",quadel[5],",   ",quadel[1]
            endif
        endfor


    ;-elem S[i,j+1,k+1] contributes with faces: F1,F5,F6 -------------------------------
        for n=0, nquadel-1 do begin
            if (S[i,j+1,k+1] EQ quadel_structure[0,n]) then begin
                quadel=quadel_structure(*,[n])
                PRINTF,lun,'800010,',quadel[1],",    ",quadel[2],",   ",quadel[3],",   ",quadel[4]
                PRINTF,lun,'800011,',quadel[3],",    ",quadel[7],",   ",quadel[8],",   ",quadel[4]
                PRINTF,lun,'800012,',quadel[4],",    ",quadel[8],",   ",quadel[5],",   ",quadel[1]
            endif
        endfor

    ;-elem S[i+1,j,k] contributes with faces: F2,F3,F4 -------------------------------
        for n=0, nquadel-1 do begin
            if (S[i+1,j,k] EQ quadel_structure[0,n]) then begin
                quadel=quadel_structure(*,[n])
                PRINTF,lun,'800013,',quadel[5],",    ",quadel[8],",   ",quadel[7],",   ",quadel[6]
                PRINTF,lun,'800014,',quadel[1],",    ",quadel[5],",   ",quadel[6],",   ",quadel[2]
                PRINTF,lun,'800015,',quadel[2],",    ",quadel[6],",   ",quadel[7],",   ",quadel[3]
            endif
        endfor

    ;-elem S[i,j,k+1] contributes with faces: F1,F3,F6 -------------------------------
        for n=0, nquadel-1 do begin
            if (S[i,j,k+1] EQ quadel_structure[0,n]) then begin
                quadel=quadel_structure(*,[n])
                PRINTF,lun,'800016,',quadel[1],",    ",quadel[2],",   ",quadel[3],",   ",quadel[4]
                PRINTF,lun,'800017,',quadel[1],",    ",quadel[5],",   ",quadel[6],",   ",quadel[2]
                PRINTF,lun,'800018,',quadel[4],",    ",quadel[8],",   ",quadel[5],",   ",quadel[1]
            endif
        endfor

    ;-elem S[i+1,j,k+1] contributes with faces: F1,F3,F4 -------------------------------
        for n=0, nquadel-1 do begin
            if (S[i+1,j,k+1] EQ quadel_structure[0,n]) then begin
                quadel=quadel_structure(*,[n])
                PRINTF,lun,'800019,',quadel[1],",    ",quadel[2],",   ",quadel[3],",   ",quadel[4]
                PRINTF,lun,'800020,',quadel[1],",    ",quadel[5],",   ",quadel[6],",   ",quadel[2]
                PRINTF,lun,'800021,',quadel[2],",    ",quadel[6],",   ",quadel[7],",   ",quadel[3]
            endif
        endfor

    ;-elem S[i,j,k] contributes with faces: F2,F3,F6 -------------------------------
        for n=0, nquadel-1 do begin
            if (S[i,j,k] EQ quadel_structure[0,n]) then begin
                quadel=quadel_structure(*,[n])
                PRINTF,lun,'800022,',quadel[5],",    ",quadel[8],",   ",quadel[7],",   ",quadel[6]
                PRINTF,lun,'800023,',quadel[1],",    ",quadel[5],",   ",quadel[6],",   ",quadel[2]
                PRINTF,lun,'800024,',quadel[4],",    ",quadel[8],",   ",quadel[5],",   ",quadel[1]
            endif
        endfor
```

2. search for the coordinates of the centroid of the cluster, corresponding to the position of the third

node in the node connectivity scheme of element S [i, j, k]. At the found coordinates, it generated the reference node for the cavity.

```
;-define centroid
    for m=0, narrn-1 do begin
        if (quadel[3] EQ array_nodes(0,[m])) then begin
            cx=array_nodes(1,[m])
            cy=array_nodes(2,[m])
            cz=array_nodes(3,[m])
        endif
    endfor

    PRINTF,lun,FORMAT="('*NODE,NSET=fluidn')"
    PRINTF,lun,'900000, ',cx(0,0),",     ",cy(0,0),",",cz(0,0)
    active_s(5,[nn])=cx(0,0)
    active_s(6,[nn])=cy(0,0)
    active_s(7,[nn])=cz(0,0)
```

3. define properties (density and bulk modulus) of the fluid filling the cavity

```
PRINTF,lun,FORMAT="('*ELSET,elset=flux_elements,generate')"
PRINTF,lun,FORMAT="('800001,    800024, 1')"
PRINTF,lun,FORMAT="('**------------------------------------------------------------- END DEFINITION CAVITY')"

PRINTF,lun,FORMAT="('*FLUID PROPERTY,ELSET=flux_elements,REF NODE=fluidn,TYPE=HYDRAULIC')"
PRINTF,lun,FORMAT="('*FLUID DENSITY')"
PRINTF,lun,FORMAT="('2370.27')"
PRINTF,lun,FORMAT="('*FLUID BULK MODULUS')"
PRINTF,lun,FORMAT="('4.50e9')"
PRINTF,lun,FORMAT="('**------------------------------------------------------------- END DEFINITION FLUID PROPERTIES')"
```

4. generate the cavity by removing all the eight structural elements of the cluster in the Abaqus step

```
            ;-remove the solid element to let apply the flux to the cavity
PRINTF,lun,FORMAT="('*************************************************************************************')"
PRINTF,lun,FORMAT="('************************     STEP: fluid')"
PRINTF,lun,FORMAT="('** ----------------------------------------------------------------')"
PRINTF,lun,FORMAT="('**')"
PRINTF,lun,FORMAT="('*Restart, write, frequency=0')"
PRINTF,lun,FORMAT="('*PREPRINT,MODEL=NO,HISTORY=NO,ECHO=NO')"
PRINTF,lun,FORMAT="('*Step, name=fluid')"
PRINTF,lun,FORMAT="('*Static')"
PRINTF,lun,FORMAT="('1., 1., 1e-05, 1.')"
PRINTF,lun,FORMAT="('*MODEL CHANGE, TYPE=ELEMENT, REMOVE')"
PRINTF,lun,S[i+1,j+1,k+1]
PRINTF,lun,S[i+1,j+1,k]
PRINTF,lun,S[i,j+1,k]
PRINTF,lun,S[i,j+1,k+1]
PRINTF,lun,S[i,j,k]
PRINTF,lun,S[i+1,j,k]
PRINTF,lun,S[i,j,k+1]
PRINTF,lun,S[i+1,j,k+1]
```

3.8.2 Array of source-elements and verification of the cubic pressure sources with McTigue

The use of a single cubic hexahedral element, or a cubic-shape cluster of cubic hexahedral elements, as source raises questions about the pertinence of geometry of the sources (i.e. cubic cavities on which a change of pressure is applied) and about the suitable size of the sources, as it affects the solution of the problem by determining the mesh of the domain. Therefore, in order to be able to correctly apply this geometric configuration, we verify the validity of the cubic sources, intended as expanding sources, and the mesh generated by the chosen distribution and size of the cubic hexahedral elements. This is done by comparing the FEM solution of an over-pressurized cubic cavity to the analytical McTigue solution of a problem whose source center is in the same position of the cubic cavity center (Tab. 3.8.1) and whose source volume is comparable with the volume of the cubic cavity to be tested. An isotropic pressure, equal to that used in the McTigue model, is applied to the internal faces of the cubic cavity, facing outward, in order to simulate an overpressure inside the cavity (Fig. 3.8.3, c).

The domain of the testing model is modeled by a hemisphere whose hemispheric boundaries are pinned and whose flat surface corresponds to the free-surface (Fig. 3.8.3, a). The distribution of material properties is homogeneous and isotropic over the entire domain (E=10e^9 Pa, ν=0.25). Two different meshes are tested. In the first mesh, the domain is tessellated with 36,815 tetrahedral elements (Abaqus code: C3D4) outside the array of cubic sources, and 640 cubic hexahedral elements (Abaqus code: C3D8) to form the array of cubic sources (Fig. 3.8.3, b). In the second mesh, the domain is tessellated with 113,939 tetrahedral elements (Abaqus code: C3D4) outside the array of

cubic sources, and 5120 cubic hexahedral elements (Abaqus code: C3D8) to form the array of cubic sources (Fig. 3.8.3, d). In both cases, each node over the faces of the prismatic array of cubic hexahedral elements is connected to the corresponding node of the external tetrahedral elements in a way that the displacements at the nodes of the faces of the array are fully coupled (Abaqus command: *MPC, TIE constraint, node-to-node). Tie constraints are used to tie together the nodes of two surfaces for the duration of the simulation. Each slave node (nodes of tetrahedra on the array faces) is constrained to have the same motion as the master node (nodes of hexahedra on the array faces). For a structural analysis, this means that the translational (and, optionally, the rotational) degrees of freedom are constrained (*Abaqus* 2009). Tie constraints are particularly useful for rapid mesh refinement between dissimilar meshes.

In the different tests, the cubic cavity, on whose walls the pressure is applied to simulate the center of expansion, is generated by removing one cubic hexahedral element (1e) from the first or the second mesh, or four cubic hexahedral elements (4e) from the second mesh (Fig. 3.8.3, b and d). Tests of the three different kind of cubic sources, with different size and different number of elements, are run at four different positions of the source array to verify the validity of the sources against the McTigue analytical model. The three different kind of cubic sources are:

1. cubic source made of one cubic hexahedral element of 500 m side
2. cubic source made of one cubic hexahedral element of 250 m side
3. cubic source of 500 m side, made of a cluster of eight cubic hexahedral elements of 250 m side each

The tested cavities' size, their complexity in terms of number of constituting elements, and their position in the regular array of cubic hexahedral elements are shown in Fig. 3.8.3 (b and d). The cubic shape allows to isotropically apply the pressure (Fig. 3.8.3, c), simulating an isotropically expanding source (Segall, 2010). Depth and size of the tested sources are illustrated in Fig. 3.8.3 (b and d) and summarized in Tab. 3.8.1, where the results are also summarized. Comparisons between FEM solutions and analytical solutions (Fig. 3.8.3, e-h) are done at each position in the array for a maximum vertical deformation of about 8 cm that corresponds to a deformation in the LOS direction of about 6 cm (with LOS=[-0.617, -0.131, 0.775]), which is the annual deformation registered at Rabaul caldera (see sub-chapter 2.4.3). The chosen maximum value of displacement is purely indicative as it does not correspond to the displacement generated by only one source. It is more likely due to the contribution of several sources. To generate such a deformation, the pressure inside the single source needs to be unrealistically high; this is not a concern as the goal of this verification phase is to only compare the FEM solution with the analytical McTigue solution. Therefore, the pressure values are not reported.

The source behavior is considered compatible with the McTigue expansion source when the solutions at the surface are compatible. Solutions from the FEM are compared with the analytical McTigue solution for sources at different positions in the array: at the corner, on the edge, on the face, and at the bottom of the array. All McTigue solutions are very similar (solid lines in Fig. 3.8.3, e-h), and tend to overlap for all cubic cavities along the faces (blue and pink solid lines in Fig. 3.8.3, f); in the case of inner sources, they are wider for the shallower sources and more peaked for the deeper ones, due to a deeper and a shallower position of the source center, respectively (orange solid lines is the McTigue solution in Fig. 3.8.3, e-h). Solutions from models in which the source is made of a single cubic hexahedral element (1e) of 500 m side are in bad agreement with the analytical McTigue solution (Tab. 3.8.1), showing smaller displacements (Fig. 3.8.3, light blue dots in Fig. 3.8.3, e-h). By reducing the element size of the single-element source from 500 m to 250 m, we do not find any significant solution improvement by the mesh refinement required by the smaller size of the

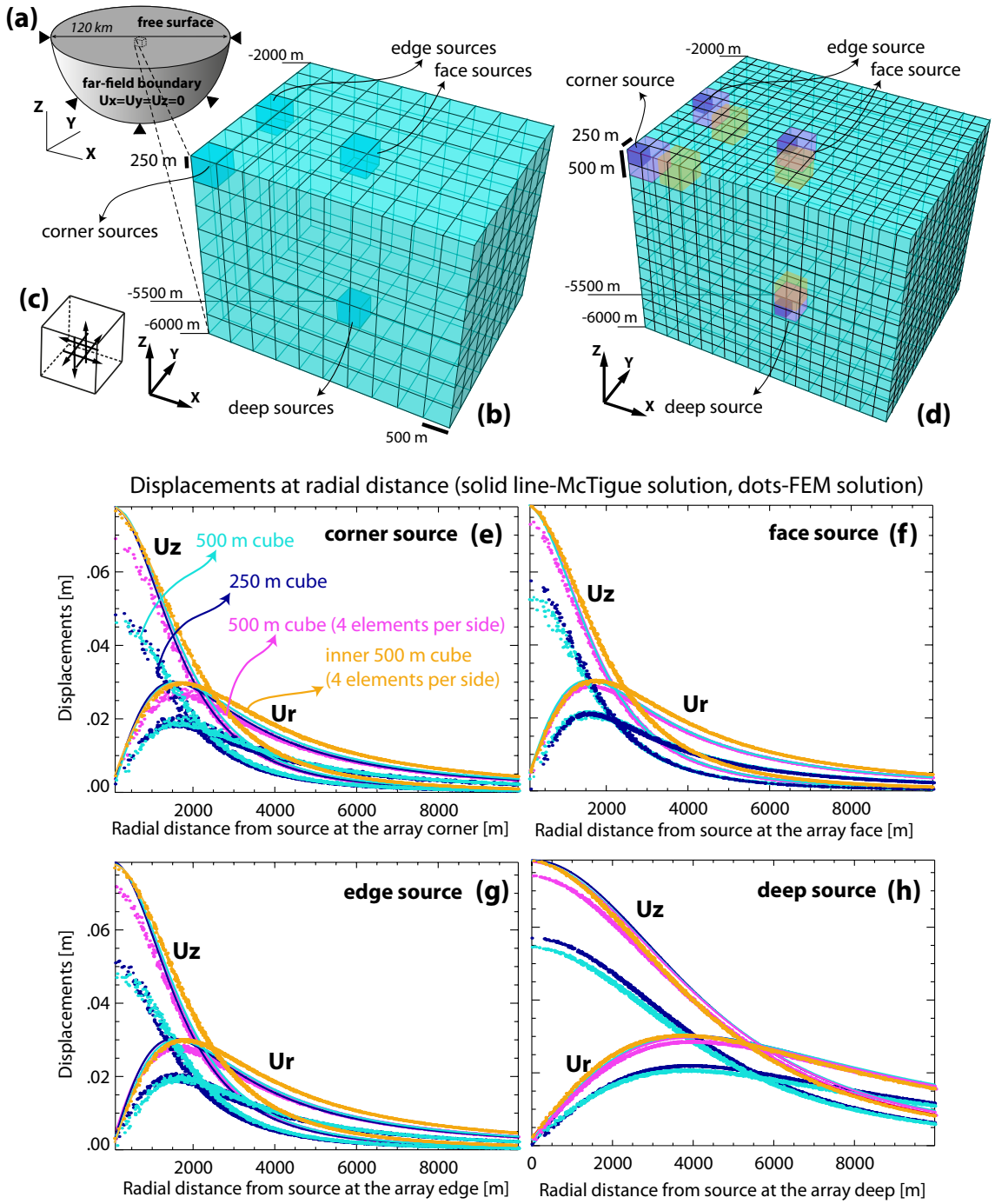

Figure 3.8.3. Array of cubic sources and test of cubic element-sources. *(a) Boundary conditions of the FEM domain. (b) Details of the prismatic array of 500 m size cubic hexahedral elements. Cubic cavity made of one single cubic hexahedral element of 500 m size (light blue) at the corner, along the edge, on the side, and at the bottom of the array are illustrated. (c) Center of expansion, pressure applied to the inner faces of the cubic source. (d) Details of the array of 250 m size cubic hexahedral elements. Cubic cavities made of one single cubic hexahedral element of 250 m size (dark blue), and cubic cavities made of a cluster of eight cubic hexahedral elements located along the faces (pink) and in inner position (orange) are illustrated. (e-h) Displacements generated by the tested cubic sources at the four locations inside the array. The colors of the solution correspond to the color used in panels b and d to highlight the cubic cavity.*

cubes of the array. In fact, although the maximum displacements increase a little bit using 250 m single-element source (Fig. 3.8.3, dark blue dots in e-h), in both cases the misfit values are between 28% (for deeper sources) and 38% (for corner sources) for all displacement components (Tab. 3.8.1). We did not consider a further refinement, due to the excess of computation efforts required for the solution calculation of the corresponding increased number of single-element sources. As general observation, the worst misfit is obtained for sources at the corner and the edge (Fig. 3.8.3, e and g). This general observation is still valid in the case of the 8-elements source for which the solution is extremely improved to misfits between 4% and 9%, but still unacceptable for sources at the corner and at the edges if we take the common threshold of 5% misfit. In fact, the overpressure in a cavity in which the faces are tessellated with four elements produces better (with bigger displacements), but still improvable solutions (pink dots in Fig. 3.8.3, e-h).

As the acceptable compromise between the solution approximation and the mesh resolution is a misfit of 5%, we continue our investigation testing the solution of internal elements (8e int) in order to find acceptable solutions for elements in all positions of the source array. For internal sources of 8-elements and 500 m size we intend those not directly located on the faces of the array, but one row of elements further inside the array (Fig. 3.8.3, d). For these sources the solutions are improved to acceptable misfit values smaller than the 5% threshold at any position of the array and for any deformation components (Tab. 3.8.1). The solutions (orange dots in Fig. 3.8.3, e-h) are almost entirely aligned to the McTigue solution, showing a very good agreement over any radial distance.

The performed tests lead us to some considerations and observations that guide us to the use of the cubic hexahedral element sources for further applications:

1) by applying the pressure over flat single-faces of a cavity, made by removing a single cubic hexahedral element, we simulate an expanding point-source similar to loading the faces with three double couple forces and three dipoles (*Trasatti et al.*, 2008). The assumption of the expanding point is that the forces are applied on an infinitesimal surface. This can lead to the discrepancies with the FEM solution where the forces are applied on finite surfaces of the elements. This aspect is revealed by the consistent FEM bad approximation for single-element sources (1e) for elements of 500 m and 250 m side. The vicinity of the sources to the surface is also a reason why the point source assumptions are non-respected. Reducing the size of the element should eventually lead to conditions where the point source assumptions are met. This, however, requires a considerably higher number of elements to be used as sources.

2) the bad FEM approximation of the analytical McTigue solution of sources on the sides of the array may be related to a non-isotropic source expansion due to the change of elements along the array sides. In fact, around a source located on the array sides, the mesh passes from hexahedral elements on the sides of the source inside the array to tetrahedral elements on the sides of the source facing the domain external to the source array. Thus, a bad, non-isotropic, mesh is at the origin of the bad FEM solution.

3) the bad solution due to sources located on the sides of the array can easily be overcome by generating a shell of hexahedral elements (inactive sources) around the array of active sources. This guarantees a common behavior of all the sources of the array.

Parameter corner source	**500 m (1e)**	**250 m (1e)**	**500 m (8e)**	**500 m (8e int)**
Radius McTigue source [m]	310.175	155.087	310.175	310.175
Depth source center [m]	2250.	2125.	2250.	2500.
Max Ulos McTigue (m)	0.066	0.066	0.066	.006
Misfit Ux McTigue-FEM (δp)	**0.378**	**0.381**	**0.091**	**0.013**
Misfit Uy McTigue-FEM (δp)	**0.378**	**0.374**	**0.085**	**0.010**
Misfit Uz McTigue-FEM (δp)	**0.384**	**0.385**	**0.092**	**0.017**
Misfit Ur McTigue-FEM (δp)	**0.377**	**0.376**	**0.087**	**0.009**
Misfit Ulos McTigue-FEM (δp)	**0.373**	**0.372**	**0.081**	**0.020**
Max difference Uz McTigue-FEM [m]	0.031	0.029	0.009	0.002
Max difference Ulos McTigue-FEM [m]	0.026	0.025	0.007	0.002
Parameter edge source	**500 m (1e)**	**250 m (1e)**	**500 m (8e)**	**500 m (8e) int.**
Radius McTigue source [m]	310.175	155.087	310.175	310.175
Depth source center [m]	2250.	2125.	2250.	2500.
Max Ulos McTigue (m)	0.066	0.066	0.066	.006
Misfit Ux McTigue-FEM (δp)	**0.357**	**0.358**	**0.072**	**0.011**
Misfit Uy McTigue-FEM (δp)	**0.360**	**0.353**	**0.053**	**0.010**
Misfit Uz McTigue-FEM (δp)	**0.356**	**0.366**	**0.069**	**0.012**
Misfit Ur McTigue-FEM (δp)	**0.358**	**0.355**	**0.060**	**0.007**
Misfit Ulos McTigue-FEM (δp)	**0.347**	**0.356**	**0.062**	**0.016**
Max difference Uz McTigue-FEM [m]	0.031	0.028	0.007	0.002
Max difference Ulos McTigue-FEM [m]	0.025	0.022	0.005	0.002
Parameter face source	**500 m (1e)**	**250 m (1e)**	**500 m (8e)**	**500 m (8e) int.**
Radius McTigue source [m]	310.175	155.087	310.175	310.175
Depth [m]	2250.	2125.	2250.	2500.
Max Ulos McTigue (m)	.066	.066	.006	.006
Misfit Ux McTigue-FEM (δp)	**0.327**	**0.325**	**0.035**	**0.009**
Misfit Uy McTigue-FEM (δp)	**0.326**	**0.325**	**0.037**	**0.010**
Misfit Uz McTigue-FEM (δp)	**0.331**	**0.328**	**0.047**	**0.013**
Misfit Ur McTigue-FEM (δp)	**0.326**	**0.324**	**0.035**	**0.006**
Misfit Ulos McTigue-FEM (δp)	**0.330**	**0.330**	**0.043**	**0.012**
Max difference Uz McTigue-FEM [m]	0.026	0.021	0.005	0.001
Max difference Ulos McTigue-FEM [m]	0.021	0.019	0.004	0.001
Parameter deep source	**500 m (1e)**	**250 m (1e)**	**500 m (8e)**	**500 m (8e) int.**
Radius McTigue source [m]	310.175	155.087	310.175	310.175
Depth [m]	5750.	5625.	5750.	5500.
Max Ulos McTigue (m)	.066	.066	.066	.066
Misfit Ux McTigue-FEM (δp)	**0.316**	**0.280**	**0.038**	**0.008**
Misfit Uy McTigue-FEM (δp)	**0.318**	**0.276**	**0.040**	**0.010**
Misfit Uz McTigue-FEM (δp)	**0.322**	**0.288**	**0.056**	**0.011**
Misfit Ur McTigue-FEM (δp)	**0.317**	**0.277**	**0.039**	**0.007**
Misfit Ulos McTigue-FEM (δp)	**0.319**	**0.289**	**0.056**	**0.010**

Table 3.8.1. Source parameters and misfit with McTigue solution.

Chapter 4

Results of methods applied to Rabaul caldera

4.1 Rabaul geologic parts identification and 3-D construction in Abaqus CAE environment

The choice of control points, necessary to control the splines construction and used as input for the Python code to build the solids (see subchapter 3.3.1), was guided by the *Finlayson et al.* (2003) tomography and the *Heming* (1974) geologic map previously geo-referenced to the Universal Transverse Mercator (UTM) projection system through the open-source GIS software package QGIS (2011). The control point coordinates were thus provided as UTM coordinates; the Y axis and X axis assumed, respectively, the North-South and West-East direction. In the process of choosing the control points, we selected those points that led to the construction of complex, but smooth 3-D bodies. The purpose of building smooth bodies is kept in mind during the 3-D body construction, as smooth bodies generally are easier to mesh and reduce the sharp and small scale features, thus reducing the number of elements and the computational time.

Two tomographic works (*Finlayson et al.*, 2003; *Bai and Greenhalgh*, 2005) based on the same geophysical survey, conducted in the Rabaul region between August 1997 and January 1998 (RELACS, *Gudmundsson et al.* 1999), have been published. Both their tomographic images identified low-velocity anomalies that the authors interpreted as magma bodies with 12% degree of melting (*Bai and Greenhalgh*, 2005). In addition, *Bai and Greenhalgh* (2005) recognized a new velocity zone located at Tavui caldera. We chose to use the *Finlayson et al.* (2003) tomography because of its better detail in defining the shallow (<8 km) geological blocks. The additional information about a possible magma batch under Tavui caldera provided by *Bai and Greenhalgh* (2005) is irrelevant for our model. In addition, the lack of geological explanation or support of the highly positive velocity perturbation that their tomographic image shows all around the highly negative perturbation area (magma chamber) makes it difficult to use it as reference for the 3-D model construction.

We chose to represent the domain volume with six geologic regions of different elastic properties (Tab. 4.1.1). These regions were constructed as 3-D deformable solid parts, or bodies, by using the lofting technique, partitions, and boolean operations in the Abaqus Assembly module. Based on the properties distribution derived from the tomographic sections and geological map, the upper part of the model (first 8 km of the upper crust) was subdivided into four solids: the Baining Mountains, the volcanic deposits external to the caldera, the infill deposits, and the dike complex (Fig. 4.1.1,

b and Tab. 4.1.1), plus the void representing the magma chamber. The remaining two regions, the mantle and the crust (Fig. 4.1.1, d), complete the deeper part of the hemispheric domain and do not present complex geometries

Tomography and geology provided detailed information about the property distribution in an area of about 15 km radius centered on Rabaul caldera. Outside of this perimeter, tomographic information is missing. We overcame this lack of information by radially extending the geological (G) or the tomographic (T) information of Baining Mountains and Extra-caldera sediments volumes till the domain boundaries.

Static moduli of the rocks and soils of the Rabaul caldera area are not available, so we calculated the dynamic moduli, rescaled them to static values using the empirical relationship formulas previously discussed, and compared the obtained values to real static values of similar material from other study areas from the literature. Elastic dynamic properties of the first 8 km were calculated from the Vp distribution derived by the velocity contrast of the *Finlayson et al.* (2003) tomography study (see sub-chapter 2.2.4) using the empirical relationship between seismic velocities and mechanical properties together with elastic formulas. In the next section, a detailed procedure for the calculation of each material property and 3-D parts constructions for the Rabaul case is provided. The elastic properties are summarized in the following Tab. 4.1.1.

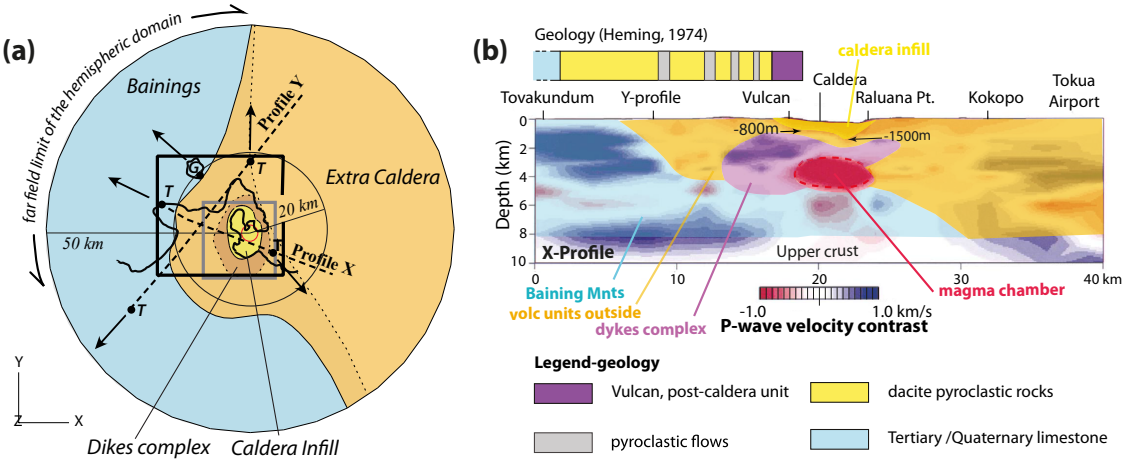

Figure 4.1.1. Model domain extension and principal parts.
(a) Above view of the parts (in the first 8 km) of Rabaul model, and location and coverage of Fig. 2.2.1 geologic map (black solid box), tracks of tomographic profiles (dashed black lines) and extension of the tomographic slices (gray solid box) (from Finlayson et al. (2003)). In dotted lines are the borders of subsurface dike complex and the deeper north-southeast border of Baining Mountain block. The bullets, marked with G or T, refer to the most external position (with respect to the center of the caldera), at the surface or at depth, of geological (G) and tomographic (T) spatial information of the presence of Baining Mountain block. From these points, the Baining Mountains block is extended to the far field limit of the model domain (50 km from the center of the model) to complete the 3-D model (black arrows). (b) Simplification of approximate geometry of five geologic sub-domains from interpretation of Finlayson et al. (2003), modified from Ronchin et al. (2013).

4.1.1 Model mantle (50-30 km depth) and lower crust (30-8 km depth)

In our model the Moho, discontinuity between the crust and the underlying mantle, is located at a depth of 30 km; this assumption is justified by previous studies (*Finlayson and Cull*, 1973b;

Wiebenga, 1973; *Johnson et al.*, 2010). The density of the mantle is 3300 kg/m^3 (*Finlayson and Cull*, 1973b), while the Young's modulus and Poisson's ratio of the mantle are chosen after *Turcotte and Schubert* (2002). For elastic properties value, see Tab. 4.1.1.

The properties of the crust between 8 km and 30 km depth are chosen following *Got et al.* (2008). A density of 2900 kg/m^3 is a reasonable value for the area and corresponds to the higher average value found by other authors for this area (*Finlayson and Cull*, 1973b and references therein). The presence of oceanic crust is consistent with the active subduction along the trench under New Britain Island, and the high thickness is also consistent with a doubling of subduction slabs in agreement with the Miocenic reversal arc polarity proposed by *Falvey and Pritchart* (1982) and *Kroenke* (1984).

4.1.2 Model parts of the upper crust (8-0 km depth)

Intra-caldera fill

The intra-caldera fill, or caldera infill, (Fig. 4.1.2) is defined by a region of low velocity detected by the tomography X-Profile (*Finlayson et al.*, 2003) in the area of Blanche Bay and Vulcan edifice, filling the caldera topographic depression and gradually deepening from -500 m in the North up to about -1500 m in the South, below Karavia bay (Fig. 4.1.2, b). A deepening of bathymetry and a thickening of sedimentary sequences of tephra (*Greene et al.*, 1986) corresponds to the deepening of the low velocity region below Karavia bay and is consistent with complexities in subsidence geometry of the caldera floor that might suggest a piecemeal-like collapse (*Lipman*, 1997). The maximum thickness of the deposits in correspondence with a local minimum of the bathymetry in Karavia bay could in fact be consistent with the filling of a deeper depression left by the caldera block that shrunk most during the collapse. *Bai and Greenhalgh* (2005) tomography is in agreement with *Finlayson et al.* (2003) in showing the shallow low velocity volume representing the soft sediments. However, the tomography of *Finlayson et al.* (2003) shows more useful details for the construction of the geometry. Although the horizontal and vertical resolution of the tomography near the surface were $<$ 3 km and $<$ 1 km, respectively (*Finlayson et al.*, 2003), the shape of the low velocities shown in the Profile X results is consistent with geological considerations and therefore was chosen as reference for the geometry for the 3-D part construction (Fig. 4.1.2, c-d). The Low velocities in the tomographic slice at 1 km depth(*Finlayson et al.*, 2003) are found in this area and are interpreted to be part of the signal of the infill deposits in its deeper part.

In Fig. 4.1.2 (a-c) the control points chosen to build the splines and loft the solid are shown, following the method proposed in the methods section of this work (sub-chapter 3.3.1). The infill block reaches its maximum lateral extension between 0 and 500 m depth (note that the 0 m and the -500 m contour have the same shape and same extension). Its furthest limits extend up to the borders of caldera collapses marked by *Heming* (1974). Therefore, the volume includes the intra-caldera fill and the post caldera cones (Tavuvur and Vulcan), including also the Palangiagia cone that hosts the recent post-caldera Rabalanakaia crater (250-230 BP, *Johnson et al.*, 2010 and reference therein) that retains a quasi-permanent thermal activity (*Perry and Crick*, 1974). Below 500 m depth, the body starts to gently shrink to the south in a syphon-like shape until it reaches its maximum depth of -1500 m below Karavia Bay. In areas where no geological or tomographic data were available (contours -750 m and -1000 m), the control points have been chosen in a way favorable for the building of a smooth 3-D geometry using the Abaqus tools.

Gravity and deformation-based estimates suggest that the density of the intracaldera-fill is 1900 kg/m^3 (*McKee et al.*, 1987). This corresponds to the lower value of wet compacted sands

Elastic formulas	
Vs from Vp	In a isotropic medium, the P-wave and S-wave velocities are related through the Poisson's ratio ν: $V_p{}^2 = V_s{}^2(1-\nu)/(0.5-\nu)$ Thus the Poisson's dynamic modulus is: $\nu_d = \frac{0.5(V_p/V_s)^2-2}{(V_p/V_s)^2-1}$
Elastic formulas	G=$Vs^2 \cdot \rho$ and E=2G·(1+ν), where G is the shear modulus and Vs was computed from Vp velocities, inferred from tomography (Finlayson et al., 2003)

3-D part	**Description (volume and properties)**	**References**
Chamber volume	9.6+e09 m^3	in agreement with the volume proposed by Jones and Steward (1979) and Patia (2004) and respectful of seismicity (Jones and Steward, 1979; Saunders, 2001)
Intracaldera-fill	Volume= 6.61e+010 m^3 Density=1900 kg/m^3 V_p= 1500 m/s V_s=337 m/s E_{dy}=0.5x10^9 Pa ν_{dy}= 0.47 E_{st}= **0.2 x10^9 Pa** ν_{st}= **0.15**	(McKee et al., 1984; Jaeger et al., 2007) From Finlayson et al. (2003) tomography From Vp velocities (Brocher, 2005 Eq.6) From elastic theory formulas From wave velocities (Christensen, 1996 Eq.1)
Extra-caldera	Volume= 2.48e+013 m^3 Density=2052 kg/m^3 V_p= 2375 m/s Vs=882 m/s E_{dy}=**4.08x10^9 Pa** ν_{st}=**0.28** E_{st}= E_{dy}	(Brocher, 2005 Eq.1, Rodriguez et al., 2009) from Finlayson et al. (2003) tomography from Vp velocities (Brocher, 2005 Eq.6) From elastic theory formulas (Rodríguez-Losada et al., 2009; Shultz and Li, 1995) (Price and Jones, 1982; Rodríguez-Losada et al., 2009)
Baining Mountains	Volume= 3.69e+013 m^3 Density= 2627 kg/m^3 V_p= 5200 m/s Vs= 2854 m/s E_{dy}= 54.98x10^9 Pa ν_{dy}= **0.28** E_{st}=**47.86 x10^9 Pa** ν_{st}= ν_{dy}	(Gardner et al., 1974) from wave velocities From Finlayson et al. (2003) tomography From Vp velocities (Brocher, 2005 Eq.6) From elastic theory formulas From wave velocities (Christensen, 1996 Eq.1) (Eissa and Kazi, 1988 Eq.7, for low porosity rocks)
Dikes complex	Volume= 5.48e+011 m^3 Density= 2936 kg/m^3 V_p= 6100 m/s Vs= 3322 m/s E_{dy}=85.53x10^9 Pa ν_{dy}= **0.29** E_{st}= **56.45 x10^9 Pa** ν_{st}= ν_{dy}	(Christensen, 1996) from wave velocities From tomography (Finalyson et al., 2003) From Vp velocities (Brocher, 2005 Eq.8) From elastic theory formulas From wave velocities (Christensen, 1996 Eq.1) (average equation from Morales and Marcinew, 1993)
Crust (oceanic crust)	Volume= 1.45e+014 m^3 Density=3300 kg/m^3 E= **100x10^9 Pa** ν= **0.25**	(Finalyson and Cull, 1973) (Got et al., 2008) (Got et al., 2008)
Mantle	Volume= 5.46e+013 m^3 Density=3300 kg/m^3 E= **174.59x10^9 MPa** ν= **0.28**	(Finlayson and Cull, 1973) (Turcotte and Shubert, 2002) (Turcotte and Shubert, 2002)
Elastic properties of the homogeneous model (HOMO)		
homo	Density=2052 kg/m^3 E_{dy}=**4.08x10^9 Pa** ν_{st}=**0.28** E_{st}= E_{dv}	Extra-caldera properties

Table 4.1.1. Elastic formulas. Dimension and elastic properties of the 3-D geological parts.

(*Jaeger et al.*, 2007). Vp is estimated to be 1500 m/s from the tomography (*Finlayson et al.*, 2003), while Vs computed from Vp is 337 m/s using the "Brocher's regression fit," Eq.6 of *Brocher* (2005). The dynamic Poisson's ratio, 0.47, computed from the velocities, is indicative of saturation in loose

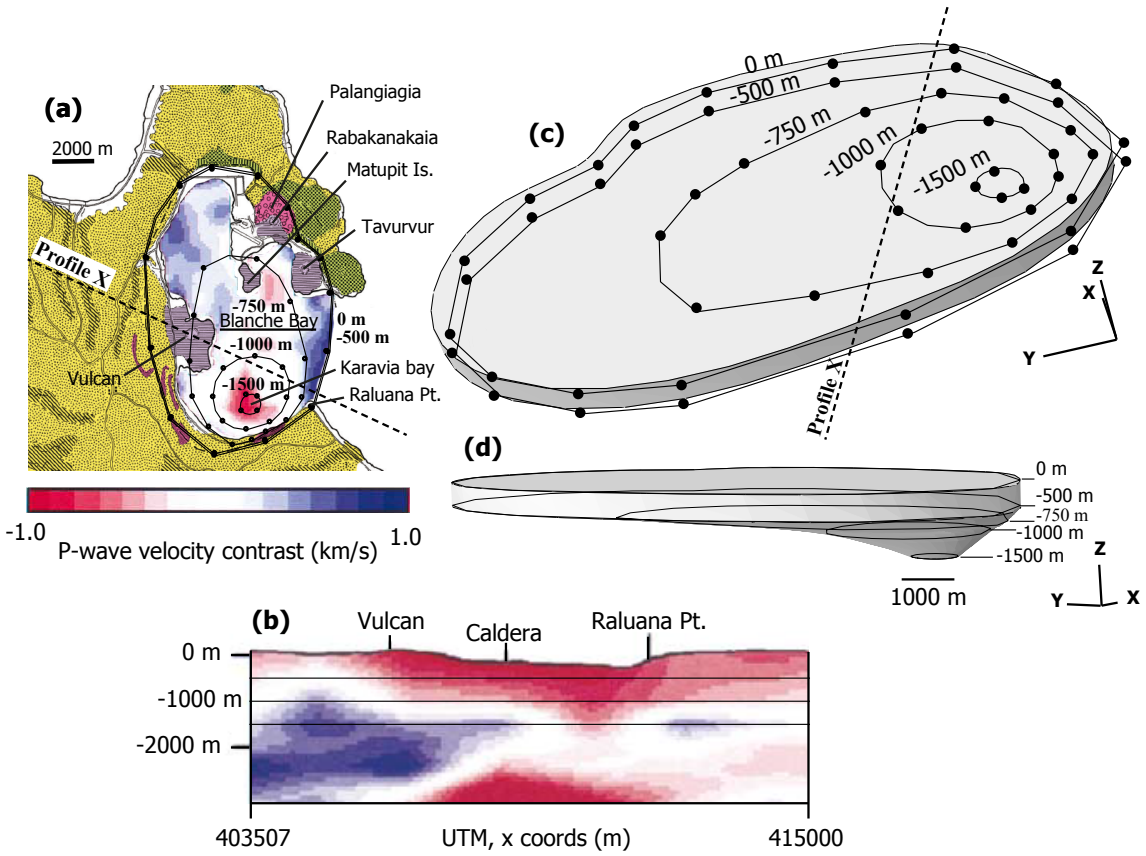

Figure 4.1.2. Infill part study and construction.
(a) Geologic map of the Rabaul caldera deposits, post caldera cones, and peripheral cones (sector of map modified from Heming, 1974, see Fig. 2.2.1 for color references). Results of horizontal section of velocity contrast at -1000 m are overlapped to cover Blanche Bay's lack of information about material properties (modified from Finlayson et al., 2003). The black dots are the control points chosen to build the splines and the solid loft. The contour lines represent positions at the same depth in the caldera structure. The dashed line marks the track of the portion of Profile-X velocity contrast used in this study. (b) Profile-X velocity contrast (modified from Finlayson et al., 2003), the negative contrast indicates the low velocity signal of the deposits filling the caldera depression. (c-d) views of the geometry built to model the infill deposits. In (c) the control points, the contour lines (splines), the solid loft, and the track of the tomographic velocity contrast Profile-X are represented.

sediments and it is reported by other authors in coastal areas (*Karastathis et al.*, 2007). As most of this model part represents the sediments that fill the caldera occupied by the bay, and is partially composed by volcanoclastic deposits in areas interested by high hydrotermalism, the found dynamic Poisson's ratio is reasonable for saturated sediment that fill the caldera. Dynamic Poisson's values from literature support the high value calculated from the velocities: for natural marine sediments the dynamic Poisson's ratios vary from above 0.49 at the sea floor to about 0.41 at 1000 m depth (*Hamilton*, 1979a). Other authors found that the static modulus of unconfined and undrained Poisson's ratios of near-surface sediments range from 0.4951 to 0.5 (*L'Esperance et al.*, 2013). Due to the fact that in the literature there is no univocal relationship between the dynamic and the static Poisson's ratio, we cannot derive the static value from the dynamic value found from the Vp. Nevertheless, based on the agreement of fact that the static Poisson's ratio of soils is much lower that the dynamic counterpart, and assuming that drained conditions prevail for long-term deformation in the inner caldera as suggested by other authors (*Trasatti et al.*, 2005), we can conclude that

the very high dynamic Poisson's value found cannot be used for a realistic representation of the Rabaul caldera filling sediments. Thus, we used the Poisson's value of 0.15, which was already used in FEM by other authors to represent similar geologic parts (*Masterlark*, 2007; *Masterlark et al.*, 2012) and to account for the relatively week and saturated materials (*Wang*, 2000). Furthermore, this value is in general agreement with the values of the drained Poisson's ratio (0.17) achieved using the approximation (Eq. 3.4.13 this work) provided by *Trautmann and Kulhawy* (1987) for a drained friction angle of 30°, typical of medium clayey sand soils (*Bery and Saad*, 2012). Using the elastic theory formulas, we estimate the dynamic Young's modulus to be 0.5 GPa. Following the observations about the relationship between dynamic and elastic modulus of previous authors (*Lama and Vutukuri*, 1978; *Tutuncu et al.*, 1998) an approximately value reduced to 0.2 MPa can reasonably take into account for the static Young's modulus. This value falls in between 0.6 MPa value of pyroclastic deposits used by *Apuani et al.* (2005), that could represent the shallow products of the post caldera cones, and 0.1 GPa already used by *Geyer and Gottsmann* (2010) for a compliant layer of 300 m to represent the soft caldera fill in their Rabaul model.

Dikes swarm

Finlayson et al. (2003) imaged high-velocity features around the magma chamber and under the rim of Rabaul caldera that were interpreted to be mafic intrusive rocks representing a swarm of mafic dikes. The RELACS geophysical survey does not have the resolution capacity to enable the mapping of fine structures, such as dikes and conduits (*Johnson et al.*, 2010). Therefore the dike complex is represented by a spread low velocity zone with negative velocity contrast. The presence of mafic dikes is supported by the finding of diorite blocks xenolites in the Rabaul deposits (*Heming*, 1974). Other authors with different techniques found anomalies that they interpreted to be the mafic intrusions: *Almond* (1981) mapped large magnetic anomalies coinciding with Tovanumbatir, Kabiu, and Turangunan and he suggested the existence of old conduits dipping toward a source located at about 10 km beneath the actual caldera, while *Harrison* (1971) explained the reported gravity values over Watom, Tuvanumbatir, and Palangiagia higher than elsewhere in the Blanche Bay area, as a distribution of rocks with greater densities, presumably corresponding to solidified conduits and dikes of mafic materials. Another confirmation of the evidence of more dense material below the volcanoes located at the caldera peninsula is supported by the Bouguer gravity anomalies found by *Brooks et al.* (1971). The Bouguer gravity anomalies are characterized by contours circumferential to a point below the present Rabaul caldera. This arcuate shape is also shown by the shallow structure of Tovanumbatir at 1 km depth slice of the *Finlayson et al.* (2003) tomography (Fig. 4.1.3, a).

The formation of similar structures is common in volcanic areas, found in other areas and already largely discussed by other authors (*Acocella and Neri*, 2009, and references therein; *Gudmundsson*, 1984, and references therein; *Burchardt et al.*, 2011). At caldera complexes there is a widespread evidence for the presence of circumferential dikes, mostly reported along the sides of the caldera, lying at deeper level within the volcanic edifice (*Acocella and Neri*, 2009, and reference therein). These circumferential dikes usually form at the periphery of a shallow magma chamber resulting from changes in magma pressure (*Gudmundsson*, 2006, and reference therein). Lateral propagation of dikes usually occurs when the magma reaches the level of neutral buoyancy with the host rock (*Morita et al.*, 2006; *Rubin and Pollard*, 1987)); in the case of the Rabaul caldera area this, could happen at the same depth of the Baining Mountain slab, explaining why the dike complex is laterally more spread at its deeper levels. The part representing the dikes swarm is thought to be composed by a combination of sub-vertical dikes and sub-horizontal, or inclined, sheets.

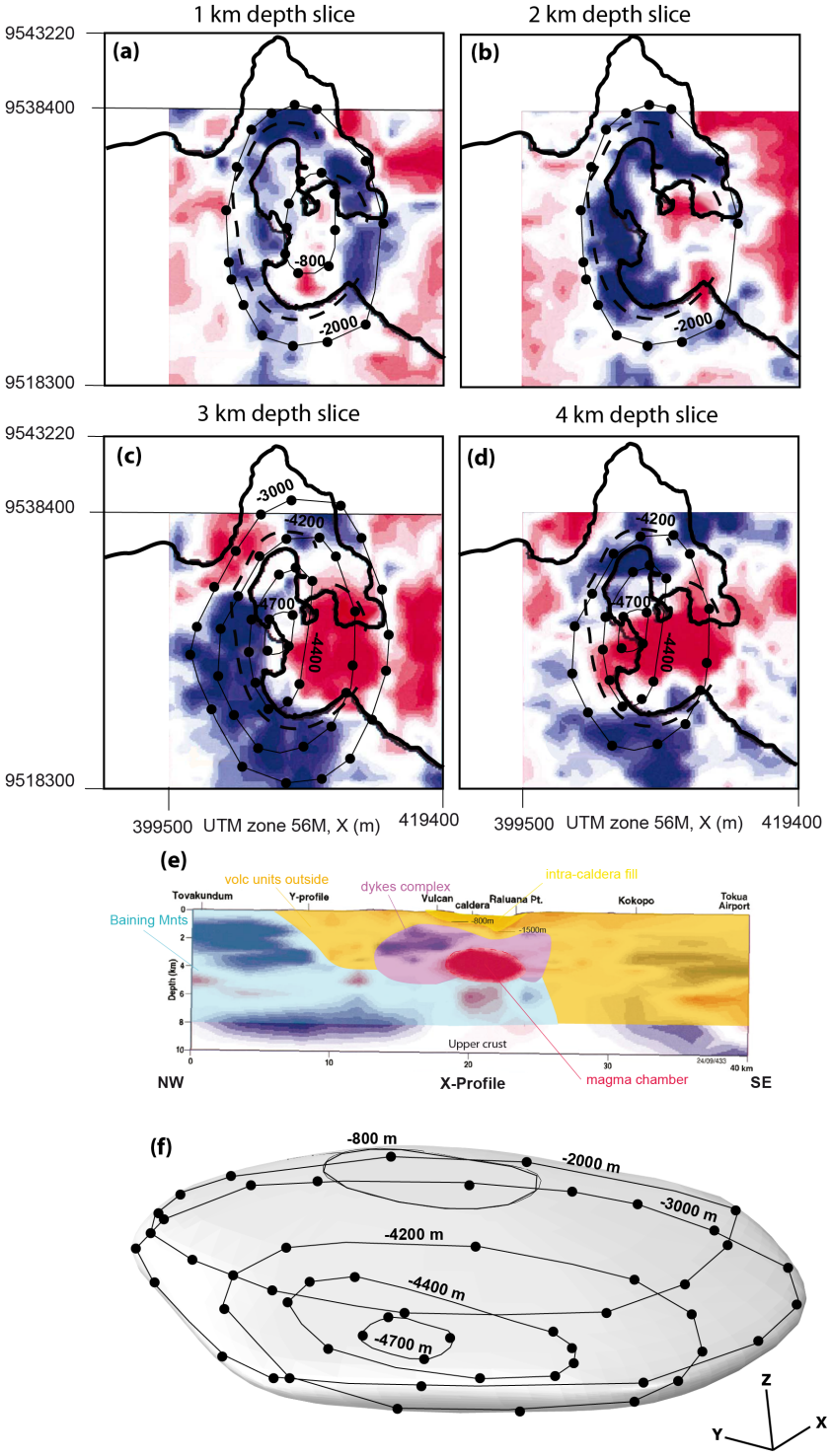

Figure 4.1.3. Construction of the dike complex block.
(a-d) splines and control points (black lines and filled dots, respectively) overlapped to the horizontal sections of the velocity contrast at -1000 m, -2000 m, -3000 m, and -4000 m, respectively (modified from Finlayson et al., 2003). Dashed lines mark the structural caldera border (from Heming, 1974). (e) X-profile of tomographic velocity contrast (modified from Finlayson et al., 2003. See Fig. 4.1.1 for colors reference) and conceptual subdivision into geological domains of different material properties. (f) View of the 3-D geometry of the dike complex. Contour points and splines used to build the geometry are overlapped for better understanding of the process construction of the lofted geometry. Note that this is not the final shape of the dike complex, but the volume before the subtraction of the magma chamber and the extra-caldera and infill deposits.

The coexistence and orientation of these extensional fractures injected from the magma chamber was first shown in formal terms by *Anderson* (1936) who calculated the orientation of the principal stress, s1, departing from the nucleus of strain (excess of pressure in the magma chamber) located in a homogenous, isotropic elastic half space. Since the dikes and sheets are mostly extensional features, they follow the trajectories of the maximum principal compressive tress, s1 (*Gudmundsson*, 2002, 2006) helping the movement of magma, fluids, and the emplacements of dikes and sheets along the s1 trajectories (Fig. 4.1.4, a). An overpressure exceeding the lithostatic pressure tends to generate a stress field compatible with sheet dikes at a magma chamber depth of buoyancy and vertical cone dikes above the magma chamber towards the surface. In addition, at calderas, circumferential dikes of arcuate patterns concentric to the caldera may also be facilitated and associated with the pre-existing faults or fractures (*Acocella and Neri*, 2009). All these aspects support the theory of the existence of swarms of mafic dikes in the area, with a wider lateral spread at deeper levels (due to the neutral buoyancy) and a "U" shape due to the influence of the trajectories of the principal compressive stress above the magma chamber and the pre-existing faults or fractures. The complex of mafic dikes swarm, which is here treated as a single volume of homogeneous material properties, can thus have been formed in several steps, during both pre-cauldron and post-cauldron stages (*Geshi*, 2005), consistent with the multiple caldera stages/events of the area.

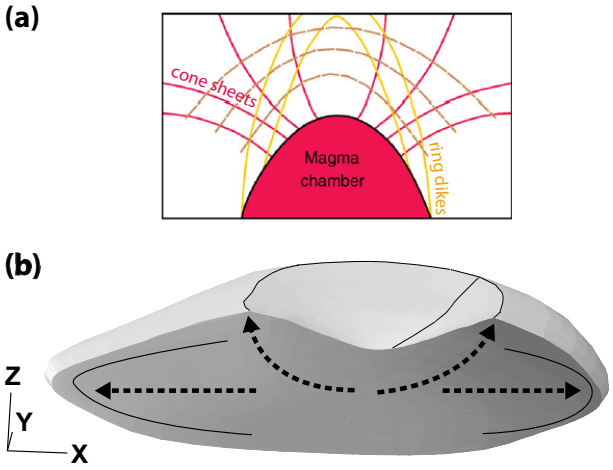

Figure 4.1.4. Distribution of stresses and dikes swarm part around the magma chamber. *(a) Model for the formation of inclined (cone) circumferential sheet dikes (red solid lines) and ring dikes (yellow solid lines) (modified from Gudmundsson, 2006; after Anderson, 1936). When the pressure source exceeds the lithostatic pressure, the dashed brown lines represent the trajectories of s3 and the orthogonal solid red lines the trajectories of s1 followed by the cone sheets. (b) W-E section (at UTMy=9.526e+06) of the final dikes swarm part (after its top boudary is shaped by removing the infill block through boolean operation). Dashed arrows indicate the possible spreading directions of inclined circumferential dikes.*

In the Rabaul model, the swarm of mafic dikes is conceptually interpreted and built as a unique block. There is no evidence of dike injection at the surface, so the only support to choose the control points to build this complex part is the tomography. Fig. 4.1.3,f shows the control points chosen to build the splines and loft the solid following the method proposed in methods section of this work (Chapter 3.3). At 1 km depth (Fig. 4.1.3, a) the dike complex already reaches a lateral extension similar to the one it has at 2 km depth. Thus, in order to generate a smooth shape, the shallowest spline was generated picking reference points at -800 m. The vertical extension of the dike complex is deduced by the vertical high velocity contrast at the Profile-X (from *Finlayson*

et al., 2003); from a depth of -800 m to a depth of -5000 m. From north to south the dike complex extends from Tovanumbatir cone to almost Mount Varzin. In the western side the high velocity signal is strong and wide, while in the eastern part of the caldera it is masked and interrupted by the presence ofa low velocity signal at 3 and 4 km depth. In order to give continuity and a smooth shape to the dikes body at these depths, the shape of the splines in the eastern side is extrapolated. Therefore, the dike complex part will embed the low velocity zones. This allows us to generate a single 3-D smooth body (Fig. 4.1.3, f) that enormously facilitates the application of further Boolean operations to remove from it the volume occupied by a possible magma chamber (low velocities at 3 and 4 km depth, Fig. 4.1.3, c-d) and the volume occupied by the extra-caldera deposits and the infill caldera sediments in the upper part (Fig. 4.1.3, e).

Based on Vp velocity of 6100 m/s, derived from the tomography (*Finlayson et al.*, 2003), and a density ρ of 2800 kg/m^3 consistent with a diorite (*Christensen*, 1996), the Vs, 3322 m/s, was computed from (*Brocher*, 2005, eq. 8) for the dike complex. Successively, we estimated the dynamic elastic properties: the Poisson's ratio of 0.29 (*Christensen*, 1996, eq.1) and the Young's modulus of 85.53 GPa (elastic formula) were calculated. For this unit, the static Young's modulus, 56.45 GPa, was computed from the dynamic one using the general formula proposed by *Morales and Marcinew* (1993); the value found is very close to the lowest value proposed by *Turcotte and Schubert* (2002) for a diorite and is thus acceptable. The static Poisson's ratio was assumed to be equal to the dynamic Poisson's ratio due to the natural low porosity of the diorite; the value found is in the range of literature values (*Turcotte and Schubert*, 2002; *Gercek*, 2007).

Baining Mountains Complex

Another high Vp region occurs west of Rabaul caldera, from the surface down to 5-6 km depth, and represents the Baining Mountains range (*Finlayson et al.*, 2003), which is made up of tertiary volcanoclastic sequences, volcanic sediments, and limestones all intruded by leucogabbros, adamellites, and granites. This range can possibly extend as a slab interfingered with unconsolidated sediments under the Rabaul Caldera, making part of the caldera basement (*Heming*, 1974; *Madsen and Lindley*, 1994; *Finlayson et al.*, 2003). Some gabbro xenolites from the Varzin area resemble the leucogabbro from Baining Mountains (described by *Macnab*, 1970) and provide some evidence of the nature of basement and the extension of Baining Mountains slab beneath Rabaul (*Heming*, 1974). The tomographic profiles show a slab with a variable dipping angle of 5°. In the proximity of Rabaul caldera, the Baining Mountains are mainly represented by limestone, as can be deduced from the presence of Rembar Range limestone about 20 km west of the caldera (*Heming*, 1974; *Nairn et al.*, 1995) and limestone about 20 km north-west of the caldera, in Watom island (*Heming*, 1974) (Fig. 2.2.1). The shallow heterogeneous distribution of sandstone, lithic tuff, breccias, volcanics from the Nengmutka caldera, and minor limestone, that are found at about 20 km south of the caldera have been also included in this part. Therefore, due to this oversimplification of the model, the chosen material properties in these areas may not be representative of the real materials. Nevertheless, since hard materials are still found south-east of the Rabaul caldera at depth of (in profile X, see Fig. 4.1.3), and can be thus interpreted as a prolongation of the slab towards the St.George channel, this oversimplification is restricted to the upper deposits. Furthermore, this area is further away from the 20 km radius where the deformation (both Ur and Uz) tends to zero and thus is not an area of interest.

Control points for the shallow splines were chosen on the basis of the geologic map (*Heming*, 1974), following the maximum extension of the pyroclastic Rabaul units. The control points for the

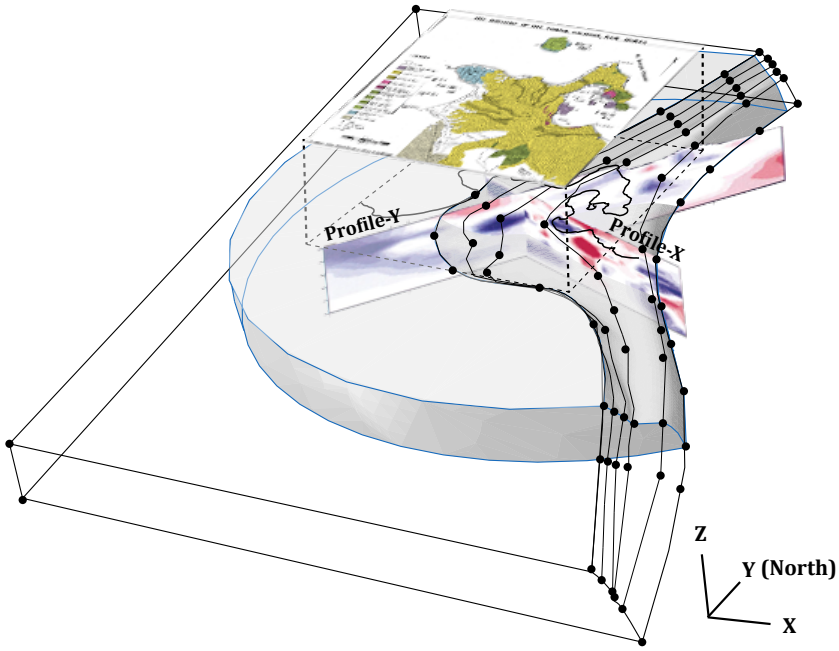

Figure 4.1.5. Baining Mountains block construction.
The black box and contours represent the shape of the part after lofting the body through the chosen control points (black dots). The blue edges and the shaded volume represent the final shape of Baining Mts. block after the cut with a hemispherical mold to adapt it to the hemispherical domain. Two profiles of tomographic velocity contrast (Finlayson et al., 2003) and the geologic map compiled by Heming (1974) used to choose the control points are also plotted for reference.

deeper splines were chosen in order to generate a smooth slab that starts from the superficial spline and deepens towards the caldera, following the high velocity contrast areas recorded in the Profiles -X and -Y (*Finlayson et al.*, 2003) that dip toward the north-east and south-east, respectively.

Gardner's rule (*Gardner et al.*, 1974), derived for sedimentary rocks and valid for Vp between 1500 and 6100 m/sec, was used to calculate the density from Vp 2627 kg/m^3, is in agreement with the value range of limestone *Turcotte and Schubert* (2002). Vs was computed from Vp (*Brocher*, 2005, eq.6) and the dynamic Poisson's ratio was computed from the velocities (*Christensen*, 1996, eq.1). The resulting Poisson's ratio is 0.28, in agreement with values of limestone and sandstone *Turcotte and Schubert* (2002). The corresponding dynamic Young modulus is 54.98 GPa. The static Young's modulus, 47.86 GPa, computed using the correlation proposed by Eissa and Kazi (1989, Eq. 7) is a good compromise to represent a material of which Young's modulus is an average of limestone and granite moduli *Turcotte and Schubert* (2002).

Extra-caldera sediments

The sediment and rock units outside the caldera are prevalently non-welded tuff (*Heming*, 1974; *Heming and Carmichael*, 1973; *Nairn et al.*, 1995). The geometry of this volume was mainly inferred from the geologic map (*Heming*, 1974) and tomographic sections (*Finlayson et al.*, 2003) (Fig. 2.2.2, a). It represents the indifferenciate Rabaul rocks mapped by Lindley (1988).

This part of the 3-D Rabaul model was built by using the Abaqus Boolean operation that allows the subtraction of the previous parts and the magma chamber from an extended plate with thickness of 8 km. The western side of the Extra-caldera deposits part is therefore complementary of the Baining Mountain eastern side.

Elastic properties for the extra caldera sediments, mainly non-welded tuff (*Heming*, 1974;

Heming and Carmichael, 1973; *Nairn et al.*, 1995), were calculated knowing the Vp velocity 2375 m/sec from the tomography (*Finlayson et al.*, 2003), which is in agreement with Vp range values of non-welded ignimbrite found by Rodríguez-Losada et al. (2009). The density value of 2052 kg/m^3 was estimated from the Vp velocity using the Eq.1 of Brocher (2005). The Vs, 882 m/s, is computed from Vp using the "Brocher's regression fit," Eq.6 of Brocher (2005). The Poisson ratio for extra-caldera deposits was assumed to be 0.28, a value already proposed for non-welded tuff by other authors (*Shultz and Li*, 1995; *Rodriguez-Losada et al.*, 2009) and for pyroclastic deposits (*Apuani et al.*, 2005). The estimated dynamic Young's modulus, 4.08 Gpa, using the elastic theory formulas is in agreement with the Young's modulus of massive non-welded tuff (*Price and Jones*, 1982; *Rodriguez-Losada et al.*, 2009) and therefore was taken as representative of the static Young's modulus.

Rabaul magma chamber and magma bulk modulus, β

At Rabaul caldera, seismic hypocentral locations define an ellipsoidal volume with horizontal major and minor axes of 10 and 5 km, respectively (Fig. 2.2.1 and Fig. 2.2.2). This volume is interpreted as bounded by ring faults overlying a central region of low seismicity at depths between 2-4 km that is deduced to represent the present-day magma chamber (*Mori et al.*, 1989; *Lipman*, 1997). The Rabaul reservoir cavity was first determined from tomographic slices (Fig. 4.1.6, a). A region of magma accumulation under Blanche Bay was deduced from anomalously low P-velocity (Vp) distribution shown by the tomographic data (*Finlayson et al.*, 2003). With the help of tomographic slices (*Finlayson et al.*, 2003) and distribution of earthquake focuses (*Mori and McKee*, 1987a; *Jones and Stewart*, 1997; *Saunders*, 2001), we inferred the size and shape of the magma chamber. The outward-dipping ring fault structure overlying the central region of low seismicity is outlined by the location of the earthquake focuses of the above mentioned studies. Jones and Stewart (1997) recognized two elliptical faults at different depths: an outer elliptical fault, which embraces a smaller inner elliptical fault in its northern end (Fig. 4.1.6, a). As faults cannot propagate in molten rocks, we assumed that the magma chamber should be enclosed into the ring fault structure with a narrower and shallower intrusion below the northern end of the outer ring fault, south of Matupit Island. This ring-fault complexity reflects the complex shape of the magma chamber and also defines the extension of the shallow magma body.

Due to the feasibility of making an arbitrary 3-D shape in Abaqus, we simulate the pressure source as a distributed load pressure in a single 3-D reservoir having a complex shape with variable roof depth. We outline closed contours around the low velocity zone of the tomographic slices at 2, 3, and 4 km depth of the tomography of *Finlayson et al.* (2003) and pick some control points (cPt) (Fig. 4.1.6, a and b). Then, we use the Python script to import the control points and to generate a spline curve for each relevant contour of the magma chamber in CAE. Finally, we loft a solid through the sections defined by the splines in CAE. In order to create the smooth solid part representing the magma chamber (Fig. 4.1.6, b), the splines curves are sequentially lofted from the bottom (contour 4500 m below the sea level) to the uppermost spline. The modeled magma chamber has a volume of 32x10^9 m^3, in agreement with the volume calculated by *Finlayson et al.* (2003) and has a roof with variable depth: 1900 m under Greet Harbour, in good agreement both with the depth of 1800 m previously estimated from leveling and gravity data (*McKee et al.*, 1989) and with the depth of 2000 m estimated from tilt data (*McKee et al.*, 1985), and 3000 m under Vulcan in agreement with tilt measurements (*McKee et al.*, 1985) and with the low velocity zone shown in the X-profile of the tomography of *Finlayson et al.* (2003). The magma chamber bottom reaches its maximum depth of

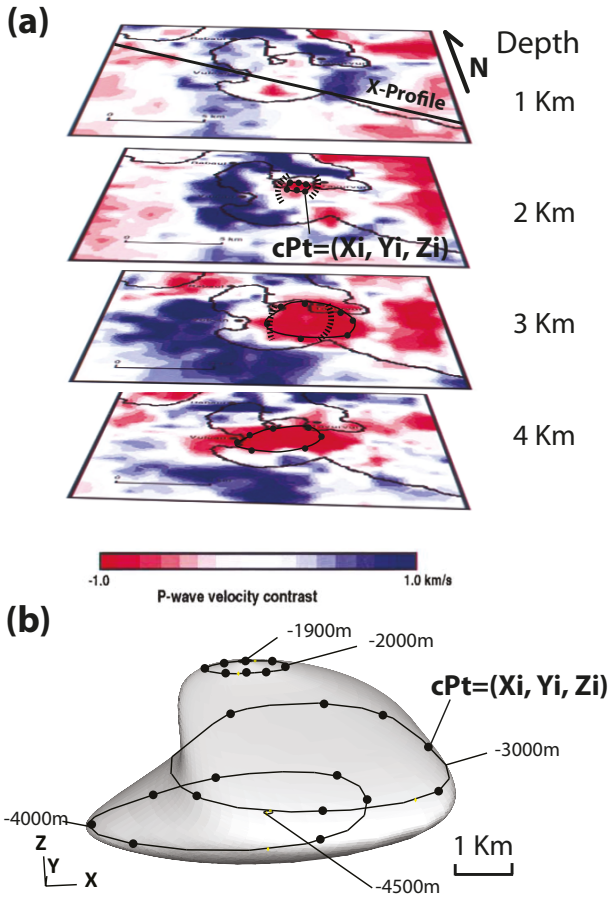

Figure 4.1.6. Magma chamber construction modified from Ronchin et al. (2013). *(a) Slices at 1, 2, 3, and 4 km depths under the central Rabaul caldera adapted from Finlayson et al. (2003). Solid lines are the contours used as reference for the magma chamber's closed splines. Control points coordinates, cPt=(Xi,Yi,Zi), are chosen along these contours. Dashed lines on the slices at 2 km and 3 km represent the seismically active portions of the ring fault above 2 km and below 3 km, respectively. (b) Abaqus 3-D solid part representing the magma chamber with splines and control points superimposed for clarity. The geometry of the magma body is achieved by lofting the solid through five horizontal closed sections at different depths (closed splines). Depths refer to sea level. Points in figure are the control points used to create the closed splines.*

4500 m centrally under Blanche Bay.

Although the volume of the magma chamber generated by the first selection of control points along the limits of the low velocity tomographic contrast anomaly is in good agreement with the volume of 30 km^3 of the shallow magma chamber proposed by *Finlayson et al.* (2003), it is unrealistic and not probable because it intersects the epicenters of the seismic ring (Fig. 4.1.6, a) well defined by previous studies (*Mori and McKee*, 1987a; *Jones and Stewart*, 1997). Considering that no shears are possible in the fluid cavity and keeping in mind the caution recommended by *Gudmundsson et al.* (2004) about inferring the volume and shape of the large molten body interpreted from the tomographic images, new considerations should be made in order to ensure that a realistic magma chamber model is built considering both seismic and tomographic studies. In order to do so, we have decided to rescale the volume of the shallow magma chamber obtained from the tomography to a value inferred from the seismicity (Fig. 4.1.7, a). We first build an oblate ellipsoid inscribed in the seismic annulus (Fig. 4.1.7, b). Its volume resulted to be 9.6 km^3, in agreement with the values proposed by *Jones and Stewart* (1997) and *Patia* (2004). Therefore, the magma chamber

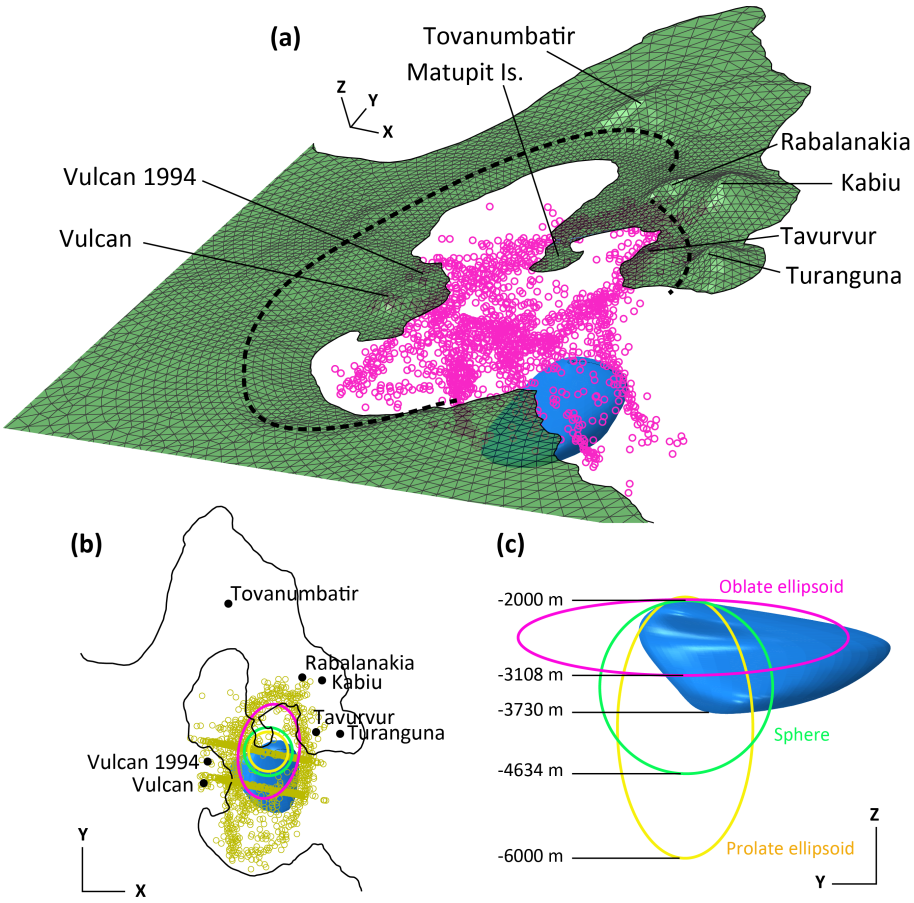

Figure 4.1.7. Magma chambers used in this work.
Y is the North direction, X is East direction, and Z up. (a) 3-D view of the Rabaul caldera topography, profiles, and horizontal projection of epicenters (pink circles) digitalized from Saunders (2001), and new size and position of the blob-shape magma chamber (blue shape) rescaled from the one inferred from the tomographic contrast of Finlayson et al. (2003). The dashed line represents the border of the caldera. (b) Plain view of the epicenters (yellow circles), the blob-shape magma chamber, and the regular-shape corresponding (same volume of about 9.5 km^3) magma chambers (oblate ellipsoid-pink, sphere-green, prolate ellipsoid-yellow). (c) Vertical view of the magma chambers used in this work (in scale).

part is rescaled of a value of 0.6678 to reach a volume equivalent to the one of the oblate ellipsoid (from 32.2 km^3 to 9.6 km^3). Finally, a clockwise rotation of 20° around a vertical axis adjusts the position of the complex volume to be surrounded by the epicenters of the annular shape seismicity. This way, the magma chamber is enclosed in the ring fault structure with its lowest tip almost under the Vulcan edifices and oriented toward the 1994 eruptive vent. It has to be noted that after resizing, the agreement of position and depths of the different part of the magma chamber with the literature mentioned above are still valid. Other two magma chambers with same volume but different shapes (a spherical and a prolate one) are built for further investigation of the effects of the magma chamber shape on the deformation field (Fig. 4.1.7, b and c). All geometric information as well as construction information about the magma chambers are summarized in Tab. 4.1.2.

The phenocryst content of Rabaul 2006 products (but also of 1994, 1937, and 1878) ranges from 5-15 vol% for the pumice and 15-40 vol% for the lavas; crystals include plagioclase, clino- and ortho-pyroxene (Caroline Bouvet de Maisonneuve, personal comm.). An average of mass crystals of 0.2 is considered representative of the Rabaul magma. As the density of the crystals depends

Type of chamber (not in scale)	Information
	**Geometry** Volume: 32.2 E+09 m^3
	Notes Position: 410.48558082E+03,9.53078511649E+06,-1.9E+03 (western upper node) Shape and volume inferred from the tomography (Finlayson et al., 2003) Sat file name: BLOBFY.sat
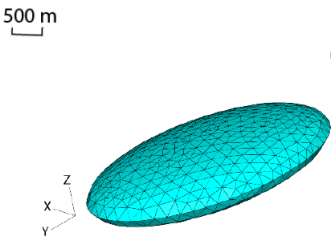	**Geometry** Volume: 9.61 E+09 m^3 SEMI-Axis a (y-direction+ clockwise rotation: 10°): 2.564805595E+03 SEMI-Axis b (x-direction clockwise rotation: 10°): 1.614577822E+03 SEMI-Axis c (z-direction): 0.554291087E+03 Volume centroid: 410293.13,9.53e+006,-2.55e+003 Top chamber: 410.287E+03,9.53009E+06,-2.E+03 m Bottom chamber: 410.287E+03,9.53009E+06,-3.108E+03 m
	Notes Volume generated with Rhyno () Shape and volume inferred from the seismicity constraints Sat file name: OBellip-350_0_91.sat
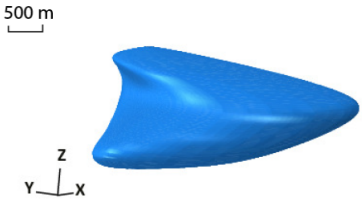	**Geometry** Volume: 9.60 E+09 m^3 Volume centroid: 410369.09,9.53e+006,-2.90e+003 Top chamber: 410.287E+03,9.53009E+06,-4.E+03 m (wester upper node) Bottom chamber: 410.287E+03,9.53009E+06,-3.727E+03 m
	Notes Scaled from the BLOBFY.sat of a factor 0.6678 and rotated around Z-axis of 20° Sat file name: BLOBFY-0_6678.sat
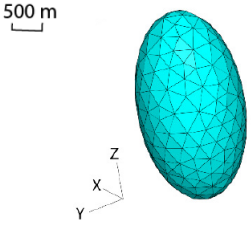	**Geometry** Volume: 9.56 E+09 m^3 SEMI-Axis a (z-direction): 2.0 E+03 m SEMI-Axis b=c (x and y-direction): 1.0686 E+03 m Volume centroid: 410287.00,9.53e+006,-4.00e+003 Top chamber: 410.287E+03,9.53009E+06,-2.E+03 m Bottom chamber: 410.287E+03,9.53009E+06,-6.E+03 m
	Notes Sat file name: PROellip-a2000bc1068_6.sat
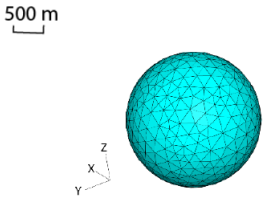	**Geometry** Volume: 9.56 E+09 m^3 Radius: 1.3168 E+03 m Volume centroid: 410287.00,9.53e+006,-3.32e+003 Top chamber: 410.287E+03,9.53009E+06,-2.E+03 m Bottom chamber: 410.287E+03,9.53009E+06,-4.364E+03 m
	Notes Sat file name: SPH-r1316_8.sat

Table 4.1.2. Shapes, volumes, and other aspects of the magma chambers used in this work.

on the mineral precipitated, and plagioclase is the most dominant one for Rabaul products (15-20% from *Cunningham et al.*, 2009), we can estimate an average density value of 2800 kg/m^3 for the crystals. The density of the andesitic melt, 2480 kg/m^3, was estimated using the Density-Temperature-Pressure graph for dry andesitic melts (*Malfait et al.*, 2014).

From tomographic studies the shallow magma chamber is located between 2 and 5 km depth (*Finlayson et al.*, 2003, see Fig. 2.2.2). The shallow magma at Rabaul is found to be under relatively dry conditions (~3 wt% H2O) and at a temperature of 950°C (*Bouvet de Maisonneuve et al.*, 2014) The pressure in the depths range 2-5 km is calculated considering the above column of materials.

At depth of 2 km this is composed of ~900 m caldera infill, ~500 extra-caldera sediments, and ~600 m of dike swarms complex. At greater depth the column has the corresponding additional dike thickness. Using the formulas discussed in section 3.4.5 and all parameters summarized in Tab. 4.1.3, we calculate for reservoir depth of 3.5 km (±1.5 km) an average magma density of 2370.37 kg/m^3 and an average bulk modulus of 4.50x10^9 Pa (Tab. 4.1.4).

Parameter	Value	Description
ρ_c	2800	[kg/m^3], crystals density
ρ_r	1900	[kg/m^3], density caldera infill
	2052	[kg/m^3], density extra caldera deposits
	2936	[kg/m^3], density dike swarm
ρ_m	2480	[kg/m^3], melt density (Malfait et al., 2014)
x	0.2	crystal mass fraction of partially crystalized magma
T	1223.15	[°K], temperature of magma equivalent to 950°C
g	9.8	[m/s^2], gravity acceleration
N	0.03	wt% mass fraction of volatiles (water)
H	2000-5000	[m], depth
p	0.19-11.64x10^7	[Pa], lithostatic pressure (p=g·H·$\rho_{rock\ column}$)
E_r	56.45x10^9	[Pa], Young's modulus of host rocks (Dike swarm)
υ	0.28	Poisson modulus of host rocks (Dike swarm)
β_r	8.28x10^9	[Pa], Bulk modulus of the host rocks β_r=E_r/3(1-2υ)
s	4x10^{-6}	[Pa$^{-1/2}$]
R	462	[J K^{-1}kg^{-1}], gas constant

Table 4.1.3. Values of parameters used to calculate the bulk modulus of Rabaul magma.

Depth [m]	Pressure [Pa]	Density [kg/m^3]	Bulk modulus [Pa]
2000	4.41 x10^7	1988.83	1.93 x10^8
3000	7.28 x10^7	2416.64	1.23 x10^9
4000	1.02 x10^8	2538.01	8.28 x10^9
5000	1.30 x10^8	2538.01	8.28 x10^9
	Mean ρ and β	**2370.37**	**4.50 x10^9**

Table 4.1.4. Values of lithostatic pressure calculated at different depths under the Rabaul caldera considering the above column of materials (caldera Infill, extra-caldera deposits, and dike swarm). Magma density and bulk modulus computed at different depths and their mean values.

4.2 Results of the Rabaul 3-D forward models

One of the purposes of the following models is to investigate how the material properties affect the deformation field. The other purpose is to quantify the contribution of the material properties to the signal to see if it is significant for the data (InSAR). With these models we want to investigate the sensitivity of the three-dimensional variations in elastic moduli and of topography on surface displacements.

4.2.1 Assembling the parts in a 3-D model with topography

Once we have all the parts needed (one for each geologic region), we can assemble the model was in the CAE Assembly module (Fig. 4.2.1). With the use of boolean operations, two or more solids can be combined. Solid combination by boolean operators provides great flexibility to create a variety of shapes. First, all parts are reshaped using boolean operations in order to fit the neighbor part surfaces. The advantage of using boolean operations is that they allow us to obtain new objects whose surfaces are precisely coincident with the adjoining parts, avoiding the formation of unwanted gaps between the blocks in the model. With this strategy we model the final shape of the Baining Mountais block by removing from it the parts overlapping the Dikes swarm block (Fig. 4.2.1, a). The Dike complex block is modelled by removing from its top a volume corresponding to an Infill block volume (Fig. 4.2.1, c) shifted of 500 m; this way, the Infill block and the Dike block are not in contact but separated by a volume filled by the material of the Extra caldera sediments which in this case represents the collapsed caldera roof (Fig. 4.2.1, a). The Extra caldera sediments block is modelled by removing the previous blocks (i.e. Baining Mountain block, Infill block, and Dike complex block) from a rectangular parallelepiped of 8 km height. The resulting parts were then joined and stacked together from the upper crust parts to the mantle part forming a pile. The cavity for the magma chamber is created by subtracting the magma chamber solid (Fig. 4.2.1, b) from the pile, while the far field is shaped as a hemisphere by building a mold as a separate object and using it, through boolean operation cutting tools, to remove any exceeding volumes (outside of the wanted far field boundaries) of the piled layers (Fig. 4.2.1, d).

Once the desired internal structure of the problem domain is built, the next step is to refine the geometry of the top of the problem domain in order to be more representative of the real land surface and sea floor. We used the Pinned Mesh Perturbation (PMP) method described by Masterlark et al. (2012) to generate the complex geometry of topographic and bathymetric relief of the stress-free surface. The terrain relief describing the geometry of the Earth's surface for both onshore and offshore regions of the model domain is compiled from three types of data having different resolution: the 90 m resolution SRTM data from the EROS-USGS website, the relatively coarse resolution (1-minute) gridded bathymetry data available from the GEBCO project website, and bathymetric data of Blanche Bay (RVO data from HMAS 'Flinders' survey, 1995). In order to avoid excessive element distortion during the perturbation of the mesh, we refine the mesh, reducing the size of the elements for areas having steep slopes, and smooth the displacements applied to the free surface nodes through a spatial filter that uses a modified Gaussian function (Fig. 4.2.2), which preserves the displacements in the central area of the free surface domain and reduces the applied displacements to zero along the border of the free surface. This way, the free surface is faithfully adapted to the topography in the area of interest while avoiding large distortion due to the oceanic trench present in the areas far from the caldera center.

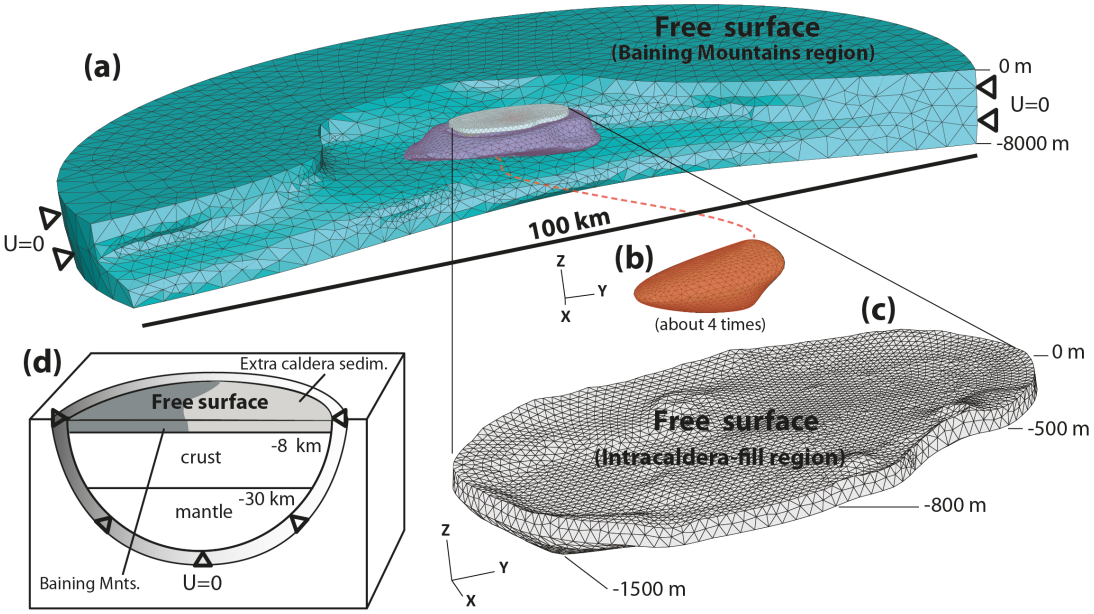

Figure 4.2.1. Assembling the 3-D Rabaul caldera model.
Spatial distribution of blocks in the 3-D model assembly modified from Ronchin et al. (2013). (a-b-c) Parts of the upper eight km. Color blocks indicate different material properties resumed in Tab. 4.1.1. (a) Baining Mountains block (sky blue), dikes complex block (violet), and intra-caldera fill block (light gray). Extra-caldera deposits block has been ignored to permit the visualization of inner parts. (b) Magma chamber magnified about four times for clarity. (c) Magnification of intra-caldera fill block. (d) General scheme of piling the parts and cutting the pile to generate the hemispheric shape of the far field model domain. The pinned boundary conditions applied to the far field are represented by triangles.

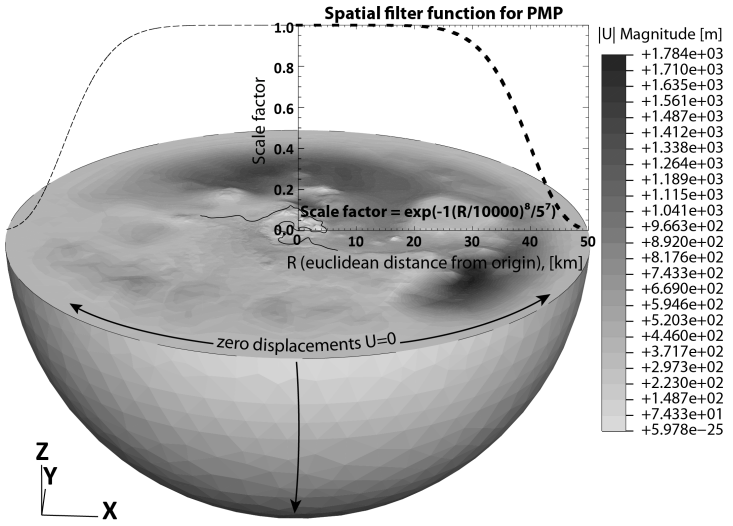

Figure 4.2.2. Topography of the 3-D Rabaul caldera model.
Filter used to control distortion of the elements while applying the PMP to the free surface nodes in order to add the topography to the FEM. The FEM topography resembles the real topography at the center of the free surface and presents a smooth transition to zero towards the boundaries of the free surface accordingly to the filter used.

4.2.2 Boundary conditions and mesh validation

Because we are treating the deformation induced by the pressure source as elastic deformations, we test the validity of the FEM configuration to ensure it is a correct representation of the elastic

deformation. This validation allows us to isolate the sensitivities of the predictions to the distribution of material properties, rather than some other artifact of the FEM configuration.

To perform the validation, we construct a modified version of the FEM that has uniform material properties following the approach of other authors (e.g. *Masterlark and Hughes*, 2008; *Pascal et al.*, 2014). The model domain configuration and properties are summarized in Tab. 4.2.1. The three-dimensional model domain approximates a solid hemisphere centered on the caldera and having a radius of 50 km. The outer surface of the hemisphere represents the far-field and depth extent of the domain. The far-field nodes are constrained to be pinned (zero displacements in all directions). The Uz component of the deformation field decays to 2.5% of its maximum values within 10 km, while the Ur component decays to 4% of its maximum values within 25 km. As a rule of thumb, the domain size must be at least twice the deformation field extent in order to obtain accurate numerical solution (*Currenti et al.*, 2008). We can thus say that the far-field boundary located at 50 km from the source of deformation ensures a domain to be big enough to avoid numerical artefacts in the solution due to the finite boundary conditions.

The top of the domain is represented by a flat free surface which is centered on top of the source of deformation and has mesh resolution decreasing with increasing distance from its center.

The source of deformation is simulated as a pressurized spherical cavity. The McTigue analytical model is the model taken as reference to test the validity of the mesh. McTigue is the appropriate analytical model because, due to the high ratio of the cavity radius to the source depth ($r_s/C_{0(z)} = 0.25$), the source cannot be analytically approximated to a point source and the FEM solution needs to be compared with an analytical model that simulates a finite-size cavity.

Because the models will be used to simulate a subduction of the Rabaul caldera, the model for the validation of the mesh also simulates a deflation through a depressurization of the spherical cavity (see Tab. 4.2.1). The pressure value is roughly calibrated with the InSAR data in order to simulate displacements in the order of magnitude of the observed displacements. The deformation parameters used in the validation process are: Uz, Ur, and Ulos. The maximum Ulos observed values and maximum values for the three parameters of deformation simulated by the McTigue model are summarized in Tab. 4.2.1.

As the William and Wadge (2000) misfit does not take into account the scale of the values being compared, during the validation process we need to take into consideration the accuracy of the data to be simulated in order to bring the validation process to a realistic point of view. We want to be sure that, within the detection limits of the data, the FEM and the analytical models predict the same deformation. As discussed in the previous section, the InSAR data used in this work have accuracy of about 1 cm. In order to perform the validation analysis we track and plot all the Uz discrepancy values > 0.01 m. This is the general accuracy limit of continuous GPS and InSAR data (Fernandez et al., 1999).

The nodes used as benchmarks to calculate the misfit between the models are chosen from the free-surface nodes at a distance smaller than 20 km. This allows to include in the calculation areas corresponding to the Rabaul caldera, but also the area west to the caldera, toward the Baining Mountains where a long wave Ulos signal is observed.

Aspect		**Specification**			
Domain space origin		x=0 at UTM zone 56M Easting 409121 m, y=0 at UTM zone 56M Northing 9530090 m, z=0 at mean sea level			
Center of cavity, $\mathbf{C_{0(x,y,z)}}$		[410287 E, 9530090 N, -3316] m			
Radius of cavity (r_s)		1316 m			
Analysis type		Elastic			
Maximum domain depth		50 km			
Maximum domain radius		50 km			
E (Young's modulus)		0.1 GPa			
υ (Poisson's ratio)		0.25			
ΔP		-0.0975 MPa			
Far-field boundary conditions		Zero displacements, pinned			
Top of model domain		Flat free surface (zero traction)			
L (line-of-sight, LOS), [east, north, up]		[-0.617, -0.131, 0.775] Max U_{LOS} displacement from InSAR data: -0.28 m			
Maximum Uz displacement (McTigue)*[1]	-0.403 m				
Maximum Ur displacement (McTigue)*[1]	0.152 m				
Maximum U_{LOS} displacement (McTigue)*[1]	-0.342 m				
Elements (1st order tetrahedra)*[2]			Misfit FEM-McTigue U_z	U_r	U_{LOS}
Mesh_1 (21 sec) 10 seeds for MC semi-circumference	73,081 infill dikes Fs-test*[3]	 2,641 24,612 657 (ΔUz_{MAX}: 0.031 m)	0.084	0.073	0.078
Mesh_2 (25 sec) 20 seeds for MC semi-circumference	81,031 infill dikes Fs-test*[3]	 3,529 29,439 781 (ΔUz_{MAX}: 0.025 m)	0.068	0.059	0.065
Mesh_3 (33.6 sec) 25 seeds for MC semi-circumference	118,352 infill dikes Fs-test*[3]	 11,338 47,126 1,219 (ΔUz_{MAX}: 0.021 m)	0.055	0.047	0.053
Mesh_4 (32 sec) 30 seeds for MC semi-circumference	109,962 infill dikes Fs-test*[3]	 9,415 47,252 1,656 (ΔUz_{MAX}: 0.018 m)	0.049	0.041	0.047
Mesh_5 (39 sec) 35 seeds for MC semi-circumference	127,684 infill dikes Fs-test*[3]	 9,415 56,447 1,959 (ΔUz_{MAX}: 0.017 m)	0.050	0.040	0.046
Mesh_6 (55 sec) 35 seeds for MC semi-circumference	170,465 infill dikes Fs-test*[3]	 18,611 56,800 4,242 (ΔUz_{MAX}: 0.016 m)	0.048	0.035	0.045

*[1] Analytical reference solution for the validation of the FEM model

*[2] Only the number of elements of the dike and infill caldera parts is provided. Due to the fact that these parts surround the magma chamber, the numbers of elements in which they are divided is sufficient to give an idea about the mesh refinement around the magma chamber.

*[3] Fs-test: free surface nodes tested during the validation analysis

Table 4.2.1. Configuration of the model for mesh validation and characteristics of the mesh tested. MC-magma chamber

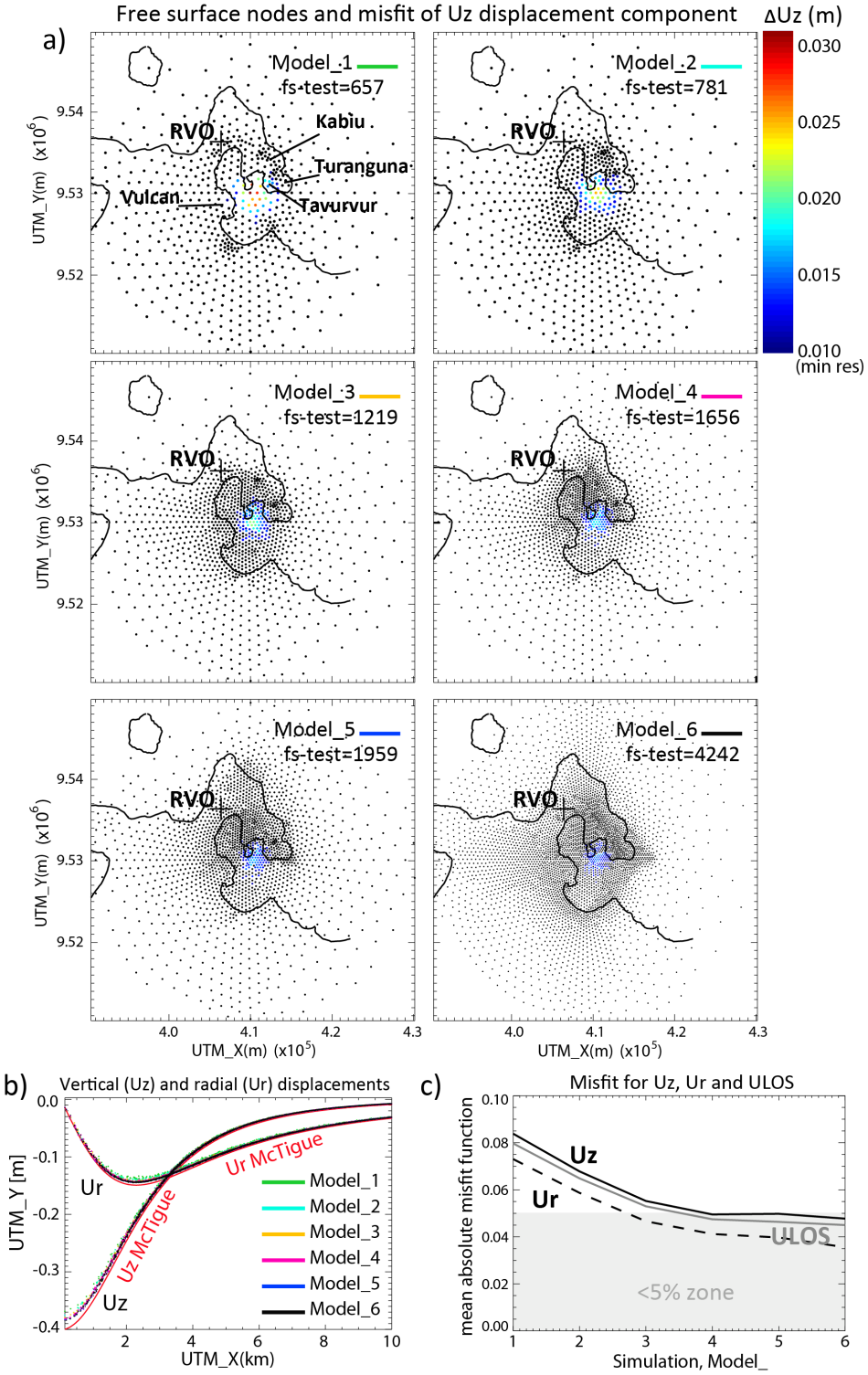

Figure 4.2.3. Benchmark nodes, their Uz and Ur displacements and misfit values for increasing mesh refinement.

(a) Free-surface nodes used for the mesh validation of six models with increasing mesh refinement. Where the discrepancies between the FEM and analytical model are bigger 0.01 m, they are plotted in color; the 0.01 m threshold is the minimum resolvable Uz value for continuous GPS and InSAR (Fernandez et al, 2009). Due to the increasing number of nodes on the free surface, the points size in the maps decreases within the panels to better see the nodes position. The base benchmark for leveling campaigns (RVO - point at the Rabaul Volcano Observatory) is pointed out with a cross. (b) Vertical and radial displacements of all models tested for validation. The reference McTigue analytical model is in red. (c) Uz, Ur, and Ulos normalized misfit computed using the Williams and Wadge (2000) misfit equations; this is the absolute mean misfit normalized by the mean component displacements. The gray area represents the misfit values below the threshold of 0.05 that represent the maximum misfit value for the acceptable models.

Local refinements of the mesh are performed by manually increasing the number of seeds along the parts' edges in order to subdivide the volumes in finer elements and approximate the FEM solution to the exact solution. Particular attention is given to the refinement of the volumes surrounding the spherical cavity, where the elements are subjected to higher deformations, and to the refinement of the free-surface areas of interest of Rabaul Caldera (Matupit Island, Vulcan, and Tavurvur). The discretization of the sphere tends to reduce the volume of contraction and thus the deformation at the surface (*Masterlark et al.*, 2012). Thus, a right discretization of the source is necessary in order to generate an accurate solution at the free surface. As general idea, the free-surface areas east of the caldera are less refined due to the fact that they represent the St.George channel where no InSAR or GPS signal are recorded, whereas the free-surface areas west of the caldera are more refined due to the interest of modeling their InSAR displacement signal.

The maps of nodal discrepancies of the vertical component (ΔUz), that is the component that shows the highest misfit, show the areas where the misfit is higher than the minimum resolvable displacements and guides the refinement of the mesh at the free surface (Fig. 4.2.3, a). For example, from the first maps it is clear that more nodes are needed at the free-surface in the area of Matupit and Tavurvur.

The refinement of the spherical source improves the solution by increasing the displacements of Uz and Ur (Fig. 4.2.3, b) towards the McTigue analytical solution till 30 seeds per half-circumference. Further mesh refinements do not seem to significantly improve the solution (see Molde_5, Fig. 4.2.3, a and b, and Tab. 4.2.1).

The misfit of all three parameters (Uz, Ur, and Ulos) is calculated and demonstrate that the FEM and the McTiguesolutions reach statistical agreement starting for Model_4 (Fig. 4.2.3, c) and no significant improvements are obtained when the mesh refinement is increased. For the Model_4, 5, and 6, the ratios Δ(Up)/M(Up) are less than 0.05 for all parameters (Tab. 4.2.1).

We performed a further refinement of the model (Model_6). This further refinement is applied to those areas around the caldera occupied by volcanic cones with higher topography (Vulcan, Kabiu, and Turagunan) in order to accommodate the stretching of the free-surface during the topography creation (Pinned Mesh Perturbation method, see *Masterlark et al.*, 2012). This avoids having deformed element with low quality near the surface.

The mesh used for the following investigations, the Model_6, has characteristic length of the element edges at the free surface of about 200-300 m above the source, where a higher displacement gradient is expected, and gradually increasing of characteristic length up to about 7000 m near the far-field boundary, where the lower displacement gradient is expected and nodes at the boundary are pinned.

4.2.3 Results of 3-D Rabaul Abaqus models

Here we present the results of the study of the effects of material properties, chamber shape, topography on the deformation signal components Uz, Ur, and Ulos of Rabaul area. The deformation signals are observed over the entire area and along two representative profiles, North-South and West-East (Tab. 4.2.2), that pass over the maximum extension of the upper pats (caldera fill and dikes swarm) and the maximum extension of the long-length wave deformation, respectively. This is to better catch the displacements over areas where the presence of shallower bodies is more extended and were the long-length wave deformation signal that we want to simulate is recorded.

Extension of study area and study profiles (UTM zone 56M)			
Area		xmin= Easting 394860 m xMAX= Easting 417860 m ymin= Northing 9520893 m yMAX= Northing 9543890 m	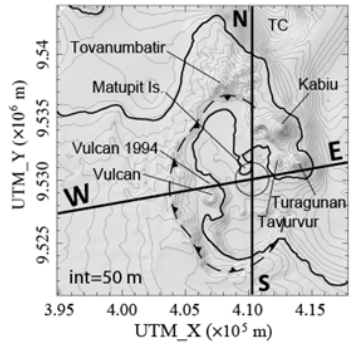
W-E profile	Western pt. Eastern pt.	xW= Easting 394860 m yW= Northing 9527360 m xE= Easting 417860 m yE= Northing 9531430 m	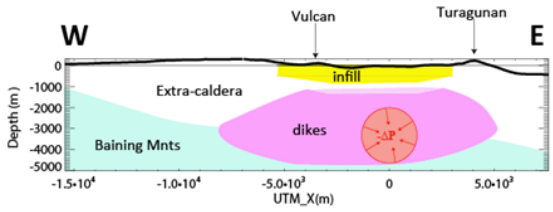
N-S profile	Northern pt. Southern pt.	xN= Easting 410287 m yN= Northing 9543890 m xS= Easting 410287 m yS= Northing 9520893 m	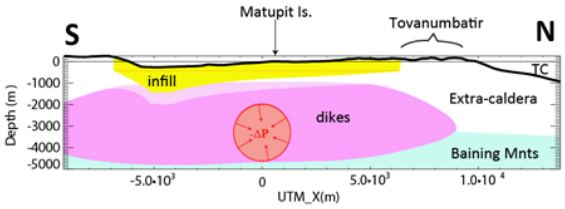

Table 4.2.2. Area and profiles of deformation field study.
The left column provides the location of the area and profiles of this study. The right column provides the topographic features of the area of study and material heterogeneities along the study profiles.

In the studies of the effects of the 3-D elastic heterogeneities due to the geologic bodies built in the previous section, the solutions of heterogeneous models are compared to the homogeneous (HOM) model, whose first 8 km are totally represented by the elastic properties of the extra-caldera sediments. A summary of the models used in this part is provided in Tab. 4.2.3. The values of the elastic properties, derived from the seismic Vp velocities and adapted to static elastic property values, are summarized in Tab. 4.1.1. Because the PMP add the topography by perturbing the existing mesh, we can use the same mesh for all models and generate the different distributions of material properties by substituting material values of the blocks of the existing mesh. This way the comparison of deformation at the free surface nodes (at the same position for all models) is straightforward without need of interpolations. This way we avoid the uncertainties introduced by the interpolation.

In the case of the study of the source shape effects, the models need to be re-meshed due to a change of source geometry. Due to a change of mesh, the position of nodes at the free surface is different for each model. In order to compare the solutions at the free surface, an interpolation is required. We therefore will also provide a test of the interpolation method used in order to quantify the uncertainties introduced by the interpolation.

	Active Part								Topo
	Exc	Inf (E, x10⁹)			Inf (υ)			Ds	Bmt	
Model name		**0.2**	**0.05**	**5.**	**0.15**	**0.25**	**0.47**			
RF_HOMO	X									
RT_HOMO	X									X
Changing Poisson's ratio, υ										
RF_inf_E02_ni015	X	X			X					
RF_inf_E02_ni025	X	X				X				
RF_inf_E02_ni047	X	X					X			
RT_inf_E02_ni015	X	X			X					X
RT_inf_E02_ni025	X	X				X				X
RT_inf_E02_ni047	X	X					X			X
Changing Young modulus, E										
RF_inf_E005_ni015	X		X		X					
RF_inf_E5_ni015	X			X	X					
RT_inf_E005_ni015	X		X		X					X
RT_inf_E5_ni015	X			X	X					X
Single part active										
RT_inf_E02_ni015	X	X			X					X
RT_exc_Ds	X							X		X
RT_exc_Bmt	X								X	X
Combination of parts active										
RT_exc_inf_Ds	X	X			X			X		X
RT_exc_inf_Bmt	X	X			X				X	X
RT_exc_inf_Ds_Bmt	X	X			X			X	X	X

Table 4.2.3. Summary of the models

Summary of the models and the active parts that characterize the shallower 8 km of each model. Exc – extra caldera deposits, Inf – Caldera infill, Ds – Dike swarms, Bmt – Baining Mountains complex, Topo – topography.

Preliminary study of the topographic effects on surface deformation related to changes in material properties

A preliminary study of the average of the effects of the topography among all models listed in Tab. 4.2.3 provides a general idea about the importance of taking into account the topography for Rabaul models. The MAPD (Mean Absolute Percent Difference) maps in Fig. 4.2.4 (a, b, and c) show the areas where the deformation components Uz, Ur, and Ulos, due to depressurization of a spherical source, are mostly affected by the presence of the topography. The MAPD is calculated as follows:

$$MAPD = \left(\left(\sum_{m=0}^{n^{\circ}models} \mid U_{iTOPO} - U_{iFLAT} \mid / U_{iFLATMAX} \right) / n^{\circ}models \right) \times 100$$

where i = z, r, or los.

The MAPD being a mean of the absolute difference between the topo and the flat model for all the models considered, it does not provide any information about the entity of the under/over estimation of the solution due to the flat-top assumption. However it provides a good tool to recognize the most affected areas and an average evaluation of the % difference at each point of the surface.

The biggest effects on Uz, MAPD equal 5.5% (Fig. 4.2.4, a), are mainly localized above the spherical source of deformation and mostly on its southern edge where they show a systematic distribution as a function of distance from the southern point of the source of deformation and where bathymetry started to deepen towards south.

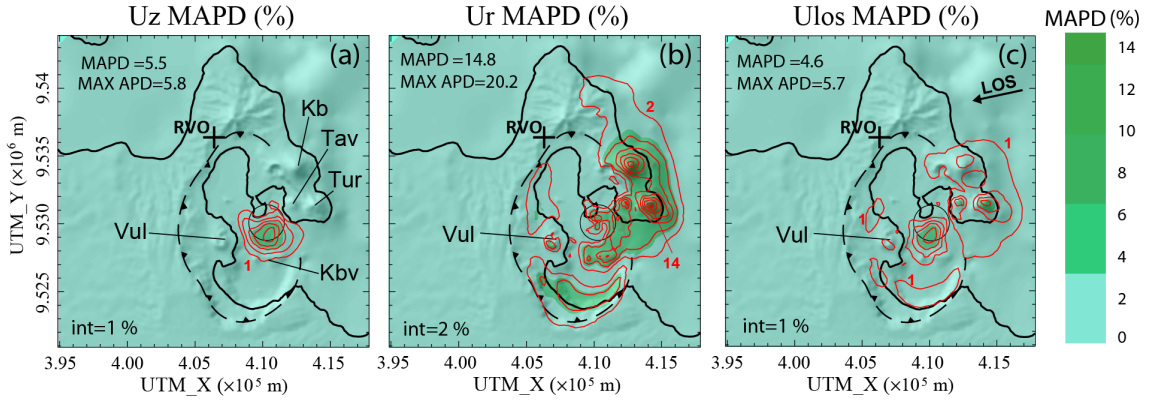

Figure 4.2.4. Mean of the absolute percent difference (MAPD) between the solutions calculated from all the models with topographic relief and the models with flat-top free surface.

The mean is calculated from the difference Topo-Flat solutions of all models and is displayed in percentage both with colors and contours for (a) the vertical displacements (Uz), (b) the horizontal displacements (Ur), and (c) the displacements projected into the InSAR line-of-sight (LOS). The black arrow in panel c shows the surface projection of the mean LOS unit vectors. Significant contours are displayed for an easier comparison between the MAPD of the displacement components. The contour interval for each panel is shown as black text at the bottom left corner. Note that, due to higher Ur MAPD values, the intervals' value of contours for the Ur component is bigger to make the figure easier to read. The black barbed line in all three panels indicates the caldera edges. The projection of the source on the surface is shown as a gray circle at the center of the caldera. The black cross next to the north-eastern edge of the caldera shows the position of the Rabaul Volcano Observatory (RVO). Volcano edifices are also indicated.

A systematic difference in horizontal displacements above the source of deformation is not observed due to the complexity of the MAPD of the horizontal component of the deformation (Fig. 4.2.4, b). The distribution of MAPD values for Ur seems to resemble the topographic relief with higher values in correspondence with higher slope gradients (Kabiu, Turangunan, Tavurur, Vulcan, Karavia Bay Volcanics and the southern slopes of the caldera wall).

The distribution of MAPD values for the Ulos component (Fig. 4.2.4, c) is a combination of the MAPD values of the Uz and Ur components, showing higher values of discrepancies between the models above the southern edge of the source of deformation and in correspondence with the more pronounced relief and Tavurvur edifices.

In summary, the absolute maximum difference (APD) is about 6% for the Uz component and about 20% for the Ur component, which corresponds to about 8% of the max Uz displacement. The higher MAPD values are mainly localized in the vicinity of the source of deformation, on the side of the deepening bathymetry for the Uz component and in correspondence with steeper slopes for the Ur component. The displacements at RVO, the reference benchmark for the geodetic measurements at Rabaul Caldera, seem not to be affected by the presence of the topographic relief. While not large, these differences are sufficiently systematic to suggest using the realistic estimates of the topographic relief for all subsequent Rabaul models.

Effects of the Poisson's ratio and Young's modulus

Having found some uncertainties in defining the material properties of the Infill block, we decided to study the effects of different infill material properties on the deformation signal. We first study the effects of changing the Poisson's ratio, υ, from 0.10 to 0.47 (Fig. 4.2.5), while keeping the same Young's modulus, E, (0.2 GPa) for all models. The second study is about the effects of Young's

modulus changes on the deformation signal. We therefore sweep E from 0.003 to 5. GPa (Fig. 4.2.6), while keeping the same Poisson's ratio (0.15) for all models. A third study includes all possible combinations of material parameters among the E and υ chosen range and helps summarize the results and observations in a more generalized way.

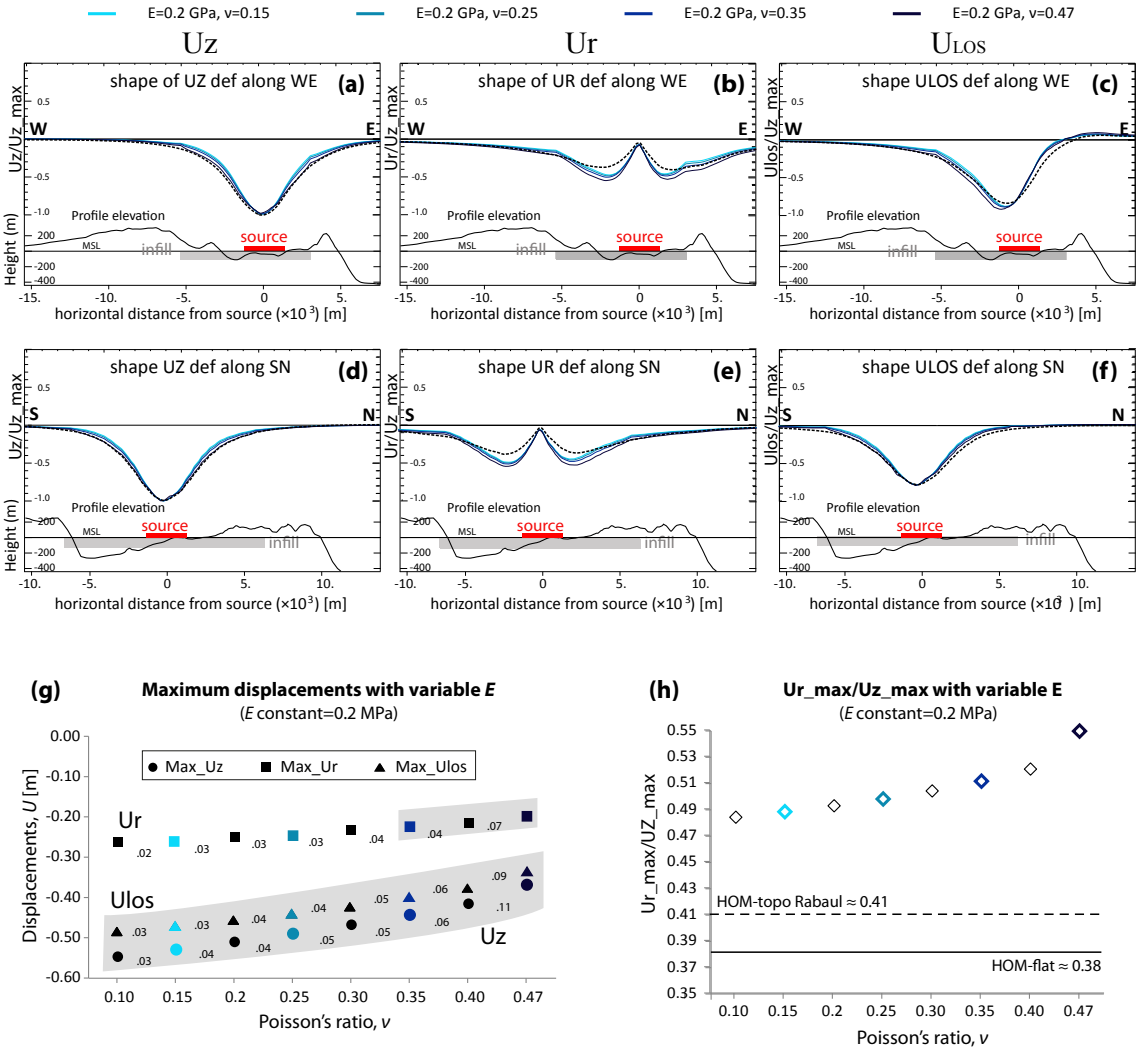

Figure 4.2.5. Subsidence signal shape, maximum displacement, and Ux_max/Uz_max ratios due to spherical source deflation and variable Poisson's ratio of Infill part.
Uz, Ur, and Ulos are normalized by Uz_max of the model. Dashed lines represent the signal of the HOM model. (a-c) WE profile of normalized Uz, Ur, and Ulos surface displacements. (d-f) NS profile of normalized Uz, Ur, and Ulos surface displacements. See Tab. 4.2.2 for the position and track of the WE and NE profiles in the Rabaul area. For clarity of the graphs, only few model signals are represented. At the bottom of each profile the topographic profile is shown for reference (vertical exaggeration x5). The horizontal position and extension of the infill block (grey) and the source of deformation (red bar representing the diameter of the spherical source) are shown for reference. (g) Maximum displacements of Uz, Ur, and Ulos of all modes run in the study. Blue colors are the same used in plots (a) to (f). The gray boxes highlight the changes in maximum displacements bigger than 1 cm. The number at each interval corresponds to the relative percent difference in the interval expressed in decimal form. (h) Ratio of maximum Ur and maximum Uz displacements for each model run in this study. Blue colors are the same used in plots (a) to (f). The ratios of a homogeneous flat model and a homogeneous model with the Rabaul topography are shown for reference.

When increasing υ, the Infill block becomes more incompressible. While Uz max has a sig-

nificant reduction especially at higher υ, Ur does not show the same strong reduction, presenting a quasi-flat Ur max trend and thus becoming a stronger component of the signal as υ increases (Fig. 4.2.5, g).

When increasing υ, the shape of the deformation signal becomes broader both for Uz and Ur (light blue to dark blue signals in Fig. 4.2.5, a-f). Both Uz and Ur changes affect distal areas propagating to areas located out of the Infill borders (Fig. 4.2.5, a-e). This is more evident for the Ur component (Fig. 4.2.5, b and e) and for the Uz component on the eastern side of the caldera where the source of deformation is closer to the Infill edge (Fig. 4.2.5, a). On the western Infill edge, the effects on Uz are more confined above the Infill. Although the effects of the Poisson's ratio on the shape signal are small, in general the Ur shape seems to be more affected with a higher signal widening by the increase of Poisson's ratio especially in the eastern side of the caldera, outside the Infill borders (Fig. 4.2.5, b). Changes at higher Poisson's ratios seem to result in more significant shape changes than changes at lower Poisson's ratios; this is consistent with the higher rate changes of both Uz_max and Ur_max at the intervals between higher Poisson's values (Fig. 4.2.5, g). Increasig υ, the Ulos shows shrinkage of the signal, more evident at its western side, and a shift of Ulos maximum towards west (Fig. 4.2.5, c).

In terms of maximum displacements, both Ur and Uz maximum values decrease with the increase of the Poisson's ratio, although Ur seems not to be affected as much as the Uz component (Fig. 4.2.5, g), showing a slower decrease with respect to Uz. This results in an increase of the ratio between the maximum Ur and the maximum Uz (Fig. 4.2.5, h) between 0.48 and 0.54 and bigger normalized Ur displacements (Fig. 4.2.5, b and e) with respect to their relative normalized maximum Uz (Fig. 4.2.5, a and d). Although the variations in the max displacements for an increasing υ intervals are small (3-11% for Uz, 2-8% for Ur, and 3-11% for Ulos), for the considered Uz and Ulos magnitude of deformation they correspond to significant differences, included in the limit of detectable displacements with InSAR (>1 cm). In all models the Ur_max/Uz_max is considerably higher than the one characteristic for the Mogi or McTigue model (Ur_max/Uz_max ≈ 0.38) and also higher than the one resulting from a homogeneous FEM model with Rabaul topography (≈ 0.41) (Fig. 4.2.5, h). The higher value of the topographic model is probably related to fact that, for shallow sources, the volcano slopes augment the effect of the free surface on Ur, because parts are not horizontally confined (*Lungarini et al.*, 2005).

When increasing the Young modulus, E, the material composing the body becomes stiffer and more resistant to deformation. Both Uz and Ur are subjected to a reduction, more significant for E increasing at higher values, but Ur appears to be more reduced becoming a less strong component as E increases (Fig. 4.2.6).

With increasing the E, the shapes of the signal components become broader (colors from light green to dark green in Fig. 4.2.6, a-b and d-e). On the other hand, a reduction of E generates shrinkage of both Uz and Ur signals with the formation of notches at the Infill edges, whose length extends beyond the limits of the Infill border; these notches are totally obliterated as E of the Infill approaches the value of the Extra-caldera one (4.08 GPa). The notch of Uz is more pronounced at the eastern Infill edge where the source of deformation is closer to the edge of the Infill (where the change of material properties is located) (Fig. 4.2.6, a). For higher E, Ur also becomes broader (Fig. 4.2.6, b and e). In fact, for small E, the Ur signal appears to be more peaked at its two maximums (with the higher value at the western peak, located in correspondence of a topographic low). Its notches at the borders of the Infill block appear to be more evident with lower values of E. This results in higher differences between the low notch values and the max normalized Ur values (Fig. 4.2.6, b and e) and in a general shrinkage of the signal. By decreasing the E, the Ulos

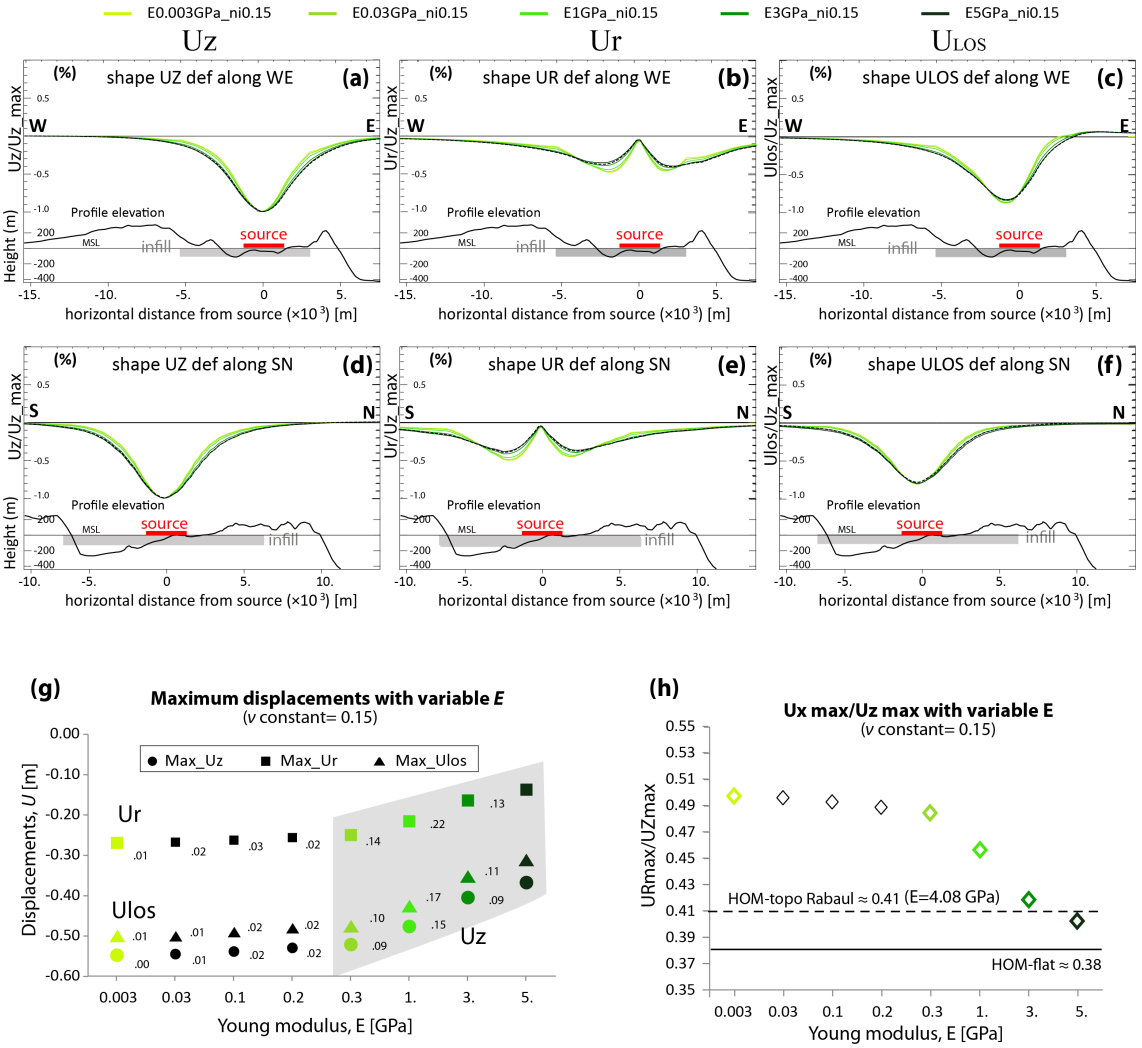

Figure 4.2.6. Subsidence signal shape, maximum displacement, and Ux_max/Uz_max ratios due to spherical source deflation and variable Young modulus of Infill part.
Uz, Ur, and Ulos are normalized by Uz_max of the model. Dashed lines represent the signal of the HOM model. (a-c) WE profile of normalized Uz, Ur, and Ulos surface displacements. (d-f) NS profile of normalized Uz, Ur, and Ulos surface displacements. See Tab. 4.2.2 for the position and track of the WE and NE profiles in the Rabaul area. For clarity of the graphs, only few model signals are represented. At the bottom of each profile the topographic profile is shown for reference (vertical exaggeration x5). The horizontal position and extension of the infill block (grey) and the source of deformation (red bar representing the diameter of the spherical source) are shown for reference. (g) Maximum displacements of Uz, Ur, and Ulos of all modes run in the study. Green colors are the same used in plots (a) to (f). The gray boxes highlight the changes in maximum displacements bigger than 1 cm. The number at each interval corresponds to the relative percent difference in the interval expressed in decimal form. (h) Ratio of maximum Ur and maximum Uz displacements for each model run in this study. Green colors are the same used in plots (a) to (f). The ratios of a homogeneous flat model and a homogeneous model with the Rabaul topography are shown for reference.

shows shrinkage of the signal in any direction (Fig. 4.2.6, c) and an increase of its maximum value. Changes at higher E seem to result in more significant shape changes than changes at lower E; this is consistent with the higher rate changes of both Uz_max and Ur_max at the intervals between higher E values (between 0.3 and 5) and very low changes for lower E values (Fig. 4.2.6, g).

In terms of of maximum displacements, both Ur and Uz maximum values decrease with the

increase of the Young modulus. Both Uz and Ur maximum seem not to be very affected by increasing of E at low values (between 0.003 and 0.3 GPa) showing a flat trend. Indeed, they show evident decreasing values with decreasing E at higher values (Fig. 4.2.6, g). The maximum Ur and the maximum Uz thus show a quasi-flat trend at low E values and abrupt decreasing for increasing E at higher values (Fig. 4.2.6, h). This is consistent with the change of proportion of the two components of the signal maximum with Ur_max becoming smaller more rapidly than Uz max (Fig. 4.2.6, g) and with smaller normalized Ur displacements (Fig. 4.2.6, b and e) with respect to their relative normalized maximum Uz (Fig. 4.2.6, a and d). Although the variations in the max displacements for an increasing E intervals are small (0-9% for Uz, 1-13% for Ur, and 1-11% for Ulos), for the considered Uz and Ulos magnitude of deformation, at higher values of E, they correspond to significant differences, included in the limit of detectable displacements with InSAR (>1 cm). In the models with low E, the Ur_max/Uz_max is considerably higher than the one characteristic of the Mogi or McTigue model (Ur_max/Uz_max ≈ 0.38) or the one resulting from a homogeneous FEM model with Rabaul topography (Ur_max/Uz_max ≈ 0.41) (Fig. 4.2.5, h). Increasing E, the value of the ratio approaches the E value of the material outside of the caldera; thus the ratio Ur_max/Uz_max tends to the ratio of a homogeneous model with the Rabaul topography, this also find correspondence in the fact the U signals are very similar to those of a homogeneous model (Fig. 4.2.6, a-f).

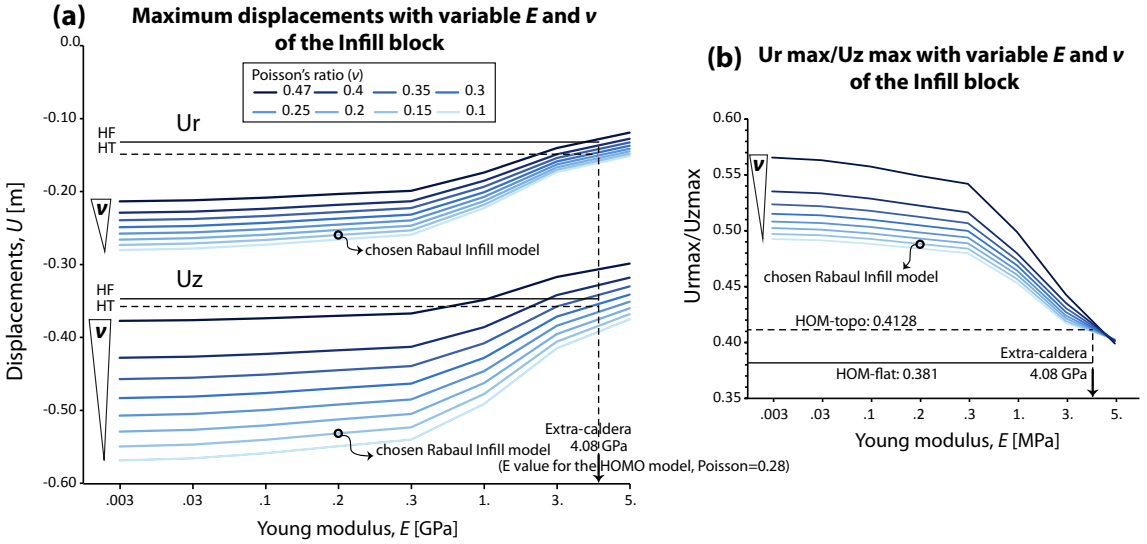

Figure 4.2.7. Maximum displacements and Ur_max/Uz_max ratios of topographic models with variable E and υ of the Infill block.
HOM-topo model: E=4.08 GPa, υ =0.28. (a) Ur and Uz maximum displacements of models with increasing E and variable υ of the Infill block. Maximum displacements of the homogeneous-flat (HF) and the homogenous-topo (HT) models are also plot for reference. All the values of the HT reference model are plotted with dashed lines. (b) Ratios of Ur maximum and Uz maximum for increasing E and variable υ. Ratios of the homogeneous model with flat free surface (HOM-flat) and the homogenous model with the Rabaul topographic surface (HOM-topo) are shown as reference. Colors are consistent with panel a. The circle indicates the values of the model which Infill is characterized by the material properties chosen for the Rabaul area (E=0.2 GPa and υ=0.15).

By combining the model solution for variable values of υ and E, we obtain a range of possible maximum Ur and Uz that guides us in understanding the variations to which these parameters are subjected.

With respect to the homogenous models, both Ur and Uz maximums show higher values at

small E with the tendency to decrease towards the values of the HOM-topo models as E and υ of the Infill block increases and tends to the value of the surrounding materials (E=4.08 GPa, υ =0.28) (Fig. 4.2.7, a). Ur and Uz maximum values have small variations for values of E between 0.003 and 0.3 GPa, and decrease rapidly for E>0.3 GPa. With respect to the reference HT model, the Ur and Uz maximum displacements are discordant with the υ variations: they are higher and lower with decreasing or increasing of υ, respectively (Fig. 4.2.7, a). This is consistent for all values of E, with enhanced effects for lower E. In fact, both Ur and Uz displacements are more minimized and maximized with the increasing and decreasing of υ at lower E values of the Infill (left side of the graph, Fig. 4.2.7, a)

The effects of υ variations result in a more spread maximum displacements variations for Uz than for Ur: higher υ values produces higher decrease of max Uz that max Ur; this results in higher Ur_max/Uz_max ratios for higher υ (Fig. 4.2.7, b). Ratio values are more spreads for low values of E, in accordance with the spreader Ur and Uz variations at low E (Fig. 4.2.7, a). Increasing E, the ratio Ur_max/Uz_max decreases for all values of υ. Looking at this trend in more detail, for values of E between 0.003 and 0.3 GPa, the ratio trend has a low slope, accordingly with the small decreases of Ur and Uz (Fig. 4.2.7, a). For E>0.3 GPa, all ratios start to decrease, with steeper slopes for higher υ, in a way that they converge to similar values approaching E of the Infill equal to 5. GPa (Fig. 4.2.7, b).

Influence of the geologic bodies-single parts

Once we have decided that the topography and the material properties are important for the Rabaul area, we can start to check the influence of different block properties on the deformation fields. The vertical and horizontal diplacements, affected by the presence of the heterogeneities, are compared and normalized to the predictions of the maximum vertical displacement obtained from an isotropic homogeneous model, Uz_hom_max. This kind of normalization has two advantages: first, it allows an immediate estimation of the signal perturbation induced by the presence of the heterogeneous distribution of material properties; second, the results become independent of source overpressure (*Folch and Gottsmann*, 2006). This representation shows well how the presence of heterogeneities affects the absolute values of vertical (Uz) and horizontal (Ur) surface displacements.

Infill-part effects

With respect to the HOM model, the presence of a soft geologic body representing the caldera infill generates larger deformations with larger displacements, especially for Uz and for Ulos component (Fig. 4.2.8, a, c, d, and f).

The difference in maximum Uz component shows that the HOM model underestimates the Uz displacements of -48% (Fig. 4.2.8, a). The larger difference is localized on top of the source of deformation and quickly drops to zero before reaching the external border of the soft infill. This is particularly evident in the western side of the WE profile (Fig. 4.2.8, d) and at both sides of SN profile (Fig. 4.2.8, g), where the edges of the infill are about 7 km from the source center which corresponds to a distance of about 4.5 times the source radius.

The Ur component of the displacement is smaller than Uz. Thus, the measured differences in m are smaller than those of the Uz component (Fig. 4.2.8, b, e, h). Nevertheless, in proportion Ur is more affected by the presence of the soft sediments. The larger Ur discrepancy is about -35% of the maximum Uz of HOM model and -85% of the maximum Ur, where the negative sign indicates that subsidence is bigger for the HET model.

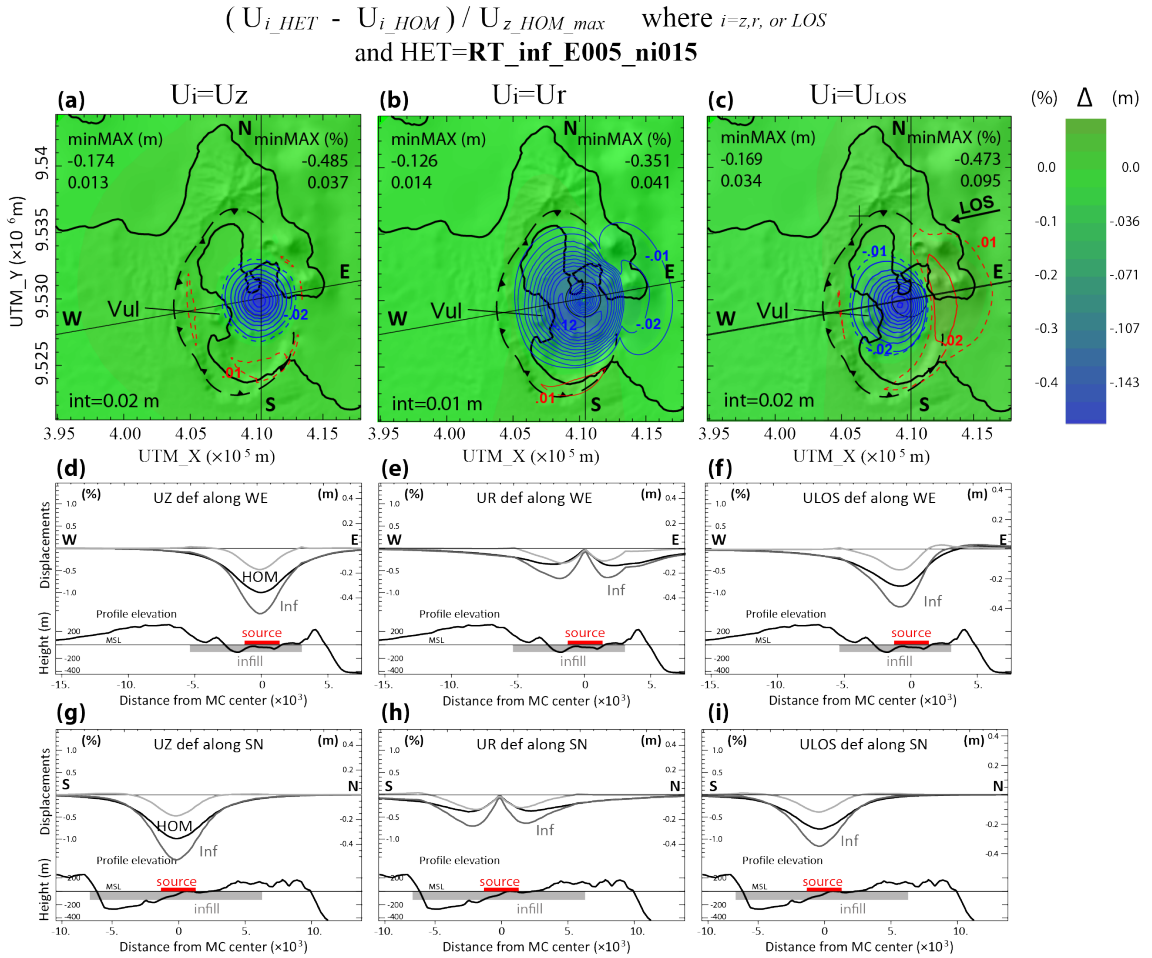

Figure 4.2.8. Infill part effects study.

Absolute and % differences in decimal form. Differences in surface displacements between the heterogeneous and the homogeneous material model with topographic relief, HOM, are normalized to the maximum value of displacements of the HOM model (Uz_HOM_max=0.358 m) in order to calculate the % differences. The gray circle at about the center of the caldera is the projection of the depressurized cavity that generates the displacements. The black barbed line in all the three panels indicates the caldera edges. The differences are mapped for (a) the vertical component (Uz), (b) the radial component (Ur), and (c) for the LOS displacements. The black arrow shows the surface projection of the mean line-of-sight (LOS) unit vectors. Maximum and minimum differences in m and in % (as a decimal) are also provided in the upper left and upper right corners of the panel, respectively. The contour interval of the differences (in m) for each panel is shown as black text at the bottom left corner. Significant contours are displayed for an easier comparison of the differences between the components of the displacement. For the same purpose, the 0.01 m contour is represented by dashed lines in those panels where the contour interval is bigger than 0.01 m. Remembering that the models simulate a subsidence, the blue and the red colors indicate that surface displacements in the heterogeneous model are larger and smaller than those in the HOM model, respectively. Track of West-East and North-South profiles are marked in maps. (d and g) Profiles of vertical surface displacements (Uz) along the lines WE and SN, respectively. Values of displacements normalized to the maximum value of Uz displacements of the HOM model are indicated on the left axis. The black and dark gray lines represent the Uz surface displacements for the homogeneous and the heterogeneous model, respectively. The light gray line represents the Uz difference between the heterogeneous and the homogeneous model. As reference, the topographic profile (vertical exaggeration x5) and the projections of the material properties active in the heterogeneous model are plotted on the bottom of each profile. Position of points along the profiles are reported in distance from the projection of the center of the spherical cavity on the surface. (e and h) Similar to panels d and g but showing differences in radial displacements. (f and i) Similar to panels d and g but showing differences of displacements projected into the LOS direction.

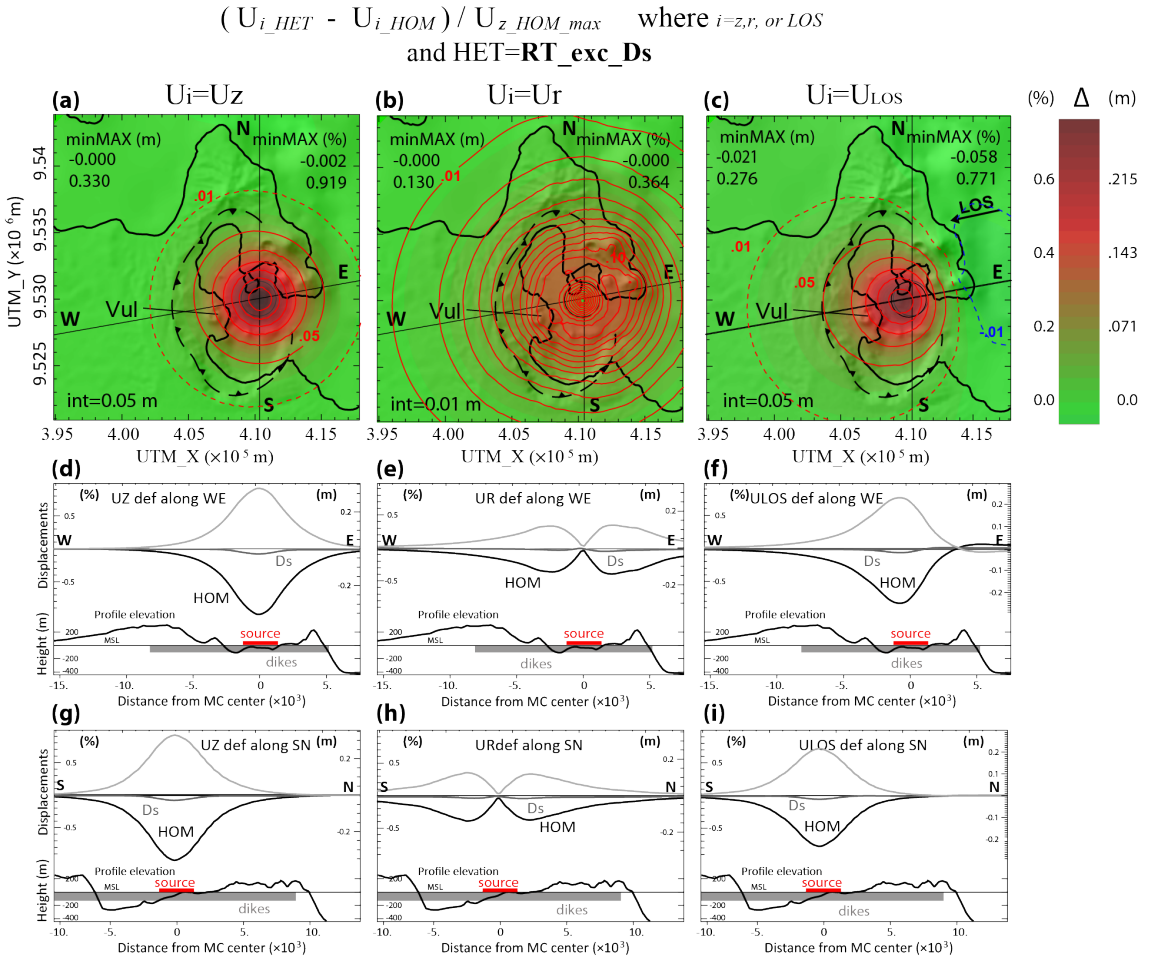

Figure 4.2.9. Dikes swarm part effects study.

Absolute and % differences in decimal form. Differences in surface displacements between the heterogeneous and the homogeneous material model with topographic relief, HOM, are normalized to the maximum value of displacements of the HOM model (Uz_HOM_max=0.358 m) in order to calculate the % differences. The gray circle at about the center of the caldera is the projection of the depressurized cavity that generates the displacements. The black barbed line in all three panels indicates the caldera edges. The differences are mapped for (a) the vertical component (Uz), (b) the radial component (Ur), and (c) for the LOS displacements. The black arrow shows the surface projection of the mean line-of-sight (LOS) unit vectors. Maximum and minimum differences in m and in % (as a decimal) are also provided in the upper left and upper right corners of the panel, respectively. The contour interval of the differences (in m) for each panel is shown as black text at the bottom left corner. Significant contours are displayed for an easier comparison of the differences between the components of the displacement. For the same purpose, the 0.01 m contour is represented by dashed lines in those panels where the contour interval is bigger than 0.01 m. Remembering that the models simulate a subsidence, the blue and the red colors indicate that surface displacements in the heterogeneous model are larger and smaller than those in the HOM model, respectively. Track of West-East and North-South profiles are marked in maps. (d and g) Profiles of vertical surface displacements (Uz) along the lines WE and SN, respectively. Values of displacements normalized to the maximum value of Uz displacements of the HOM model are indicated on the left axis. The black and dark gray lines represent the Uz surface displacements for the homogeneous and the heterogeneous model, respectively. The light gray line represents the Uz difference between the heterogeneous and the homogeneous model. As reference, the topographic profile (vertical exaggeration x5) and the projections of the material properties active in the heterogeneous model are plotted on the bottom of each profile. Position of points along the profiles are reported in distance from the projection of the center of the spherical cavity on the surface. (e and h) Similar to panels d and g but showing differences in radial displacements. (f and i) Similar to panels d and g but showing differences of displacements projected into the LOS direction.

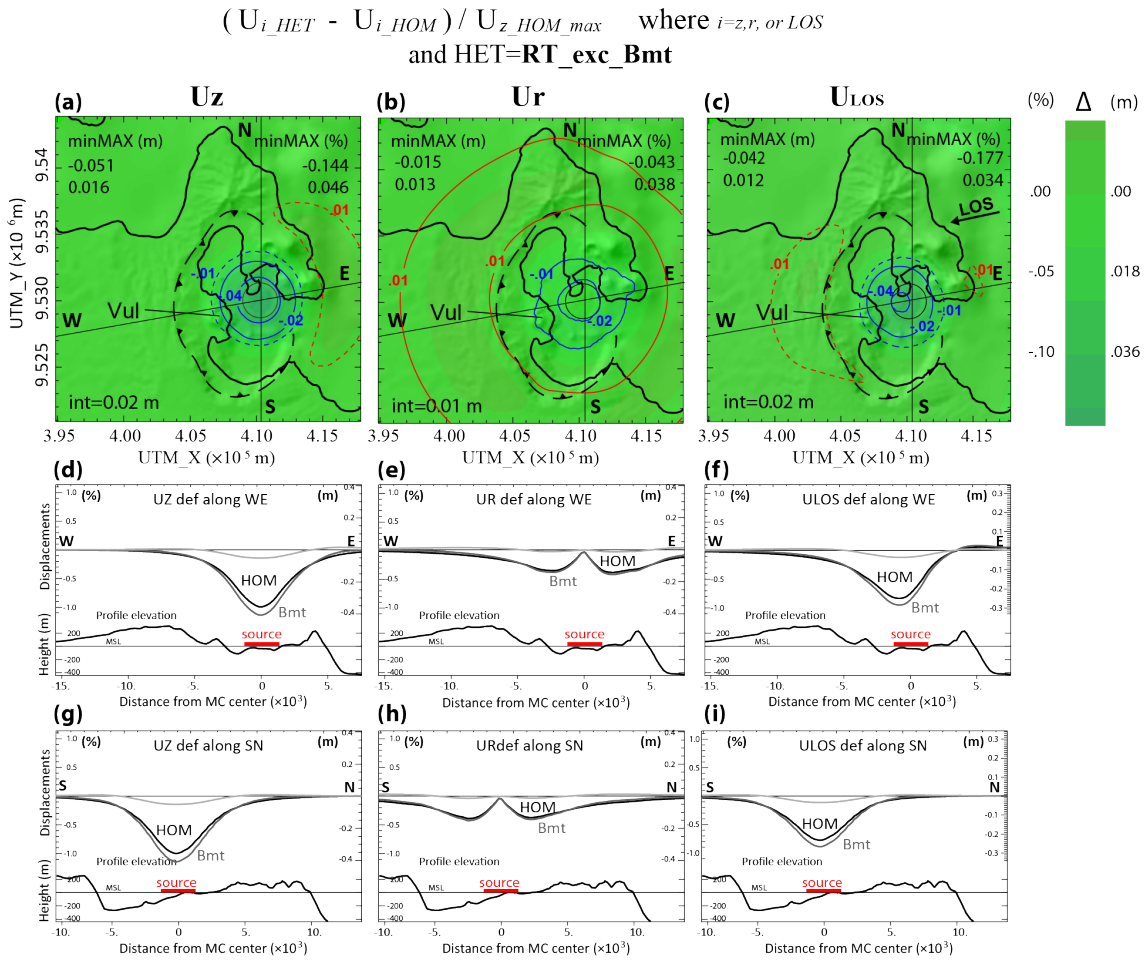

Figure 4.2.10. Baining Mountain part effects study.

Absolute and % differences in decimal form. Differences in surface displacements between the heterogeneous and the homogeneous material model with topographic relief, HOM, are normalized to the maximum value of displacements of the HOM model (Uz_HOM_max=0.358 m) in order to calculate the % differences. The gray circle at about the center of the caldera is the projection of the depressurized cavity that generates the displacements. The black barbed line in all three panels indicates the caldera edges. The differences are mapped for (a) the vertical component (Uz), (b) the radial component (Ur), and (c) for the LOS displacements. The black arrow shows the surface projection of the mean line-of-sight (LOS) unit vectors. Maximum and minimum differences in m and in % (as a decimal) are also provided in the upper left and upper right corners of the panel, respectively. The contour interval of the differences (in m) for each panel is shown as black text at the bottom left corner. Significant contours are displayed for an easier comparison of the differences between the components of the displacement. For the same purpose, the 0.01 m contour is represented by dashed lines in those panels where the contour interval is bigger than 0.01 m. Remembering that the models simulate a subsidence, the blue and the red colors indicate that surface displacements in the heterogeneous model are larger and smaller than those in the HOM model, respectively. Track of West-East and North-South profiles are marked in maps. (d and g) Profiles of vertical surface displacements (Uz) along the lines WE and SN, respectively. Values of displacements normalized to the maximum value of Uz displacements of the HOM model are indicated on the left axis. The black and dark gray lines represent the Uz surface displacements for the homogeneous and the heterogeneous model, respectively. The light gray line represents the Uz difference between the heterogeneous and the homogeneous model. As reference, the topographic profile (vertical exaggeration x5) and the projections of the material properties active in the heterogeneous model are plotted on the bottom of each profile. Position of points along the profiles are reported in distance from the projection of the center of the spherical cavity on the surface. (e and h) Similar to panels d and g but showing differences in radial displacements. (f and i) Similar to panels d and g but showing differences of displacements projected into the LOS direction.

The significant Ur differences are spread over most of the surface of the infill block and overcome its eastern boundaries over Kabiu and Turangunan slopes, where the topography is more important (Fig. 4.2.8, b) and where the infill edge is close to the source. From the profiles can be observed that the HET model predicts higher displacements that overcome the infill edge (eastern side of WE profile in Fig. 4.2.8, e) when the infill edge is close to the source. When the edge is at about 6 km from the source (a distance equal to about 4.4 times the source radius), the differences drop to zero at the edge (western side of WE profile in Fig. 4.2.8, e). At distances bigger than 6 km, the differences change sign, meaning that the HOM model slightly over-predicts the radial displacements Ur (southern and northern side of SN profile in Fig. 4.2.8, h).

Due to the LOS direction towards west, the Ulos displacements associated to a subsidence are asymmetrical with respect to the source of deformation, with positive values for the surface point east of the source and negative values for the surface points west of the source of deformation. Thus, the contribution of larger Ur displacements generates stronger positive displacements in the LOS direction over the eastern side of the caldera (Fig. 4.2.8, c). The combination of Ur and Uz differences generates stronger negative displacements along the LOS direction above the source and towards west from the source; this is confined above the caldera infill and does not extend further to the west (Fig. 4.2.8, c and f). The Ulos larger discrepancy is about -47% of the larger Uz of the HOM model and -56% of the largest ULOS of the Infill model.

Dikes swarm part effects

With respect to the HOM model, the presence of a stiff geologic body representing the swarm of dike intrusions generates smaller deformations with very small displacements for both Uz and Ur components. This leads to large discrepancies and large positive difference values as shown in Fig. 4.2.9, a, b, c.

The Uz HET displacements at the surface have an extension in the order of magnitude of the source. The 92% Uz positive differences show a smooth shape localized in the center of the caldera, on top of the source (Fig. 4.2.9, d).

On the other hand, the Ur positive differences show smaller values having a broader shape with a slightly more articulated signal that shows a bump at the eastern side of WE profile (Fig.4.2.9,e), in correspondence to higher topographies. This means that the contribution of the topography to the HOM deformation signal is not registered in the HET signal and, therefore, the HET model with stiff material appears to be less affected by the topography. The Ur larger discrepancy is about 36% of the maximum Uz of HOM model and 88% of the maximum Ur, where the positive sign indicates that subsidence is smaller for the HET model.

The displacements in the LOS direction show a positive signal slightly extended westwards (Fig. 4.2.9,c). The larger Ulos discrepancy is about 77% of the maximum Uz of the HOM model and 92% of the maximum Ulos of the largest Ulos of the HOM model.

No evident perturbations of the signal are observed at the surface in correspondence to the edges of the geologic body.

Baining Mountains part effects

The presence of a block of stiff material dipping eastwards and passing under the source of deformation generates slightly bigger deformations localized on top of the source (Fig. 4.2.10, a and b).

Uz negative surface displacements of the HET model are higher and more restricted over the area above the source with respect to the HOM model. Thus, the amplified and shrunk signal of the

HET model generates negative residuals localized in the center of the caldera, above the source of deformation (Fig. 4.2.10, a, d, and g). Uz component of the subsidence at the HET model is about 14% higher with respect to the HOM model.

Although differences between the Ur component in the HET and HOM models are very small (Fig. 4.2.10, e and h), it can be observed that the Ur signal is also slightly amplified and even more shrunk (Fig. 4.2.10, b), generating positive residuals in the areas out of the caldera. Residuals are also negative for the Ur component on top of the source. In addition, they show positive values at larger distance from the source, where the signal shrinks (Fig. 4.2.10, b). Again, the Ur component seems to be more affected by the topography with more complex residual distribution in the vicinity of the source of deformation than the Uz component (Fig. 4.2.10, b). The larger Ur discrepancy is about -4% of the maximum Uz of HOM model and -10% of the maximum Ur, where the negative sign indicates that subsidence is bigger for the HET model.

The residuals of displacements in the LOS direction show negative values on top of the source and small positive values west of the caldera borders (Fig. 4.2.10, c). This means that the LOS displacements in this area are underestimated by a model that includes the Baining Mountain block. The larger Ulos discrepancy is about -12% of the larger Uz of the HOM model and -14% of the largest Ulos of the HOM model.

Combined parts effects

Combined effects of the caldera Infill part and the Dikes swarm part

The combination of the effects due to the presence of a caldera infill and a swarm of dikes generates displacements with an amplitude similar to those generated by the dike swarm alone, both for the vertical and horizontal component. So, if we compare the signals to the HOM one (Fig. 4.2.8, d-i), we see that the effects of the soft infill are minimized or totally obliterated by the presence of the stiff material and the displacements are very small (Fig. 4.2.11). However comparing the signals to those generated by a model with dike swarm alone allows us to observe the contribution of both the infill and dike swarm part (Fig. 4.2.11).

The Ds part shrinks the Uz signal above the source and amplifies it in the farther areas. It maintains the signal at constant value over the extension of the part and it lets it drop in the farther areas, giving the signal the shape of a margarita glass (Fig. 4.2.11, d and g). This is very evident if we compare the signal shape with those of Fig. 4.2.8 (d-i). This shape is dominant also for the signal of Fig. 4.2.11, with the addition of the contribution of the infill above the infill part. As previously observed, the infill contributes by amplifying the signal mainly on top of the magma chamber. In fact, the residuals are localized on top of the source of deformation and quickly drop to zero before reaching the external further borders of the soft infill (Fig. 4.2.11, a, d and g). Compared to the 48% amplification of the HOM signal due to the infill part, the 24% amplification of the Ds model is small, but still able to infer significant changes to the Uz signal shape.

The effects of Ds are less evident on the Ur component, but still visible. The two negative lobes are more peaked (compared to the HOM model, see Fig. 4.2.8, e and h) due to the fact that the Ds shrinks the signal and the signal is maintained in the farther areas (Fig. 4.2.11, e and h). The contribution of the infill part is confined above the part (Fig. 4.2.11, b, e and h) and the absolute amplification it generates (38% of the Ur of the Ds signal) is much smaller than the one imposed to the Ur of the HOM model (85%). Thus, the presence of the Ds dumped the effects of the Infill part. The resulting signal is a combination of the shrinkage due to the Ds and the amplification together with the widening above the infill part.

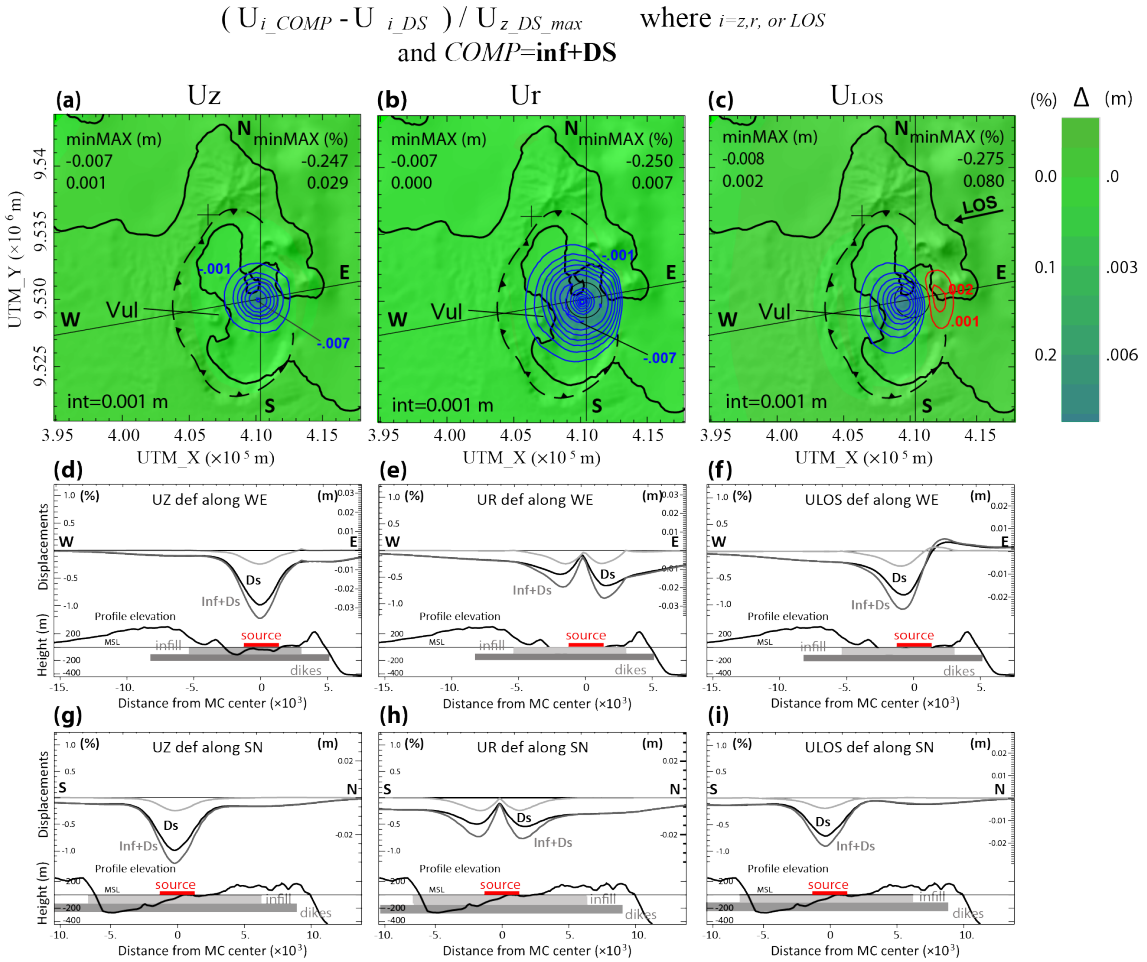

Figure 4.2.11. Infill and dikes swarm parts combined effects study. *Absolute and % differences, in decimal form, of surface displacements between two models with heterogeneous properties distribution in the shallower 8 km. COMP stands for "composite model" and indicates the study model. Differences in surface displacements between the COMP model and the heterogeneous reference model with topographic relief are normalized to the maximum value of displacements of the reference model in order to calculate the % differences. The gray circle at about the center of the caldera is the projection of the depressurized cavity that generates the displacements. The black barbed line in all three panels indicates the caldera edges. The differences are mapped for (a) the vertical component (Uz), (b) the radial component (Ur), and (c) for the LOS displacements. The black arrow shows the surface projection of the mean line-of-sight (LOS) unit vectors. Maximum and minimum differences in m and in % (as a decimal) are also provided in the upper left and upper right corners of the panel, respectively. The contour interval of the differences (in m) for each panel is shown as black text at the bottom left corner. Significant contours are displayed for an easier comparison of the differences between the components of the displacement. Remembering that the models simulate a subsidence, the blue and the red colors indicate that surface displacements in the COMP model are larger and smaller than those in the reference model, respectively. Track of West-East and North-South profiles are marked in maps. (d and g) Profiles of vertical surface displacements (Uz) along the lines WE and SN, respectively. Values of displacements normalized to the maximum value of Uz displacements of the reference model are indicated on the left axis. The black and dark gray lines represent the Uz surface displacements for the homogeneous and the heterogeneous model, respectively. The light gray line represents the Uz difference between the heterogeneous and the homogeneous model. As reference, the topographic profile (vertical exaggeration x5) and the projections of the material properties active in the heterogeneous model are plotted on the bottom of each profile. Position of points along the profiles are reported in distance from the projection of the center of the spherical cavity on the surface. (e and h) Similar to panels d and g but showing differences in radial displacements. (f and i) Similar to panels d and g but showing differences of displacements projected into the LOS direction.*

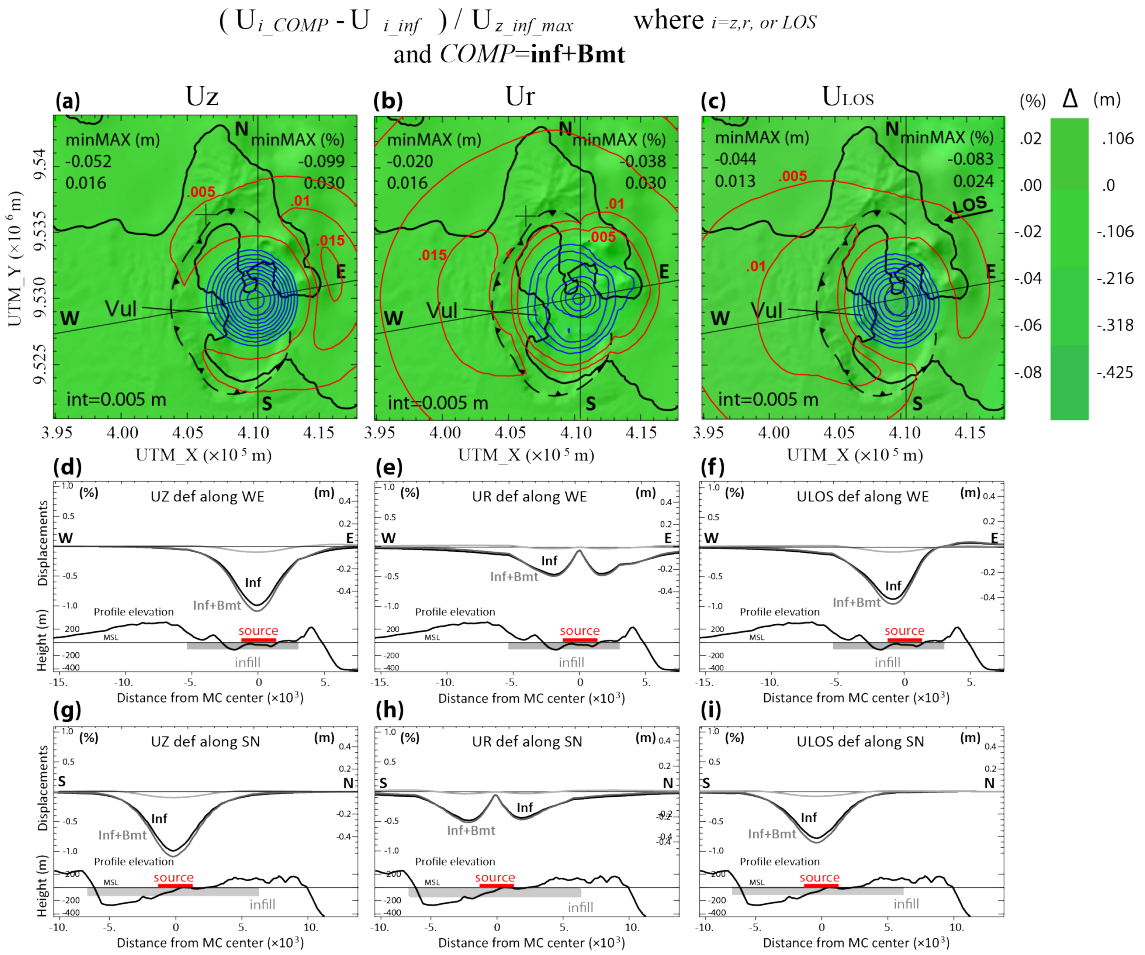

Figure 4.2.12. Infill and Baining Mountain parts combined effects study

Absolute and % differences, in decimal form, of surface displacements between two models with heterogeneous properties distribution in the shallower 8 km. COMP stands for "composite model" and indicates the study model. Differences in surface displacements between the COMP model and the heterogeneous reference model with topographic relief are normalized to the maximum value of displacements of the COMP model in order to calculate the % differences. The gray circle at about the center of the caldera is the projection of the depressurized cavity that generates the displacements. The black barbed line in all three panels indicates the caldera edges. The differences are mapped for (a) the vertical component (Uz), (b) the radial component (Ur), and (c) for the LOS displacements. The black arrow shows the surface projection of the mean line-of-sight (LOS) unit vectors. Maximum and minimum differences in m and in % (as a decimal) are also provided in the upper left and upper right corners of the panel, respectively. The contour interval of the differences (in m) for each panel is shown as black text at the bottom left corner. Significant contours are displayed for an easier comparison of the differences between the components of the displacement. Remembering that the models simulate a subsidence, the blue and the red colors indicate that surface displacements in the COMP model are larger and smaller than those in the reference model, respectively. Track of West-East and North-South profiles are marked in maps. (d and g) Profiles of vertical surface displacements (Uz) along the lines WE and SN, respectively. Values of displacements normalized to the maximum value of Uz displacements of the reference model are indicated on the left axis. The black and dark gray lines represent the Uz surface displacements for the homogeneous and the heterogeneous model, respectively. The light gray line represents the Uz difference between the heterogeneous and the homogeneous model. As reference, the topographic profile (vertical exaggeration x5) and the projections of the material properties active in the heterogeneous model are plotted on the bottom of each profile. Position of points along the profiles are reported in distance from the projection of the center of the spherical cavity on the surface. (e and h) Similar to panels d and g but showing differences in radial displacements. (f and i) Similar to panels d and g but showing differences of displacements projected into the LOS direction.

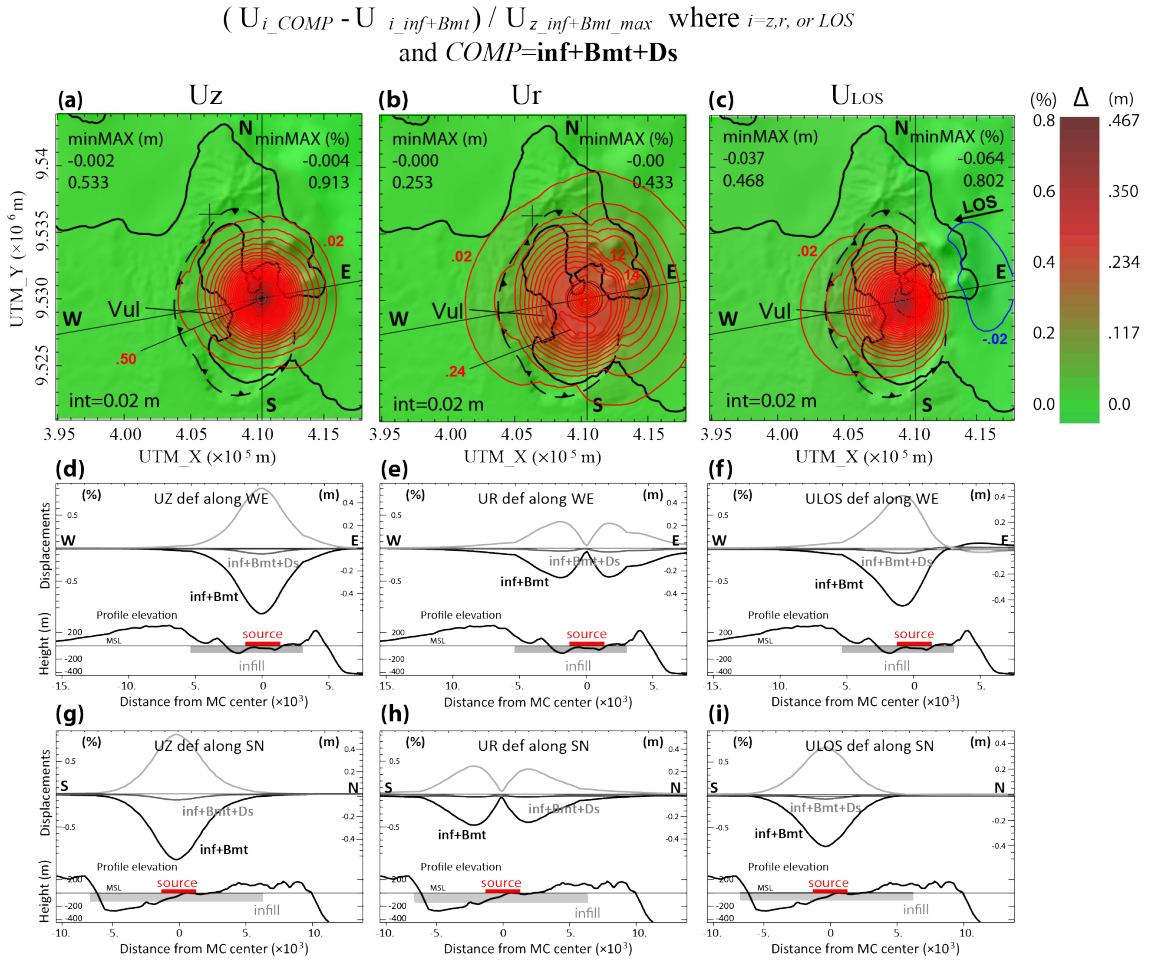

Figure 4.2.13. Infill, dike swarms, and Baining Mountain parts combined effects study *Absolute and % differences, in decimal form, of surface displacements between two models with heterogeneous properties distribution in the shallower 8 km. COMP stands for "composite model" and indicates the study model. Differences in surface displacements between the COMP model and the heterogeneous reference model with topographic relief are normalized to the maximum value of displacements of the COMP model in order to calculate the % differences. The gray circle at about the center of the caldera is the projection of the depressurized cavity that generates the displacements. The black barbed line in all three panels indicates the caldera edges. The differences are mapped for (a) the vertical component (Uz), (b) the radial component (Ur), and (c) for the LOS displacements. The black arrow shows the surface projection of the mean line-of-sight (LOS) unit vectors. Maximum and minimum differences in m and in % (as a decimal) are also provided in the upper left and upper right corners of the panel, respectively. The contour interval of the differences (in m) for each panel is shown as black text at the bottom left corner. Significant contours are displayed for an easier comparison of the differences between the components of the displacement. Remembering that the models simulate a subsidence, the blue and the red colors indicate that surface displacements in the COMP model are larger and smaller than those in the reference model, respectively. Track of West-East and North-South profiles are marked in maps. (d and g) Profiles of vertical surface displacements (Uz) along the lines WE and SN, respectively. Values of displacements normalized to the maximum value of Uz displacements of the reference model are indicated on the left axis. The black and dark gray lines represent the Uz surface displacements for the homogeneous and the heterogeneous model, respectively. The light gray line represents the Uz difference between the heterogeneous and the homogeneous model. As reference, the topographic profile (vertical exaggeration x5) and the projections of the material properties active in the heterogeneous model are plotted on the bottom of each profile. Position of points along the profiles are reported in distance from the projection of the center of the spherical cavity on the surface. (e and h) Similar to panels d and g but showing differences in radial displacements. (f and i) Similar to panels d and g but showing differences of displacements projected into the LOS direction.*

In comparison to the Ds Ulos signal, the composite model signal shows more peaked positive values above the easternmost area of the infill block (Fig. 4.2.11, a and f). The signal is also characterized by a negative maximum above the magma chamber and a log wavelength extending towards west and south and still visible along the northern profile (Fig. 4.2.11, f and i). The largest Ulos discrepancy is about -27% of the larger Uz of the Ds model and -34% of the largest Ulos of the combined model.

Combined effects of the caldera Infill part and the Baining Mountain part

The presence of the slab of stiff material expanding from west to east under the magma chamber produces, with respect to a model with only the infill part, a slightly higher subsidence of the areas above the infill. In addition, west of the caldera a wide area is characterized by less radial displacements with respect to the Infill model. This two combined effects result in a shrinkage of the signal with a slight amplification respect to a model characterized only by the presence of the Infill block.

The Uz component is mainly amplified above the magma chamber, over an area well inside the borders of the Infill block. Uz is damped over an area that does not totally surround the caldera, but shows asymmetry with higher dumping of the signal on the eastern side, where the slab is deeper and does not surrounds the caldera. It is less damped on the western side, where the slab is shallower and surround the caldera (Fig. 4.2.12, a).

The maximum amplification of the Ur component is about 3% of the maximum Uz. It is slightly bigger (about 7.7%) if calculated with respect to its own maximum displacement. The amplification seems to be somehow affected by the topography (Fig. 4.2.12, b), showing isolines that extend over the edifices closest to the source of deformation (Vulcan, Tavuvur, and Turanguna). The presence of Bmt block shrinks the Ur component all around the source of deformation, more on the west of the caldera, with higher positive residual values, and less in correspondence with the higher topographies (eastern side of the caldera) (Fig. 4.2.12, b).

The combination of the Ur and Uz component results in a Ulos signal amplified on top of the magma chamber (negative values in Fig. 4.2.12, c) and damped over the area that covers the western side of the caldera (positive values) inside the caldera border and a portion west of the caldera, out of the caldera border. The maximum amplification with respect to the Uz_max is 8.3%. The absolute Ulosamplification is slightly higher: 9.4%.

Combined effects of the caldera Infill part, the Dikes Swarm part, and the Baining Mountain part

The presence of the Ds in a model that also includes the Infill and Baining mountains blocks reduces the deformation that is mainly focused on top of the magma chamber and over the infill part, but also extends out of the infill border and the caldera edges (Fig. 4.2.13, a, b, and c). The Uz component is greatly dumped, by 91% of its maximum displacement, (Fig. 4.2.13, a, d, and g) mainly on top of the source of deformation with a lobe towards west. The Ur component is also dumped by the Ds part by about 43% of Uz maximum displacement, but reaches 90% dumping of its maximum displacement in a model that includes only Infill and Baining mountains.

The dumping effects of the Ds part on Ur component are maximum inside Blache Bay, but extend also out of the Infill borders with a little lobe towards west and a more complex distribution east of the caldera, where the effects appear to be influenced by the topography and stronger in correspondence with the volcanic edifices (Tavurvur, Turanguna, and Kabiu) (Fig. 4.2.13, b). The

dumping effects of the Ds are also visible on the distribution of the displacements in the LOS direction (Fig. 4.2.13, c). The reduction of displacements is represented by positive values of the residuals, with higher values on top of the source of deformation and higher gradient on the left side of the source (Fig. 4.2.13, c). The maximum dumping corresponds to about 80% of the Uz maximum displacement, but reaches 90% dumping of the Ulos maximum displacement.

Magma chamber shape effects

We investigate the alteration of the surface deformation field due to three different shapes of magma chamber with respect to the one generated by the sphere. The assumptions and construction of the chosen source shapes are described in chapter 4.1.2. All the magma chambers considered have the same volume, and the top of the cavities is located in the same position and at the same depth (see Tab. 4.1.2 for more details).

The introduction of a different source in the model (such as a different magma chamber with different volume and/or shape) modifies the volumes to be parceled during the meshing process. Therefore, the subdivision of the volume into elements will be different with a consequent different position of mesh nodes. When comparing two solutions (in our case, the displacements at the free surface nodes) computed by two different geometric models, the comparison is usually made between different numbers of solutions (due to different numbers of mesh nodes at the free surface) computed at different positions. We therefore need to interpolate one of the two solutions at the node positions of the other one. Every method of interpolation introduces some errors that need to be estimated in order to avoid using erroneous interpolated solutions during the study and interpretation of the comparisons. The interpolation method used is a linear method, where the grid points are linearly interpolated from triangles formed by Delaunay triangulation. In our case, the solution of each new model will be interpolated at the free surface nodes of the reference model (the one with the spherical magma chamber). Therefore, a pair of free surface node distributions will be used during the interpolation process. The errors introduced by the interpolation method using the different node configurations (pair of free surface node distributions) of each comparison were estimated using the William and Wadge (2000) solution error estimator. The estimated errors were found to be insignificant ($<$0.001 %) and the interpolation method was considered optimal for the further comparisons of the study.

The deformation field generated from the depressurization of a cavity with non-spherical shape greatly differs from the one generated by the depressurization of a spherical chamber. With respect to the deformation generated by the spherical source, an oblate flat ellipsoid and an irregular shape source generate bigger deformations, whereas a prolate, vertically elongated ellipsoid generates smaller surface deformations (Fig. 4.2.14).

An oblate source greatly amplifies the deformation (Fig. 4.2.14, a-c, l-m, and o-p). The maximum Uz amplification, about 4 times the maximum Uz of the reference model, is observed to be centered on top of the source and with a regular shape that resembles the oblate shape and smoothly decays in the further areas (Fig. 4.2.14, a). The Ur amplification is smaller, about one time the Uz max of the reference model (2.7 times the reference model Ur), and presents a more irregular shape in the areas where the topography is more pronounced (Rabalanakia, Kabiu, and Turanguna edifices) (Fig. 4.2.14, b). The highest amplification values are distributed in a "U" shape above the perimeter of the ellipsoidal shape of the magma chamber, with maximum values at the north-west and east sides. The shape of the residuals is slightly asymmetrical in the western side, where it is more extended, and highly irregular in the north-east in correspondence of the irregular

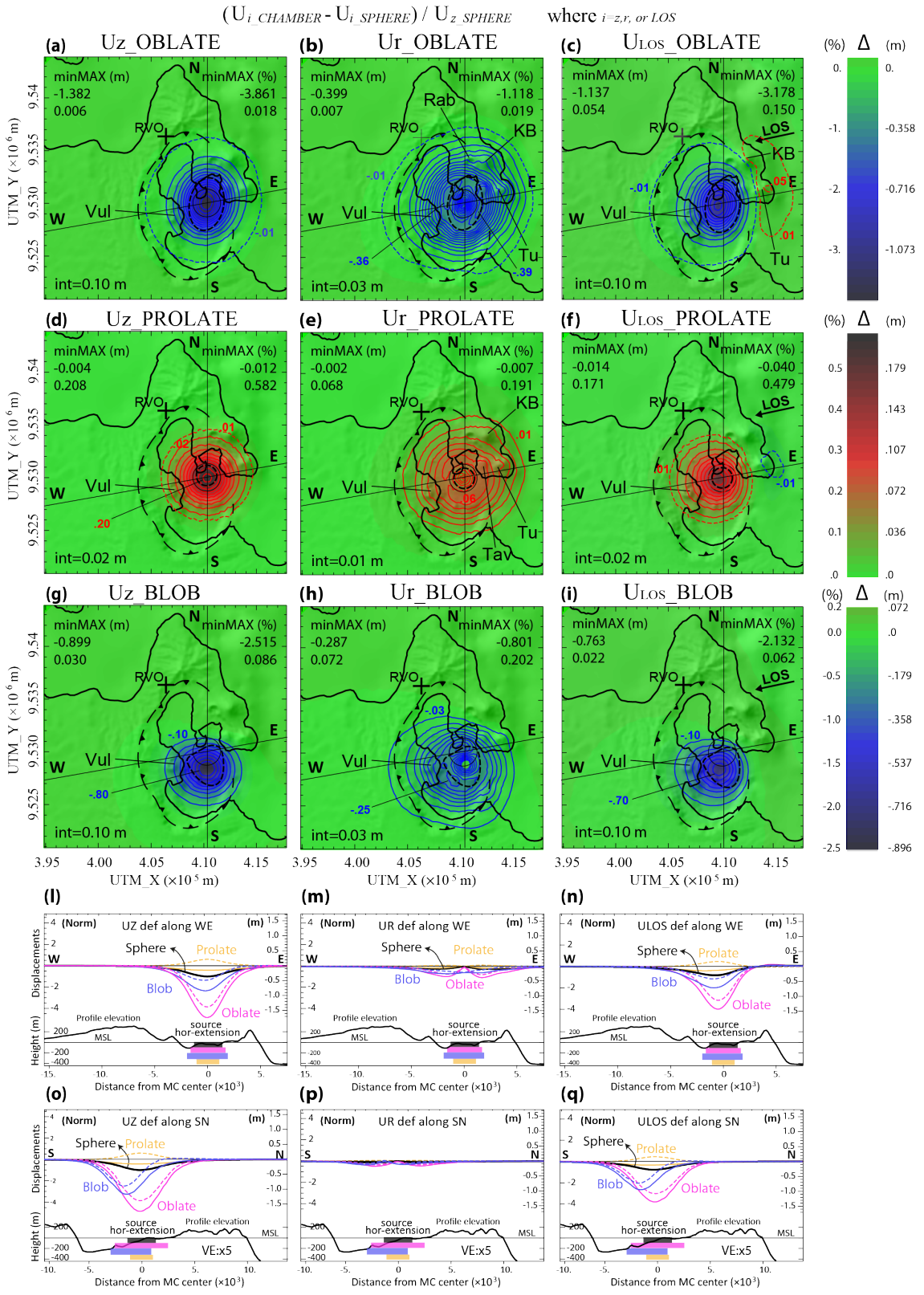

Figure 4.2.14. Study of the effects of the source shape.

Figure 4.2.14 Absolute and % differences, in decimal form, in surface displacements between the topographic homogeneous models (see Tab. 4.1.1 for more details) with irregular or ellipsoidal sources and the reference model with a spherical source. The differences are normalized to the

maximum value of displacements of the reference model (Uz_SPHERE_max=0.358 m) in order to calculate the % differences. The displacements are generated by the depressurization of cavities with different geometries (see Tab. 4.1.2 for more details) whose projection on the surface are represented by the black dashed line in about the center of the caldera. The maps show the Uz, Ur, and Ulos normalized residual displacements due to the change in pressure in: an oblate ellipsoid (a-c), a prolate ellipsoid (d-f), and a cavity with irregular shape (blob)(g-i). The color scale to the right shows both the % differences and the corresponding differences in meters on the left and right side of the scale, respectively. The contour interval of the differences (in m) for each panel is shown as black text at the bottom left corner. Significant contours are displayed for an easier comparison of the differences between the components of the displacement. For the same purpose, the 0.01 m contour is represented by dashed lines in those panels where the contour interval is bigger than 0.01 m. Remembering that the models simulate a subsidence, the blue and the red colors indicate that surface displacements in the models with ellipsoidal or blob shape chamber are larger and smaller than those in the reference model, respectively. The black arrow shows the surface projection of the mean LOS unit vectors, while the black barbed line in all three panels indicates the caldera edges. The Rabaul Volcano Observatory (RVO) position is marked with a cross on the north-western border of the caldera. Tracks of West-East and North-South profiles are marked in maps. (d and g) Normalized profiles of vertical surface displacements, Uz, (solid lines) and residuals (dashed lines) due to different source along the lines WE and SN, respectively. The scales in % and in meters are plotted at the left and right axis, respectively. As reference, the topographic profile (vertical exaggeration x5) and the horizontal extension of the different sources are plotted on the bottom of each profile. Position of the points along the profiles are reported both in UTM x coordinates and in distance from the projection of the top of the cavities on the surface. (e and h) Similar to Fig. 4.2.13, d and Fig. 4.2.13, g but showing differences in radial displacements. (f and i) Similar to Fig. 4.2.13, d and Fig.4.2.13, g but showing differences displacements projected into the LOS direction.

topography. The normalized Ulos residuals are concordant with the amplification of the Uz and Ur and show positive values (higher movements towards the satellite) in the area of the eastern slopes of Kabiu and Turanguna, and negative values (higher movements far away from the satellite) above the source of deformation (Fig. 4.2.14, c).

The prolate source produces less deformation; thus, the normalized residuals are positive for the two components, Uz and Ur, and the Ulos (Fig. 4.2.14, d-f). Maximum normalized Uz residuals are about 60% of the Uz maximum of the reference model; they are centered above the source top and are symmetrical, with regular concentric isolines (Fig. 4.2.14, d). Normalized Ur displacements are concentrically distributed over the source with maximum values localized concentrically and symmetrically above the external perimeter of the spherical source. The normalized Ur residuals lose the concentric symmetry above the relief at the eastern side of the caldera, where the islolines have irregular shape, extending the shape of the distribution (Fig. 4.2.14, e). Normalized Ulos displacements are consistent with a reduced deformation with respect to the deformation of the reference model, showing negative values (less movements toward the satellite) in the eastern areas and concentric positive isolines on top of the source (Fig. 4.2.14, f).

The source having the chosen irregular shape generates bigger deformations with respect to the spherical source leading to negative normalized residuals for the two displacement components, Uz and Ur, and for Ulos (Fig. 4.2.14, g-i, l-m, and o-p). The maximum normalized residuals are not centered on top of the magma chambers, but south of the perimeter of the spherical chamber

(Fig. 4.2.14, g). This is consistent with the maximum Uz produced by the irregular source, which is 2.5 times the Uz maximum of the reference model and which is shifted in this position (Fig. 4.2.14, o). The distribution of the normalized Uz residuals has a shape slightly elongated along the W-E axis (Fig. 4.2.14, g). The normalized Ur residuals are concentric to the irregular shape with highest values localized above the irregular perimeter (Fig. 4.2.14, h). They are slightly elongated towards west. The normalized Ulos residuals are consistent with the higher deformation generated by the irregular shape source showing negative values on top of the source (Fig. 4.2.14, i).

Combined effects of magma chamber shape and soft caldera infill

In this section, we study the combined effects of source geometry and a part of the complex model, the caldera infill, by calculating the difference between the homogenous and heterogeneous models for each geometric source.

In the case of an oblate, planar source, the presence of the caldera infill mainly generates an amplification of the signal (Fig. 4.2.15, a-c). The normalized Uz residuals show an amplification that is mainly localized above the source, with a maximum of about 58% of the Uz maximum of the homogenous case (Fig. 4.2.15, a). The Uz signal shrank due to the presence of the infill in a way that, around the amplification at the center of the caldera, some part inside the caldera present a lower deformation, reduced of about 4%, respect to the homogeneous model. The Ur component is also amplified (Fig. 4.2.15, b) mainly above the caldera infill. The Ur also shrinks resulting in less displacements with respect to the HOM model (positive values of the normalized residuals) above the border of the caldera infill (Fig. 4.2.15, b). In accordance with the shrinking of the signal, normalized Ulos residuals are negative inside the caldera, slightly positive over the western border of the caldera infill, and positive above the eastern side of the infill border (Fig. 4.2.15, c).

In the case of the prolate vertical source, the presence of the infill part generates a stronger shrinkage of the deformation signal with respect to the oblate case, in particular on the western side. The Uz components are amplified over an area centered above the source and extendi over an area about twice the horizontal source extension. Areas with less Uz displacements respect to an HOM model are recognizable along the caldera border, west of the source (Fig. 4.2.15, d). The Ur component shows a broad area of signal amplification with respect to the HOM model (negative normalized residuals) that extends over almost the entire caldera, including the highest eastern relief (Kabiu and Turanguna), with highest values concentric to the source and located at the south-west of the source (Fig. 4.2.15, e). The maximum amplifications of the Ur component are relatively high, with a value of 37% of the maximum Uz of the HOM model. This is almost comparable to the 41% amplification registered for the Uz component. The normalized residuals of Ulos show positive values on the eastern side of the caldera with higher values localized along the infill border and negative values inscribed in the caldera (Fig. 4.2.15, f).

In the case of the irregular source, the presence of the caldera infill also generates an amplification of the signal that is not centered on the caldera top, but more or less above the center of the source (Fig. 4.2.15, g-i). The amplification of the Uz displacement field is localized over an area mainly restricted above the source; displacements slightly smaller than the HOM model contribute to the shrinkage of the signal and are presented all around the amplified area, with a wider extension on the western side (Fig. 4.2.15, g). The normalized residuals of the Ur component also show the shrinkage of the signal with respect to the HOM model. Negative values (amplified signal) are distributed over most of the caldera. Along the perimeter of the caldera infill, slightly smaller displacements with respect to the HOM model, are present, resulting in small positive values of the

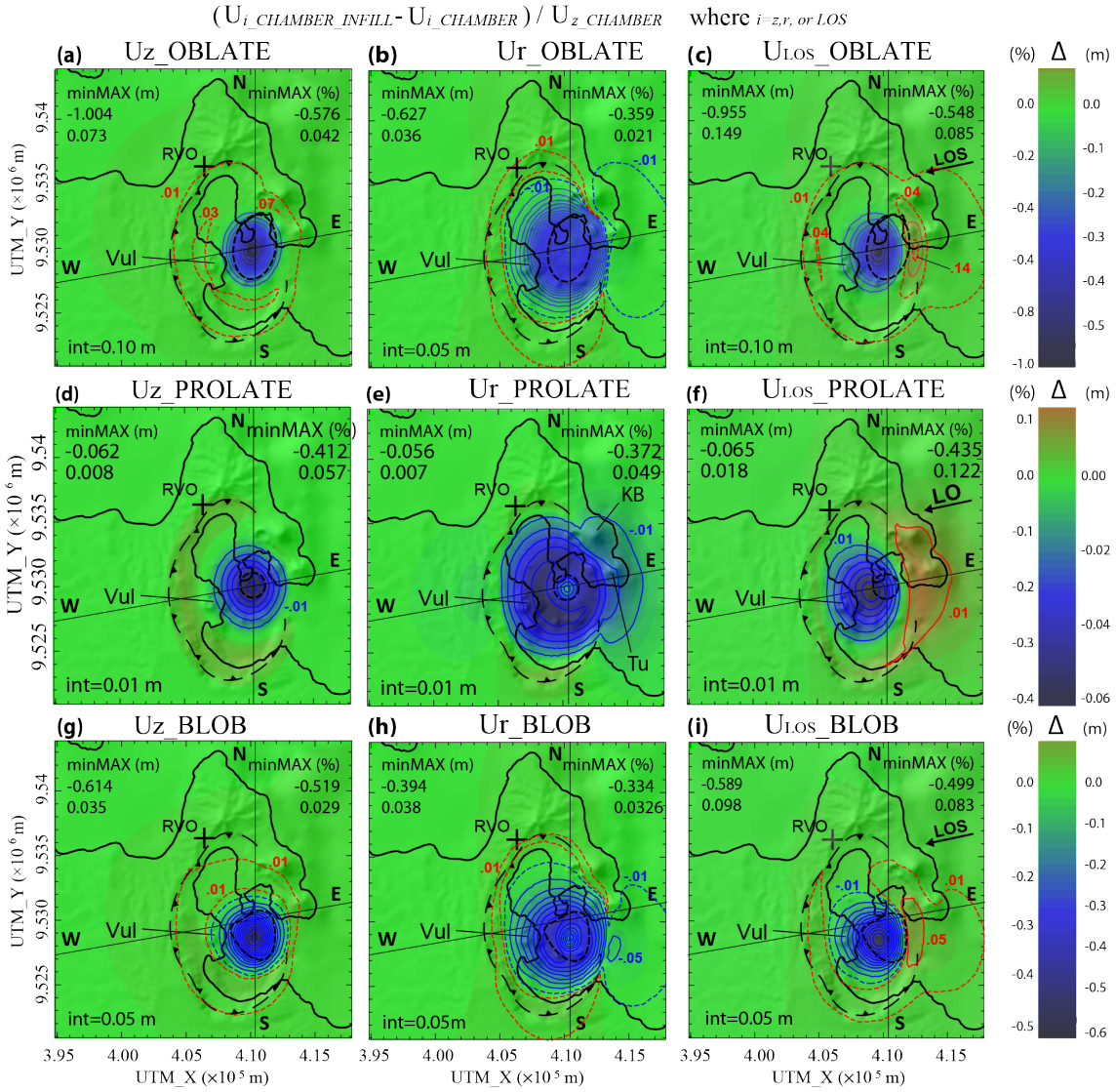

Figure 4.2.15. Study of the combined effects of source shape and caldera infill

Absolute and % differences, in decimal form, in surface displacements between the topographic heterogeneous model (see Tab. 4.1.1 for more details) with irregular or ellipsoidal sources and the relative homogenous model normalized to the maximum value of displacements of the latter one. The displacements are generated by the depressurization of cavities with different geometries (see Tab. 4.1.2 for more details) whose projection on the surface are represented by black dashed line about in the center of the caldera. The maps show the Uz, Ur, and Ulos normalized residual displacements due to the change in pressure in: an oblate ellipsoid (a-c), a prolate ellipsoid (d-f), and a cavity with irregular shape (blob) (g-i). The color scale to the right shows both the % differences and the corresponding differences expressed in meters at the left and right side of the scale, respectively. The contour interval of the differences (in m) for each panel is shown as black text at the bottom left corner. Significant contours are displayed for an easier comparison of the differences between the components of the displacement. For the same purpose, the 0.01 m contour is represented by dashed lines in those panels where the contour interval is bigger than 0.01 m. Remembering that the models simulate a subsidence, the blue and the red colors indicate that surface displacements in the heterogeneous model are larger and smaller than those in the reference model, respectively. The black arrow shows the surface projection of the mean LOS unit vectors, while the black barbed line in all three panels indicates the caldera edges. The Rabaul Volcano Observatory (RVO) position is marked with a cross on the north-western border of the caldera. Tracks of West-East and North-South profiles are marked in maps.

normalized residuals (Fig. 4.2.15, h). Concordant to the shrinkage of the signal shown by the Ur and Uz component, the distribution of normalized Ulos residuals shows amplified displacement in the inner part of the caldera with negative values and positive values along the infill perimeter (Fig. 4.2.15, i).

All results summarized

We have already seen how the presence of a soft caldera infill affects the displacement field in different ways depending on the source shape. We can thus assume that every part of the heterogeneous model affects the displacement field in different ways depending on the source shape. We therefore extend our study to all material combinations of material properties and magma chamber shapes.

As one of the goals of this study is the understanding of the influence of material properties on the deformation signal in order to find a model that better predicts the observed data, we collect the displacement signatures of all models along a profile for each magma chamber (Fig. 4.2.16 and Fig. 4.2.17). As the comparison of the entire datasets (all nodes of the free surface) for all models is difficult, we decided to drive the comparison of the signal along a significant profile. In the case of Rabaul, the LOS displacements occurring along profile WE are those that show the more complex and strong signal in all synthetic models, also including the long length wave LOS displacements on the west of the caldera (Fig. 2.4.4). Therefore, this profile was chosen to summarize all the signals.

The components of the displacements of each model, Ur and Uz, are normalized by the model's maximum Uz displacement. This normalization, besides allowing a direct comparison of signal shape between models, shows how the heterogeneities affect the deformation pattern and how the perturbation of the deformational field is distributed in its components (Uz and Ur). With this normalization we lose the information about the real deformation, but this is of a less importance due to the fact that in this section we perform parametric studies applying an arbitrary overpressure. Ulos displacements are normalized by the maximum value of Ulos.

Note that the profile passes above the top of prolate, oblate, and spherical sources, above their center, where the deformation reaches its maximum and where thus Uz/Uzmax is equal to one. In the case of blob source, where the maximum deformation is south of its top, the maximum normalized Uz along the consodered profile is lower than 1. The same considerations are valid for the normalized LOS displacements. Unfortunately, the part of the InSAR signal with highest displacements is missing due to the fact that it corresponds to the submerged caldera, so is not possible to plot the observed LOS displacements on the normalized plots for a direct comparison. Still, important considerations can be done from the forwards models about the signal alterations due to the material parts and from the general similarities with the observed signal.

With the introduction of heterogeneities in the model, the alteration of the Uz, Ur, and Ulos signals generated by a irregular-blob shape and oblate ellipsoid shape source are mainly localized over an area above the caldera infill and do not extend much beyond the caldera borders (Fig. 4.2.16). In the case of spherical and prolate ellipsoid source, the introduction of all heterogeneities affects the shape of the signals in more pronounced and variable ways (Fig. 4.2.17).

In both the blob and oblate ellipsoid source cases, the presence of the Bmt block (blue solid line) does not modify the HOM signal significantly, generating an overlapping of the two signals along the entire profile (Fig. 4.2.16, a-f). In both cases, the introduction of heterogeneities generates shrinkage of the Uz component, more pronounced for the oblate ellipsoid source. The presence of the Ds part (violet solid line in Fig. 4.2.16) shrinks and amplified for both sources and the additional presence of the infill amplifies these effects (Fig. 4.2.16, c and d). Ulos variations are concordant

with the shrinkage of the Uz and Ur signals, mainly restricted above the infill block, due to the presence of the heterogeneities; signals show slightly asymmetrical shapes with positive values in the eastern part of the caldera and with a slightly longer negative tail on the western side (Fig. 4.2.16, e and f).

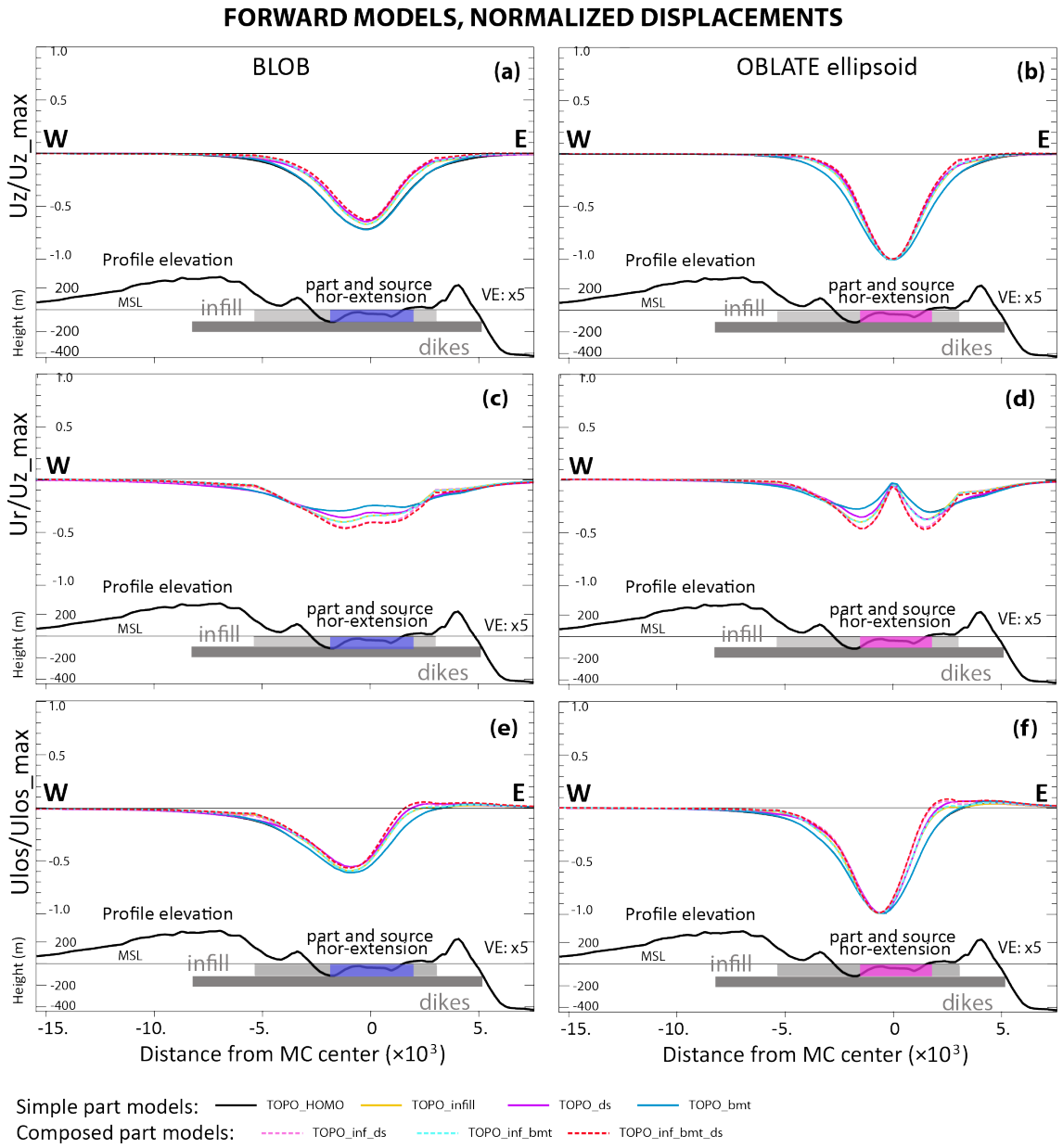

Figure 4.2.16. Normalized displacements of heterogeneous models having blob or oblate-ellipsoid sources (WE profile).

Uz and Ur signal components of each model are normalized to the max Uz displacement of the model, while Ulos are normalized to the maximum of Ulos of the model. Solid lines show the signals of the HOM and simple-part models. Dashed lines show the signals of models with a combination of two or more blocks. For both sources, Uz (a and b), Ur (c and d), and Ulos (e and f) are plotted. As reference, the topographic profile (vertical exaggeration x5), the horizontal extension of the different sources, caldera infill and dikes swarm blocks are plotted on the bottom of each profile. The position along the profile is reported in distance from the projection of the cavities top on the surface.

At the presence of the heterogeneities, the spherical Uz signals (Fig. 4.2.17, a) show a general

higher shrinkage than the signals generated by the blob-shape and the prolate ellipsoid sources (Fig. 4.2.16). As general observation, the Ds greatly shrink the Uz signal, while the soft infill generates a more gentle shrinkage. While the presence of the Bmt slightly affects the Uz signal generated by a spherical source by shrinking it (Fig. 4.2.17, a), it has a bigger impact on the signal produced by the prolate ellipsoid (Fig. 4.2.17, b). The Ds presence modifies the signals of sphere and prolate ellipsoid sources in a

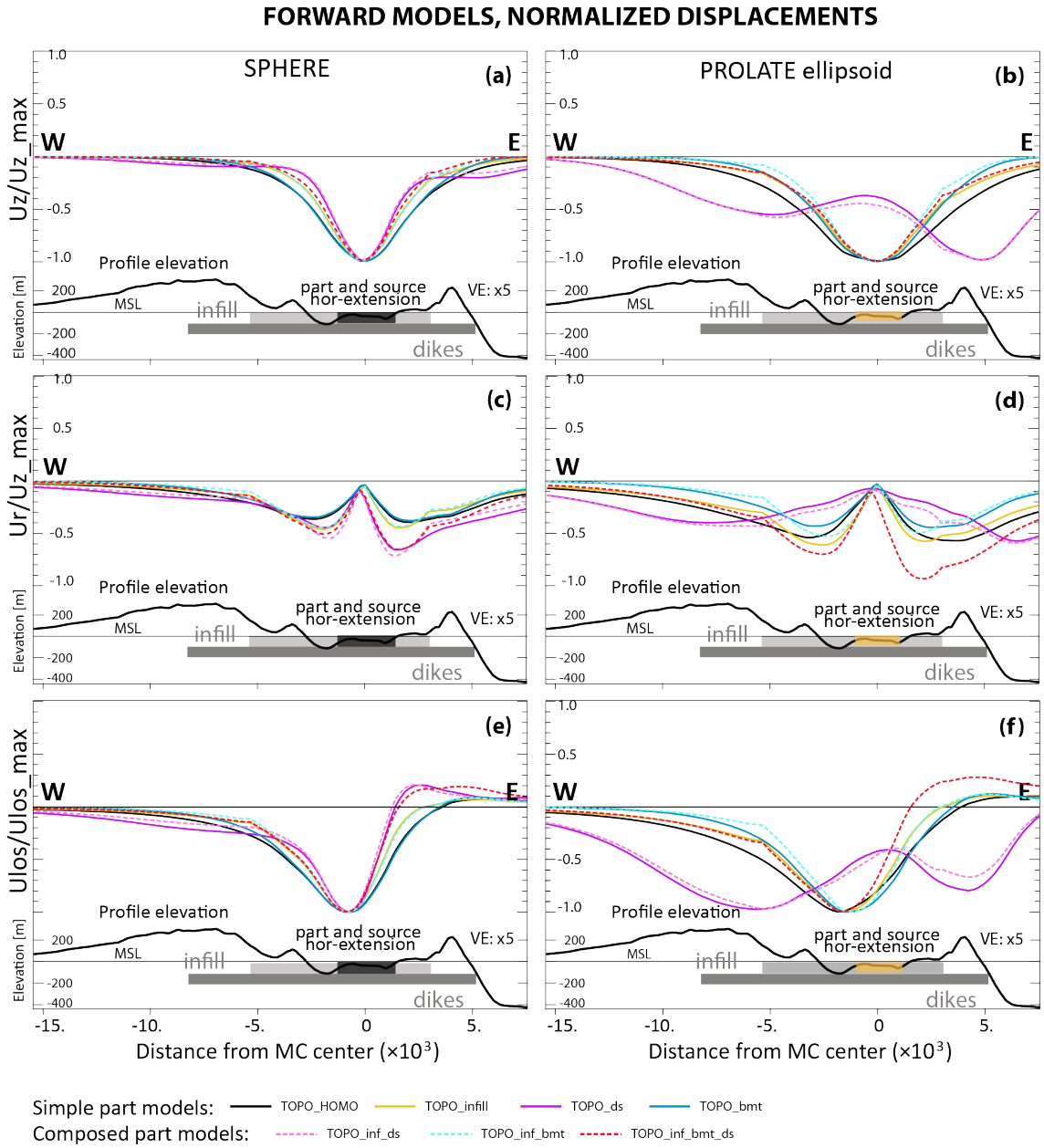

Figure 4.2.17. Normalized displacements of heterogeneous models having spherical or prolate-ellipsoid sources (WE profile).

Uz and Ur signal components of each model are normalized to the max Uz displacement of the model, while Ulos are normalized to the maximum of Ulos of the model. Solid lines show the signals of the HOM and simple-part models. Dashed lines show the signals of models with a combination of two or more blocks. For both sources Uz (a and b), Ur (c and d), and Ulos (e and f) are plotted. As reference, the topographic profile (vertical exaggeration x5), the horizontal extension of the different sources, caldera infill and dikes swarm blocks are plotted on the bottom of each profile. The position along the profile is reported in distance from the projection of the cavities top on the surface.

more significant way with respect to the signal produced by the blob-shaped and oblate ellipsoid sources (Fig. 4.2.17, a-f). Among all models, the signal shapes most affected by the presence of the Ds block are those generated by a prolate ellipsoid (Fig. 4.2.17, b and d, violet solid line); the addition of the caldera infill block dumps the Uz drop by enhancing Uz over the area confined above the infill block and amplifies the Ur signal generating a more articulated signal over an area above the entire Ds extension (Fig. 4.2.17, b and d). The signals produced by the spherical and especially those produced by the prolate ellipsoid have wider length with respect to those produced by blob and oblate sources. This is observable also for the Ulos that generally have stronger asymmetric shapes with a long tail of negative values in the western side outside of the caldera and higher positive values on the eastern side of the caldera, in correspondence with Tavurvur and Turanguna (Fig. 4.2.17, e and f).

4.3 Rabaul PS-InSAR quadtree reduction

Due to the fact that the resulting persistent scatterers (PS) processed by StaMPS are a list of pixels rather than an array of pixels, the quadtree algorithm is applied to the geographic coordinates (UTM, x and y) rather than the radar coordinates (range and azimuth). The result is a list of squared polygons (quadrants) that contain groups of PS whose average value (average of the mean PS velocities in time) is assign to the center of the correspondent polygons.

The area of interest at Rabaul includes approximately 23x10^3 (Fig. 4.3.1, a). Using the quadtree reduction, we reduced the amount of data to a number of data that represents the deformation without losing important information, with particular emphasis on the deformation component characterized by a long wavelength constant in time. The application of the quadtree algorithm to the Rabaul area PS-InSAR reduces the number of data by about two orders of magnitude, depending on the characteristic of the InSAR image and on the parameter threshold chosen (Tab. 4.3.1).

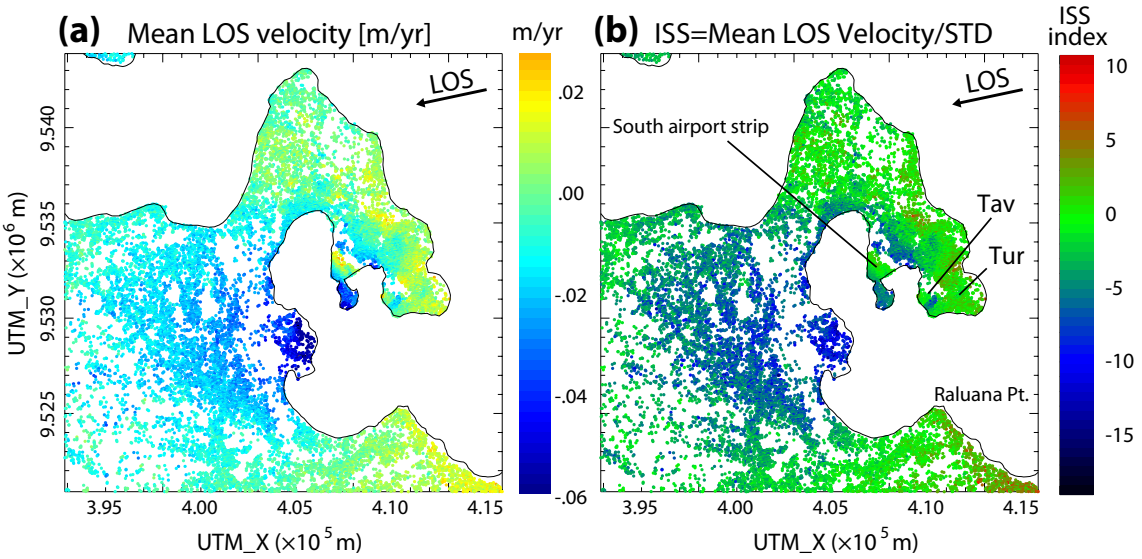

Figure 4.3.1. Mean LOS velocity and index of strength and stability (ISS) for Rabaul area. *(a) Mean LOS velocity map. Negative and positive values represent movements along the line-of-sight (LOS), away from the satellite and towards the satellite. The black arrow represents the projection of the LOS on the surface (direction towards the satellite). (b) ISS map for Rabaul area. Higher negative and positive values represent more consistent negative and positive movements along the LOS in time, respectively. Black arrow is as previous panel. The Raluana Point, Tavurvur (Tav), and Turanguna (Tur) cones are indicated as well as the area south of the airport strip.*

For our preferred quadtree image, we set the maximum size of the quadrants to 1000 m and the minimum size to 300 m. We set the variance threshold for the PS in the quadrants to the variance value of the InSAR accuracy, which is a measure of deformation resolution of the InSAR imagery. As the accuracy of ALOS PALSAR images is in the order of 1 cm/yr (0.01 m/yr), by choosing this value as variance threshold in the quadtree algorithm (VARLIM) we stop the quadrant subdivision when the PS variance of the quadrants falls below the VARLIM value. By specifying the variability less than the resolution of the InSAR imagery, we would increase the number of quadrants, making the reduced image matching the parent image better, although without increasing the amount of useful information. We decided to retain only polygons that contain more than five pixels to avoid big quadrants along the coast line. The threshold value for the ISS parameter is somewhat subjective

and depends on the component of the signal that we want to emphasize for the inversion process. The choice of the ISSLIM value can be guided by observations of the ISS map (Fig. 4.3.1, b).

Parameter	Qtree1	Qtree2	Qtree3	Qtree4
MAXsize [m]	2000	1000	1000	1000
Minsize [m]	300	300	300	300
nminPS	5	5	5	5
VARLIM [m²/yr]	0.0001	0.0001	0.0001	0.0001
ISSLIM	5.	5	4	3.5
N° Qtree	353	666	763	802
	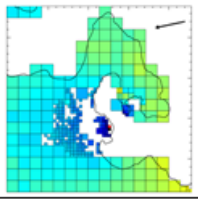	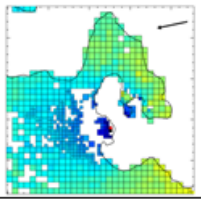	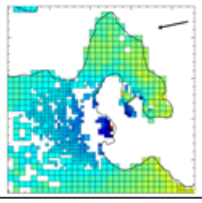	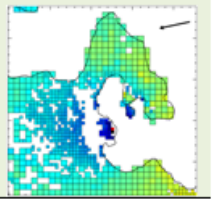

Parameter	Qtree5	Qtree6	Qtree7	Qtree8
MAXsize [m]	1000	1000	1000	1000
Minsize [m]	300	300	300	300
nminPS	4	3	3	4
VARLIM [m²/yr]	0.0001	0.0001	0.0001	0.0001
ISSLIM	3.5	3.5	4	4
N° Qtree	841	886	837	797
	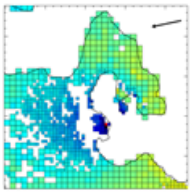	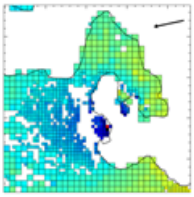	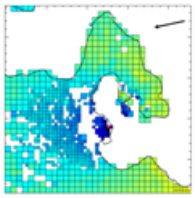	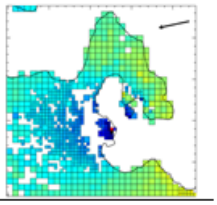

Table 4.3.1. Quadtree reduction results using different parameter inputs. *In gray is shown the parameter that changes respect to the previous quadtree reduction. The preferred quadtree reduction, Qtree4, is highlighted in light green.*

Parameter	Limit value	Description
MAXsize [m]	2000	Defines the maximum possible size of the quadrants
Minsize [m]	300	Defines the minimum possible size of the quadrants
nminPS	5	Minimum number of PS in the quadrant
VARLIM [m²/yr]	0.0001	Variance threshold, equal to the square of InSAR accuracy (0.01 m/yr)
ISSLIM	3.5	Threshold of the mean index of strength and stability of the signal

Table 4.3.2. Input parameters for the quadtree reduction of Rabaul mean velocity data

As already discussed in the methods section 3.6 that describes the quadtree algorithm used for the reduction, the ISS parameter was preferred to the simple variability of the data in time as it also takes into account the magnitude of the signal, giving more weight to bigger deformation with lower variability in time. By using the simple variability (Fig. 2.4.6 in data chapter), the long term steady component of the signal would have been penalized in those areas where it is stronger but

masked by the high frequency signal component (with high STD) due to local shallow sources. At each PS, the ISS value provides the characterization of the heterogeneity of the velocity in time. A map of the ISS values of all PS provides an overview of the consistency of the velocity in time and space (Fig. 4.3.1, b). From the ISS map we can first observe that the variability of the PS is not strictly related to the overall magnitude of the sample as the ISS values are not constant over the entire area. By observing the variable distribution of ISS values in the area and relating the sample variability to different sources with different behavior in time, we can therefore use a threshold of ISS to generate a better coverage to the preferred component of the signal generated by the source that we want to characterize with the inversion. From the maps of mean LOS velocity and ISS (Fig. 4.3.1, a and b), we can observe that the long wave negative LOS signal extending towards west is quite stable in time (high negative ISS values). Areas with low ISS values are those that we want to be less represented in the final quadtree reduction; they correspond to areas that have very high variability with respect to the overall magnitude of the signal due to either very low signal (not moving areas external to the main signal) or very strong high frequency signal component (areas affected to local source impulses like: south airport strip, Tavurvur, and Turanguna). Areas of stable positive LOS displacements are observed in the low areas east of the caldera both on the gentle slopes of the eastern peripheral cones and south east of Raluana Point. As we are interested in the deformation component characterized by a long wavelength constant in time, we chose the threshold for the ISS equal to 3.5 that also allows a good coverage of the area affected by the long wavelength deformation. The values of input parameters for the quadtree reduction of Rabaul mean velocity data are summarized in Tab. 4.3.2. The resulting quadtree image is shown in Fig. 4.3.2.

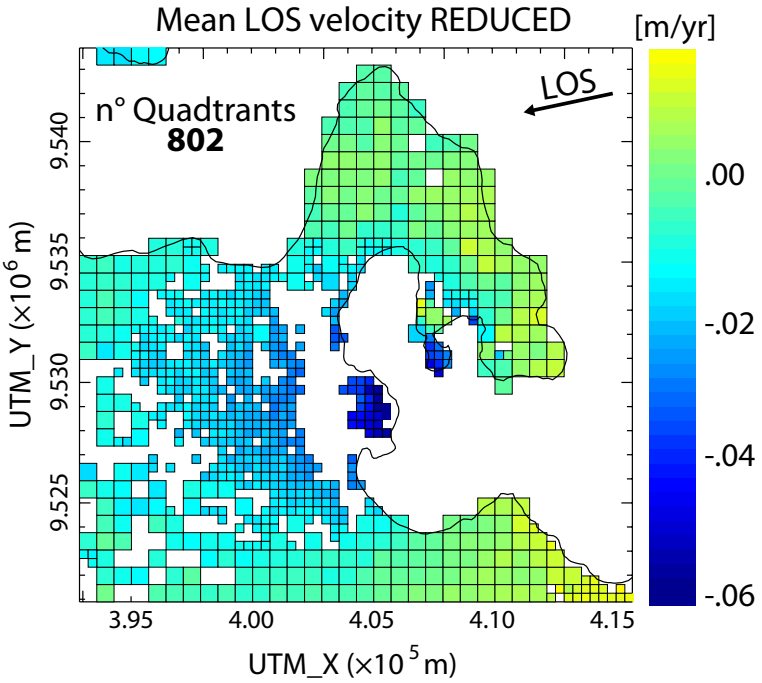

Figure 4.3.2. Preferred Rabaul PS-InSAR reduction.
The data are reduced to 802 quadrants. The black arrow represents the projection of the LOS on the surface (direction towards the satellite).

4.4 Results of Rabaul inverse models using a-priori sources

The same forward models used to study the influence of material properties and magma chamber shapes on the deformation signal, as described in the previous section, are here implemented with fluid elements (F3D3) to allow the introduction of a flux of fluid from or into the magma chamber as source of deformation (see chapter 3.8). This way, the FEMs simulate quasi-static displacements driven by a mass of flux, **q**, of the cavity. The fluid used has the properties calculated for the Rabaul magma in section 4.1.2 (ρ=2370.29 kg/m^3 and K=4.50x10^9 Pa). The results of the FEMs are used to build the Green Functions (GFs) that are involved in the inversion process to estimate the pressure in the cavity.

The forward problem takes the formula:

$$\hat{\mathbf{G}}\hat{\mathbf{s}} = \hat{\mathbf{d}} \tag{4.4.1}$$

where

$$\hat{\mathbf{G}} = (\mathbf{WG\ xy1})\,; \quad \hat{\mathbf{s}} = \begin{pmatrix} \mathrm{q} \\ a \\ b \\ c \end{pmatrix}\,; \quad \hat{\mathbf{d}} = (\mathbf{d}) \tag{4.4.2}$$

where **G**, the vector that contains the solutions for the unity source is pre-multiplied by a weighting matrix, **W**, which defines the contribution of each individual data error (see chapter 3.7.2). **G** is then is appended with three column vectors corresponding to the position of the InSAR data (x and y) and a unity vector. This way, the inversion is able to account for the phase ramping in the InSAR image, caused by the uncertainties of the satellite position (*Massonnet and Feigl*, 1998). The unknown parameters of the plane (a, b, and c) are appended to q, the unknown source paramenter to form $\hat{\mathbf{s}}$.

In order to generate the GFs from the FEM displacement solutions and compare the inversion predictions with the real InSAR data, the resulting displacements at the nodes of the FEM's free surface need to be projected into the LOS and interpolated at the position of the InSAR point. After the data reduction, these sampling points correspond to the center of the Quadtree quadrants, (X_{dr}, Y_{dr}). To assure that the interpolation process is not introducing any error in the forward modeled LOS displacements, we tested the quality of the interpolation method over an area of about 20 km radius around the center of the caldera for the surface node of all model meshes. The test consists first of generating McTigue solutions both at the mesh nodes and at the quadtree nodes (X_{dr}, Y_{dr}); secondly, it involves at each point (X_{dr}, Y_{dr}) the comparison between the McTigue solutions and interpolated McTigue solution from the mesh nodes. The errors are estimated using the William and Wadge (2000) solution error estimator. The estimated errors were found to be insignificant (much smaller than the significant value of 0.05) and the interpolation method was considered adequate. Results are summarized in Tab. 4.4.1.

In the inversion process, the observed data are weighted by their uncertainties. These uncertainties are introduced in the system of equations as a diagonal matrix whose $\mathbf{W}_{i,i}$element is the multiplicative inverse (reciprocal) of the variance σ_i of the i-th datum d_i (in our case, this is the variability of di about its mean in the considered time lapse).

For an easy comparison between all models, the residuals of all models whose absolute value is bigger than 1 cm (rough accuracy estimated for the InSAR data) are plotted in the same image

Model mesh (x_m,y_m)	Misfit at PS-InSAR position(x_d,y_d)	Misfit at PS-InSARreduced (x_{dr},y_{dr})
Sphere	0.0010	0.0007
Oblate ellipsoid	0.0010	0.0006
Prolate ellipsoid	0.0008	0.0005
Blob	0.0010	0.0008

Table 4.4.1. Interpolation test of surface LOS displacements of different meshes at the PS position.
William and Wadge (2000) error estimates for node position of the entire data set (x_d, y_d) are reported in the central column; error estimates for node position of the reduced data (x_{dr}, y_{dr}) are reported in the right column.

which also contains the estimates of the source strength (flux of fluid, change in pressure, change in volume) and the maximum negative and positive estimate errors (Fig. 4.4.1). Maps of residuals give an idea about how the signal is predicted in different areas.

Residuals for oblate and blob source

Residuals estimated from the solution of models with an oblate source (Fig. 4.4.1, c1-7) and a blob source (Fig. 4.4.1, d1-7) show similar patterns, which are consistent over all their different material properties configurations. For all models with oblate and blob sources, the area west of the caldera is extensively characterized by negative residuals with magnitude bigger than 1 cm, although such negative residuals are more extensively present in the case of the oblate sources, where they extend to the east over Vulcan edifice (Fig. 4.4.1, c1-7). Contrarily, in the case of blob sources, the displacements at Vulcan area are well predicted showing just few residuals bigger than 1 cm (Fig. 4.4.1, d1-7). Matupit Is. presents consistent positive residuals in all models having blob and ellipsoidal sources, with higher values in the case of oblate source. On the other hand, the peninsular area north of Matupit Is. shows a very complex distribution of negative and positive residuals for all models with oblate and blob sources.

Estimates of fluid flux calculated for models with blob and oblate sources change concordantly, although results from blob sources generally show higher values (about 2 to 3 times higher). The highest value estimated for blob sources with Ds properties configuration (Fig. 4.4.1, d3) is -30 x10^9.

Residuals for prolate and spherical source

Plots a and b of Fig. 4.4.1s show a consistent distribution of residuals between models with spherical and prolate sources, for all properties configurations, in all areas. The exceptions are: the area west of the caldera, where most of the models with prolate source visually predict the deformation better (less residuals in Fig. 4.4.1, b1, b2, b5, and b7), and the area of Matupit Is., where the models with prolate source and Ds and Inf+Ds properties configuration underestimate the LOS displacements (negative residuals in Fig. 4.4.1, b3 and b5), unlike all other models of this study. In all models, the areas of Matupit Is. or the peninsula north of it show the highest residual values due to a poor simulation of the displacements of this area.

For both prolate and spherical sources, models including Ds (Ds and Inf+Ds) show peculiar positive residuals over broad areas north, east, and south of the caldera (Fig. 4.4.1, b3 and b5). These models show a good fit, with few residuals, in the area west of the caldera. Except for Bmt and Inf+Bmt material configurations, for which residuals of all sources in the area west of the caldera are similar, for models with prolate and spherical sources, the areas west of the caldera are characterized by less residuals with lower values with respect to the models with oblate and blob source. Few residuals are observed in this area for models with spherical source and Ds or Inf+Ds

material configuration (Fig. 4.4.1, a3-7) and for most of the material configurations in models with prolate source (Inf+Bmt and Ds configuration excluded) (Fig. 4.4.1, b1-3, b5, and b7).

Pressure estimates for models with prolate source are higher than for the models with spherical source, except for the cases of Ds and Inf+Ds properties configuration.

Scatter plots

Scatter plots of all models are grouped in one image where, RMSE as well as minimum and maximum values of predicted displacements are provided (Fig. 4.4.2). Scatter plots of predicted versus observed LOS displacements visually help to identify the model that better predicts the observed data. Ideally, for data with no errors, the more the points are aligned to the red diagonal, the better the predictions. In practice, due to data uncertainties and errors, we do not want to perfectly predict the data, because this would mean to also predict their intrinsic errors. Therefore, we define two other red lines, above and below the red diagonal line, that help to account for the ± 1 cm roughly estimated accuracy of the InSAR method, identifying a buffer zone where the points should lie.

The strongest negative LOS displacements observed at Matupit and Vulcan (left-most points in the scatter plots) lie out of the buffer zone in most of the scatter plots. Exceptions are observed for the plots of the blob source (Fig. 4.4.2, d1-7). Points of all models with oblate source generally do not show a diagonal trend, and most of the points fall out of the buffer zone (Fig. 4.4.2, c1-7). For comparison, models with blob source seem to have more points falling inside the buffer zone, but still are clustered and do not show a diagonal trend mainly due to high residuals in the area west of the caldera (Fig. 4.4.2, d1-7). For models with oblate source, points having highest negative coordinates along the horizontal axis of observations (points at Matupit Is. and Vulcan) lie far away from the buffer zone indicating bad predictions (Fig. 4.4.2, c1-7). The same points are generally better predicted in the case of blob source (Fig. 4.4.2, d1-7).

In models with a blob source and for all property configurations, RMSE are smaller than the models with oblate source. The lowest RMSE value for the oblate source is reached with HOM property configuration (Fig. 4.4.2, c1), whereas for blob source RMSE is minimum in the case of Ds property configuration (Fig. 4.4.2, d3).

In models with spherical and prolate source, the points seem to show better diagonal trend, excluding the models with Ds and Inf+Ds material configuration, where many points have positive residuals bigger than 1 cm, especially for the case of a prolate source (Fig. 4.4.2, a3 and a5, b3, and b5).

Points corresponding to Matupit Is. and to Vulcan lie out of the buffer zone in all models with spherical source (Fig. 4.4.2, a1-7). The best prediction for these points is the one shown in the plot of the model with homogenous property distribution (Fig. 4.4.2, a1). These points lie out of the buffer zone also for most of the models with prolate source. The only exception are models with prolate source and HOM, Inf and Inf+Bmt+Ds materials configuration (Fig. 4.4.2, b1-2, and b7).

Among RMSE of models with spherical and prolate sources, both lower than RMSE of models with oblate and blob sources, the RMSE values of prolate source are generally lower than those of spherical sources. This is also evident in Fig. 4.4.1, where PRO models generally show lower residuals. Exceptions are the models with Ds and Inf+Ds material properties.

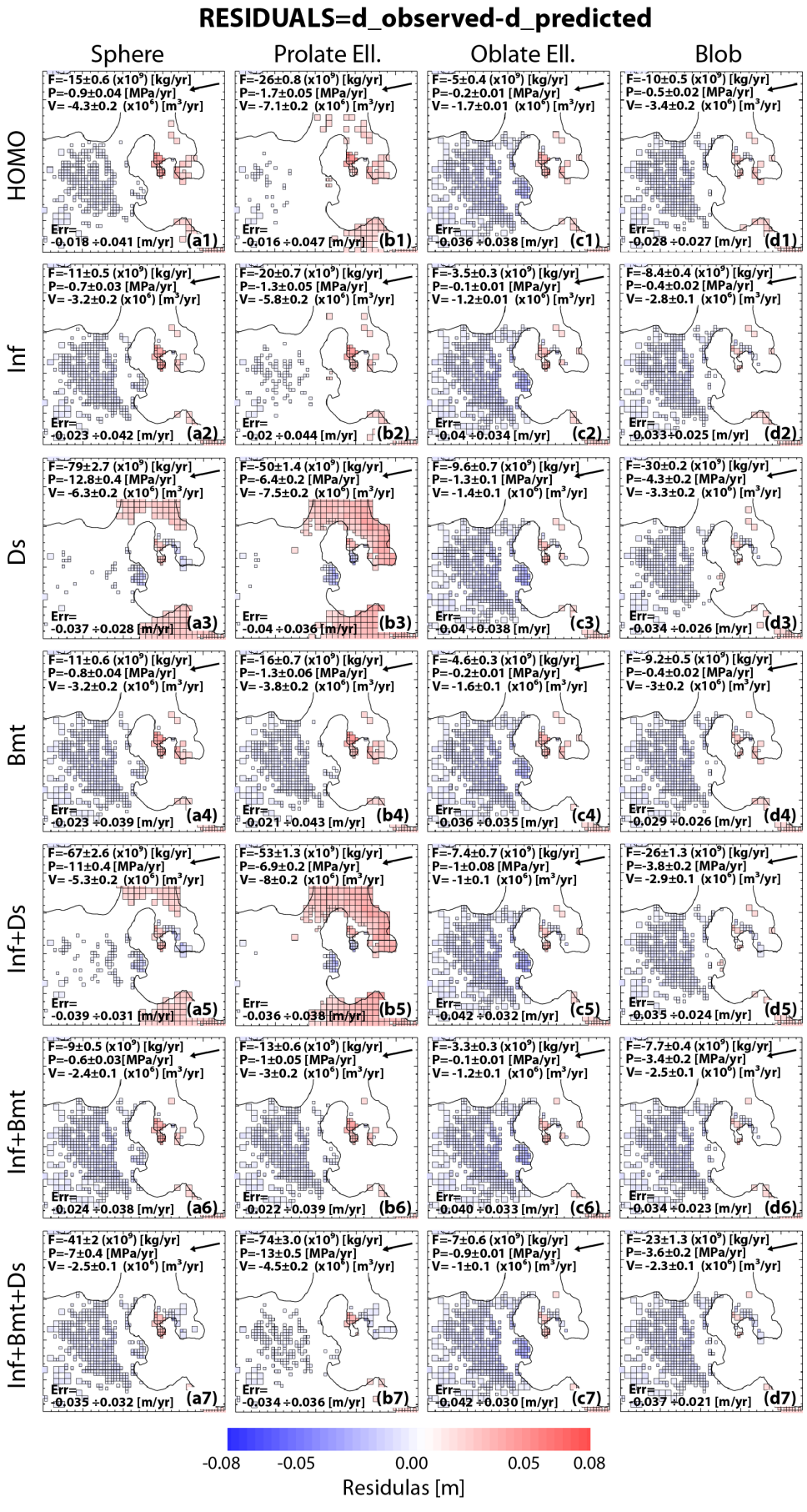

Figure 4.4.1. Residuals (observed data – predicted data) of 28 models (4 magma chambers x 7 material property distributions). *Only quadrants residuals > 1cm and < -1 cm are plotted. Colors of all panels refer to the scale at the bottom of the grid. UTM coordinates are not plotted to simplify the figure. As spatial reference, the southwest corner of the squared area (side of 23000 m) has UTM (zone 56M) coordinates: x= 394860 m, y=9520893 m. The black arrow in the upper corner of each panel shows the horizontal projection of the LOS vector towards the direction of the satellite. Letters group models with same source of deformation, numbers group models with same distribution of material properties. The best estimates for the pressure (P), and volume (Vol) are reposted as well as the range of residual values (Err).*

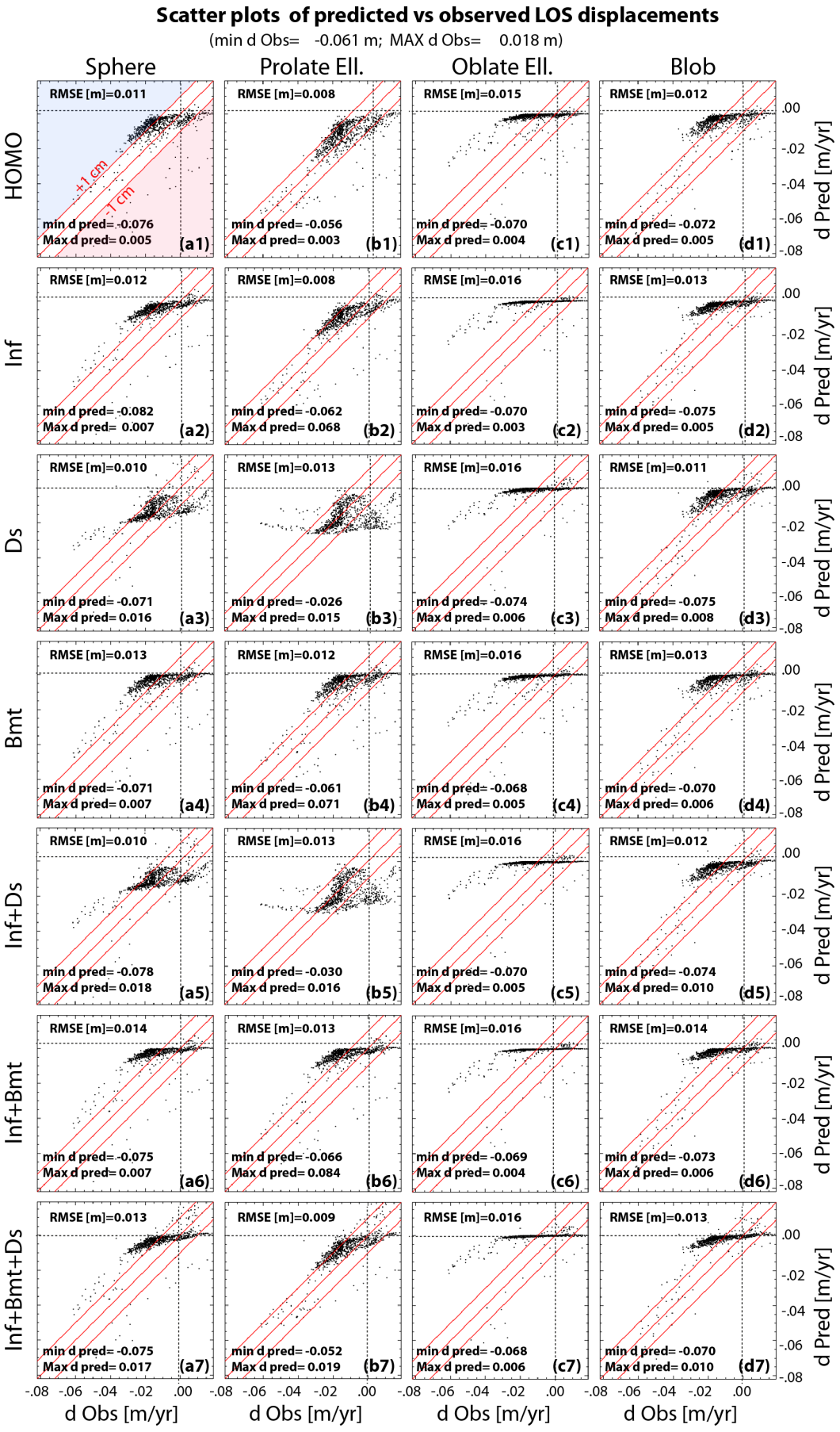

Figure 4.4.2. Scatter plots of the predicted data (d Pred) vs observed data (d Obs) of 28 models (4 magma chambers x 7 material property distributions).

In the panels, the dashed lines indicate the zero value for both predicted and observed data. The central red line represents the diagonal position of perfect predictions (d Pre=d Obs). The other two red lines are located at +1cm and -1cm from the diagonal and identify a buffer zone that represents the accuracy of the InSAR. The minimum and maximum observed values are reported at the top of the grid. Minimum and maximum predictions are reported in each panel. Letters group models with same source of deformation, numbers group models with same distribution of material properties.

Source strength estimates

For every magma chamber, two trends of flux and pressure distribution are recognizable. We divide them into lower and upper trends (Fig. 4.4.3, dashed and solid lines, respectively), corresponding to models not having the dike complex and having the dike complex, respectively. The lower trends include models with homogeneous property distribution, infill, Bmt, and Inf+Bmt. These trends show a decrease in flux and pressure estimates from the homogeneous case to the case in which Infill and the Bmt regions are combined. It is important to note that models with Inf and Bmt show similar flux and similar pressure estimates (Fig. 4.4.3, a and b), although the Ulos predictions are very different (Fig. 4.4.2, a-c, 2 and 4). Changing the geometry of the magma chamber, these trends span over different flux and pressure values. The highest values reached by the prolate source are followed by trends that span lower values of estimates corresponding, in decreasing values, to the spherical source, the blob source and the oblate source, in order. A noticeable difference between flux and pressure lower trends is that the flux lower trends are more spread, while the pressure lower trends are more flat.

The upper trends show contrasting behaviors for different magma chamber shapes: decreasing estimates from Ds, Inf+Ds, and Inf+Ds+Bmt are common for oblate, blob, and spherical sources. The trend of the model with a prolate magma chamber outstands the general upper trends due to reasons related to the design of the model. In fact, contrary to the other sources, the bottom part of the prolate magma chamber is not totally included in the dike swarm body. This means that in the case of Ds and Inf+Ds properties configurations the bottom part of the source acts directly on relatively soft extra-caldera deposits, hence the lower estimates with respect to the trends of the other sources.

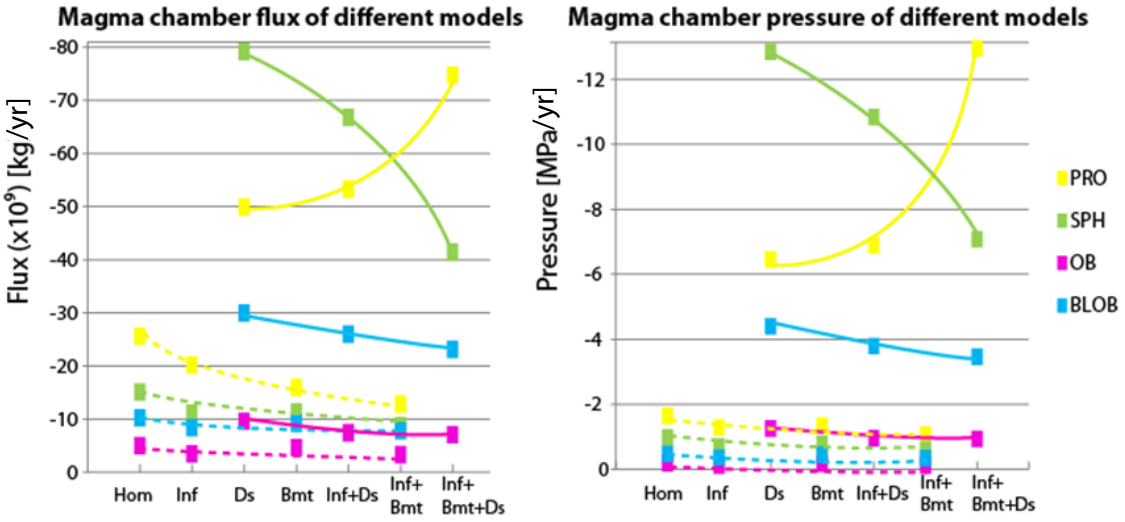

Figure 4.4.3. Estimates of fluid flux and drop of pressure for 28 models with different material properties setting and different magma chamber shapes.
Lower trends (dashed lines) connect models in which the dike swarm block is not present, while upper trends (solid lines) connect models in which the dike swarm block is present. (a) Estimates of fluid flux for all tested models. (b) Estimates of drop of pressure for all tested models.

4.5 Results of Rabaul inverse model using a 3-D source array

The domain of the reference model used for the computation of the forward solutions that are used to build the Green matrix at the base of the FEM-inversion is modeled by a hemisphere whose volume is divided into regions of different material properties and elements (see chapter 4.1). The far field of the domain is represented by a pinned (Ux=Uy=Uz=0) hemispherical surface having a radius of 50 km and centered in the center of the caldera. The free surface (zero stresses) has the shape of the topography.

Following the indication provided in the methods section (chapter 3.8), the domain is partitioned into two main parts: a first part made of 6 region whose shape, size, and material properties are already described in a previous section (chapter 4.1); the second part is a rectangular prism totally included in the dikes part and characterized by the same material properties. The two parts are then tied together along the sides of the prismatic array. The rectangular prism is made up of two regions (Fig. 4.5.1, a): a prismatic core that represents the source array, meshed with 17,280 cubic hexahedral elements (C3D8) of 150 m side, and a surrounding shell of 150 m thickness, meshed with a layer of cubic hexahedral elements (C3D8). All other regions of the domain are meshed with tetrahedral elements (C3D4). Characteristics of the mesh and the problem size are summarized in Tab. 4.5.1.

(Part-n) Region	N° of elements	N° of nodes	Element type
(Part-2) Sources array	17,280	19,437	linear hexahedral elements of type C3D8
(Part-2) Source shell	4,480	8,972	linear hexahedral elements of type C3D8
(Part-1) Dike swarm	71,288	15,254	linear tetrahedral elements of type C3D4
(Part-1) Caldera infill	13,720	3,276	linear tetrahedral elements of type C3D4
(Part-1) Extra caldera dep.	39,824	9,256	linear tetrahedral elements of type C3D4
(Part-1) Baining Mtns.	12,809	3,369	linear tetrahedral elements of type C3D4
(Part-1) Lower crust	3,669	875	linear tetrahedral elements of type C3D4
(Part-1) Mantle	524	175	linear tetrahedral elements of type C3D4
Cubic source	16	25	Hydrostatic hexahedral element F3D4
Total	**163,618**	**52,527**	**157,579 (total number of variables)**

Table 4.5.1. Mesh characteristics and problem size of the FE model with one cubic source of mass flux. Mtns.=mountains, dep.=deposits.

Cavities equivalent to cubes made of eight hexahedral elements of 150 m side (Fig. 4.5.1, b) that belong to the source array (Fig. 4.5.1, b) represent the volume and position of the cubic sources whose strength will be calibrated during the inversion process. The cavities have non-overlapping elements, that is, each hexahedral element is associated with one cavity and thus removed only once to generate one cavity. This way, from a total of 17,280 hexahedral elements constituting the sources array, we obtain an array of 2,160 cubic cavities or sources of 300 m side (Fig. 4.5.1, a), with 9 layers of sources in the z-direction, 16 in the y-direction, and 17 in the x-direction. The sources are generated by removing the eight elements and coating the cavity with hydrostatic elements to take into account the flux of magma responsible for the expansion of the sources. The cavity thus formed is considered to be full-filled with fluid, but able to accommodate its volume to the input of new fluid or to the drainage of fluid from the cavity. The analyses performed involve hydrostatic fluid elements that allow us to generate a source overpressure in the cavity by a positive or negative flux. The fluid properties used for the forward analyses are the same calculated for Rabaul magma (4.1.2). The unit flux of magma, applied to each unit source, is fully described by its amount ($10x10^9$ kg), the magma density (2370.27 kg/m^3), and the magma bulk modulus ($4.50x10^9$ Pa).

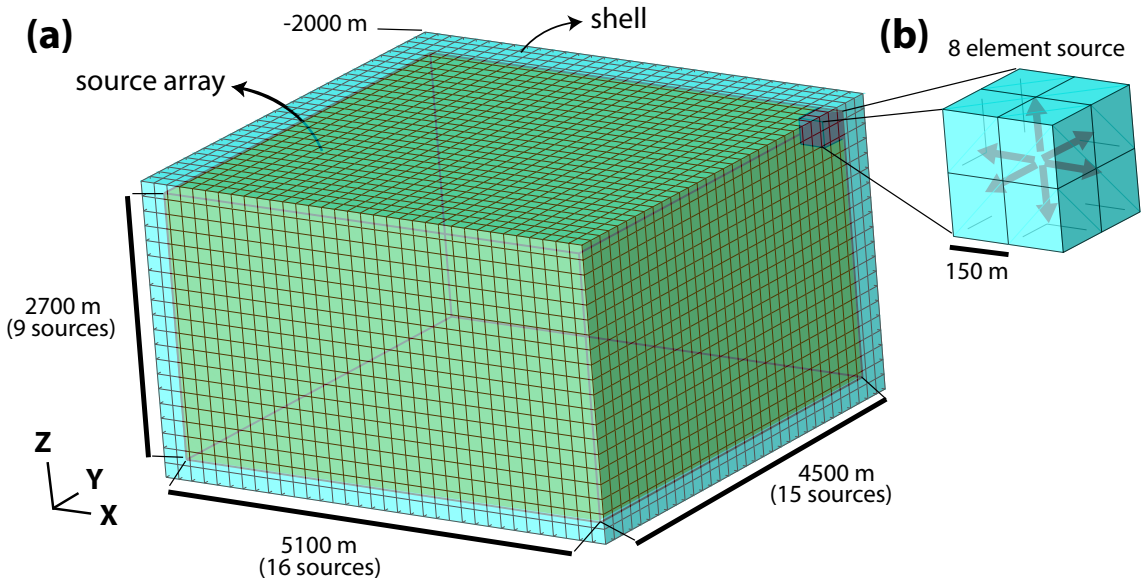

Figure 4.5.1. Mesh of cubic hexahedral elements of the source array.
(a) Source array mesh (yellowish) and the surrounding shell (blue). (b) Eight cubic elements that, being removed, form the cubic cavity on whose walls a pressure is applied due to the flux of magma (in this case, the arrows indicate an expansion of the cavity).

As suggested in the methods section 3.8.2, in order to obtain a consistently good FEM solution approximation for all the array sources, we built a shell made of one layer of cubic hexahedral elements of 150 m side around the prismatic array of cubic hexahedra elements of the sources (Fig. 4.5.1).

The rectangular prism of sources and shell is then located in the middle of the caldera. The center of the sources and their position relative to the seismicity at Rabaul caldera are illustrated in Fig. 4.5.2. As the goal of the models is to study the flux of magma in the shallow reservoir already identified by other authors (*Finlayson et al.*, 2003; *Bai and Greenhalgh*, 2005; *Johnson et al.*, 2010), we confined the rectangular prismatic volume between -2000 m and -5000 m depth, ignoring the feeding dikes from below and the shallower dikes that connect the reservoir to the Tavurvur eruptive center. The rectangular prism is thus fully included in the dike-swarm part.

The prism, equivalent to the array if sources, needs to be bigger than the ideal magma chamber in order to limit the effects of the boundaries and account for the boundary conditions applied to the array of sources during the inversion process. The prism considered is smaller than the entire velocity zone identified by Finlayson et al. (2003). Although this looks like a limitation, it is not conceptually wrong due to the fact that the low velocities could represent damaged areas instead of volumes of partially molten rocks (magma). In addition, portions of the low velocity zone are inconsistent with the hypocenters location (Fig. 4.5.2, b, c, and d). Representing the entire velocity zone with cubic sources would be a very conservative choice, but computationally unaffordable. In the end, although our prism of hexahedral elements does not occupy the entire low velocity zone, it represents most of the low velocity zone imaged by the tomography and laterally encloses the hypocenters. This way, considering the hypocenters as lateral boundaries for the magma storage zone in the upper part of the reservoir, we estimate that the volume of sources investigates the possible source distribution in a conservative way. The depth of 5000 m is far below the deeper hypocenters registered along the elliptical faults and below the bottom of the shallow chamber imaged by the tomography, ensuring the investigation of the possible shallow reservoir of magma constrained by the geophysical studies.

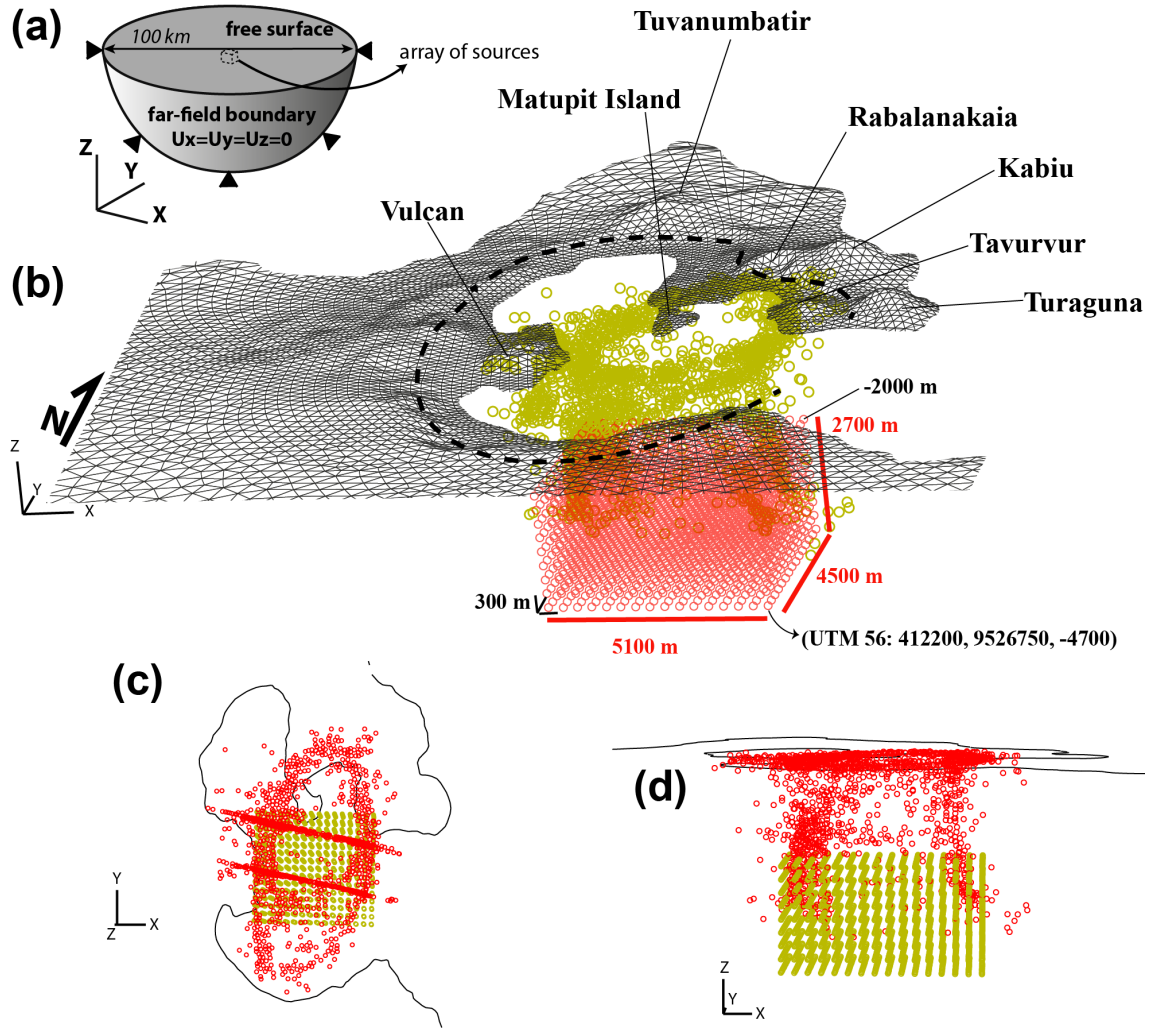

Figure 4.5.2. Position of FE source array in relation to the seismicity. *(a) Extension and boundary condition of the model. For all models, positive y-direction corresponds to the North direction and positive x-direction corresponds to East direction. (b) Meshed topography of Rabaul caldera. Position of hypocenters and epicenters digitalized from Saunders (2001) (yellow circles). Centers of FEM 8-element cubic sources are marked with red circles. The shallower south-west corner of the array is located at the position: 412200, 9526750, -4700 UTM (zone 56). The dashed black line indicates the border of the caldera. (c-d) Vertical and north view of relationship between the seismicity and the source position.*

We tested the solutions of the flat FEM by comparing them to the solutions generated by the corresponding McTigue analytical model. We tested the validity of the FEM for the worst case misfit scenario generated by a source at the corner of the source array. We tested the solution for radial (Ur) and vertical (Uz) displacements at 2,335 nodes of the flat free surface (Fig. 4.5.3) of a model having homogeneous material properties distribution, with Young's modulus equal to 10×10^9 Pa and Poisson's ratio equal to 0.25. Displacements in both FEM and analytical model are generated by an overpressure of 30 MPa. The FEM solutions are in very good agreement with the reference analytical solution (Fig. 4.5.3). Considering a 5% threshold of misfit acceptance, the found maximum misfit of about 2% for the Uz component confirms the validity of the model.

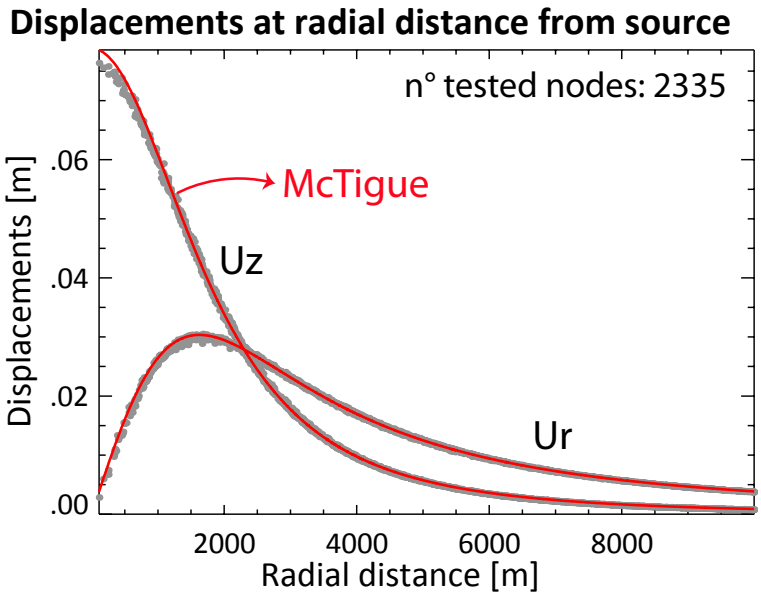

Figure 4.5.3. Test for the validity of the FEM model.
Ur and Uz displacements of points on the flat free surface, at radial distance from a source on the corner of the source array, are plotted for the FEM solution (gray dots) for the relative McTigue (1987) solution (solid red lines).

The forward solution for a distribution of displacements at the free surface of the FEM, caused by a distribution of expanding cavities, is the superposition of the displacement distribution generated by each of the sources. The forward solution takes the form:

$$\mathbf{Gq} = \mathbf{d} \tag{4.5.1}$$

where G is a matrix of Green's functions each representing the impulse-response of the system to the single source of deformation (impulse-response function, IRF), $\mathbf{q}$ is the vector of the source strength (flux), and $\mathbf{d}$ is the vector of observed displacements. Each component of the Green's function matrix, $\mathbf{G}_{ij}$, is the predicted displacement, caused by the i-source, for the location j projected onto the LOS vector, $\mathbf{n}$:

$$\mathbf{G}_{ij} = \mathbf{u}_{ij} \bullet \mathbf{n} \tag{4.5.2}$$

where $\mathbf{u}$ is the vector of three-component displacements of the FEM generated at the location j by the unit flux of magma in the cavity i.

The *j-th* location corresponds to the position of InSAR data at which the FEM solutions need to be sampled in order to build the Greeen's function matrix. We tested the interpolation scheme used to sample the FEMs solutions at the InSAR data position by comparing the McTigue analytical solutions, directly computed at the i-th positions, and the analytical solution resulting from the interpolation, at the *i-th* positions, of a solution first computed at the nodesof the flat FEM free surface. The misfit between the two solutions is low (Tab. 4.5.2) and shows that the interpolation scheme is valid.

802 nn of nodes in the misfit evaluation process of the interpolation method (Misfit calculation following Williams and Wadge (2000)):				
Ux	Uy	Uz	Ur	Ulos
0.00071998762	0.00089706817	0.0010383736	0.00063850338	0.00081200729

Table 4.5.2. Results of the test of interpolation method.

The deformation in the FEMs is driven by a unity mass flux, q, equal to $10x10^9$ kg into each cubic cavity, thus simulating the quasi-static displacement. Each cavity represents an expanding source activated one at a time. A total of 2,160 sources are acivated for a same amount of FE forward models, renerating. The impulse-response functions (IRFs) thus generated by the FEM are assembled in the matrix of Green's functions for displacements, **G**, that represents the impulse response of the system to all sources. The hexahedral elements around each active source, not used to generate the cavity and thus being part of the non-active sources, have material properties of the dike swarm part. The computational time and resources needed to run 2,160 forward models are summarized in Tab. 4.5.3.

Computational resources	**Single forward model**	**Total 2160 forward models**
IDL computation time Abaqus computation time	INP GENERATION (SEC)=27 USER TIME (SEC) = 129.90 SYSTEM TIME (SEC) = 2.6 TOTAL CPU TIME (SEC) = 132.50 WALLCLOCK TIME (SEC) = 140	360,720 s (~100.2 hrs., ~4.18 days)
TOTAL TIME	WALLCLOCK TIME (SEC) = 167	
Storage memory	372 kb	803,520 kb (~0.8 GB)

Table 4.5.3. Computational time and resources.
Computational time and resources for the single forward model and for the 2160 forward models run using a laptop PC with dual core CPU, 2.20 GHz, and 4 GB RAM.

The relationship in equation (4.5.1) is appended to a form that includes a priori information such as the data weight and constraints to minimize the roughness of the 3-D source strength distribution. In fact, a Laplacian operator **L** (*Freymueller et al.*, 1994) is appended to **G** allowing to control the solution roughness and impose expansion boundary conditions on the three dimensional source array. A damped least square method (DLS) is used to solve for the parameters $\hat{\mathbf{s}}$. The forward solution takes the form:

$$\hat{\mathbf{G}} = \begin{pmatrix} \mathbf{WG} & \mathbf{xy1} \\ \beta\mathbf{L} & \mathbf{000} \end{pmatrix}; \quad \hat{\mathbf{s}} = \begin{pmatrix} \mathbf{q} \\ a \\ b \\ c \end{pmatrix}; \quad \hat{\mathbf{d}} = \begin{pmatrix} \mathbf{d} \\ \beta\mathbf{0} \end{pmatrix} \tag{4.5.3}$$

where **W** is the matrix of the data weights, **L** is the Laplacian smoothing operator and β is the damping parameter that controls the relative importance of minimizing the roughness of the solution versus fitting the data. L is built as discussed in chapter 3.7.3. We assume no sources outside the three-dimensional source array and apply Dirichlet-type boundary conditions (*Wang and Anderson*, 1982) to $\hat{\mathbf{s}}$. The relationship is conditioned to account for phase ramping in the InSAR image caused by the uncertainties in the satellite position (*Massonnet and Feigl*, 1998) by appending **G** with three column vectors corresponding to the centroidal position of the quadrant (x and y) and a unity vector. The coefficients for a plane $ax+by+c$ are appended to the source vector **q**. This allows simultaneously fitting the sources strength and a plane.

The value of the damping parameter, β, that weights the smoothing factors, is determined from the trade-off analysis between misfit of the predicted displacements versus the observed displacements and the roughness of the FEM-based inversion solution. The trade-off curves allows to identify the preferred damping parameter; in fact, by performing the inversion using the value of the beta parameter at the knee of the curve, we optimize the inversion for solutions that are a good compromise between the misfit and the complexity of the model.

The estimates, **q**, of the source strength are scaled by the unity source strength, used to

generate the Green's matrix, in order to obtain the solution of the model for the flux. Solutions for change in pressure due to the flux can also be estimated. In fact, the change in pressure in the cavity generated by the flux of fluid is an output of the hydrostatic fluid flux analysis in Abaqus. Being the change in pressure at each source linearly correlated to the flux injected in the source, we can scale the unity hydrostatic change in pressure in each cavity by the correspondent source estimate, s_i.

$$P_i = Pun_i * s_i$$

Where P_i, Pun_i, and s_i are the change in pressure that predict the displacements, the change in pressure generated by the unity flux, and the estimate of the source strength at each *i-th* source of the array, respectively.

By doing this, we obtain the distribution of change in pressure among the source array that predicts the displacements.

Synthetic test

We tested the inversion strategy by inverting synthetic LOS displacements generated by a cubic cluster of 27 FEM sources of he array having 10x10^9 km flux of fluid (total of flux of magma in the system: 270x10^9 kg). The used fluid has density equal to 2370 kg/m^3 density and bulk modulus of 4.5x10^9 Pa selected from the source array generated for the Rabaul 3-D model.The sources used for the test are organized in three layers of 3x3 sources each and are marked with a black frame in Fig. 4.5.4 (panels i, l, and m). The chosen beta value at the knee of the trade-off curve (Fig. 4.5.4, a) ensures a very good agreement between predicted and synthetic displacements (Fig. 4.5.4, b) and thus a very small misfit (Fig. 4.5.4, a). Considering that the synthetic data we inverted do not have errors, a very small misfit is desirable. The solutions found (Fig. 4.5.4, f-p) are in good agreement with the sources used to generate the synthetic deformation: the overall flux of fluid predicted by the inversion, 270.53x10^9 kg, is very similar to the one used to produce the synthetic deformation.

The distribution of sources predicts a source slightly shallower than the one used to generate the synthetic displacements. This is due to the fact that the shallower sources have a stronger impact on the deformation signal, thus resulting in shallower estimates. This aspect needs to be taken into account while interpreting the results. Also, it is important to note that, although the synthetic source used is a cubic distribution of sources, the predicted source appears smeared, with a smooth rounded shape. This is perfectly acceptable and understandable due to the fact that, by applying a Laplacian smoothing operator, we want to find a smooth solution and therefore we are not able to predict sharp edges and corners as the ones of the cubic distribution of synthetic sources.

Resolution

To investigate the model resolution, we created a synthetic distribution of unity sources in a checkerboard pattern illustrated in Fig. 4.5.5 (1-3). The checkerboard test gives an indication of how well details are resolved by the inversion used. Resolution is higher at shallower levels (Fig. 4.5.5, a-c), but rapidly decreases for deeper levels. At the sides of the array of sources, the resolution is higher due to the fact that the data are distributed on the land, around the array, and no data coverage is present over the bay. Squared shapes of about 1 km side are still recognizable in the first three levels and at the sides of the fourth, while at deeper levels the resolution is lower and the elements of the synthetic sources pattern are smeared.

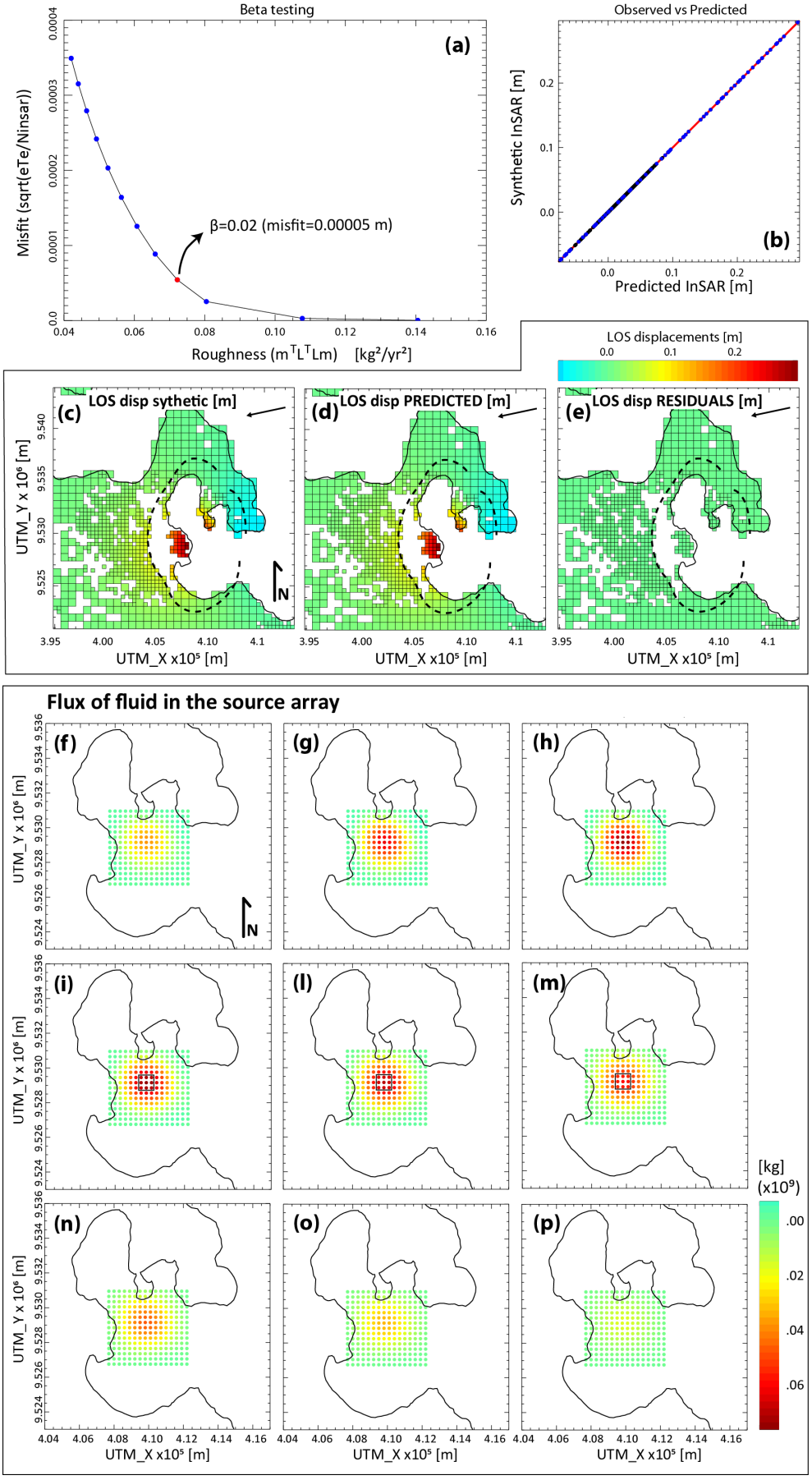

Figure 4.5.4. Testing the inversion process: inversion results for a synthetic deformation. *(a) Calibration of the model, the L-curve gives the trade-off between misfit (RMSE) and model roughness. The preferred solution is obtained for value of beta at the knee of the L-curve. (b) Synthetic versus predicted LOS displacements. The diagonal red line shows the line of perfect correspondence between synthetic and predicted solutions. Blue dots represent displacements at points inside the caldera; black dots represent displacements that are mainly out of the caldera borders. (c) Synthetic LOS displacements. (d) Predicted LOS displacements. (e) Residuals between predicted and synthetic LOS displacements. (f-p) Solutions of the FEM-based inversion. The solutions represent the flux of fluid at each source of the source array. The source solutions are shown for each of the 9 levels of 15x16 sources at different depths. The 27 sources used to generate the synthetic deformation are marked with a black box. Red colors represent a positive flux that means that a mass of fluid is entering the source.*

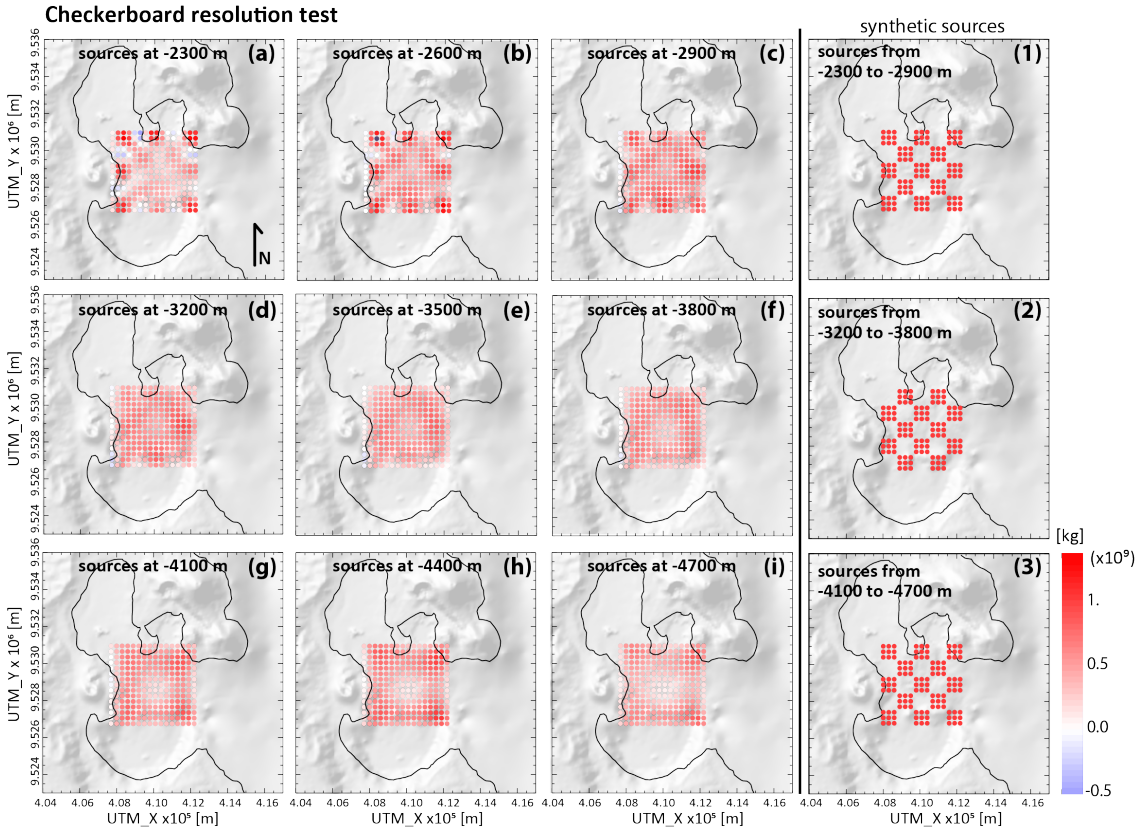

Figure 4.5.5. Results of the checkerboard resolution test.
For each line of panels (e.g. a-b-c), the synthetic sources pattern to be obtained through the inversion is shown on the last panel (e.g. 1). (a-i) Estimated models from the checkerboard input on the right. (1-3) Checkerboard pattern used for the resolution test.

Regularized inversion

We estimated the strength distribution of sources for the InSAR data reduced in chapter 4.3 by inverting the equation (4.5.3) and sweeping through a range of damping values of β. The result is an L-curve of points where reducing the misfit is obtained at the expense of increasing the roughness of the model solution (Fig. 4.5.6, a). The preferred solution is visually identified on the L-curve at its knee and is a compromise between fitting the data versus minimizing the solution roughness and satisfying the boundary conditions. The preferred damping value, β=200., corresponds to an RMSE of 0.0091 m/yr and is chosen in a way that data are neither significantly over-fit, nor under-fit with respect to the estimated data errors. This misfit is acceptable because it has the same order of magnitude as the roughly estimated accuracy (0.01 m/yr) of the InSAR data used for the inversion.

Observed versus estimated LOS displacements (Fig. 4.5.6, b) show diagonal distribution of points scattered along the diagonal mostly included in the 1 cm buffer area, roughly representing the accuracy of the observed InSAR displacements. Almost all the points located outside the caldera borders (black dots in Fig. 4.5.6, b) fall into the 1 cm accuracy threshold. The highest misfit are recorded for the points inside the caldera border (blue dots in Fig. 4.5.6, b (I)) and in particular for the areas north of Matupit Island (MI) (Fig. 4.5.6, e (I)). These are the points with highets misfit that fall out of the 1 cm accuracy threshold (Fig. 4.5.6, b).

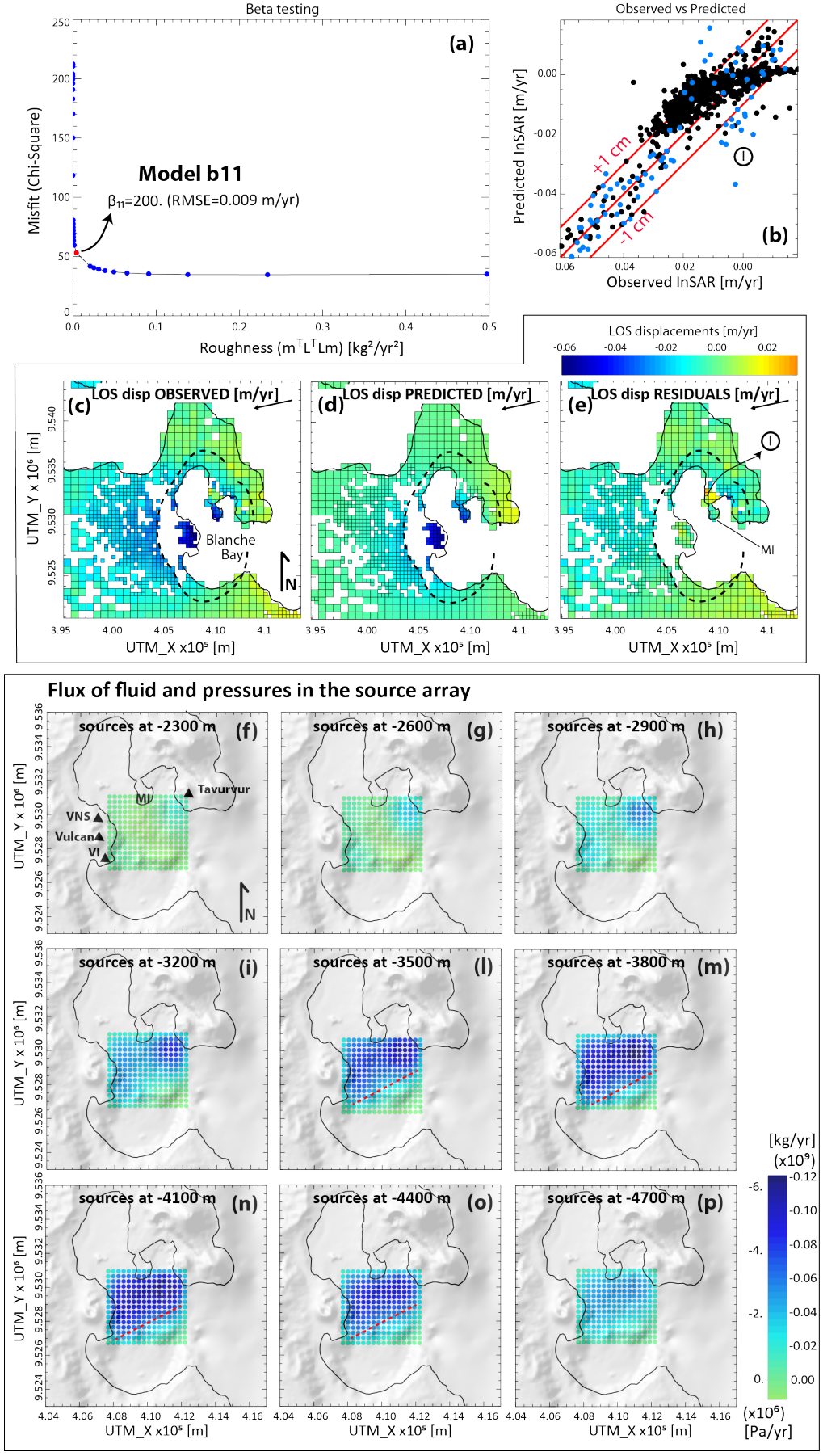

Figure 4.5.6. InSAR data inversion with beta=200. (model b11). *(a) Calibration of the model. The L-curve gives the trade-off between the Chi-Square values (calculated between the observed and the predicted displacements) and model roughness. The preferred solution is obtained for the value of beta at the knee of the L-curve. (b) Observed versus predicted LOS displacements. The central diagonal red line shows the line of perfect correspondence between observed and predicted solutions. The two red lines located at +1cm and -1cm from the diagonal identify a buffer zone that represents the accuracy of the InSAR. Blue dots represent displacements at points inside the caldera; black dots represent displacements of points that are mainly out of the caldera borders. (c) Observed LOS displacements. (d) Predicted LOS displacements. (e) Residuals: observed-predicted LOS displacements. (f-p) Solutions of the FEM-based regularized inversion at different depths. The solutions represent the flux of fluid (or change in pressure) at each source of the source array. Blue values represent a negative flux (i.e. a mass of fluid flowing out of the source).*

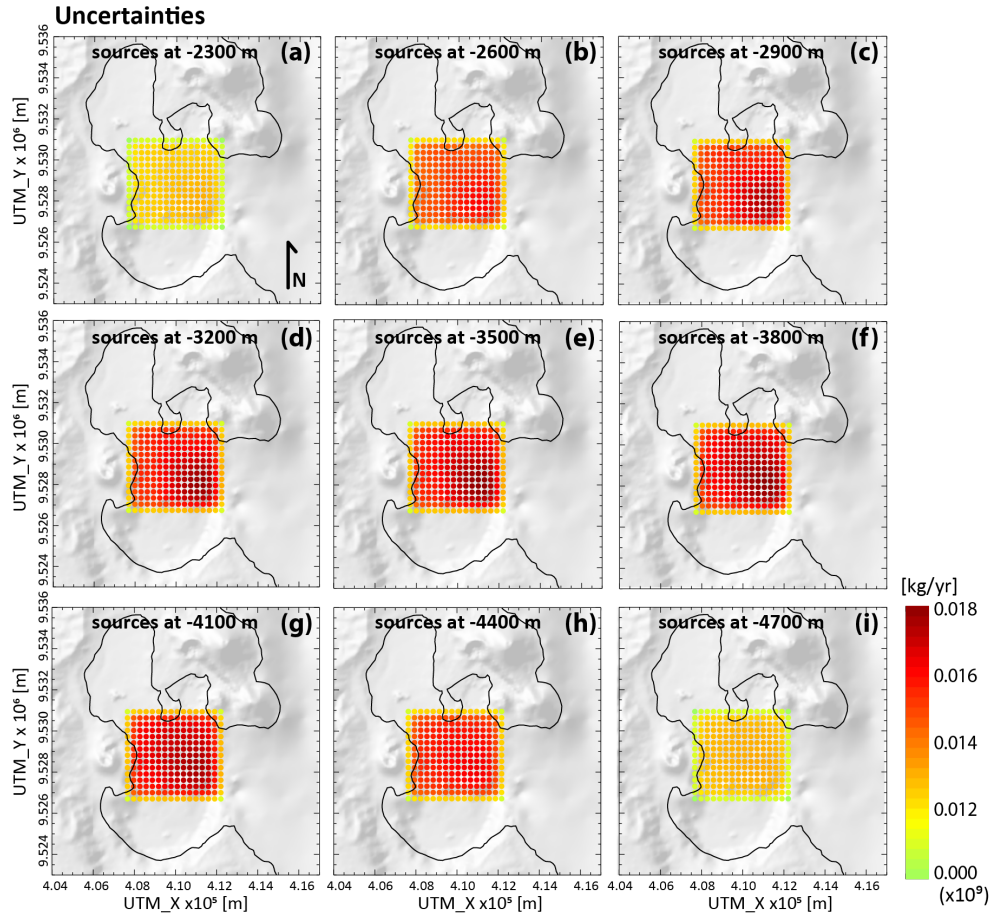

Figure 4.5.7. Model parameter uncertainties of the scaled problem, derived from the covariance matrix.
(a-i) distribution of solution uncertainties at each level of the array of sources.

The solutions of the WLSD inversion show the distribution of fluid flux in the source array, thus identifying the source features required to predict the deformation shown in the InSAR image. The main negative flux of fluid is registered on a diagonal line in the direction Vulcan-Tavurvur. Modulations of this general pattern are shown by local complexities in the flux distribution.

In fact, the overall distribution of clusters of negative fluxes is elongated diagonally in the direction of Vulcan cones and the active Tavuvur cone, showing a diagonal trend between these eruptive centers. Values of flux vanish on the shallower and deeper layers of the source array (Fig. 4.5.6, f, g, and p). The main features are identified as two lobes that connect to form the diagonally elongated distribution, whose diagonal aspect is particularly emphasized on the southern side (red dashed line in Fig. 4.5.6, l-n). The first lobe, laterally isometric, is located on the south-west of Tavurvur volcanic center, clearly starting from 2900 m depth (Fig. 4.5.6, h). The flux under this position is quite consistent over all the layers in depth (Fig. 4.5.6, h-p), although it remarkably diminishes in the deeper layer. This lobe looks to be gradually connected in depth to a second lobe, starting at 3200 m, at the western side of Blanche Bay, in front of Vulcan, with a shape slightly elongated north-south (Fig. 4.5.6, i-o). The total magnitude of the source array flux is -74.5x10^9 kg/yr. The maximum negative flux values are located under the first lobe at 3500 m, 3800 m, and 4100 m depth (Fig. 4.5.6, l-n), and under the northern part of the second lobe, north-east of Vulcan, at 4100 m depth (Fig. 4.5.6, n). The highest negative flux is -0.12x10^9 kg/yr reached in the first lobe at 3800 m depth (Fig. 4.5.6, m).

Model uncertainties

The model uncertainties (Fig. 4.5.7) are obtained by computing the model covariance matrix and calculating the square root of its diagonal elements. Results are shown in Fig. 4.5.7. In computing the covariance matrix, we normalized the inverse problem by scaling each equation by the standard deviation of the correspondent data value. The model parameter covariance matrix describes the uncertainties associated with the estimates. The calculated uncertainties are reasonable with respect to the source estimates provided in Fig. 4.5.6. Uncertainties distribution shows higher values for source estimates in the south-east corner of the source array (Fig. 4.5.7, c-g). This is reasonable due to the fact that this area is located far away from the coast line and, therefore, away from the data. Estimates of sources closer to the data show smaller uncertainties (for western and northern sources of the array).

Chapter 5

Discussion

Rabaul caldera and the areas west of it experienced a long, broad subsidence in the period between February 2007 and December 2010, as recorded by ALOS-PALSAR InSAR images. The LOS displacements at Rabaul caldera show a general subsidence with higher amplitude at Vulcan and Matupit Is. and with a longer wavelength at the western side of the caldera. The main goals of this work were to generate a first fully 3-D FEM of Rabaul caldera and use it in a linear inverse analysis of the InSAR data to provide some insights about the shallow magmatic system under the caldera. In pursuing these goals, we provided some strategies to build complex 3-D bodies, whose shapes and material properties were constrained by all information (geological, geophysical, seismc, etc.) available for the area and collected in the first part of this work.

Due to the limitations in constraining the magma chamber shape, modeled as a single cavity in the FEM, and in applying a unique pressure to the cavity walls, the least squares solutions computed within the linear inversion were not satisfactory in terms of insights provided for the shallow magmatic system. This encouraged us to extend our research and move the linear inversion into a more exploratory investigation. We therefore proposed an approach based upon a FEM-based inversion in which we do not prescribe a specific geometry of the source, but rather allow the inverse analysis to look for an arbitrary 3-D distribution of sub-surface sources strength.

In the following sections, we will discuss the main findings of this research work and provide some explanations about the configurations chosen for the models and about the methods used.

5.1 Geometry of the models

All complex 3-D Rabaul FEMs proposed in this study are built by combining, through boolean operations, bodies having complex shapes. The generation of complex bodies was carried out by using the strategies proposed by Ronchin et al. (2013), described in this work in the methods section (3.3.1). The control points for splines, through which the bodies are lofted, are easily obtained combining the information from geological and geophysical studies. The strategy proposed is particularly useful and straightforward in the case of a block that has only one complex side. For the Rabaul model, this is the case of the Baining Mnt. block (4.1.5). This block can be easily compared to the side of a fault. This means that the strategy can be easily applied to build FEMs of faults, allowing a loyal representation of the fault plane. In the case of more complex bodies, with rounded or particularly irregular shapes, attention needs to be paid in choosing the control points of the splines, as very complex splines can make the lofting process impossible. For the Rabaul model, this is the case with the Infill and Dike swarm blocks.

Many authors emphasize the importance of taking into account full 3-D topographic effects when interpreting geodetic measurements at volcanoes (*Cayol and Cornet*, 1998; *Williams and Wadge*, 2000; *Lungarini et al.*, 2005; *Charco et al.*, 2007; *Currenti et al.*, 2008; *Meo et al.*, 2008; *Lyons et al.*, 2012). Topography effects can be significant for magma bodies beneath steep-sided volcanoes (*Segall*, 2010). Although Rabaul area does not present prominent topographic features, such as a high central volcano edifice, it does present steep-sided cones that could affect the solutions of FEMs. We studied the effects of Rabaul topography on the surface deformation of FEMs with a common spherical magma chamber, and with variable material properties (Tab. 4.2.3). In agreement with other authors (*Cayol and Cornet*, 1998; *Segall*, 2010), the results show that both Uz and Ur components are more affected in those areas where the slopes are steeper with a maximum percent misfit average of 6% and 15% for Uz and Ur, respectively. While not large for the Uz component, these misfits are relevant for the Ur component and are sufficiently systematic to suggest the use of realistic topographies for the subsequent Rabaul models of this work.

5.2 On the importance of choosing the material properties

The fact that topographic effects are different for different material properties configurations and also within variations in Poisson's ratio of the soft saturated caldera Infill led us to consider a further investigation of the effects of the material properties of this block. Furthermore, the lack of a unique empirical relation between static and dynamic moduli, especially for the Poisson's ratio, generates uncertainties in choosing this material property whose effects need to be considered.

Although many studies investigate the effects of heterogeneous distribution of material properties, most of them only consider the heterogeneities in terms of stiffness variations (Young's modulus, E) across the domain, keeping the Poisson's ratio constant at a value of 0.25. A Poisson's ratio of 0.25 is widely and uniformly used for all material properties of volcanic models. This is because the volcanic materials that commonly constitute volcanoes are considered to have a narrow range of Poisson's ratio about 0.25 (*Gudmundsson*, 2006; *Bell*, 2000), although most of the time saturated conditions are not considered. Very few studies (*Trasatti et al.*, 2003; *Masterlark*, 2007) also take into account variation of the Poisson's ratio among the complex domain. Considering that the Poisson-solid assumption ($\upsilon = 0.25$) represents the lower boundary of the range of Poisson's ratios for crustal rocks, rather than the bulk average (*Masterlark*, 2007), the models should take into account more carefully the Poisson's ratios used. Other authors (*Hsu et al.*, 2011) pointed out that the variation of Poisson's ratio may play an important role when υ is larger than 0.25 and the rupture source is dilatational such as volcano deformation. As we know, there are no studies that address the problem of the sensitivity to the Poisson's ratio in volcanic models. Thus, we decided to perform a study of sensitivity of the Young modulus and Poisson's ratio of the infill block of the 3-D Rabaul model.

As a result of increasing the incompressibility of the Infill block, generated by increasing its Poisson's ratio, the system responses with smaller displacements (Fig. 4.2.5, g, and Fig. 4.2.7, a). The response of the system also includes a reassessment among the two displacement components, Ur and Uz. In fact, Ur becomes a more predominant component. This is consistent with the fact that more incompressible materials are less prone to change volume, but more prone to change shape to maintain the same volume (incompressible behavior). Thus, in response to a vertical traction, a more incompressible Infill reacts by showing a relative higher lateral reduction (higher Ur) trying to maintain the volume of the body.

Results show (Fig. 4.2.7, a) that the effects of uncertainties in choosing the Poisson's ratio

are more significant in case of materials with lower Young modulus. That is, deformations of soft materials are more sensitive to changes in Poisson's ratio. This suggests that sensitive studies need to be performed when studying deformations of volcanic areas characterized by shallow, weak, and saturated materials.

Based on the fact that the value of 0.25 for the Poisson's ratio is the most accepted, widely used, and undisputed Poisson's value for models, the main objective of this part of the study was to assess the sensitivity of the Rabaul model to this parameter. For the Young modulus of the Infill block of our model (0.2 GPa), a change of Poisson's ratio between 0.15 (value corresponding to loose, weak, and saturated materials (*Wang*, 2000)) and 0.25 implies a variation of 8%, 6%, and 7% in the Uz, Ur component, and Ulos, respectively (Fig. 4.2.5, g). For the displacement studied in this work, these misfits are not a concern as they correspond to values that do not pass the threshold of the instrument accuracy. However, they should be taken into account while modeling higher displacements.

5.3 Effects of Rabaul material properties on the displacements signals

With a further study, we investigated the effects of every block of the Rabaul 3-D model on the deformation signals.

With a spherical source, the weak caldera infill amplifies and shrinks the signal (Fig. 4.2.8). The signal shows a jump in correspondence with the change of material properties, where the edges of the infill reach the surface. In the case of Uz, the effects are mainly confined to the extension of the infill. For Ur, the effects extend out of the infill border in the areas where the topography is more prominent and where the change of material properties is close to the source. No jumps at the edge of the blocks are observed for the blocks that are buried and do not reach the surface (Fig. 4.2.16 and Fig. 4.2.17). This is the case for the dike swarm and Baining Mts block. The first one generates a reduction of deformation due to the fact that they introduce a higher stiffness around the magma chamber (Fig. 4.2.9), while the second shrinks the signal by amplifying it (about 4%) above the magma over an area of about 2.5 times the magma chamber and reducing the signal for further areas (Fig. 4.2.10).

The main result of combined blocks is an amplification of the effects of Baining Mts due to the presence of the infill combined with a dumping effect due to the presence of the stiff dikes swarm block.

The effects of these blocks look about symmetric and concentric for Uz, while Ur shows a generally more complex distribution, possibly due to the combined effects of change in material properties and the topography (e.g. Fig. 4.2.13, b; Fig. 4.2.9, b; Fig. 4.2.12, b). As a rule of thumb, the horizontal component always appears to be more sensitive to the changes of material properties in those areas characterized by a more prominent topography where Ur shows more complex distributions. A similar behavior is also observed in the case of changes in source shape, confirming the importance of taking into account the topography in the FEMs.

The results of combined interaction between Infill and chamber shape are enormously different (Fig. 4.2.15) due to the fact that the displacement fields generated by different chambers are different as well. This is particularly evident in the case of the blob source for which, due to the complex shape of the chamber, the deformation field is not centered above the top of the magma chamber but on a point south of it (Fig. 4.2.15, g-i). This led us to consider all combinations of material properties and

sources to investigate the wide range of signals that can be generated from the interaction between material properties and the chamber shape. As the goal of this study is also to understand the long broad deformation recorded along the west-east profile, we summarized all signals along this profile (Fig. 4.2.16 and Fig. 4.2.17).

With the introduction of heterogeneities in the model, the alteration of the Uz, Ur, and Ulos signals generated by an irregular-blob shape and oblate ellipsoid shape source are mainly localized over an area above the caldera infill and do not extend much beyond the caldera borders. In the case of the spherical and prolate ellipsoid source, the introduction of all heterogeneities affects the shape of the signals in more pronounced and variable ways. This may be related to the fact that the bottoms of the sources deepen with oblate ellipsoid, blob, sphere, and prolate ellipsoid in order. A source that affects deeper areas of the model generates stresses that interest a wider area at the surface and that are affected by all the material properties that constitute the volumes above. Shallower sources produce a more localized deformation affected by the material properties above and around the source which, due to the reduced space between the magma chamber and the surface, includes fewer parts. This is also consistent with the fact that in both the blob and the oblate ellipsoid source cases, the presence of the Bmt block (which in these models is far below the bottom of the sources) does not significantly modify the HOM signal (blue solid line), generating an overlapping of the two signals along the entire profile (Fig. 4.2.16, a-f).

In the case of the oblate and blob source, for all material properties configurations, except for the presence of the single Bmt, which does not have effects as discussed above, the Uz signals are shrunk whereas the Ur signals are shrunk and amplified. Infill and Ds are therefore responsible for the signal shape change: Ds part (violet solid line in Fig. 4.2.16) shrinks and amplifies Ur for both sources; the additional presence of the infill amplifies these effects (Fig. 4.2.16, c and d). Ulos variations are concordant with the shrinkage of the Uz and Ur signals. For shallower sources like the blob and the oblate one, the part of soft sediments is the dominant part that controls signal shrinkage. In fact, when the infill block is present, the peturbations of the signals are mainly restricted above the infill block. It is important to note that LOS signals show slightly asymmetrical shapes with positive values in the eastern part of the caldera and with a slightly longer negative tail on the western side (Fig. 4.2.16, e and f). This is due to the geometry of the LOS on which the deformations are sampled. Although asymmetry is evident for all signals of blob and prolate sources, none of the signals generated by different material properties configurations can account for the long wave tail that is registered by the InSAR data on the area west of the caldera. This may suggest a deeper source or a source whose bottom reaches deeper depths.

As expected for sources that reach higher depths, this is the case with the sphere and prolate source: the Ds presence modifies the signals of sphere and prolate ellipsoid in a more significant way with respect to the signal produced by the blob-shaped and oblate ellipsoid (Fig. 4.2.17 and Fig. 4.2.16, a-f). This suggests the importance of introducing the dikes in the model whenever we model a deeper source. In the case of the sphere and prolate source, the signals have wider length and produce stronger asymmetric Ulos shapes with a long tail of negative values in the western side outside the caldera and higher positive values on the eastern side of the caldera (Fig. 4.2.17, e and f). This is consistent with the observed LOS displacements, thus suggesting that a deeper source may be responsible for the long wave displacement of the area west of the caldera.

5.4 Model assumptions

As the main goal of this study is to understand the causes of the subsidence recorded between February 2007 and December 2010 through the use of FEM and to better understand the shallow magmatic system, we here discuss some assumptions that justify the use of FEMs proposed in this work.

After the eruption of October 2006, a long period without clear deformation lasting until about July 2007 was observed. After this long period of no deformation, a long period of steady subsidence started. Although we cannot totally exclude that a visco-elastic relaxation component of the deformation occurred after the October 2006 eruption, we do not observe a prominent visco-elastic component among the sources of the observed behavior of the Rabaul system. In other words, we do not observe the signature of visco-elastic relaxation that would present a continuous subsidence with decreasing intensity in time. Therefore, we assume that an elastic model could reasonably represent the system's response to a contracting source.

The lack of information about the petrography of the volcanic products erupted during the continuous vulcanian eruptions of the investigated period pushes us to consider the products erupted in 2006 as representative. Thus, the properties of the fluid used in our simulations are calculated based on the petrographic data of the magma erupted in October 2006. The use of October 2006 magma properties to model the source of the following sub-continuous eruptions is justified by a report of RVO (*Smithsonian Institution-National Museum of Natural History*, 2013). In the report, the RVO confirmed the presence of 2006 magma in the shallow magmatic system by attributing the June-July 2007 eruptions to magma remaining from the October 2006 eruption.

The properties of the fluid are assumed to be constant during the period of investigation. This goes along with the condition of a half-opened system that we simulate with our model. In assuming the system half-opened, we assume that the mass of fluid can only flow out of the shallow magmatic system and no new fluid is hosted in the system (i.e. fed from deeper reservoirs). Although we cannot exclude the feeding of new magma from deeper reservoir(s), we consider the half-open system condition to be a reasonable approximation. This is based on the fact that the general constant subsidence recorded by the continuous GPS at Matupid Is. and the absence of petrographic changes in the volcanic products (*Smithsonian Institution-National Museum of Natural History*, 2013) suggest that no significant replenishments of the shallow reservoir occur during the study period.

5.5 Influence of material properties and magma chamber geometries on deformation predictions and pressure estimates

Inverse modeling is a common strategy to test how well the models predict the observed deformation and to estimate the strength of the source. The strength of source investigated in the 28 inverse models proposed in Chapter 4.4 is a flux of fluid in the cavity of the FEMs that simulates a quasi-static deformation. The fluid used has an average density of 2370.37 kg/m^3 and average bulk modulus of 4.50x10^9 Pa. These properties have been calculated using the formulas proposed by Huppert and Woods (2002), considering the characteristics of the volcanic andesitic products erupted from Tavurvur during the 2006 eruption. The density calculated is slightly lower than the lower value of the andesite density range, 2400-2700 kg/m^3, as described in the literature (*Judd et al.*, 1989; *Folch*

and Martí, 2009). This is consistent with the fact that the formula of Huppert and Woods (2002) used is a more realistic and complete calculation, as it also takes into consideration the less dense and more compressible exsolved gas phase.

A weighted Quad-tree reduction allowed us to perform the inversion with a more manageable number of data, reducing the original $23x10^3$ data to 802 data in a way that the interesting area west of the caldera, which experienced a long, steady, and broad subsidence, is well represented by good coverage of data (Fig. 4.3.2).

By inverting models with different magma chambers and different material properties configurations, we wanted to investigate the improvements in data predictions and finally choose the best model configuration, with particular attention to the constant, long wavelength deformation west to the caldera, as well as to the highest LOS displacements of the signal at Matupit Is. and Vulcan.

Inversions confirm the observations from the profiles (Fig. 4.2.16 and 4.2.17). Sources that reach higher depths (spherical and prolate sources) generally better predict the long wavelength of LOS displacements west of the caldera, while shallower sources (oblate and blob sources) are not able to satisfactorly predict these displacements. In particular, none of the models with blob and oblate source is able to predict the long wavelength signal west of the caldera, leading to negative residuals distributed in a delta shape over this area (Fig. 4.4.1, c1-7, d1-7). This led us to suppose, once more, that deeper sources are responsible for the signal in this area. In fact, some of the models with prolate and blob source nicely predict this part of the signal (Fig. 4.4.1, a3, a5, b1-3, b5 and b7). Even though some of the models with spherical and prolate source can predict the long wavelength signal well, very few can predict those at Vulcan and, except the prolate source combined with Infill+Bmt+Ds (Fig. 4.4.1, b7), none of the models can adequately predict displacements at Matupit Is. In general, the models with the complex blob magma chamber can better predict the strongest displacements at the center of the caldera, at Vulcan and Matupit Is. (Fig. 4.4.1, d1-7), but they consistently miss to predict the long wavelength deformation west of the caldera for all material properties configurations. General under-prediction at Vulcan using prolate, spherical, and oblate sources may suggest a shallower source or a source located closer to Vulcan edifice (more to the west with respect to those used for the inversions). The good prediction at Vulcan due to the blob elongated under Vulcan seems to confirm this hypothesis. All in all, a more complex magma chamber shape, like the blob shape, would efficiently predict the part of deformation at Vulcan and Matupit Is., while a deeper source seems to be more appropriate to predict the long wavelength displacement signal west of the caldera. This suggests that the solution may be a combination of the two types of sources.

In general, better displacement predictions (lower RMSE) are obtained, in order, by models with oblate, blob, spherical, and prolate source. The prolate source predicts the displacements better than the sphere source for all material configurations except for Ds and Inf+Ds (Fig. 4.4.1, d3 and 5). This is due to the higher positive residuals north and south of the caldera. The high positive residuals found for both sphere and prolate with these material properties configuration could be due to the fact that the dikes at deeper levels are more extended to the west, introducing in the model a wider stiffer volume in this area. Sources not included in the stiff dike swarm block could generate the asymmetric deformation. This effect is more evident for the deeper source that strongly interacts with the deeper dike swarm, like the prolate one. Ds and Bmt do not seem to affect the signal inside the caldera much, but do influence the signal outside the caldera. In order to take advantage of the wide coverage of InSAR signal for the understanding of the magmatic system, it is recommended to use all parts.

Estimates of fluid flux and pressure can be grouped in two different trends to better understand the influence of the material properties and chamber shapes on the estimates (Fig. 4.4.3). The estimates of fluid flux per year (Fig. 4.4.3, a) range between -3.3x10^9 m^3 and -74x10^9 m^3. In the span of the study period, this corresponds to a fluid volume withdrawl of about 8x10^6 and 120x10^6 m^3, respectively. As we do not have an independent estimate of the amount of volcanic products erupted during the period spanned by the InSAR, we do not have a reference value for our estimates. Nevertheless, we can consider that the DRE volume of the 2006 eruption (VEI=4), 80x10^6 m^3 (estimates of VOGRIPA updated with data from *Bouvet de Maisonneuve et al.*, 2014 (in press), gives us an idea about the volume the Rabaul actual system is able to withdraw. The lower trends (Fig. 4.4.3) show decreasing values when introducing the Infill and the Bmt. Introducing these two blocks in the model means to introduce two elements that amplify the deformation: 1) the weak caldera infill on top of the magma chamber and 2) the deep Bmt block that traps the deformation field above it, amplifying the deformation at the center and shrinking the signal. In the case of a source with deeper roots (Prolate case), closer to the Bmt blocks, these effects are more evident, leading to lower estimates than the case with only the Infill block. Shallower sources (i.e. oblate and prolate), far from the deep transition of material properties, do not interact much with this change of material properties. The signal is therefore not that affected by the deep material transition. This produces the flat lower trends (generated by similar flux predictions for different material configurations) and upper trends estimates not departing too much from the lower trend estimates. This also results in consistent misfits for shallower sources with changing material properties. Along the upper trends, by adding the Infill and Bmt to the Ds configuration, we are again adding two components of amplification of the deformation. Again, for shallower sources this does not affect the estimates much (sub-horizontal trend for oblate and blob source) as the dumping of dikes is the dominant process. The upper trends show common behavior among oblate, blob, and spherical sources. The trend of the model with a prolate magma chamber is the only one with an opposite direction (Fig. 4.4.3). As already mentioned in the results section, this is due to the low values of the models with Ds and Inf+Ds properties configurations related to the fact that the prolate magma chamber is not totally included in the dike swarm body. In these configurations, its bottom part is in contact with the weak extra caldera deposits that thus generate lower estimates.

Estimated pressures generated by the flux of fluid in the chambers (Fig. 4.4.3, b) show trends similar to those of the relative flux estimates. The most noticeable difference between flux and pressure estimates is observed for the lower trends. The fluxes of the lower trends are more spread, while the pressure lower trends are more flattened and close to each other. This is a peculiar aspect of the lower trends and could be related to the fact that the shallower part of the models corresponding to these trends is made of soft materials. These materials can accommodate more the flux of magma with a wider range of responses, leading to higher variations (estimates spreads) of flux with respect to the pressure.

Most of the pressure estimates are between -0.1 and -7 MPa/yr, with a maximum pressure estimate of -13 MPa/yr. These values need to be multiplied by a factor of 3.7 to calculate the pressure estimates over the period of investigation. This way, many of the estimated drops of pressure occurring in the cavities between February 2007 and December 2010 are between -0.37 and -21 MPa, and the maximum drop of pressure reaches a value of -48 MPa. The shear strength range of diorite, the material of the dike swarm block around the cavities, is 14-50 MPa (*Bernt Sigve and Looyeh*, 2011). In previous models, Folch and Martì (2009) use the value of -40 MPa as critical value of the pressure drop in the magma chamber for the initiation of subsidence; this value is an average natural value for shear strength of the crust in volcanic environments (*Judd et al.*, 1989). Pressures lower

than the shear strength of diorite prevent the rock from catastrophic slip fractures, while pressures that overcome the shear strength of the rock may induce slip fractures and the consequent collapse of the chamber structure. In the study period, catastrophic slip fractures with collapses were not observed. This validates models in which the drop of pressure in the single cavity does not exceed the shear strength of the surrounding rock. Most of the models estimate a conservative drop of pressure smaller than 14 MPa, which is the lowest value of the shear strength range of diorite (*Bernt Sigve and Looyeh*, 2011). Some models with spherical and prolate magma chambers show a drop of pressure during the study period that exceeds the lower shear strength limit. In particular, the model with prolate source and Inf+Bmt+Ds material properties configuration reaches the highest value of -48 MPa, close to the upper boundary of shear strength of diorite. Attention needs to be paid when considering this model as representative of the Rabaul magmatic system.

The models with prolate source and both with homogeneous material properties or with the Infill configuration have the lowest RMSE. RMSE are a good, quick method to compare the results of the inversions, but in order to state that a model predicts the deformation better than another, the improvements need to be statistically valid. F-tests are run to compare the model results and statistically assess which model better fits the data under a certain level of significance.

To do so, we test the null hypothesis $H_0 : S_0^2 = S_1^2$ using the F-test:

$$F = \frac{S_0^2}{S_1^2} \qquad with\ S^2 = \frac{1}{(N-1)} \sum_{i=1}^{N} e_i^2 \tag{5.5.1}$$

where S_0^2 refers to the reference model, S_1^2 refers to the newer model (Menke, 1989) and e is the error vector of each model. The F-test thus provides a bulk comparison of the variance from the predictions of the two models. The null hypothesis is $H_0 : S_0^2 = S_1^2$, and it is true if the value of the F-test is less than a critical value. Considering that the number of degree of freedom of the problem for the test in all models is d=N-M=802-1, for a significance level of α=.05 the critical value is c=1.12. The null hypothesis is rejected with 95% confidence if the value of the F-test is smaller than the critical value, *c*. F-tests generated for the 28 3-D Rabaul models are grouped into two groups:

1) The first one permits us to understand the improvement of model predictions due to material properties for each magma chamber geometry. The predictions of all material property configurations are compared among models that have the same magma chamber geometry. This leads to four groups of comparison, the results of which are summarized in Tab. 5.5.1. For the spherical chamber, the Ds configuration is the one that statistically better predicts the displacements (Tab. 5.5.1, a). For the prolate chamber (Tab. 5.5.1, b), the model with higher material complexities (Infill+Bmt+Ds) provides statistically better predictions of all models except for the HOM and the Infill. Although the prolate HOM and Infill models have the same RMSE, the F-test shows that the Infill model does not predict the displacements statistically better than the HOM configuration. For the oblate chamber, no model predicts the displacements statistically better than the reference model (Tab. 5.5.1, c). That is, no improvement of predictions is added by adding more complexities to the HOM model. Among the blob models, the one with Ds configuration is the only one that predicts the displacements statistically better (Tab. 5.5.1, d).

2) The second group investigates the improvements of model prediction by introducing magma chamber shapes different from the spherical one. The results are summarized in Tab. 5.5.2. As

SPHERE	HOMO	Inf	Ds	Bmt	Inf+Ds	Inf+ Bmt	In+Bmt +Ds
HOMO	1	0.834	1.25	0.716	1.187	0.646	0.776
Inf		1	1.498	0.859	1.423	0.774	0.93
Ds			1	0.573	0.95	0.516	0.62
Bmt				1	1.657	0.901	1.083
Inf+Ds					1	0.544	0.653
Inf+Bmt						1	1.201
Inf+Bmt+ Ds	(a)						1

PROLATE	HOMO	Inf	Ds	Bmt	Inf+Ds	Inf+ Bmt	In+Bmt +Ds
HOMO	1	0.951	0.463	0.521	0.454	0.474	0.927
Inf		1	0.487	0.548	0.477	0.498	0.974
Ds			1	1.125	0.98	1.022	2
Bmt				1	0.871	0.908	1.778
Inf+Ds					1	1.043	2.041
Inf+Bmt						1	1.957
Inf+Bmt+ Ds	(b)						1

OBLATE	HOMO	Inf	Ds	Bmt	Inf+Ds	Inf+ Bmt	In+Bmt +Ds
HOMO	1	0.922	0.948	0.97	0.896	0.905	0.881
Inf		1	1.028	1.051	0.971	0.982	0.955
Ds			1	1.023	0.945	0.955	0.929
Bmt				1	0.924	0.934	0.908
Inf+Ds					1	1.011	0.983
Inf+Bmt						1	0.973
Inf+Bmt+ Ds	(c)						1

BLOB	HOMO	Inf	Ds	Bmt	Inf+Ds	Inf+ Bmt	In+Bmt +Ds
HOMO	1	0.874	1.137	0.856	0.984	0.772	0.803
Inf		1	1.301	0.979	1.125	0.883	0.919
Ds			1	0.753	0.865	0.679	0.706
Bmt				1	1.149	0.902	0.938
Inf+Ds					1	0.785	0.816
Inf+Bmt						1	1.04
Inf+Bmt+ Ds	(d)						1

Table 5.5.1. F-test results for comparisons of all material property configurations. *Columns represent the model being tested and the rows represent the reference model for the test. (a) Model with spherical source. (b) Model with prolate source. (c) Model with oblate source. (d) Model with irregular shape source inferred from the tomography. Grey cells indicate the values that exceed the critical value (c=1.12), which means that the tested model predicts the data better than the reference model.*

already observed, the F-tests confirms that the prolate models predict the displacement better that the spherical models, except for the cases of Ds and Inf+Ds, as already discussed above. Oblate and blob sources do not introduce any statistically valid improvement of displacements prediction with respect to the spherical chamber.

The F-tests confirm the information obtained from the RMSE in a statistic way. Among all models, the preferred model has a prolate source and homogeneous material properties. The flux of fluid predicted by this model is -26x10^9 kg/yr. Over the period spanned by the InSAR data, this corresponds to a withdrawl volume of fluid of about 42x10^6 m^3. These comparisons are bulk comparisons, however, and require geologic context before any meaning is applied to the implications of the results. Although the model with the prolate source and homogeneous material properties predicts the InSAR displacements well, it lacks in representing the medium in a reasonable way. We know, in fact, that the homogenous model is an over-approximation of the distribution of the material properties that composite that upper crust. Furthermore, the over-simplification of the magma chamber represented by the prolate cavity cannot provide much information about the shallow magmatic system. This is strictly related to the limitation of applying only one unique and evenly distributed pressure -the hydrostatic drop of pressure generated by the fluid removal- to the walls of the cavity. This limitation encouraged us to consider a more explorative inversion approach, still based on the 3-D FEM of Rabaul, in which we allow the inverse model to look for an arbitrary distribution of sources instead of prescribing an a priori specific geometry of the source.

SPHERE	PROLATE	OBLATE	BLOB
HOMO	1.609	0.509	0.861
Inf	1.834	0.563	0.902
Ds	0.596	0.386	0.783
Bmt	1.171	0.689	1.028
Inf+Ds	0.615	0.384	0.713
Inf+Bmt	1.180	0.714	1.029
Inf+Bmt+ Ds	1.922	0.578	0.891

Table 5.5.2. F-test results for comparisons between spherical source and all other source shapes (prolate, oblate, and blob) for each material property configuration.
Columns represent the model being tested and the rows represent the reference model for the test. Grey cells indicate the values that exceed the critical value (c=1.12), which means that the tested model predicts the data better than the reference model.

5.6 Search of magma withdrawal through the inversion based on FE array of sources

The explorative inversion approach based on elastic half-space solutions has already been successfully applied to investigate clusters of sources responsible for volcanic surface deformations (e.g. *Vasco et al.*, 2000, 2002; *Masterlark and Lu*, 2004a). Other authors (*Trasatti et al.*, 2008) worked on applying the same approach to FEMs, thus implementing the investigation with all the advantages of the FE models (e.g. realistic topography and distribution of material properties). *Trasatti et al.* (2008) proposed an approach similar to the one proposed in this work, but they limited the investigation to a single-element source, loading the element faces with three dipoles and three double-couples. By simulating the point-source with six stress components applied to each single-element source, the number of parameters to be solved through the inverse problem (six for each source) for an array of sources could be quickly unaffordable. In this dissertation, the method applied requires only one parameter to fully describe the strength of each FE source, a change in pressure or a flux of fluid, thus reducing the parameters of the inversion to a manageable number. This way, we are able to take a step forward, accomplishing the more interesting goal of imaging a more realistic source made of a distribution of single sources, with a free geometry dictated by the displacements data. Mesh independency of the simulations is a desirable advantage (*Charco and Galán del Sastre*, 2014) due to the fact that preventing remeshing can greatly reduce the computational time of the analysis. The method proposed here holds the advantage of preventing remeshing the domain at each source considered, thus minimizing the computational time needed to run all the forward models used to assemble the GFs matrix for the inverse model.

The forward model in this work is a library of numerical displacement solutions, where each entry is the surface displacement generated by a unity flux of mass applied to each single source. The elements around the source, part of the array representing the non-active sources, have the material properties of the rock surrounding the array. This assumption leads us to build the Green function by simulating independent sources embedded in the rock, but the results will be interpreted

as a distribution of mass change over a body through which a possible fluid connection is assumed. Although the way we build the model breaks the concept of truly continuous fluid, this interpretation is still possible due to the principle of superposition. Moreover, we have to remember that the assumption that any non-active source is filled with dike swarms material is a requirement due to the initial assumption of the problem that we want to solve. In fact, at the beginning we assume that we do not know which sources are solid and which are liquid.

The mathematically preferred distribution of fluid flux, resulting from the FEM-based inverse model (Fig. 5.6.1, a-i), is obtained by choosing the solution at the knee of the trade-off curve, where the corresponding dumping parameter value is β=200. (Fig. 5.6.1, a).

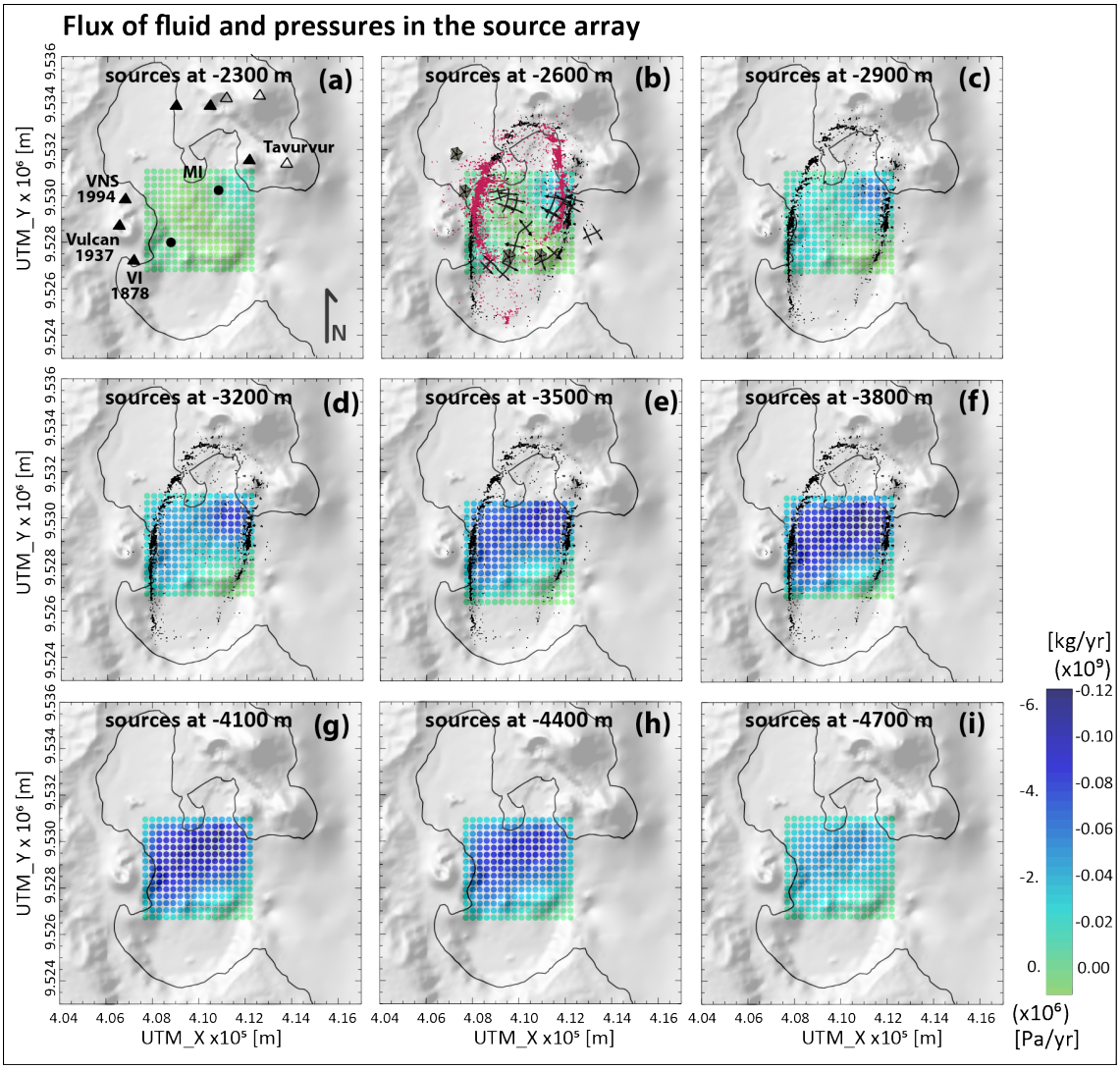

Figure 5.6.1. Flux of fluid and pressure source solutions for beta=200. In these panels, we overlap the solutions of the inverse model with geological features that help interpret the results.

In these panels, we overlap the solutions of the inverse model with geological features that help interpret the results. In particular, in panel (a) MI-Matupit Island, VNS-Vulcan North Shore, VI-Vulcan Island. Black triangles represent the post-caldera cones, hollow triangles represent pre-caldera cones, filled circles represent the inflation centers proposed by McKee et al. (1984). In panel (b) Folds mapped by seismic reflection surveys (Pono, 1990), shallow (<2 km) and deeper seismicity (between 2 and about 3.8 km depth) are marked with red and black dots, respectively. Gray stars represent submarine cones

The resulting distribution of fluid flux shows an elongated shape oriented SW-NE between Vulcan and Matupit Is. and centered at about 3500 m depth. By overplotting the shallow seismicity recorded at Rabaul between 1971 and early 1992 (dots in Fig. 5.6.1, b-f), which is thought to represent elliptical faults inside the caldera (*Saunders*, 2001), we notice that the extension of the distribution of negative predicted fluxes does not overpass the seismicity. This is consistent with the assumption that the faults cannot propagate in the molten rock and would rather define a physical constraint for the batch of magma. In particular, we observe that the distribution of fluid flux in the levels is included in the shallower seismicity ($<$ 2 km depth, red dots in Fig. 5.6.1, b), resembling its shape in the south eastern direction. This suggests a possible relationship between the extension of the imaged chamber and the faults related to the shallower seismicity.

The distribution of mass removal shows a complex distribution made of two areas of high mass removal. A first lobe located at the NE corner of the array, starting at shallower levels and with persistent higher flux values among the layers, merges at higher depths (between -3500 and -4400, in Fig. 5.6.1, e and f) with a second lobe located on the western side of the caldera and centered NE of Vulcan. By considering the lobes as possible sources of deformation, we have to keep in mind the resolution of the inversion model used. In our case, the resolution of the model (Fig. 4.5.5) allows us to detect the presence of two lobes at the borders of the source array at shallower levels (Fig. 5.6.1, b-d). For depths deeper than 3500 m (Fig. 5.6.1, e-i), no further details than two smeared lobes can be achieved due to the lower model resolution which tends to smear the sources (Fig. 4.5.5, e-i).

Although these results are very encouraging, we have to note that the distribution of the flux values extends in some layers (Fig. 5.6.1,e-g) to the northern side of the array almost entirely bordering it. This suggests that the chosen array of sources may be too small. This distribution of values in the northern side, by resembling the shape of the array, could in fact be a border effect. We have to remember that the array of sources was built taking into account the physical boundaries imposed by the seismicity and for computational reasons it does not extend much further than these boundaries. This could be the reason why the distribution of sources is entirely included in the elliptical seismicity. A bigger array would give us more confidence about interpreting the results. Boundaries effects are not observed on top and bottom sides of the array as the solutions extinguish vertically.

Nevertheless, we can still get important information about the shallow magmatic system and we can find other correspondences between the found distribution of sources and the geological features, petrographic informations, as well as observations of the volcanic activity. The submarine cones inside the caldera are also located at the border of the imaged magma chamber (Fig. 5.6.1, b) suggesting a possible relation with the southernmost extension of the chamber. Folds mapped during seismic reflection surveys (*Pono*, 1990) show SW-NE trends on top of the imaged magma chamber resembling the elongation of the chamber itself (Fig. 5.6.1, b).

The shallower NE lobe, located SW of Tavurvur with higher flux values and higher vertical extension, is consistent with a higher withdrawl in this area. This withdrawl reaches shallower layers due to the continuous vulcanian eruptions at Tavurvur during most of the considered period. The western lobe is consistent with a batch of magma that could have fed the 1994 eruption at Vulcan North Shore (VNS). Its elongated NS shape, with slightly higher values on its northern part (Fig. 5.6.1, f) is consistent with the distribution of historical cones (Vulcan Island, Vulcan, and Vulcan North Shore) on the western side of the caldera (Fig. 5.6.1, a). The connection of the lobes at depth finds correspondence in the products erupted in October 2006 and during the study period, as well as products erupted at Rabaul during previous eruptions. In fact, the andesites erupted during

October 2006 are the results of the mixing and mingling of two magmas from the same system at a depth calculated between 2.7 km and 3.8 km: a replenishing basalt and a resident dacite (*Bouvet de Maisonneuve et al.*, 2014). Less evolved magmas are erupted from Tavurvur, on the eastern side of the caldera suggesting the feeding with basaltic magmas from a deeper part of the system on this side of the caldera. Dacitic products are only erupted from vents on the western side of the caldera (*Roggensack et al.*, 1996), thus suggesting that the western lobe imaged by the solutions could represent part of the resident dacite batch. The fact that the solutions of the two lobes merge at depth shows a possible migration and interaction of fluids from the two lobes in this volume, which is consistent with the mixing and mingling processes registered in the composition of the erupted products at Tavurvur during and after the October 2006 eruption.

The total amount of flux withdrawl per year is -74.5x10^9 kg, which means an estimated total volume withdrawl of 119x10^6 m^3 during the entire study period. This is a reasonable value considering the DRE volume of the 2006 eruption, 80x10^6 m^3, as a reference limit of volume that the Rabaul actual system is able to withdrawl in a short period. Pressure values calculated at the sources are smaller than the shear strength of diorite in which the sources are located. Although in the case of FEMs with big unique cavities, having a drop of pressure lower than the shear strain of the rock was a main concern in order to avoid catastrophic collapses, in the case of an array of sources this assumption may be relaxed. This is due to the fact that local high drop of pressure (pressure measured at the single source) could generate failures that, due to their local aspect, do not lead to catastrophic collapses. Pressure values higher than the threshold may be used to track the possible expansion of the magma chamber and the migration of the fluid in the system by finding a correspondence with the seismicity recorded.

Previous analytical half-space homogenous models, based on the data collected during the seismo-deformational crisis of 1983-85, suggested two sources inside the caldera (Fig. 5.6.1, a): one located south-east of Matupit Is., at depth between 1.2 and 2 km, and one under Vulcan at depth of 3 km (*McKee et al.*, 1984; *Archbold et al.*, 1988; *McKee et al.*, 1989). These two sources are comparable with the two lobes (i.e. batches) proposed in this study and imaged in Fig. 5.6.1, although our study suggests deeper sources. The source that our results image south of Matupit Is. is positioned more to the east, toward Tavurvur, and it is significantly deeper, about 2600 m depth, with respect to those calculated for the seismo-deformational crisis. The Vulcan source is located slightly to the north of the one previously calculated and at slightly deeper levels (3500 m depth). As the depth of sources is likely to change in time in a very active area like Rabaul caldera, we can ignore the differences in depth of the sources proposed, thus focusing on the important information, which is the duality of sources recognized among the years under the caldera by different models. In addition, our solution images the connection between the two batches of magma where the mixing/mingling of the two magmas can occur, as already hypothesized by petrographic studies (*Patia*, 2004; *Bouvet de Maisonneuve et al.*, 2014). The two-batches model indicates a different distribution of magma composition with respect to the one suggested by Roggensack et al. (1996), for which the more evolved magma erupted from Vulcan was tapping the top of a unique magma chamber. From the distribution of the sources in our study, we can derive that the variation of magma composition is more likely a lateral variation than a vertical one, along a column of single magma chamber. A deeper source at Vulcan, visible in our study, would not be consistent with the concept of a single chamber topped by more evolved magma, but could be consistent with a lateral transition. Recently, *Ampana and Kimata* (2011) suggested a Mogi source at 2 km depth under Greet Harbor by inverting the InSAR data of a similar period of the InSAR data used in this work. The chamber imaged in

our mathematically preferred model (Fig. 5.6.1) could be comparable to the estimate of *Ampana and Kimata* (2011).

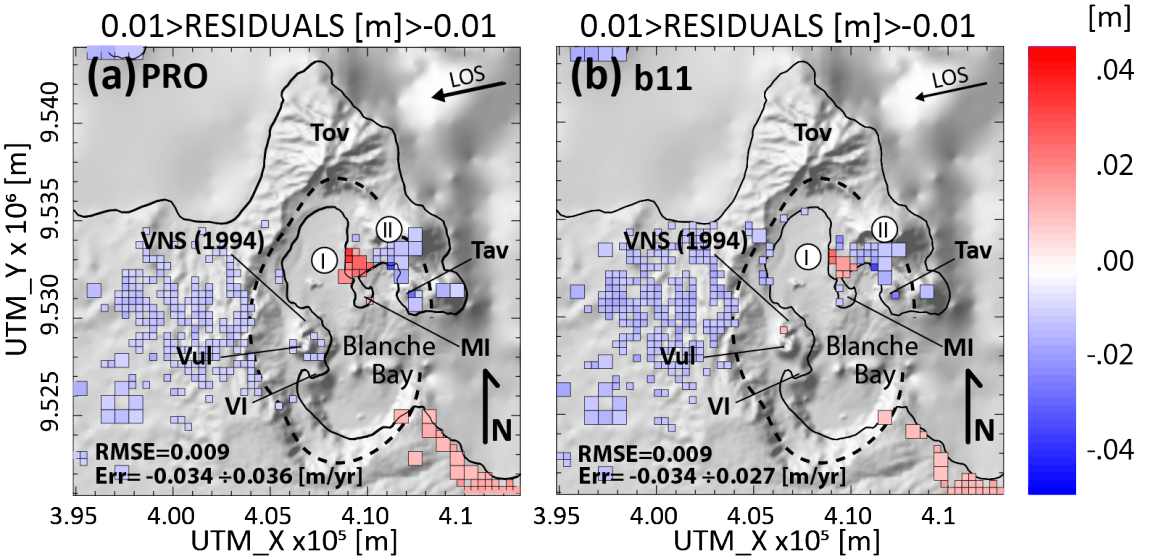

Figure 5.6.2. Residuals of models PRO(Inf+Ds+Bmt) and b11.
Tov-Tovanumbatir, Vul-Vulcan, VNS-Vulcan North Shore, VI-Vulcan Island, Tav-Tavurvur, MI-Matupit Island. (a) Residuals bigger than 1 cm for the model with a prolate ellipsoid cavity source and heterogeneous distribution of material properties (Inf+Ds+Bmt). (b) Residuals bigger than 1 cm for the preferred mathematical solution (b11) of the model with array of sources and heterogeneous distribution of material properties.

The best predictions of model b11 (Fig. 4.5.6, d) are very similar to those predicted by the best heterogeneous model with single magma chamber, that is the model with prolate source and all material parts active (Fig. 4.4.1, b7). The two models are comparable because they share the same material properties configuration. From the comparison of the residuals greater than 1 cm both of the model with single source (prolate ellipsoid source and Inf+Bmt+Ds properties distribution) and model b11 (Fig. 5.6.2), we notice that the distributions of the residuals are also similar. Both models cannot account for the clusters of residuals at the area north of Matupit Is., in correspondence with the old airport strip (positive residuals in Fig.5.6.2, a and b, I) and north of Tavurvur (negative residuals in Fig. 5.6.2, a and b, II). This could be due to the fact that the signal in these areas may be generated by other processes not accounted by the model (i.e. hydrological or hydrothermal processes). Residuals slightly bigger than 1 cm are present west of the caldera for both models, although b11 predicts the displacements south west of Vulcan better. The presence of these residuals may be due to over-dumping effects of the dike complex thus requiring reconsideration of its material properties or its extension for future models.

The agreement between the two models means that a deeper source is not required to predict the measured displacements as expected from the inversion of simple source models. Instead, a shallow source made of a complex distribution of fluid flux could be equally responsible for the observed displacements at Rabaul area. Furthermore, in choosing our preferred model, we have to remember that the pressure estimate for the model with prolate cavity and Inf+Bmt+Ds properties configuration was close to the upper boundary of shear strength of the hosting rock. Therefore, caution needs to be paid in considering this model representative of the Rabaul magmatic system. In addition, with the advantage of finding correspondence with independent observations (e.g. geological, petrographic, etc.) and providing a more realistic source, model b11 is likely to be the

preferred model.

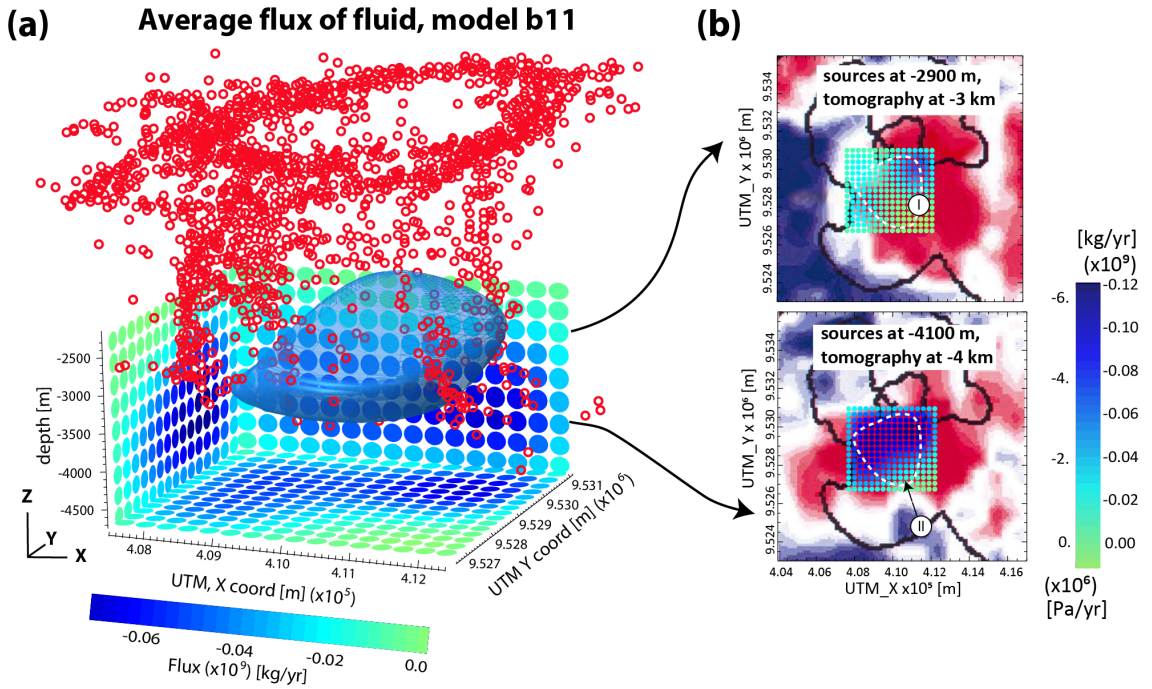

Figure 5.6.3. Comparison between blob magma chamber, b11 flux distribution, and tomographic slices.

(a) View of average flux values of b11 model projected on three orthogonal planes with blob magma chamber superimposed. (b) P-velocity contrast distribution on tomograhic slices at 3 and 4 km depth (modified from Finlayson et al., 2003). For each tomographic slice, the closest layer of mass flux solutions of model b11 is superimposed. Dashed white lines represent the projection of the maximum extent of the blob source. For both panels (a) and (b) the seismicity from Saunders (2001) is superimposed.

The blob shape (Fig. 5.6.3, a) resulting from complex lofting, smoothing, and scaling operations is the final compromise to meet the requirements mainly of seismicity and tomography. The blob shape is mostly inferred from the tomography. It is fully surrounded by the seismicity, but due to rescaling processes it reaches the maximum depth of about 3720 m, missing to represent the deeper part of the low velocity area imaged by the tomography at 4-5 km depth (Fig. 5.6.3, b). The control points that define the splines, and thus the shape of the body, were chosen from the tomographic slices following the shape of the p-wave anomaly. They were chosen in a somewhat arbitrary way due to the ambiguities of the tomographic anomaly in defining fluid bodies. The two main aspects of the chamber inferred from the tomography were: a source with shallower roof close to Tavurvur, at 2 km depth, and a deeper roof close to Vulcan, at 3 km depth. To be more conservative, with the array of sources we investigated slightly deeper levels, but due to computational reasons the array is optimized with shallower sources at 2300 m depth.

Due to the discussed discrepancies, the depth of shallower active sources of the array cannot be compared with the shallow roof of the blob. Instead, we can compare the general shape of the distribution of active sources in the array, the blob shape, and the p-velocity contrast of the tomography. The common aspect among the three models is the shallower source toward Tavurvur and a deeper one towards Vulcan. The broad extension at the eastern side of the caldera of the p-velocity contrast at 3 km (Fig. 5.6.3, b, I), as well as the broad shape of the inferred blob that extend to the south (Fig. 5.6.3, b, II), do not find any correspondence in the b11 model, where the

distribution of active sources on the eastern side is extended only diagonally towards Tavuvur. This discrepancy could be due to the fact that the low velocities on the eastern side of the caldera could reflect a more fractured and disrupted area, which is consistent with the fact that on the eastern side the caldera rim is missing, letting the ocean enter in Blanche Bay. A bigger array of sources should extend further to the west in order to better investigate the estended low velocity zone under Vulcan at about 4 km depth.

Chapter 6

Conclusions, recommendations and future works

6.1 Conclusions and recommendations

In this work, methods and strategies are developed to build a 3-D FEM with structural complexities and integrate it into a linear least squares damped analysis. The methods are applicable to any volcanic area. Here, all methods and models are applied to Rabaul caldera with the main goal of imaging the shallow magma chamber, intended here as a volume of the model through which fluids can migrate. The application to a real case motivated us to study many of the aspects of the model in detail, coming up with general considerations about modeling natural volcanic areas in more realistic ways.

The topography needs to be taken into account, even in the case of non-prominent features, whenever steep slopes are present in the vicinity of the sources, such as in the case of Rabaul caldera. In case very weak material is constituting the upper part of the model (e.g. the saturated material of the Rabaul caldera infill) and no *in-situ* elastic properties estimation is available, a sensitivity test to the Poisson's ratio is recommended. The fact that a sharp transition of material properties closer to the source impacts the deformation more highlights the importance of modeling the medium with right material properties close to the source. This means that when the source is deeper, we also need to make sure to model the deeper material well. Furthermore, a magma chamber inferred from the tomography and seismic data does not predict the displacements better than a spherical one with the same volume. This is due to the fact that, although using a complex geometry, we have the limitation that we can only apply one single pressure uniformly over the walls of the cavity. Due to this limitation and to the ambiguity of the sources of low tomographic velocities, it is fairly difficult to achieve a good model of the magma chamber modelled as a cavity based on tomographic images. Nevertheless, the tomography provides a great guide to define a volume of investigation for the array of sources at the base of the method proposed in this dissertation.

We propose a method to implement a linear least squares inversion with FEM for the estimation of an arbitrary distribution of mass change among a volume of the FEM. This leads to the possibility of imaging the magma chamber through the inversion of geodetic data, thus providing more insights about the magmatic system with respect to the over-simplified a-priori cavity used to simulate the magma chamber. The method pushes FEM-based inverse models a step forward with the result of being able to image the magmatic system in a more realistic way through simple linear

inversion strategies.

By applying the strategies and methods to the active Rabaul caldera, we are able to image the extension of the magma chamber under the caldera. This could have implications for future evaluation of the possibility of catastrophic collapses. In fact, the imaged volume, included in the area defined by the shallow seismicity, looks to be sufficient to explain the observed deformation, with no need of a bigger magma chamber as it would be suggested by the laterally extended low velocity contrast of the tomographic images. This has implications for hazard assessment in the sense that the dimension of a possible worst-case scenario could be estimated.

Our study confirms the presence of two main sources at opposite sides of the caldera hypothesized by previous analytical models, and images the interconnection between these two sources. Thus, the Rabaul shallow magmatic system seems to act like a unique reservoir instead of different disconnected magma reservoirs. This implies a high mobility of magma between different parts of the system. Thus, as shown by the deformational period studied, a big eruption at one of the centers, Tavuvur in this case, can trigger a long term deflation of the entire system, Vulcan batch included. The imaged connection could have implications for the dynamics of future twin eruptions. Our study may thus help to understand the dynamics of this kind of eruptions and forecast them.

6.2 Future works

Although this study images the magma chamber under Rabaul caldera, we have to remember that border effects have been observed on the estimates of the inversion, especially on the northern side of the FE source array. In future works, a bigger array of sources could be used in order to avoid border effects, to be able to investigate the full low velocity zone shown by the tomography of Finalyson et al. (2003), and to extend the study to deeper depths in order to investigate the effects of deeper reservoirs on the surface displacement signal. Furthermore, although not much of the hydrothermal system is known until now (*Johnson et al.*, 2010), future studies will perhaps allow us to extend the model to shallower levels in order to investigate the effects on the hydrothermal system of the surface deformations and better predict the area north of Tavurvur.

The estimated distribution of pressures looks reasonable, encouraging us to use the model in future studies for the understanding of stress changes and failure mechanisms of the area. A more realistic model in terms of stress distribution should also include geostatic conditions.

In this study, the domain in which the sources are included is modeled using elastic materials inferred from seismic velocities and geologic observations. Future studies could investigate alternative rheologies (e.g. visco-elasticity) to better describe the domain rheology.

At this point, the study is limited to the inversion only of 1-D ascending InSAR data. For future studies, we hope that we will have access to a 3-D description of the signal, and thus hope to integrate the InSAR data with GPS data in order to have a more robust inversion.

As our models predict mass movements through the magmatic system, in future studies we could also calculate the related gravity anomalies and introduce the gravity anomalies measured at the surface into the inverse scheme. By considering these anomalies, we could detect processes other than mass flux that contribute to the surface deformation without requiring a change of mass (e.g. thermoelastic expansion).

Future studies could also combine the inversion of surface deformation and gravity anomalies with the monitored seismicity to track magma migration though the system.

By referring to the mapped flux of magma when interpreting the surface deformation, we suggest that the deformation is only due to the movement of magma within the plumbing system.

Besides the movement of magma, a wide range of magmatic processes could be responsible for the pressure variations (or volume variations) that generate surface deformation (e.g. crystallization, degassing, expansion of the hydrothermal system, remelting, etc.). As the change of pressure inside the elements and the change of volume of the elements are solutions of the forward unity flux models and they are linearly correlated to the flux solutions, we can provide maps of pressure change (Fig. 5.6.1) and volume change. By comparing these maps with values of pressure change (or volume change) due to other magmatic processes, it will be possible in the future to balance the effects of different processes and provide a more complete and realistic overview of the processes responsible for the observed deformation.

At small time intervals the response of the system can be considered elastic. An analysis of short temporal intervals could therefore take full advantage of the model here proposed. With a temporal analysis of surface displacements based on one single FEM, we can answer questions about how the magma is moving in the system, if it is being accommodated by the entire system, or if it is accumulating on one side, building up stresses on a specific area. Answers to these questions are fundamental to understand the running dynamics in the system and to forecast the next activity.

Lastly, the 3-D model proposed for Rabaul caldera could be used in new tomographic studies to better find the anomalies of velocity.

Bibliography

Abaqus (2009), Version 6.9-ef, dassault systÃšmes simulia corp., providence, ri, www.simulia.com.

Abbott, L. (1995), Neogene tectonic reconstruction of the adelbert-finisterre-new britain collision, northern papua new guinea, *Journal of Southeast Asian Earth Sciences*, *11*, 33–52.

Abbott, L., E. Silver, P. Thompson, M. Filewicz, S. Schneider, and Abdoerrias (1994a), Stratigraphic constraints on the development and timing of arc-continent collision in northern papua new guinea, *Journal of Sedimentary Research*, *B64*, 169–183.

Abers, G., and R. McCaffrey (1994), Active arc-continent collision: earthquakes, gravity anomalies, and fault kinematics in the huon-finisterre collision zone, *Tectonics*, *13*, 227–245.

Acocella, V. (2008), Activating and reactivating pairs of nested collapses during caldera-forming eruptions: Campi flegrei (italy), *Geophysical Research Letters*, *35*(17), 1–5, doi:10.1029/2008GL035078.

Acocella, V., and M. Neri (2009), Dike propagation in volcanic edifices: Overview and possible developments, *Tectonophysics*, *471*(1-2), 67–77.

Afrouz, A. (1992), *Practical Handbook of Rock Mass Classification Systems and Modes of Ground Failure*, CRC Press, Boca Raton.

Almond, R. (1981), Aeromegnetic survey of the rabaul caldera, in *Cooke-Ravial volume of Volcanological Papers. Geological Survey of Papua New Guinea Memoir*, vol. 10, edited by R. Johnson, pp. 195–200, Papua New Guinea.

Almond, R., and C. O. McKee (1982), Location of volcano-tectonic earthquakes within the rabaul caldera, *Geol. Sur. Papua New Guinea, Rep., 82/19*.

Ampana, S., and F. Kimata (2011), Post-eruptive deformation of the 2006 rabaul volcano (png) eruption detected by alos-sar data, in *Japanese Geoscience Union Meeteing*, Makuhari, Chiba, Japan.

Anderson, E. M. (1936), The dynamics of the formation of cone sheets, ring dykes and cauldron subsidence, *Proc. R. Soc. Edinburgh*, *56*, 128–163.

Anderson, M., and W. Woessner (1992), *Applied Groundwater Modeling: Simulation of Flow and Advective Transport*, Academic Press, San Diego.

Apuani, T., C. Corazzato, A. Cancelli, and A. Tibaldi (2005), Physical and mechanical properties of rock masses at stromboli: a dataset for volcano instability evaluation, *Bull Eng Geol Env*, *64*, 419–431.

Archbold, M. J., C. O. McKee, B. Talai, J. Mori, and P. De Saint Ours (1988), Electronic distance measuring network monitoring during the rabaul seismicity/deformational crisis of 1983-1985, *Journal of Geophysical Research: Solid Earth*, *93*(B10), 12,123–12,136.

ASME (2006), *Guide for verification and validation in computational solid mechanics*, *American Society of Mechanical Engineers*, vol. ASME Standard V&V 10-2006, New York.

Aster, R. C., B. Borchers, and C. H. Thurber (2004), *Parameter Estimation and Inverse Problems*, *INTERNATIONAL GEOPHYSICS SERIES*, vol. 90.

Atherton, M. P., and N. Petford (1993), Generation of sodium-rich magmas from newly underplated basaltic crust, *Nature*, *362*(6416), 144–146.

Bai, C. Y., and S. Greenhalgh (2005), 3d multi-step travel time tomography: Imaging the local, deep velocity structure of rabaul volcano, papua new guinea, *Physics of Earth and Planetary Interiors*, *151*, 259–275.

Baldwin, S. L., P. G. Fitzgerald, and L. E. Webb (2012), Tectonics of the new guinea region, *Annual Review of Earth and Planetary Sciences*, *40*(1), 495–520.

Bartel, B. A., M. W. Hamburger, C. M. Meertens, A. R. Lowry, and E. Corpuz (2003), Dynamics of active magmatic and hydrothermal systems at taal volcano, philippines, from continuous gps measurements, *Journal of Geophysical Research: Solid Earth*, *108*(B10), 2475.

Bathke, H., H. Sudhaus, E. P. Holohan, T. R. Walter, and M. Shirzaei (2013), An active ring fault detected at Tendürek volcano by using InSAR, *Journal of Geophysical Research: Solid Earth*, *118*(8), 4488–4502.

Bechor, N., and H. Zebker (2006), Measuring two-dimensional movements using a single insar pair, *Geophysical Research Letters*, *33*(L16311).

Behn, M. D., W. R. Buck, and I. S. Sacks (2006), Topographic controls on dike injection in volcanic rift zones, *Earth and Planetary Science Letters*, *246*(3-4), 188–196.

Bell, F. G. (2000), *Engineering properties of soils and rocks*, 4th ed., Blackwell Science, Oxford.

Bernt Sigve, A., and R. Looyeh (2011), *Petroleum Rock Mechanics Drilling Operations and Well Design*, 1st ed. ed., Gulf Professional Pub, Oxford.

Bery, A., and R. Saad (2012), Correlation of seismic p-wave velocities with engineering parameters (n value and rock quality) for tropical environmental study, *International Journal of Geosciences*, *3*(4), 749–757.

Bianchi, R., A. Coradini, C. Federico, G. Giberti, G. Sartoris, and R. Scandone (1984), Modelling of surface ground deformations in the phlegraean fields volcanic area, italy, *Bulletin of Volcanology*, *47*(2), 321–330.

Bianchi, R., A. Coradini, C. Federico, G. Giberti, P. Lanciano, J. P. Pozzi, G. Sartoris, and R. Scandone (1987), Modeling of surface deformation in volcanic areas: The 1970-1972 and 1982-1984 crises of campi flegrei, italy, *Journal of Geophysical Research: Solid Earth*, *92*(B13), 14,139–14,150.

Bird, P. (2003), An updated digital model of plate boundaries, *Geochemistry Geophysics Geosystems*, *4*(3).

Bonaccorso, A., S. Cianetti, C. Giunchi, E. Trasatti, M. Bonafede, and E. Boschi (2005), Analytical and 3-d numerical modelling of mt. etna (italy) volcano inflation, *Geophysical Journal International*, *163*, 852–862.

Bonforte, A., F. Guglielmino, M. Coltelli, A. Ferretti, and P. G. (2011), Structural assessment of mount etna volcano from permanent scatterers analysis, *Geochemistry Geophysics Geosystems*, *12*(Q02002).

Bouvet de Maisonneuve, C., F. Costa, H. Patia, and C. Huber (2014), Unrest and eruption in a caldera setting: Insights from the 2006 eruption of rabaul (papua new guinea), *Geological Society of London, Special publications, in press*.

Bower, A. F. (2009), *Applied mechanics of solids*, CRC Press, Boca Raton, FL.

Brocher, T. (2005), Empirical relations between elastic wavespeeds and density in the earth's crust, *Bulletin of the Seismological Society of America*, *95*(6), 2081–2092.

Brooks, J., J. Connelly, D. Finlayson, and W. Wiebenga (1971), St. georges channel - bismarck sea trough, *Nature*, *229*, 205–207.

Burchardt, S., D. C. Tanner, V. R. Troll, M. Krumbholz, and L. E. Gustafsson (2011), Three-dimensional geometry of concentric intrusive sheet swarms in the geitafell and the dyrfjöll volcanoes, eastern iceland, *Geochemistry, Geophysics, Geosystems*, *12*(7), Q0AB09.

Camacho, A. G., F. G. Montesinos, and R. Vieira (2002), A 3-d gravity inversion tool based on exploration of model possibilities, *Computers & Geosciences*, *28*(2), 191–204.

Camacho, A. G., J. Fernández, M. Charco, K. F. Tiampo, and G. Jentzsch (2007), Interpretation of 1992-1994 gravity changes around mayon volcano, philippines, using point sources, *Pure and Applied Geophysics*, *164*(4), 733–749.

Camacho, A. G., P. J. González, J. Fernández, and G. Berrino (2011), Simultaneous inversion of surface deformation and gravity changes by means of extended bodies with a free geometry: Application to deforming calderas, *Journal of Geophysical Research: Solid Earth*, *116*(B10), B10,401.

Cattin, R., C. Doubre, J. de Chabalier, G. King, C. Vigny, J. Avouac, and J. Ruegg (2005), Numerical modelling of quaternary deformation and post-rifting displacement in the asal-ghoubbet rift (djibouti, africa), *Earth Planet. Sci. Lett.*, *239*(3), 352–367.

Cayol, V., and F. H. Cornet (1998), Effects of topography on the interpretation of the deformation field of prominent volcanoes- application to etna, *Geophysical Research Letters*, *25*(11), 1979–1982.

Chang, C., M. D. Zoback, and A. Khaksar (2006), Empirical relations between rock strength and physical properties in sedimentary rocks, *Journal of Petroleum Science and Engineering*, *51*(3-4), 223–237.

Charco, M., and P. Galán del Sastre (2014), Efficient inversion of three-dimensional finite element models of volcano deformation, *Geophysical Journal International*.

Charco, M., J. Fernández, F. Luzón, K. F. Tiampo, and J. B. Rundle (2007), Some insights into topographic, elastic and self-gravitation interaction in modelling ground deformation and gravity changes in active volcanic areas, *Pure and Applied Geophysics*, *164*(4), 865–878.

Cheng, C., and D. Johnson (1981), Dynamic and static moduli, *Geophys.Res. Lett.*, *8*, 39–42.

Cheng, C. H., and D. H. Johnston (1981), Dynamic and static moduli, *Geophysical Research Letters*, *8*, 39–42.

Christensen, N. I. (1996), Poisson's ratio and crustal seismology, *Journal of Geophysical Research: Solid Earth*, *101*(B2), 3139–3156.

Ciccotti, M., and F. Mulargia (2004), Differences between static and dynamic elastic moduli of a typical seismogenic rock, *Geophysical Journal International*, *157*, 474–477.

Ciccotti, M., R. Almagro, and F. Mulargia (2004), Static and dynamic moduli of the seismogenic layer in italy, *Rock Mechanics and Rock Engineering*, *37*, 229–238.

Cifali, G., G. d'Addario, E. Polak, and W. Wiebenga (1969), Rabaul preliminary crustal seismic test, new britain, 1966. record 1969/125, *Tech. rep.*

Closs, M. (2005), Collisional delamination in new guinea: The geotectonics of subducting slab breakoff, *Geological Society of America Special Papers*, *400*, 1–15.

Coleman, P., and L. W. Kroenke (1981), Subduction without volcanism in the solomons island arc, *Geological Marine Letters*, *1*, 129–134.

Compton, S. K. (2013), Using linear invers methods and finite element models to explore sensitivity to homogeneous elastic half-space assumptions in deformation models of the 2000 eruption of hela volcano, iceland, Doctoral dissertation, The University of Alabama.

Cooper, P., and B. Taylor (1989), Seismicity and focal mechanisms at the new britain trench related to deformation of the lithosphere, *Tectonophysica*, *164*, 25–40.

Corbett, G., D. First, and S. Hayward (1991), The maragorik prospect, east new britain, papua new guinea, in *Proceedings of the PNG Geology, Exploration and Mining Conference 1991*, edited by R. Rogerson, pp. 112–116, Rabaul.

Cunningham, H. S., S. P. Turner, H. Patia, R. Wysoczanski, A. Nichols, S. Eggins, and A. Dosseto (2009), (210pb/226ra) variations during the 1994-2001 intracaldera volcanism at rabaul caldera, *Journal of Volcanology and Geothermal Research*, *184*(3-4), 416–426, doi:http://dx.doi.org/10.1016/j.jvolgeores.2009.04.018.

Cunningham, H. S., S. P. Turner, A. Dosseto, H. Patia, S. M. Eggins, and R. J. Arculus (2009a), Temporal variations in u-series disequilibria in an active caldera, rabaul, papua new guinea, *Journal of Petrology*, *50*(3), 507–529, doi:10.1093/petrology/egp009.

Currenti, G., C. Del Negro, G. Ganci, and D. Scandura (2008), 3d numerical deformation model of the intrusive event forerunning the 2001etna eruption, *Physics of the Earth and Planetary Interiors*, *168*, 88–96.

Currenti, G., R. Napoli, and C. Del Negro (2011a), Toward a realistic deformation model of the 2008 magmatic intrusion at etna from combined dinsar and gps observations, *Earth and Planetary Science Letters*, *312*(1-2), 22–27.

Currenti, G., R. Napoli, A. Di Stefano, F. Greco, and C. Del Negro (2011b), 3d integrated geophysical modeling for the 2008 magma intrusion at etna: Constraints on rheology and dike overpressure, *Physics of the Earth and Planetary Interiors*, *185*(1-2), 44–52.

Curtis, J. (1973a), The spatial seismicity of papua new guinea and the solomon islands, *Journal of the Geological Society of Australia*, *20*, 1–20.

Curtis, J. (1973b), Plate tectonics and the papua-new guinea-solomon islands region, *Journal of the Geological Society of Australia*, *20*, 21–36.

D'Addario, G., D. Dow, and R. Swoboda (1976), Geology of papua new guinea, 1:2,500,000, *Bureau of Mineral Resources, Australia.*

Das, B. M. (2008), *Advanced soil mechanics*, third ed., Taylor & Francis, London and New York.

Davies, H. L. (1973), Gazelle peninsula, new britain. 1:250 000 geological series-explanatory notes, *Australian Bureau of Mineral Resources, Geology and Geophysics, Canberra.*

Davies, H. L. (2012), The geology of new guinea-the cordilleran margin of the australian continent, *EPISODES*, *35*(1), 87–102.

Davies, H. L., P. A. Symonds, and I. D. Ripper (1984), Structure and evolution of the southern solomon sea region, *BMR Journal of Australian Geology and Geophysics*, *9*, 49–58.

Davis, J. C. (2002), Statistics and data analysis in geology.

Dawson, J., and P. Tregoning (2007), Uncertainty analysis of earthquake source parameters determined from InSAR: A simulation study, *Journal of Geophysical Research*, *112*(B09406), 1–13.

De Natale, G., and F. Pingue (1993), Ground deformations in collapsed caldera structures, *Journal of Volcanology and Geothermal Research*, *57*, 19–38.

De Natale, G., and F. Pingue (1996), Ground deformation modeling in volcanic areas, in *Monitoring and Mitigation of Volcano Hazards*, pp. 365–388, Springer Berlin Heidelberg.

De Natale, G., S. M. Petrazzuoli, and F. Pingue (1997), The effect of collapse structures on ground deformations in calderas, *Geophysical Research Letters*, *24*(13), 1555–1558.

Decriem, J., et al. (2010), The 2008 May 29 earthquake doublet in SW Iceland, *Geophysical Journal International*, *181*(2), 1128–1146.

Denham, D. (1969), Distribution of earthquakes in the new guinea-solomon islands region, *Journal of Geophysical Research*, *74*, 4290–4299.

Dieterich, J. H., and R. W. Decker (1975), Finite element modeling of surface deformation associated with volcanism, *Journal of Geophysical Research*, *80*(29), 4094–4102.

Dow, D. (1977), A geological synthesis of papua new guinea, in *Bureau of Mineral Resources Geology & Geophysics Bulletin*, vol. 201, Camberra, Australia.

Dragoni, M., and C. Magnanensi (1989), Displacement and stress produces by a pressurized, spherical magma chamber, surrounded by a viscoelastic shell, *Physics of Earth and Planetary Interiors*, *56*, 316–328.

Dzurisin, D. (2007), *Volcano Deformation: Geodetic Monitoring Techniques*, Springer, Berlin.

Eissa, E. A., and A. Kazi (1989), Relation between static and dynamic young's moduli of rocks, *International Journal of Rock Mechanics and Mining Science*, *25*, 479–482.

Emeleus, T. G. (1977), Thermo-magnetic measurements as a possible tool in the prediction of volcanic activity in the volcanoes of the rabaul caldera, papua new guinea, *Journal of Volcanology and Geothermal Research*, *2*, 343–359.

Ernst, G., M. Kervyn, and R. Teeuw (2008), Advances in the remote sensing of volcanic activity and hazards, with special consideration to applications in developing countries. international journal of remote sensing, *International Journal of Remote Sensing*, *29*(22), 6687–6723.

EROS (2011), Earth resources observation and science (eros) center, u.s. geological survey. http://earthexplorer.usgs.gov.

Falvey, D. A., and T. Pritchart (1982), Preliminary paleomagnetic results from northern papua new guinea: Evidence for large microplate rotations, in *Transactions of the Third Circum-Pacific Energy and Mineral Resources Conference, Am. Assoc. of Pet. Geol.*, pp. 593–599, Tulsa, Oklahoma.

Fernández, J., J. B. Rundle, R. D. Granell, and T.-T. Yu (1997), Programs to compute deformation due to a magma intrusion in elastic-gravitational layered earth models, *Computers & Geosciences*, *23*(3), 231–249, doi:http://dx.doi.org/10.1016/S0098-3004(96)00066-0.

Ferretti, A., C. Prati, and F. Rocca (2001), Permanent scatterers in sar interferometry, *Geoscience and Remote Sensing, IEEE Transactions on*, *39*(1), 8–20, doi:10.1109/36.898661.

Fialko, Y., M. Simons, and D. Agnew (2001), The complete (3-d) surface displacement field in the epicentral area of the 1999 mw 7.1 hector mine earthquake, california, from space geodetic observations, *Geophysical Research Letters*, *28*, 3063–3066.

Finlayson, D., and J. Cull (1973a), Time-term analysis of new britain-new ireland arc structures, *Geophys. J. R. Astron. Soc.*, *33*, 265–280.

Finlayson, D., and J. Cull (1973b), Structural profiles in the new britain/new ireland region, *J. Geol. Soc. Aust.*, *20*, 37–48.

Finlayson, D., O. Gudmundsson, I. Itikarai, Y. Nishimura, and H. Shimamura (2003), Rabaul volcano, papua new guinea: seismic tomographic imaging of an active caldera, *journal of Volcanology and Geothermal Research*, *124*, 153–171.

Fisher, N. (1939), Geology and vulcanology of blanche bay and the surrounding area, new britain, *Territory on New Guinea Geological Bulletin*, *1*, 1–68.

Fisher, N. (1976), 1941-1942 eruption of tavurvur volcano, rabaul papua new guinea, *Volcanism in Australia. Elsevier, Amsterdam*, pp. 201–219.

Fjaer, E. (1999), *Static and dynamic moduli of weak sandstones.*, Rock Mechanics for Industry, Balkema.

Folch, A., and J. Gottsmann (2006), Faults and ground uplift at active calderas, *Geological Society, London, Special Publications*, *269*(1), 109–120.

Folch, A., and J. Martí (2009), Time-dependent chamber and vent conditions during explosive caldera-forming eruptions, *Earth and Planetary Science Letters*, *280*(1-4), 246–253.

Francis, G., and D. H. Deibert (1988), Petroleum potential of the north new guinea basin and associated infra-basins, *Papua New Guinea Geological Survey Report 88/37*.

Freymueller, J., N. King, and P. Segall (1994), The co-seismic slip distribution of the landers earthquake, *Bull. Seismol. Soc. Am. 84*, pp. 646–659.

Frohlich, C. (2006), *Deep Earthquakes*, Cambridge University Press, Cambridge, England 23, 101-108, 267-279., Cambridge, England.

Fuchs, H., Z. Kedem, and S. Uselton (1977), Optimal surface reconstruction from planar contours, *Communication of the ACM*, *20*(10), 693–702.

Fukushima, Y., V. Cayol, and P. Durand (2005), Finding realistic dike models from interferometric synthetic aperture radar data: The February 2000 eruption at Piton de la Fournaise, *JOURNAL OF GEOPHYSICAL RESEARCH*, *110*(B03206).

Funning, G. J., R. Bürgmann, A. Ferretti, F. Novali, and A. Fumagalli (2007), Creep on the Rodgers Creek fault, northern San Francisco Bay area from a 10 year PS-InSAR dataset, *Geophysical Research Letters*, *34*(19), L19,306.

Gardner, G. H. F., L. W. Gardner, and A. R. Gregory (1974), Formation velocity and density-the diagnostic basics for stratigraphic traps, *Geophysics*, *39*, 770–780.

GEBCO (2011), General bathymetric chart of the oceans, british oceanographic data center. http://www.gebco.net.

Gercek, H. (2007), Poisson's ratio values for rocks, *International Journal of Rock Mechanics and Mining Sciences*, *44*(1), 1–13.

Geshi, N. (2005), Structural development of dike swarms controlled by the change of magma supply rate: the cone sheets and parallel dike swarms of the miocene otoge igneous complex, central japan, *Journal of Volcanology and Geothermal Research*, *141*, 264–281.

Geyer, A., and J. Gottsmann (2010), The influence of mechanical stiffness on caldera deformation and implications for the 1971-1984 rabaul uplift (papua new guinea), *Tectonophysics*, *483*, 399–412.

González, P. J., S. V. Samsonov, S. Pepe, K. F. Tiampo, P. Tizzani, F. Casu, J. Fernández, A. G. Camacho, and E. Sansosti (2013), Magma storage and migration associated with the 2011-2012 el hierro eruption: Implications for crustal magmatic systems at oceanic island volcanoes, *Journal of Geophysical Research: Solid Earth*, *118*(8), 4361–4377, doi:10.1002/jgrb.50289.

Goodman, R. (1989), *Introduction to Rock Mechanics*, 2nd ed., Wiley, New York, NY.

GoogleEarth (2014), https://earth.google.com.

Got, J.-L., V. Monteiller, J. Monteux, R. Hassani, and P. Okubo (2008), Deformation and rupture of the oceanic crust may control growth of hawaiian volcanoes, *Nature*, *451*(7177), 453–456.

Gottsmann, J., A. Folch, and H. Rymer (2006), Unrest at campi flegrei: A contribution to the magmatic versus hydrothermal debate from inverse and finite element modeling, *Journal of Geophysical Research*, *111*(B07203).

Graham, J., and G. Houlsby (1983), Anisotropic elasticity of a natural clay, *Géotechnique*, *33*(2), 165–180.

Graham, T., M. Swift, R. Johnson, J. Pittar, P. Musunamasi, and I. Kari (1993), Rabaul harbour heat flow project 1993 papua new guinea: Final report, *Tech. rep.*, Australian International Development Assistance Bureau.

Grandin, R., A. Socquet, M. Doin, E. Jacques, J. de Chabalier, and G. C. P. King (2010), Transient rift opening in response to multiple dike injections in the manda hararo rift (afar, ethiopia) imaged by time-dependent elastic inversion of interferometric synthetic aperture radar data, *Journal of Geophysical Research*, *115*(B09403).

Greene, G. H., D. L. Tiffin, and C. O. McKee (1986), Structural deformation and sedimentation in an active caldera, rabaul, papua new guinea, *Journal of Volcanology and Geothermal Research*, *30*, 327–356.

Griffin, T. (1983), Granitoids of the tertiary continent-island arc collision zone, papua new guinea, in *Circum-Pacific plutonic terranes: Geological Society of America Memoir*, vol. 159, edited by J. in Roddick, pp. 61–76.

Gubbins, D. (2004), *Time series analysis and inverse thepry for geophysicists*, Cambridge University Press.

Gudmundsson, A. (1984), Formation of dykes, feeder-dykes, and the intrusion of dykes from magma chambers, *Bulletin Volcanologique*, *47*(3), 537–550.

Gudmundsson, A. (2002), Emplacement and arrest of sheets and dykes in central volcanoes, *Journal of Volcanology and Geothermal Research*, *116*(3-4), 279–298.

Gudmundsson, A. (2006), How local stresses control magma-chamber ruptures, dyke injections, and eruptions in composite volcanoes, *Earth-Science Reviews*, *79*, 1–31.

Gudmundsson, A. (2008), *Magma-chamber geometry, fluid transport, local stresses, and rock behaviour during collapse-caldera formation*, pp. 313–349, Developments in Volcanology.

Gudmundsson, A. (2011), *Rock Fractures in Geological Processes*, Cambridge University Press, Cambridge, UK.

Gudmundsson, A., and S. Brenner (2004), How mechanical layering affects local stresses, unrests, and eruptions of volcanoes, *Geophysical Research Letters*, *31*(L16606).

Gudmundsson, A., and I. F. Loetveit (2005), Dyke emplacement in a layered and faulted rift zone, *Journal of Volcanology and Geothermal Research*, *144*(1-4), 311–327.

Gudmundsson, A., and S. L. Philipp (2006), How local stress fields prevent volcanic eruptions, *Journal of Volcanology and Geothermal Research*, *158*(3-4), 257–268.

Gudmundsson, O., R. Johnson, D. Finlayson, Y. Nishimura, H. Shimamura, A. Zerashima, I. Itikarai, and C. Thurber (1999), Multinational seismic investigation focuses on rabaul volcano., *Transactions of the American Geophysical Union*, *80*(24), 269–273.

Gudmundsson, O., D. M. Finlayson, I. Itikarai, Y. Nishimura, and W. R. Johnson (2004), Seismic attenuation at rabaul volcano, papua new guinea, *Journal of Volcanology and Geothermal Research*, *130*(1-2), 77–92.

Hall, R. (2002), Cenozoic geological and plate tectonic evolution of se asia and the sw pacific: computer-based reconstructions, model and animations, *Journal of Asian Earth Sciences*, *20*, 353–434.

Hamilton, E. L. (1979a), Vp/vs and poisson's ratios in marine sediments and rocks, *The Journal of the Acoustical Society of America*, *66*, 1093.

Hamilton, W. (1979b), Tectonics of the indonesian region, in *U.S. Geological Survey, Professional Paper 1078*, p. 345, Washington, DC.

Harrison, J. (1971), Investigations of crustal structure in the new britain/new ireland region, 1969. part1: Geophysical and geological data., in *Bureau of Mineral Resources*, edited by J.A.Brooks, Record 1971/131, pp. 26–28, Canberra, Australia.

Hautmann, S., J. Gottsmann, R. S. J. Sparks, G. S. Mattioli, I. S. Sacks, and M. H. Strutt (2010), Effect of mechanical heterogeneity in arc crust on volcano deformation with application to soufriÃšre hills volcano, montserrat, west indies, *JOURNAL OF GEOPHYSICAL RESEARCH*, *115*(B09203), 1–18.

Heap, M. J., S. Vinciguerra, and P. G. Meredith (2009), The evolution of elastic moduli with increasing damage during cyclic stressing of a basalt from mt. etna volcano, *Tectonophysics*, *471*, 153–160.

Heap, M. J., P. Baud, P. G. Meredith, S. Vinciguerra, and T. ReuschlÃ© (2014), The permeability and elastic moduli of tuff from campi flegrei, italy: implications for ground deformation modelling, *Solid Earth*, *5*, 25–44.

Helz, R. L. (2005), Monitoring ground deformation from space, *U.S. Geological Survey Fact Sheet 2005-3025*.

Heming, R. (1977), Mineralogy and proposed p-t paths of basaltic lavas from rabaul caldera, papua new guinea, *Contributions to Mineralogy and Petrology*, *61*(1), 15–33, doi:10.1007/BF00375943.

Heming, R., and I. Carmichael (1973), High-temperature pumice flows from the rabaul caldera papua, new guinea, *Contributions to Mineralogy and Petrology*, *38*(1), 1–20, doi:10.1007/BF00371723.

Heming, R. F. (1974), Geology and petrology of rabaul caldera, papua new guinea, *Geological Society of America Bulletin*, *85*, 1253–1264.

Hetland, E. A., P. Musé, M. Simons, Y. N. Lin, P. S. Agram, and C. J. DiCaprio (2012), Multiscale insar time series (mints) analysis of surface deformation, *Journal of Geophysical Research: Solid Earth*, *117*(B2404), 1–17, doi:10.1029/2011JB008731.

Heuze, F. (1980), *Scale effects in the determination of rock mass strength and deformability*, Rock Mech.

Hill, K., and R. Hall (2003), Mesozoic-cenozoic evolution of australia's new guinea margin in a west pacific context, *Geological Society of America, Special Paper*, *372*, 266–290.

Hoffmann, G., E. Silver, S. Day, E. Morgan, N. Driscoll, and D. Orange (2008), Sediment waves in the bismarck volcanic arc, papua new guinea, *Geological Society of America Special Paper 436*, pp. 91–126.

Hohnen, P. (1978), Geology of new ireland, papua new guinea, *Bureau of Mineral Resources, Australia, Bulletin*, *194*, 39.

Hole, J., C. Bromley, N. Stevens, and G. Wadge (2007), Subsidence in the geothermal fields of the taupo volcanic zone, new zealand from 1996 to 2005 measured by insar, *Journal of Volcanology and Geothermal Research*, *166*(3-4), 125–146.

Holloway, G., and M. Carroll (1994), *Volatiles in Magmas*, Rev. Mineral., Mineral. Soc. of Am., Washington, D. C.

Hooper, A., H. Zebker, P. Segall, and B. Kampes (2004), A new method for measuring deformation on volcanoes and other natural terrains using insar persistent scatterers, *Geophysical Research Letters*, *31*(L23611), 1–5, doi:10.1029/2004GL021737.

Hooper, A., P. Segall, and H. Zebker (2007), Persistent scatterer interferometric synthetic aperture radar for crustal deformation analysis, with application to volcÃ¡n alcedo, galÃ¡pagos, *Journal of Geophysical Research: Solid Earth*, *112*(B7407), 1–21, doi:10.1029/2006JB004763.

Hooper, A., D. Bekaert, K. Spaans, and M. Arikan (2012), Recent advances in sar interferometry time series analysis for measuring crustal deformation, *Tectonophysics*, *514-517*, 1–13.

Hsu, Y.-J., M. Simons, C. Williams, and E. Casarotti (2011), Three-dimensional fem derived elastic green's functions for the coseismic deformation of the 2005 mw 8.7 nias-simeulue, sumatra earthquake, *Geochemistry, Geophysics, Geosystems*, *12*(7), Q07,013.

Hughes, K. (2011), Coseismic and postseismic deformation of the great 2004 sumatra-andaman earthquake, Doctoral dissertation.

Huppert, H. E., and A. W. Woods (2002), The role of volatiles in magma chamber dynamics, *Nature*, *420*(6915), 493–495.

Hutchinson, D., and J. Dawson (2009), Satellite radar interferometry: Application to rabaul caldera, papua new guinea, *Tech. rep.*, Geoscience Australia.

Itikarai, I. (2008), The 3-d structure and earthquake locations at rabaul caldera, papua new guinea, Ph.D. thesis, Australian National University.

Jaeger, J., N. Cook, and R. Zimmerman (2007), *Fundamentals of rock Mechanics*, fourth edition ed., Wiley-Blackwell, Oxford.

Johnson, R. (1979), Geotectonics and volcanism in papua new guinea: a review of the late cainozoic, *BMR Journal of Australian Geology and Geophysics*, *4*, 181–207.

Johnson, R., C. McKee, S. Eggins, J. Woodhead, R. Arculus, and B. Chappel (1995), Taking petrologic pathways toward understanding rabaul's restells caldera, *Transaction of the American Geophysical Union*, *76*(17), 171–180.

Johnson, R. W., I. Itikarai, H. Patia, and C. McKee (2010), Volcanic systems of the northeastern gazelle peninsula, papua new guinea: Synopsis, evaluation, and a model for rabaul volcano, papua new guinea, in *Rabaul Volcano Workshop Report*, edited by P. N. G. D. of Mineral Policy, G. Management, and A. A. for International Development, Port Moresby, Papua New Guinea.

Johnson, T., and P. Molnar (1972), Focal mechanisms and plate tectonics of the southwest pacific, *JOURNAL OF GEOPHYSICAL RESEARCH*, *77*, 5000–5032.

Jones, R. H., and R. C. Stewart (1997), A method for determining significant structures in a cloud of earthquakes, *Journal of Geophysical Research: Solid Earth*, *102*(B4), 8245–8254, doi:10.1029/96JB03739.

Jónsson, S., H. Zebker, P. Segall, and F. Amelung (2002), Fault Slip Distribution of the 1999 Mw 7.1 Hector Mine, California, Earthquake, Estimated from Satellite Radar and GPS Measurements, *Bulletin of the Seismological Society of America*, *92*(4), 1377–1389.

Judd, W. R., Y. S. Touloukian, and R. F. Roy (1989), *Physical properties of rocks and minerals / edited by Y.S. Touloukian, W.R. Judd, R.F. Roy*, CINDAS data series on material properties. Group II, Properties of special materials ; vol. II-2, Hemisphere Pub. Corp, New York.

Karastathis, V., A. Ganas, M. J., J. Papoulia, P. Dafnis, E. Gerolymatou, and G. Drakatos (2007), The application of shallow seismic techniques in the study of active faults: The atalanti normal fault, central greece, *Journal of Applied Geophysics*, *62*, 215–233.

Kim, H. J., Y. Song, and K. H. Lee (1999), Inequality constraint in least-squares inversion of geophysical data, *Earth Planets Space*, *51*, 255–259.

Kohno, Y., T. Matsushima, and H. Shimizu (2008), Pressure sources beneath unzen volcano inferred from leveling and gps data, *Journal of Volcanology and Geothermal Research*, *175*(1-2), 100–109.

Krause, D. (1973), Crustal plates of the bismarck and solomon seas, in oceanography of the south pacific, in *Nat. Comm. for UNESCO*, edited by R. FRASER, pp. 271–280, Wellington.

Kroenke, L. W. (1984), Cenozoic tectonic development of the southwest pacific, *Tech. rep.*, Tech. Bulletin 6, Committee for Coordination of Joint Prospecting in South Pacific Offshore Areas (CCOP/SOPAC), United Nations Economic and Social Commission of Asia and the Pacific, CCOP/SOPAC.

Kümpel, H. J. (1991), Poroelasticity: parameters reviewed, *Geophysical Journal International*, *105*(3), 783–799.

Lagios, E., P. Papadimitriou, F. Novali, V. Sakkas, A. Fumagalli, K. Vlachou, and S. D. Conte (2012), Combined seismicity pattern analysis, DGPS and PSInSAR studies in the broader area of cephalonia (greece), *Tectonophysics*, *524-525*, 43–58, doi:http://dx.doi.org/10.1016/j.tecto.2011.12.015.

Lama, R., and V. Vutukuri (1978), *Handbook on Mechanical Properties of Rocks*, *Trans Tech Publications*, vol. 2, Clausthal, Germany.

Lee, S., and E. Ruellan (2006), Tectonic and magmatic evolution of the bismarck sea, papua new guinea: review and new synthesis, in *Back-Arc Spreading Systems, Geological, Biological, Chemical, and Physical Interactions: Geophys. Monogr. Ser.*, vol. 166, edited by F. C. L. S.-M. G. S. Chirstie, D.M., pp. 263–286.

L'Esperance, J. C., B. P. Boudreau, M. A. Barry, and B. D. Johnson (2013), Small-scale, high-precision and high-accuracy determination of poisson's ratios in cohesive marine sediments, *Geo-Marine Letters*, *33*(1), 75–81.

Lindley, D. (1988), Early cainozoic stratigraphy and structure of the gazella peninsula, east new britain: An example of extensional tectonics in the new britain arc-trench complex, *Australian Journal of Earth Sciences*, *35*, 231–244.

Lindley, I. (1989), Early cainozoic stratigraphy and structure of the gazelle peninsula, east new britain: An example of extensional tectonics in the new britain arc-trench complex, *Tech. rep.*, Geological Survey of Papua New Guinea Report 1989/1.

Lindley, I. (2006), Extensional and vertical tectonics in the new guinea islands:implication for island arc evolution, *Annals of Geophysics, Supplement to volume 49*, 403–426.

Lipman, P. W. (1997), Subsidence of ash-flow calderas: relation to caldera size and magma-chamber geometry, *Bulletin of Volcanology*, *59*(3), 198–218.

Lisowski, M. (2006), Analytical volcano deformation source models, in *Volcano Deformation*, Springer Praxis Books, pp. 279–304, Springer Berlin Heidelberg.

Lohman, R. B., and M. Simons (2005), Some thoughts on the use of insar data to constrain models of surface deformation: Noise structure and data downsampling, *Geochemistry Geophysics Geosystems*, *6*(Q01007), 1–12.

Lu, Z., and D. Dzurisin (2014), *InSAR Imaging of Aleutian Volcanoes: Monitoring a Volcanic Arc from Space*, Springer-Praxis, Chichester, UK.

Lu, Z., T. Masterlark, and D. Dzurisin (2005), Interferometric synthetic aperture radar study of okmok volcano, alaska, 1992-2003: Magma supply dynamics and postemplacement lava flow deformation, *Journal of Geophysical Research: Solid Earth*, *110*(B2), 1–18, doi:10.1029/2004JB003148.

Lundgren, P., and P. A. Rosen (2003a), Source model for the 2001 flank eruption of mt. etna volcano, *Geophysical Research Letters*, *30*(7), 411–414, doi:10.1029/2002GL016774.

Lundgren, P., and P. A. Rosen (2003b), Source model for the 2001 flank eruption of mt. etna volcano, *Geophysical Research Letters*, *30*(7), 1388.

Lungarini, L., C. Troise, M. Meo, and G. De Natale (2005), Finite element modelling of topographic effects on elastic ground deformation at mt. etna, *Journal of Volcanology and Geothermal Research*, *144*(1-4), 257–271.

Lyons, J. J., G. P. Waite, M. Ichihara, and J. M. Lees (2012), Tilt prior to explosions and the effect of topography on ultra-long-period seismic records at fuego volcano, guatemala, *Geophysical Research Letters*, *39*(8), L08,305.

Macnab, R. (1970), Geology of the gazelle peninsula, territory of papua new guinea record no. 1970163, *Bureau of Mineral Resources, Geology and Geophysics, 127*.

Madsen, J., and D. I. Lindley (1994), Large-scale structures on gazelle peninsula, new britain: Implications for the evolution if the new britain arc, *Australian Journal of Earth Sciences*, *41*, 561–569.

Malfait, W. J., R. Seifert, S. Petitgirard, M. Mezouar, and C. Sanchez-Valle (2014), The density of andesitic melts and the compressibility of dissolved water in silicate melts at crustal and upper mantle conditions, *Earth and Planetary Science Letters*, *393*(0), 31–38.

Manconi, A., T. R. Walter, and F. Amelung (2007), Effects of mechanical layering on volcano deformation, *Geophysical Journal International*, *170*(2), 952–958.

Manconi, A., T. R. Walter, M. Manzo, G. Zeni, P. Tizzani, E. Sansosti, and R. Lanari (2010), On the effects of 3-d mechanical heterogeneities at campi flegrei caldera, southern italy, *Journal of Geophysical Research: Solid Earth*, *115*(B8), B08,405.

Martinez, F., and B. Taylor (1996), Backarc spreading, rifting, and microplate rotation, between transform faults in the manus basin, *Marine Geophysical Researches*, *18*, 203–224.

Massonnet, D., and K. L. Feigl (1998), Radar interferometry and its application to changes in the earth's surface, *Reviews of Geophysics*, *36*(4), 441–500, doi:10.1029/97RG03139.

Massonnet, D., M. Rossi, C. Carmona, F. Adragna, G. Peltzer, K. Feigl, and T. Rabaute (1993), The displacement field of the landers earthquake mapped by radar interferometry, *Nature*, *364*(6433), 138–142.

Masterlark, T. (2003), Finite element model predictions of static deformation from dislocation sources in a subduction zone: Sensitivities to homogeneous, isotropic, poisson-solid, and half-space assumptions, *Journal of Geophysical Research*, *108*.

Masterlark, T. (2007), Magma intrusion and deformation predictions: sensitivities to the mogi assumptions, *Journal of Geophysical Research*, *112*(B06419).

Masterlark, T., and K. Hughes (2008), Next generation of deformation models for the 2004 m9 sumatra-andaman earthquake, *Geophysical Research Letters*, *35*(L19310), 1–5.

Masterlark, T., and Z. Lu (2004a), Transient volcano deformation sources imaged with interferometric synthetic aperture radar: Application to seguam island, alaska, *Journal of Geophysical Research*, *109*(B01401), 1–16.

Masterlark, T., and Z. Lu (2004b), Transient volcano deformation sources imaged with interferometric synthetic aperture radar: Application to seguam island, alaska, *Journal of Geophysical Research*, *109*(B01401), 1–16.

Masterlark, T., M. Haney, H. Dickinson, T. Fournier, and C. Searcy (2010), Rheologic and structural controls on the deformation of Okmok volcano, Alaska: FEMs, InSAR, and ambient noise tomography, *Journal of Geophysical Research: Solid Earth*, *115*(B2), B02,409.

Masterlark, T., K. L. Feigl, M. Haney, J. Stone, C. Thurber, and E. Ronchin (2012), Nonlinear estimation of geometric parameters in fems of volcano deformation: Integrating tomography models and geodetic data for okmok volcano, alaska, *Journal of Geophysical Research*, *117*(B02407), 1–17.

Mattioli, G. S., R. A. Herd, M. H. Strutt, G. Ryan, C. Widiwijayanti, and B. Voight (2010), Long term surface deformation of soufriÃšre hills volcano, montserrat from gps geodesy: Inferences from simple elastic inverse models, *Geophysical Research Letters*, *37*(19), L00E13.

McKee, C., J. Mori, and B. Talai (1989), Microgravity changes and ground deformation at rabaul caldera, 1973-1985, in *IAVCEI Proceedings in Volcanology*, edited by J. H. Latter, pp. 399–428, Springer, Berlin.

McKee, C. O., and P. de Sain-Ours (2000), How dangerous is rabaul volcano?, in *United Nations Disaster Assessment and Coordination Refresher Course*, PAPUA NEW GUINEA NATIONAL DISASTER MANAGEMENT OFFICE, Papua New Guinea.

McKee, C. O., P. Lowenstein, P. de Saint Ours, B. Talai, I. Itikarai, and J. Mori (1984), Seismic and ground deformation crises at rabaul caldera: prelude to an eruption?, *Bulletin of Volcanology*, *47*(2), 397–411.

McKee, C. O., R. Johnson, P. Lowenstein, S. Riley, R. Blong, P. de Saint Ours, and B. Talai (1985), Rabaul caldera, papua new guinea: volcanic hazards, suveillance, and eruption contingency planning, *Journal of Volcanology and Geothermal Research*, *23*, 195–237.

McKee, C. O., J. Mori, and B. Talai (1987), Microgravity changes and ground deformation at rabaul caldera, 1973-1985, *Geol. Sur. Papua New Guinea*, *Rep 87/29*.

McKee, C. O., V. E. Neall, and R. Torrence (2011), A remarkable pulse of large-scale volcanism on new britain island, papua new guinea, *Bulletin of Volcanology*, *73*, 27–37.

McTigue, D. F. (1987), Elastic stress and deformation near a finite spherical magma body: Resolution of the point source paradox, *JOURNAL OF GEOPHYSICAL RESEARCH*, *92*(B12).

Menke, W. (1989), *Geophysical data analysis: discrete inverse theory*, *INTERNATIONAL GEOPHYSICS SERIES*, vol. 45.

Meo, M., U. Tammaro, and P. Capuano (2008), Influence of topography on ground deformation at mt. vesuvius (italy) by finite element modelling, *International Journal of Non-Linear Mechanics*, *43*(3), 178–186.

Meyers, D., S. Skinner, and K. Sloan (1992), Surfaces from contours, *ACM Transaction on Graphics*, *11*, 228–258.

Minasny, B., A. B. McBratney, and D. J. Walvoort (2007), The variance quadtree algorithm: Use for spatial sampling design, *Computers & Geosciences*, *33*, 383–392.

Mogi, K. (1958), Relations between the eruptions of various volcanoes and the deformations of the ground surface around them, *Bull. Earthquake Res. Inst. Univ. Tokyo*, *36*, 99–134.

Morales, R. H., and R. P. Marcinew (1993), Fracturing of high-permeability formations: mechanical properties correlations, in *Society of Petroleum Engineers Annual Technical Conference and Exhibition, 3-6 October 1993*, vol. 26561, Houston, Texas.

Mori, J., and C. O. McKee (1987a), Outward-dipping ring-fault structure at rabaul caldera as shown by earthquake locations, *Science*, *235*, 193–135.

Mori, J., C. O. McKee, I. Itikarai, P. de Saint Ours, and B. Talai (1987b), Sea level measurements for inferring ground deformations in rabaul caldera, *Geo-Marine Letters*, *6*, 241–246.

Mori, J., C. O. McKee, I. Itikarai, P. Lowenstein, P. de Saint Ours, and B. Talai (1989), Earthquakes of the rabaul seismo-deformational crisis september 1983 to july 1985 seismicity on a ring fault, in *Volcanic Hazards: Assessment and Monitoring, IAVCEI Proceedings in Volcanology*, edited by J. H. Latter, pp. 429–462, Springer.

Morita, Y., S. Nakao, and Y. Hayashi (2006), A quantitative approach to the dike intrusion process inferred from a joint analysis of geodetic and seismological data for the 1998 earthquake swarm off the east coast of izu peninsula, central japan, *Journal of Geophysical Research: Solid Earth*, *111*(B6), B06,208.

Mossop, A., and P. Segall (1999), Volume strain within the geysers geothermal field, *Journal of Geophysical Research: Solid Earth*, *104*(B12), 29,113–29,131.

Nairn, I., C. O. McKee, B. Talai, and C. Wood (1995), Geology and eruptive history of the rabaul caldera area, papua new guinea, *Journal of Volcanology and Geothermal Research*, *69*, 255–284.

Newman, A., T. Dixon, G. Ofoegbu, and J. Dixon (2001), Geodetic and seismic constraints on recent activity at long valley caldera, california: evidence for viscoelastic rheology, *Journal of Volcanology and Geothermal Research*, *105*, 183–206.

Newman, A. V., T. Dixon, and N. Gourmelen (2006), A four-dimensional viscoelastic deformation model for long valley caldera, california, between 1995 and 2000, *Journal of Volcanology and Geothermal Research*, *150*, 244–269, doi:10.1016/j.jvolgeores.2005.07.017.

Nur, A., and J. Walder (1992), *Hydraulic pulses in the Earth's crust, in Fault Mechanics and Transport Properties of Rocks*, Academic, London.

Okada, Y. (1992), Internal deformation due to shear and tensile faults in a half-space, *Bulletin of the Seismological Society of America*, *82*(2), 1018–1040.

O'Kane, T. (2008), 3-d structure and tectonic evolution of the papua new guinea and solomons island region and its relationship to cu-au mineralisation, Unpublished bsc honours thesis, Australian National University.

Orsi, G., S. M. Petrazzuoli, and K. Wohletz (1999), Mechanical and thermofluid behavior during unrest at the campiflegrei caldera (italy), *Journal of Volcanology and Geothermal Research*, *91*, 453–470.

Page, R. (1976), Geochronology of igneous and metamorphic rocks in the new guinea highlands, *Bureau of Mineral Resources, Australia, Bulletin*, *162*, 117.

Page, R., and R. Ryburn (1977), K-ar ages and geological relations of intrusive rocks in new britain, *Pacific Geology*, *12*, 99–105.

Park, S., S. Lee, G. D. Kamenov, and S. Kwon (2010), Tracing the origin of subduction components beneath the south east rift in the manus basin, papua new guinea, *Chemical Geology*, *30*, 339–349.

Pascal, K., J. Neuberg, and E. Rivalta (2014), On precisely modelling surface deformation due to interacting magma chambers and dykes, *Geophysical Journal International*, *196*(1), 253–278.

Patia, H. (2004), Petrology and geochemistry of the recent eruption history at rabaul caldera. papua new guinea: implications for magmatic processes and recurring volcanic activity, Ph.D. thesis, Australian National University.

Pedersen, R., F. Sigmundsson, and T. Masterlark (2009), Rheologic controls on inter-rifting deformation of the northern volcanic zone, iceland, *Earth and Planetary Science Letters*, *281*, 14–26.

Perry, W., and I. Crick (1974), Aerial thermal infrared survey, rabaul area, papua new guinea. record 1974/097., Canberra, Australia.

Poland, M., R. Bürgmann, D. Dzurisin, M. Lisowski, T. Masterlark, S. Owen, and J. Fink (2006), Constraints on the mechanism of long-term, steady subsidence at medicine lake volcano, northern california, from gps, leveling, and insar, *Journal of Volcanology and Geothermal Research*, *150*, 55–78.

Pono, S. (1990), Caldera structures of rabaul harbour from seismic reflection profiles, sopac technical report 87, *Tech. rep.*, Geological Survey of Papua New Guinea.

Price, R., and A. Jones (1982), Uniaxial and compression test series on calico hills tuff, *Tech. rep.*, Sandia National Laboratories Report, SAND82-1314.

Priest, S. D. (1993), *Discontinuity Analysis for Rock Engineering*, Chapman&Hall, London.

Pritchard, M. E., and M. Simons (2004), An InSAR-based survey of volcanic deformation in the central Andes, *Geochemistry, Geophysics, Geosystems*, *5*(2), 1–42.

Pritchard, M. E., M. Simons, P. A. Rosen, S. Hensley, and F. H. Webb (2002), Co-seismic slip from the 1995 July 30 Mw =8.1 Antofagasta, Chile, earthquake as constrained by InSAR and GPS observations, *Geophysical Journal International*, *150*, 362–376.

Quantum GIS Development Team (2011), Quantum GIS Geographic Information System. Open Source Geospatial Foundation Project, http://qgis.osgeo.orgt.

Ramana, Y., and B. Venkatanarayana (1973), Laboratory studies on kolar rocks, *Int. J. Rock Mech. Min. Sci. Geomech. Abstr. 10*, pp. 465–489.

Reading, H. G. (1980), *Characteristics and Recognition of Strike-Slip Fault Systems*, pp. 7–26, Blackwell Publishing Ltd., doi:10.1002/9781444303735.ch2.

Rice, J. R., and M. P. Cleary (1976), Some basic stress diffusion solutions for fluid-saturated elastic porous media with compressible constituents, *REVIEWS OF GEOPHYSICS AND SPACE PHYSIC*, *14*(2).

Rice, J. R., and J. W. Rudnicki (1979), Earthquake precursory effects due to pore fluid stabilization of a weakening fault zone, *Journal of Geophysical Research*, *84*(B5).

Rodriguez-Losada, J. A., L. E. Hernández-Gutiérrez, C. Olalla, A. Perucho, A. Serrano, and A. Eff-Darwich (2009), Geomechanical parameters of intact rocks and rock masses from the canary islands: Implications on their flank stability, *Journal of Volcanology and Geothermal Research*, *182*(1-2), 67–75.

Roggensack, K., S. N. Williams, S. J. Schaefer, and R. A. Parnell Jr. (1996), Volatiles from the 1984 eruptions of rabaul: Understanding large caldera systems, *Science*, *273*, 490–493.

Romeyn, R., and M. Garthwaite (2012), Broad-scale volcano monitoring in papua new guinea using satellite interferometric synthetic aperture radar, *Tech. rep.*, Geoscience Australia.

Ronchin, E., T. Masterlark, J. MartÃ, S. Saunders, and W. Tao (2013), Solid modeling techniques to build 3d finite element models of volcanic systems: An example from the rabaul caldera system, papua new guinea, *Computers & Geosciences*, *52*, 325–333.

Rosen, P. A., S. Hensley, H. A. Zebker, F. H. Webb, and E. Fielding (1996), Surface deformation and coherence measurements of kilauea volcano, hawaii from sir-c radar interferometry, *Journal of Geophysical Research*, *101*(E10), 23 109–23 125.

Rosenqvist, A., M. Shimada, N. Ito, and M. Watanabe (2007), Alos palsar: A pathfinder mission for global-scale monitoring of the environment, *IEEE Trans. Geosci. Remote Sens.*, *45*(11), 3307–3316.

Rubin, A., and D. Pollard (1987), Origin of blade-like dikes in volcanic rift zones, *U.S. Geol. Surv. Prof. Pap.*, *1350*, 1449–1470.

Rundle, J. B. (1980), Static elastic-gravitational deformation of a layered half space by point couple sources, *Journal of Geophysical Research: Solid Earth*, *85*(B10), 5355–5363, doi:10.1029/JB085iB10p05355.

Ryburn, R. (1971), Geoloy, in *Investigations of crustal structure in the New Britain/New Ireland region, 1969 Geophysical and geological data, Bureau of Mineral Resources, Geology and Geophysics, Aust. Rec. 1970/62*, edited by J. A. Brooks, Canberra.

Ryburn, R. (1974), Pomio, new britain, 1:250 000 geological series-explanatory notes, *Tech. rep.*, Bureau of Mineral Resources, Geology & Geophysics.

Ryburn, R. (1975), Talasea-gasmata sheet sb/56-5 1:250 000 geological series-explanatory notes, *Tech. rep.*, Aust. Gov. Publ. Service.

Rzhevsky, V., and G. Novick (1971), *The Physics of Rocks*, MIR Publ.

Samet, H. (1990), *The Design and Analysis of Spatial Data Structures*, Addision Wesley Publishing Compnay, Inc., Reading, UK.

Samet, H., and R. E. Webber (1988), Hierarchical data structures and algorithms for computer graphics. I. Fundamentals, *Computer Graphics and Applications, IEEE*, *8*(3), 48–68.

Samsonov, S. (2010), Topographic correction for alos palsar interferometry, *IEEE Trans. Geosci. Remote Sens.*, *48*(7), 3020–3027.

Samsonov, S., J. Beavan, P. J. Gonzalez, K. Tiampo, and J. Fernandez (2011), Ground deformation in the taupo volcanic zone, new zealand, observed by alos palsar interferometry, *Geophysical Journal International*, *187*, 147–160.

Sandwell, D. T., D. Myer, R. Mellors, M. Shimada, B. Brooks, and J. Foster (2008), Accuracy and resolution of alos interferometry: Vector deformation maps of the father's day intrusion at kilauea, *IEEE TRANSACTIONS ON GEOSCIENCE AND REMOTE SENSING*, *46*(11).

Saunders, S. (2014), Extensional features at a convergent plate boundary. implication for plate dynamics and volcanism in the gazelle peninsula, papua new guinea. report in prep., *Tech. rep.*, Department of mineral policy & geohazards management, Rabaul Volcano Observatory, Papua New Guinea.

Saunders, S., H. Patia, F. Taranu, J. Kuduon, J. Cowlyn, and Y. Nishimura (2007), How to deal with unpredictable volcanoes in a developing country. cities on volcanoes conference abstracts.

Saunders, S. J. (2001), The shallow plumbing system of rabaul caldera: a partially intruded ring fault?, *Bulletin of Volcanology*, *63*, 406–420.

Saunders, S. J. (2005), The possible contribution of circumferential fault intrusion to caldera resurgence, *Bulletin of Volcanology*, *67*, 57–71.

Sawicki, A., and W. Świdziński (2007), Simple mathematical model for assessment of seismic-induced liquefaction of soils, *J. Waterway, Port, Coastal, Ocean Eng.*, *133*(1), 50–54.

Schön, J. (2004), *Physical Properties of Rocks: Fundamentals and Principles of Petrophysics*, Elsevier, Oxford.

Sedze, M., E. Heggy, F. Bretar, D. Berveiller, and S. Jacquemoud (2012), L-band insar decorrelation analysis in volcanic terrains using airborne lidar data and in situ measurements: The case of the piton de la fournaise volcano, france, in *Geoscience and Remote Sensing Symposium (IGARSS), 2012 IEEE International*, pp. 3907–3910.

Segall, P. (2010), *Earthquake and volcano deformation*, Princeton, N.J.

Shultz, R., and Q. Li (1995), Uniaxial strength testing of non-welded calico hills tuff, yucca mountain, nevada, *Engineering Geology*, *40*, 287–299.

Simmons, G., and W. F. Brace (1965), Comparison of static and dynamic measurements of compressibility of rocks, *Journal of Geophysical Research*, (70), 5649–5656.

Simons, M., Y. Fialko, and L. Rivera (2002), Coseismic Deformation from the 1999 Mw 7.1 Hector Mine, California, Earthquake as Inferred from InSAR and GPS Observations, *Bulletin of the Seismological Society of America*, *92*(4), 1390–1402.

Smith, I. E. M., and R. W. Johnson (1981), Contrasting rhyolite suites in the late cenozoic of papua new guinea, *Journal of Geophysical Research: Solid Earth*, *86*(B11), 10,257–10,272, doi: 10.1029/JB086iB11p10257.

Smithsonian Institution-National Museum of Natural History, G. V. P. (2011), Bulletin of the global volcanism network, *36*(7).

Smithsonian Institution-National Museum of Natural History, G. V. P. (2013), *Global Volcanism Program Report for Rabaul. http://www.volcano.si.edu.*

Struckmeyer, H., M. Yeung, and C. Pigram (1993), Mesozoic to cainozoic plate tectonics and palaeogeographic evolution of the new guinea region, in *Petroleum Exploration and Development in Papua New Guinea: Proceedings of the Second PNG Petroleum Convention*, edited by G. C. Carman and Z., pp. 262–290, PNG Chamber of Mines and Petroleum, Port Moresby.

Sturkell, E., F. Sigmundsson, and R. Slunga (2006), 1983-2003 decaying rate of deflation at askja caldera: Pressure decrease in an extensive magma plumbing system at a spreading plate boundary, *Bulletin of Volcanology*, *68*(7), 727–735.

Sturkell, E., et al. (2008), Seismic and geodetic insights into magma accumulation at katla subglacial volcano, iceland: 1999 to 2005, *Journal of Geophysical Research: Solid Earth*, *113*(B3), B03,212.

Stüwe, K. (2007), *Geodynamics of the lithosphere: an introduction*, Springer, Berlin.

Sudhaus, H., and S. Jónsson (2009), Improved source modelling through combined use of InSAR and GPS under consideration of correlated data errors: application to the June 2000 Kleifarvatn earthquake, Iceland, *Geophysical Journal International*, *176*(2), 389–404.

Syracuse, E., and G. Abers (2006), Global compilation of variations in slab depth beneath arc volcanoes and implications, *Geochemistry Geophysics Geosystems*, *7*(Q05017).

Tait, S., C. Jaupart, and S. Vergniolle (1989), Pressure, gas content and eruption periodicity of a shallow, crystallising magma chamber, *Earth and Planetary Science Letters*, *92*(1), 107–123.

Taylor, B. (1979), Bismarck sea: evolution of a back-arc basin, *Geology*, *7*, 171–174.

Taylor, B. (1991), Rabaul caldera, papua new guinea, seamarc ii sidescan sonar imagery, aerial photography, bathymetry, and topography, 1:25,000, pacific seafloor atlas, sheet no. 8.

Taylor, B., K. Crook, and J. Sinton (1994), Extensional transform zones and oblique spreading centers, *Journal of Geophysical Research: Solid Earth*, *99*(B10), 19,707–19,718, doi:10.1029/94JB01662.

Telford, W. M., L. P. Geldart, R. E. Sheriff, and D. A. Keys (1976), *Applied Geophysics*, Cambridge University Press, Cambridge.

Tiģrek, S., E. C. Slob, M. W. P. Dillen, S. A. P. L. Cloetingh, and J. T. Fokkema (2005), Linking dynamic elastic parameters to static state of stress: toward an integrated approach to subsurface stress analysis, *Tectonophysics*, *397*(1-2), 167–179.

Trasatti, E., C. Giunchi, and M. Bonafede (2003), Effects of topography and rheological layering on ground deformation in volcanic regions, *Journal of Volcanology and Geothermal Research*, *122*.

Trasatti, E., C. Giunchi, and M. Bonafede (2005), Structural and rheological constraints on source depth and overpressure estimates at the campi flegrei caldera, italy, *Journal of Volcanology and Geothermal Research*, *144*(1-4), 105–118.

Trasatti, E., C. Giunchi, and N. P. Agostinetti (2008), Numerical inversion of deformation caused by pressure sources: application to mount etna (italy), *Geophys.J.Int.*, *172*, 873–884.

Trautmann, C., and F. Kulhawy (1987), A computer program for compress and uplift foundation analysis and design, *Tech. rep.*, Electrical Power and Research Institute.

Tregoning, P. (2002), Plate kinematics in the western pacific derived from geodetic observations, *Journal of Geophysical Research*, *107*(B1), 1–8.

Tregoning, P., and H. McQueen (2001), Resolving slip-vector azimuths and plate motion along the southern boundary of the south bismarck plate, papua new guinea, *Australian Journal of Earth Sciences*, *48*, 745–750.

Tregoning, P., R. Jackson, H. McQueen, K. Lambeck, C. Stevens, R. Little, R. Curley, and R. Rosa (1999), Motion of the south bismarck plate, papua new guinea, *Geophysical Research Letters*, *26*, 3517–3520.

Tregoning, P., H. McQueen, K. Lambeck, R. Jackson, R. Little, S. Saunders, and R. Rosa (2000), Present-day crustal motion in papua new guinea, *Earth Planets Space*, *52*, 727–730.

Tregoning, P., et al. (1998), Estimation of current plate motions in papua new guinea from global positioning system observations, *Journal of Geophysical Research*, *103*(B6), 12,181–12,203.

Troise, C., F. Pingue, and G. De Natale (2003), Coulomb stress changes at calderas: Modeling the seismicity of campi flegrei (southern italy), *Journal of Geophysical Research: Solid Earth*, *108*(B6), 2292.

Turcotte, D. L., and G. J. Schubert (2002), *Geodynamics: Applications of Continuum Physics to Geological Problems*, 2nd ed. ed., New York.

Tutuncu, A. N., A. L. Podio, A. R. Gregory, and M. M. Sharma (1998), Nonlinear viscoelastic behavior of sedimentary rocks, part 1: Effect of frequency and strain amplitude, *Geophysics*, *63*(1), 184–194.

Van der Laat, R. (1996), Ground-deformation methods and results, in *Monitoring and Mitigation of Volcano Hazards*, edited by R. S. Tilling and R.I., pp. 147–168, Springer Verlag, Berlin.

Vasco, D. W., K. Karasaki, and C. Doughty (2000), Using surface deformation to image reservoir dynamics, *Geophysics*, *65*(1), 132–147.

Vasco, D. W., C. Wicks, K. Karasaki, and O. Marques (2002), Geodetic imaging: reservoir monitoring using satellite interferometry, *Geophysical Journal International*, *149*(3), 555–571.

Vilardo, G., R. Isaia, G. Ventura, P. D. Martino, and C. Terranova (2010), Insar permanent scatterer analysis reveals fault re-activation during inflation and deflation episodes at campi flegrei caldera, *Remote Sensing of Environment*, *114*(10), 2373–2383, doi:http://dx.doi.org/10.1016/j.rse.2010.05.014.

VOGRIPA (2013), http://www.bgs.ac.uk/vogripa/index.cfm.

Walker, G., R. F. Heming, T. Sprod, and H. Walker (1981), Latest major eruptions of rabaul volcano, *Volume of Volcanological Papers. Geol.Surv. Papua New Guinea, Mem., 10*, 181–193.

Wallace, L. M., et al. (2004), Gps and seismological constraints on active tectonics and arc-continent collision in papua new guinea: Implications for mechanics of microplate rotations in a plate boundary zone, *Journal of Geophysical Research*, *109*(B05404).

Wang, H. F. (2000), *Theory of Linear Poroelasticity: With Applications to Geomechanics*, Princeton Univ. Press, Princeton, N. J.

Wang, H. F., and M. P. Anderson (1982), *Introduction to Groundwater Modeling: Finite Differences and Finite Element Methods*, Academic, San Diego, Calif.

Watters, R. J., D. R. Zimbelman, S. D. Bowman, and J. K. Crowley (2000), Rock mass strength assessment and significance to edifice stability, mount rainier and mount hood, cascade range volcanoes, *pure and applied geophysics*, *157*(6-8), 957–976.

Weissel, J., B. Taylor, and G. Karner (1982), The opening of thewoodlark basin, subduction of thewoodlark spreading system, and the evolution of northern melanesia sincemid-pliocene time, *Tectonophysics*, *87*, 253–277.

Wesley, L. D. (2009), *Fundamentals of Soil Mechanics for Sedimentary and Residual Soils*, John Wiley and Sons Ltd, New York.

Wicks, C., C. Weaver, P. Bodin, and B. Sherrod (2013), InSAR Evidence for an active shallow thrust fault beneath the city of Spokane Washington, USA, *Journal of Geophysical Research: Solid Earth*, *118*(3), 1268–1276.

Wiebenga, W. (1973), *Crustal Structure of the New Britain-New Ireland Region, in The Western Pacific: Island Arcs, Marginal Seas, Geochemistry*, University of Western Australia Press, Nedlands.

Williams, C. A., and G. Wadge (2000), An accurate and efficient method for including the effects of topography in three-dimensional elastic models of ground deformation with applications to radar interferometry, *Journal of Geophysical Research*, *105*(B4), 8103–8120.

Wood, C., I. Nairn, C. O. McKee, and B. Talai (1995), Petrology of the rabaul caldera area, papua new guinea, *Journal of Volcanology and Geothermal Research*, *69*, 285–302.

Woodhead, J., and R. Johnson (1993), Isotope and trace element profiles across the new britain island arc, papua new guinea, *Contributions to Mineralogy and Petrology*, *113*, 479–491.

Woodhead, J., S. Eggins, and R. Johnson (1998), Magma genesis in the new britain island arc: further insights into melting and mass transfer processes, *Journal of Petrology*, *39*, 1641–1668.

Woods, A. W., and H. E. Huppert (2003), On magma chamber evolution during slow effusive eruptions, *Journal of Geophysical Research: Solid Earth*, *108*(B8), 2403.

Wright, T. J., Z. Lu, and C. Wicks (2003), Source model for the Mw 6.7, 23 October 2002, Nenana Mountain Earthquake (Alaska) from InSAR, *Geophysical Research Letters*, *30*(18), 1974.

Wright, T. J., C. Ebinger, J. Biggs, A. Ayele, G. Yirgu, D. Keir, and A. Stork (2006), Magma-maintained rift segmentation at continental rupture in the 2005 afar dyking episode, *Nature*, *442*(7100), 291–294.

Yan, C., and L. Kroenke (1993), A plate tectonic reconstruction of the southwest pacific, 0-100ma, *Proceedings of the Ocean Drilling Program, Scientific Results 130*, pp. 697–709.

Yang, X., P. M. Davis, and J. Dieterich (1988), Deformation from inflation of a dipping finite prolate spheroid in an elastic half-space as a model for volcanic stressing, *Journal of Geophysical Research*, *93*(B5), 4249–4257.

Young, P. G., T. B. H. Beresford-West, S. R. L. Coward, B. Notarberardino, B. Walker, and A. Abdul-Aziz (2008), An efficient approach to converting three-dimensional image data into highly accurate computational models, *Philosophical Transaction of the Royal Society*, *366*, 3155–3173.

Yun, S., P. Segall, and H. A. Zebker (2006), Constraints on magma chamber geometry at Sierra Negra Volcano, Galapagos Islands, based on InSAR observations, *Journal of Volcanology and Geothermal Research*, *150*, 232–243.

Zebker, H., and J. Villasenor (1992), Decorrelation in interferometric radar echoes, *IEEE Transactions on Geoscience and Remote Sensing*, *30*(5), 950–959.

Zebker, H. A., P. A. Rosen, R. M. Goldstein, A. Gabriel, and C. L. Werner (1994), On the derivation of coseismic displacement fields using differential radar interferometry: The landers earthquake, *Journal of Geophysical Research: Solid Earth*, *99*(B10), 19,617–19,634, doi:10.1029/94JB01179.

Zebker, H. A., P. A. Rosen, and S. Hensley (1997), Atmospheric effects in interferometric synthetic aperture radar surface deformation and topographic maps, *Journal of Geophysical Research: Solid Earth*, *102*(B4), 7547–7563, doi:10.1029/96JB03804.

Zhang, Z., J. Zhou, and N. Zhou (2005), Shape optimization using reproducing kernel particle method and an enriched genetic algorithm, *Computer Methods in Applied Mechanics and Engineering*, *194*, 4048–4070.

Appendix A

Script to generate closed splines in Abaqus (CAESPLINE.py)

Introduction

This appendix provides a guide for preparing the .txt file containing the cPt coordinates, the explanation for CAESPLINE.py script, and instructions to run the Python executable script in the Abaqus CAE environment.

File format for the cPt coordinates

In the text file, the control point coordinates (X_i, Y_i, Z_i) have to be recorded in three columns, one for each Cartesian coordinate component. The points need to be specified in the order tin which the spline passes through them. Finally, the first and the last point have to be coincident in order to ensure the creation of a closed spline (A.0.1, a and b). The coordinates don not need to be grouped by depths.

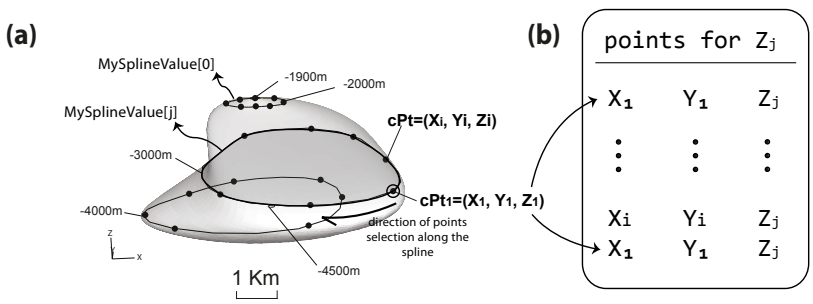

Figure A.0.1. Creation of close splines.
a) Example of control points along the splines (black points on the contour). b) Example of input.txt format for point coordinates of the j-spline.

The CAESPLINE.py script

All processes of importing points and generating closed splines are automated in the CAESPLINE.py script. The script reads the input .txt file, imports the control point coordinates, recognizes the different depth values (Z_j) encountered in the file through the group index group I=2, and calls the Abaqus function WireSpline, which generates a series of planar closed loops (one spline contour for each depth value encountered).

```
###########################################################################################
####                        Create wires from data points                              ####
###########################################################################################

from abaqus import*
from part import*
```

The user needs to define the name of the CAE Abaqus model in which the control points will be imported and the closed splines generated. By default, each new Abaqus model built in CAE is named "Model-1."

```
##################################
## --START USER INPUTS:
#--1) CHOOSE THE CAE MODEL NAME (example: Model-1) in which you want to build the
    closed splines
m=mdb.models['Model-1']
```

The Python code creates a 3-dimensional, deformable part whose name can be modified by the user, by replacing the default "part_splines":

```
#--2) CHOOSE THE SPLINES PART NAME
#- creates a three-dimensional, deformable part (name example: part_splines)
myPart=m.Part(name='part_splines', dimensionality=THREE_D, type=DEFORMABLE_BODY)
```

The user needs to provide the path of the .txt input data file containing the coordinates of the control points, cPT. Instructions about the format of the .txt file are provided in the text (Chapter 3.3).

```
#--3) SET THE PATH FOR THE .txt DATA FILE
#- read the .txt file from the path (C:\....txt) containing the coordinates of the
    control points
myDataFileS=open('C:\Rabaul_model\loft_create\chams.txt', 'r')
##################################
##--END USER INPUTS
```

Do not modify the script from this point. Abaqus CAE reads and imports the control point coordinates of closed contours from a text file through the first commands of the script.

```
#------------------------------------------------------------------------ START PROCEDURE
###--DO NOT CHANGE THE FILE FROM THIS POINT!
#--  IMPORT THE DATA POINTS and create the splines
myDataLinesS=myDataFileS.readlines()
myPointsListS=[eval(dataLine) for dataLine in myDataLinesS]
#- check the control points imported
print myPointsListS;

#- SORT THE CONTROL POINTS BASED ON THEIR DEPTH Z (index number 2 is the one that
    refers to the third coordinate, z)
groupI=2
```

```
zlist=sorted(elem[groupI] for elem in myPointsListS)
#- check the depths
print zlist

#- find the different values of depths and store them MySplineValue
MySplineValue=[]
MySplineValue.extend([0])
MySplineValue[0]=zlist[0]
print MySplineValue[0]
n=0
for i in range(len(zlist)):
    z=zlist[i]
    if z!= MySplineValue[n]:
        n=n+1
        MySplineValue.extend([n])
        MySplineValue[n]=z

#print MySplineValue

#- GENERATE THE SPLINES: for each z found (each MySplineValue), generate the closed
    spline
MySplineS=[]
for j in range(len(MySplineValue)):
    MySplineS.extend([j])
    MySplineS[j]= myPart.WireSpline(points=([elem for elem in myPointsListS if elem[
        groupI] == MySplineValue[j]]),smoothClosedSpline=ON)
#------------------------------------------------------------------------ END PROCEDURE
```

After the selection of the control points, cPt, the preparation of the .txt input file, and the compilation of the inputs necessary to properly run the script, the CAESPLINE.py script can be called and executed in Abaqus CAE by selecting: File→ Run script from the main menu bar (Fig. A.0.2). The outputs produced using the input file chams.txt are the closed spline contours generated in Abaqus CAE (Fig. A.0.2).

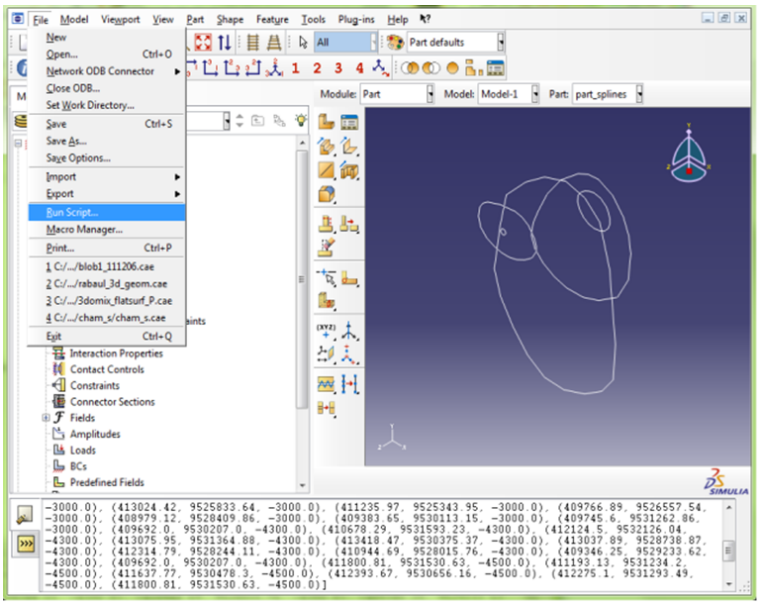

Figure A.0.2. Run script procedure and splines output in Abaqus CAE.

Appendix B

IDL procedure to compile the Laplacian operator (case with regular grid and Dirichlet boundary conditions equal zero)

The Laplacian operator of sources distributed on a regular grid with Dirichlet boundaries equal to zero is compiled in IDL with the following procedure (";" indicates the commented lines in IDL).

```
pro L3D,ne1,ne2,ne3,S,L

;-number of total sources
nsources=ne1*ne2*ne3
```

Where ne1, ne2, ne3 are the number of sources in the counting directions (1-first counting direction, 2-second counting direction, and 3-third counting direction). Example of an array of 4x4x4: ne1=4; ne2=4; ne3=4.

```
;-Structure of the sources (S): IDs of the sources in the 3-D array
S=dblarr(ne1,ne2,ne3)

for n=0,nsources-1 do begin
        nn=1
        for k=0,ne3-1 do begin
                for j=0,ne2-1 do begin
                        for i=0,ne1-1 do begin
                                S[i,j,k]=nn
                                nn=nn+1
                        endfor
                endfor
        endfor
endfor
```

Construction of Laplacian operator matrix (**L**). For each source (central node of the 7-nodes stencil) of S, in order of index, we populate the corresponding row of L with the values of the stencil nodes (Fig. B.0.1, c). The elements within the rows are filled with the values of stencil nodes accordingly with the node ID in the source structure.

```
;Laplacian operator (L) with Dirichlet boundary conditions:
```

```
L=dblarr(nsources,nsources)
nn=0

for k=0,ne3-1 do begin
        for j=0,ne2-1 do begin
                for i=0,ne1-1 do begin
```

Record -6. at the position of the central node (source).

```
                        L[k*(ne1*ne2)+j*ne1+i,nn]=-6.
```

Record 1. at the position of the satellite nodes of the 7-nodes stencil if they fall inside the array.

```
                        if ((i-1) GE 0.) then begin
                        L[k*(ne1*ne2)+j*ne1+(i-1),nn]=1.
                        endif

                        if ((i+1) LE ne1-1) then begin
                        L[k*(ne1*ne2)+j*ne1+(i+1),nn]=1.
                        endif

                        if ((j-1) GE 0.) then begin
                        L[k*(ne1*ne2)+(j-1)*ne1+i,nn]=1.
                        endif

                        if ((j+1) LE ne2-1) then begin
                        L[k*(ne1*ne2)+(j+1)*ne1+i,nn]=1.
                        endif

                        if ((k-1) GE 0.) then begin
                        L[(k-1)*(ne1*ne2)+j*ne1+i,nn]=1.
                        endif

                        if ((k+1) LE ne3-1) then begin
                        L[(k+1)*(ne1*ne2)+j*ne1+i,nn]=1.
                        endif

                        nn=nn+1
                endfor
        endfor
endfor
end
```

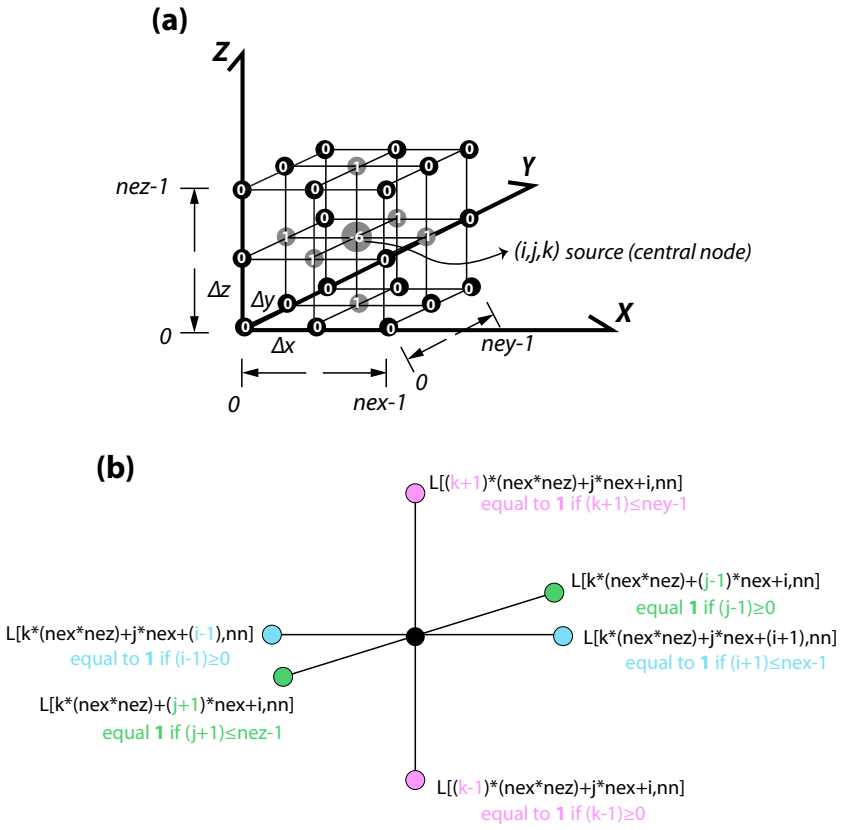

Figure B.0.1. Stencils and IDL indexes.

(a) 3-D distribution of nodes. The number of nodes along the three directions is: first counting direction (ne1)=*nex*, second counting direction (ne2)=*ney*, and third counting direction (ne3)=*nez*. IDL indexing in italics. Gray nodes correspond to the 7-nodes 3-D stencil of the Laplacian operator for the central node. For the stencil considered, in white are the values of all nodes that are used to populate the row of Laplacian operator matrix corresponding to the central node of the stencil. For each node, a row of the Laplacian matrix is populated with the values of the nodes according to the stencil and surrounding nodes' values (stencil configuration). The Laplacian operator is thus a matrix generated by the contribution of all stencils' configuration. The IDL node indices are indicated in italics. (b) IDL index in L matrix of each node of the 7-node stencil; used to populate the L matrix.